VNIVERSIDAD NACIONAL AVTENOMA DE MEXICO

UNIVERSIDAD NACIONAL AUTONOMA DE MEXICO

PROGRAMA DE MAESTRIA Y DOCTORADO EN INGENIERIA

FACULTAD DE INGENIERIA

ESTUDIO DE FACTIBILIDAD PARA OBTENER IMAGENES DE ALTO CONTRASTE CON EL INSTRUMENTO FRIDA

T E S I S

QUE PARA OPTAR POR EL GRADO DE:

DOCTOR EN INGENIERIA

INGENIERIA ELECTRICA - INTRUMENTACION

P R E S E N T A :

MAMADOU N'DIAYE

TUTORES:
DR. SALVADOR CUEVAS CARDONA
DR. KJETIL DOHLEN

2009

JURADO ASIGNADO:

Presidente:	DR.	ROBERTO ORTEGA MARTINEZ
Secretario:	DRA.	CELIA ANGELINA SANCHEZ PEREZ
1 er. Vocal:	DR.	SALVADOR CUEVAS CARDONA
2 do. Vocal:	DR.	REMY FERNAND AVILA FOUCAT
3 er. Vocal:	DR.	NEIL CHARLES BRUCE DAVISON
1 er. Suplente:	DR.	LEONARDO SANCHEZ PENICHE
2 do. Suplente:	DRA.	MARTHA ROSETE AGUILAR

Lugar o lugares donde se realizó la tesis:

INSTITUTO DE ASTRONOMIA - UNAM
LABORATOIRE D'ASTROPHYSIQUE DE MARSEILLE - UNIVERSITE DE PROVENCE

TUTOR DE TESIS:

DR. SALVADOR CUEVAS CARDONA

_____

FIRMA

VNIVERSIDAD NACIONAL AVTENOMA DE MEXICO

UNIVERSIDAD NACIONAL AUTONOMA DE MEXICO

PROGRAMA DE MAESTRIA Y DOCTORADO EN INGENIERIA

FACULTAD DE INGENIERIA

FEASIBILITY STUDY FOR HIGH CONTRAST IMAGING WITH THE FRIDA INSTRUMENT

T E S I S

QUE PARA OPTAR POR EL GRADO DE:

DOCTOR EN INGENIERIA

INGENIERIA ELECTRICA - INTRUMENTACION

P R E S E N T A :

MAMADOU N'DIAYE

TUTORES:
DR. SALVADOR CUEVAS CARDONA
DR. KJETIL DOHLEN

2009

Agradecimientos

Cette fantastique et fabuleuse expérience n'aurait pu voir le jour sans l'aide inestimable au départ de trois personnes issues de mon ancienne école d'ingénieurs, l'Ecole Nationale Supérieure de Physique de Marseille: mon ancien directeur de thèse Michel Lequime, ma professeur d'espagnol Anne-Marie Pointeau et la responsable de la scolarité Nathalie Briffa. Elles m'ont poussé, encouragé et permis de mener à bien mon projet avec énormément de générosité. Je tiens à leur exprimer toute ma gratitude ainsi que toute ma reconnaissance. Je tiens également à remercier Emmy Arts pour sa gentillesse et Ludovic Escoubas pour avoir accepté d'appuyer ma démarche avec enthousiasme.

Deseo agradecer con todo corazón a todo el equipo del Instituto de Astronomía de la Universidad Nacional Autónoma de México (IA-UNAM) y a su director, el Dr. Jose Franco, por la muy calurosa recepción, la cariñosa atención, el soporte material, computacional y administrativo así como el apoyo moral que recibí a lo largo de mi estancia. Si ésta fue tan placentera, se lo debo muchísimo a todas las personas que forman parte del IA-UNAM que supieron ponerme muy cómodo, que facilitaron mi integración y que me hicieron sentir en mi hogar desde el primer día. Quiero también agradecer al personal de la Coordinación del Posgrado de Ingeniería, del Centro de Ciencias Aplicadas y Desarrollo Tecnológico y de la Facultad de Ingeniería de la UNAM por toda la ayuda proporcionada a lo largo de mi estancia en México. En fin, le doy las gracias a la UNAM, queridísima casa de estudios donde pase cuatro años de vida estudiante tremendos e inolvidables, ¡Goooooooya! Me gustaría igualmente darles las gracias a todos los miembros del proyecto FRIDA y en particular a Alberto López, a Alan Watson y sobre todo a Beatriz Sánchez por todo el apoyo brindado y la fantástica ayuda proporcionada durante estos cuatro años en México.

Je souhaite grandement remercier tout le personnel du Laboratoire d'Astrophysique de Marseille (LAM) pour le très chaleureux accueil qui m'a été offert lors de mes differents séjours de recherche en France. En particulier, je souhaite faire part de toute ma gratitude à Gérard Lemaitre pour son extrême disponibilité, sa sagesse et sa gentillesse, ainsi qu'à Marc Ferrari, Philippe Amram, Patrick Lanzoni, Kacem Elhadi, les étudiants du LAM, Thomas et Christine pour leur attention et leur aide précieuse.

Je tiens également à remercier Marcel Carbillet et Laurent Jolissaint de m'avoir gentillement fourni les programmes CAOS et PAOLA respectivement ainsi que Rémi Soummer pour m'avoir suggéré l'utilisation de la méthode semi-analytique avec transformée de Fourier matricielle.

Quiero agradecer a todos los sinodales como a los miembros de mi comité tutoral: el Dr. Roberto Ortega Matínez, la Dra. Celia Sánchez Pérez, el Dr. Neil Bruce, la Dra. Martha Rosete, el Dr. Remy Ávila Foucat, el Dr. Leonardo Sánchez Peniche y la Dra. Graciela Velazco, que con mucho

entusiasmo, aceptaron supervisar mis estudios y revisar mi trabajo de tesis. Los diferentes comentarios, críticas y sugerencias que emitieron me ayudaron sin duda a mejorar mi trabajo. Disfruté mucho de las diferentes pláticas y las reuniones siempre muy cordiales que tuvimos en el transcurso de mi doctorado. Mil mil gracias igualmente por su paciencia durante mis múltiples visitas y su ayuda para resolver los inumerables trámites y obstáculos de la burocracia...

Mi experiencia en México fue increíble y se lo debo muchísimo a todas las personas que tuve el gusto de conocer aquí. Ellas se volvieron cuates, luego amigos y/o hermanos y hasta a veces carnales como dicen aquí en Chilangolandia. Gracias a todas ellas, he descubierto una población lindísima y una cultura con múltiples e inesperadas facetas, me he maravillado cada día con aspectos generales de la vida cotidiana en México y he seguido disfrutando de manera cotidiana el aprendizaje del castellano (sobre todo, el español mexicano y por supuesto el chilango, ¡a huevo!). Estoy convencido de que en cada nuevo país donde un individuo pasa un cierto tiempo, se relaciona con la gente y se familiariza con sus costumbres, esta persona al final acaba adquiriendo una nueva identidad que se va sumando a sus anteriores. Si hoy en día, tengo esta sensación de que México me ha dejado una huella bonita imborrable y de tener una identidad más, aparte de la senegalesa y de la francesa, es gracias a todas las personas que me encontré en el camino.
Por lo tanto, quiero agradecer en particular y con todo corazón a las siguientes personas por las charlas que tuvimos, por las ideas que compartimos, por los momentos que vivimos, por la paciencia que tuvieron conmigo y sus sonrisotas, por el espacio que me ofrecieron en su vida, y en fin y sencillamente por su amistad: Vasthi, María, Adriana, Sofia (a.k.a La Chofa), Lizzette, Anahí, Alejandra, Rosi, Ery Camara, Capricho, Paola Chapa, llka, Kryzhal, Santiago, Mariana (alias Vuyú) y Carlos, Liliana y Miguel, Erika, Don Alejandro, Verónica Flores, Ruth y Memo, Chucho Gonzalez, Sofia (a.k.a. Sofi), Itan, Veni, Nayeli, Astrid, Henrietta y Henrik, César, Cecilia (alias La Ceci), Don Patricio, Verónica Lora, Valerie, Davicho y su hermana Mariana, Hugo, Leo, Betty, Paola Romero, Lety, Ana Ali, Luz Angelica, Paola Suárez, Pablo, Marysol (mi querida roomie ¡durante más de 3 años!) y Mauricio, Akemi, Valentina, el buen Pedro, Mariana Z., el buen Chucho Z., toda la banda del básquetbol de la delegación Benito Juárez y mi "juguero" preferido Alex.
Je souhaite vivement remercier Christophe Morisset pour sa gentillesse, son extrême disponibilité ainsi que pour l'aide inestimable qu'il m'aura fourni tout au long de mon passage à la UNAM, en particulier sur des questions informatiques et bien entendu IDL (c'est un véritable senseï!) où il m'a permis de progresser de manière significative. Merci à lui et bien entendu à son épouse Marie Zapata pour leur constante attention, les invitations aux délicieux repas et la bonne humeur qu'ils propagent dans leur entourage.
Par ailleurs, je remercie les amis français que j'ai eu la chance de connaitre ici au Mexique et avec qui j'ai eu l'occasion de partager de fantastiques moments durant ces quatre années au Mexique: Julien Girard, Jérôme le Lyonnais, Marie la Marseillaise, Julien Fayat et Claire, François, Mélanie, Luc, Jean-Pierre et Chloé. Je remercie également et très chaleureusement Abdellah (a.k.a. Abdou) pour son soutien, ses précieux conseils, son dévouement et sa bonne humeur contagieuse!
Agradezco también a los amigos españoles Federico, Jorge y Ani, Luzma, Javier Fuentes y Elena por su fabuloso cariño a lo largo de mi estancia mexicana.
Quisiera también agradecer a mis compañeros estudiantes del IA-UNAM por su amistad y su amabilidad sin límites y en particular, a Giovanny y a Juan Aldebarán del cubiculo 28 por su alegría durante estos últimos meses de redacción juntos. En fin, deseo subrayar el papel increíble que tuvo

Alex (alias Don Alejandro) en mi integración en México y no sobrarían las palabras para darle las gracias por todo lo que hizo para mi. Me gustaría hacer una mención especial a todos los familiares, los amigos y/o novios de mis amigos, a los que seguramente se me olvidó mencionar en esta lista muy extendida y que me van a odiar (de antemano, ¡mil disculpas!).

Un énorme merci à Mickaël, Didier et Franck, mes amis de Nice, pour la très grande fraternité qui nous unit depuis déjà pas mal d'années... Un autre grand merci à Christophe H. et Guillaume M., également amis d'enfance de Nice, pour la très franche complicité qui nous lie depuis notre première rencontre. Je tiens à remercier chaleureusement tout mon entourage à Nice et à avoir une pensée particulière pour Mme Escamez, sa fille et sa petite-fille Valérie, M. Koné et sa famille ainsi que Christophe P. et Jean-Vivien.
Je remercie bien évidemment toute les personnes de la clique hors Nice que j'ai connu grâce à mon passage de trois ans à Marseille, la ville du soleil. Toutes les personnes issues de la "Marseille connection" ont bien évidemment constitué une pierre angulaire dans la réalisation de ce projet et restent pour moi une source de motivation inépuisable pour me lancer à la recherche de nouveaux horizons, vivre des expériences uniques et perpétuellement m'enrichir à travers de nouvelles rencontres. Mes pensées vont en premier lieu à Benjamin qui fut le principal inspirateur et le détonateur de mon périple au Mexique et à la UNAM, et m'a appris à aimer ce pays et cette univserité avant même mon arrivée, lors de son passage en 2003-2004. Mille mercis aussi à Thibault, Guillaume (a.k.a. Arsène), Fred (alias p'tit père), Sibylle, Samuel, Jean, Irwin, Laure, Domi, Audrey, l'autre Benjamin (a.k.a. Benhur), Manu (a.k.a. Manuboy alias ManuElfeDesBois!), Nawal, Emilie, Greg et Myriam, Morgan, Charlotte, Elise Maacha, Sylvain (a.k.a. Sly), Séb Michel, Flo, Cédric (alias Cheup), Baptiste, Carole, Arthur et Mimi, pour les nombreuses discussions que nous avons eu, votre écoute, vos sourires, vos encouragements, vos conseils sans oublier le merveilleux accueil dont j'ai bénéficié lors de mes brefs passages en France.
Je tiens également à remercier toutes les personnes qui sont venues me rendre visite au cours de ces quatre années et qui en ont profité pour découvrir ou redécouvrir le Mexique.

Mes remerciements finaux s'adressent bien entendu à Kjetil Dohlen et Salvador Cuevas, mes deux directeurs de thèse.
Je souhaite remercier très chaleureusement Kjetil, mon directeur de thèse en France. En dépit des contraintes due à la distance, il a maintenu un suivi permanent et très critique de mon travail. J'ai pris énormément de plaisir à travailler en sa compagnie et savouré les moments passés avec lui, notamment en laboratoire avec le banc du masque de phase de Roddier & Roddier. Pour moi, Kjetil represente un modèle de par la passion, la rigueur et la concentration avec laquelle il exerce son travail de recherche. De plus, Kjetil a une aisance à tirer les gens vers le haut et à les faire progresser. C'est un réel privilège d'avoir pu travailler avec lui et d'avoir pu profiter de ses conseils avisés. Il m'a surtout appris à perpétuellement me remettre en question et à être d'une exigence à toute épreuve avec mon travail. Je tiens à lui exprimer ma gratitude la plus sincère pour toute l'attention et pour la patience dont il a su faire preuve à mon égard.
Seguro me faltarán las palabras para ofrecer mis agradecimentos muy especiales a Salvador, mi director de tesis en México. Salvador hizo tanto para mí, desde la primera vez que me puse en contacto con él en febrero de 2004, hasta la fecha que no bastarán mis palabras para rendirle el homenaje que se merece. Salvador tiene una capacidad visualizadora exraordinaria a nivel de óptica,

de instrumentación y de los campos relacionados. Me benefició de su experiencia increíble a cada rato compartiendo anécdotas conmigo. Además, me enseñó en múltiples ocasiones astucias y trucos para resolver los problemas encontrados en mi trabajo. Sobre todo, aprendí de él a ver más allá de los resultados que yo le mostraba. Desde el inicio, se puso extremadamente exigente conmigo pero siempre con la intención de hacerme progresar y por lo tanto, se lo agradezco muchísimo. Además, Salvador fue mucho más allá de su papel como asesor: me dío un apoyo incondicional mostrándome un confianza total, desarrolló una verdadera amistad conmigo y la complicidad de un tío cuidándome como si fuera su sobrino. Con todo corazón, muchisísimas gracias a Salvador por todo. Deseo también agradecer fuertemente a Gilda, a Juan Salvador, a Adrían y a Sofía, y toda la familia de Salvador por hacerme sentir parte de ellos y el inmenso cariño que me ofrecieron. Les pido también mil disculpas por haber acaparado a Salvador tantas veces durante estos cuatro años.

Je ne peux conclure ces remerciements sans avoir une pensée émue pour ma famille. Mes parents Bacar N'Diaye et N'Deye Seyni Gadj, mes soeurs Mariyama et Boury, mon cousin Issa et mon beau-frère Ouzin n'ont eu de cesse de croire en moi et en mes projets, de me prodiguer des conseils, et de prier chaque jour sans relâche pour ma réussite scolaire et professionnelle. Je ne pourrai jamais assez leur exprimer ma gratitude et ma reconnaissance. Cette thèse leur est en très grande partie dédié. Je remercie également toute la communauté sénégalaise de N'Guith présente bien évidemment au Sénégal mais aussi au delà des frontières, entre autres en France, en Italie, en Espagne et aux Etats-Unis, pour le soutien indéfectible dont j'ai pu bénéficié.

Esta tesis corresponde a los estudios realizados con una beca otorgada por la Secretaría de Relaciones Exteriores del Gobierno de México. Agradezco a la SRE a través de la Dirección de Intercambio Académico y su personal por su muy generosa ayuda durante tres años de mi estancia en México. Les doy también las gracias al personal de la Embajada de México en Francia por facilitarme el camino para conseguir la beca y la FM3.
Quiero también agradecer al Grupo Santander a través de los Encuentros Astrofísicos Blas Cabrera (UNAM-IAC) por la ayuda que recibí durante los últimos meses de mi estancia para poder acabar la tesis y el apoyo económico para asistir a diferentes congresos.
Agradezco igualmente a la Coordinación de Estudios de Posgrado de la UNAM por otorgarme un apoyo económico para la terminación de mi proyecto de investigación.
Je remercie également le ministère des Affaires Etrangères français à travers l'Egide pour le complément de bourse généreusement accordée durant trois ans au Mexique. Je souhaite également remercier l'Ambassade de France au Mexique pour l'aide très précieuse qui m'a été fournie.
Je remercie enfin le LAM et l'Université de Provence pour l'aide inestimable qui m'a été accordée lors de mes séjours en France.

Ciudad de México, Mayo de 2009

A mon père et ma mère, à Mariyama, Boury, Issa et Ouzin.

A toute la famille issue de N'Guith au Sénégal, et en particulier à mes grand-parents, ma tante Sokhna y mon oncle Ibra, mes cousins Dame et Magueye ainsi qu'à tous ceux généralement présents à Guediawaye, Dakar.

On ne voit bien qu'avec le coeur, l'essentiel est invisble pour les yeux.
No se ve bien sino con el corazón, lo esencial es invisible a los ojos.
It is only with the heart that one can see rightly; what is essential is invisible to the eyes.

Antoine de Saint-Exupery, Le Petit Prince.
El Principito.
The Little Prince.

Abstract

FRIDA (inFraRed Imager and Dissector for the Adaptive optics system) is a second-generation instrument conceived for the Gran Telescopio Canarias (GTC). It is designed to work in the near infrared with requirements of direct imaging and Integral Field Spectroscopy. FRIDA will work in concert with GTCAO, the Adaptive Optics (AO) system of the GTC. FRIDA is planned to address a wide range of astrophysical issues. In addition, one of the design requirements is the ability to perform high contrast images. It could thus image and spectrally characterize substellar mass companions close to nearby bright stars. The main goal of this thesis work is to carry out a feasibility study to perform high contrast imaging with FRIDA. Different and feasible coronagraphic techniques and post-processing methods are considered for this instrument. The atmospheric turbulence parameters of the GTC astronomical site and GTCAO characteristics are included in our simulations. Thus, we estimate the contrast gains reachable by FRIDA with the following combination: AO+coronagraphy+post-processing techniques. The obtained results prove to be very encouraging: we show that GTCAO+FRIDA can be able to image and characterize a companion 10^5 fainter than its parent bright star at a 0.2 arcsec angular separation.

Resumen

FRIDA (inFraRed Imager and Dissector for the Adaptive optics system) es un instrumento de segunda generación para el Gran Telescopio Canarias (GTC). Está diseñado para trabajar en el cercano infrarrojo con requerimientos de formación de imagen directa y de espectroscopía integral de campo. FRIDA trabajará en concierto junto con el sistema de Óptica Adaptativa del GTC (GTCAO). FRIDA está planeado para tratar un amplio intervalo de problemas astrofísicos. Adicionalmente, uno de los requerimientos de diseño es la capacidad de formar imágenes de alto contraste. Debe entonces obtener imágenes y caracterizar compañeros de masa sub-estelar muy cerca de su estrella huésped. La motivación principal de este trabajo de tesis es hacer un estudio de factibilidad para proveer a FRIDA de la capacidad de obtener imágenes de alto contraste. Se consideran diferentes técnicas coronográficas y métodos de post procesamiento factibles. Los parámetros de turbulencia atmosférica del sitio astronómico del GTC y las características de GTCAO están incluidos en las simulaciones. Se estiman así las ganancias de contraste alcanzables para FRIDA con la combinación siguiente: AO+coronografía+técnicas de post procesamiento. Los resultados obtenidos resultan ser muy prometedores: se muestra que GTCAO+FRIDA puede ser capaz de formar la imagen y caracterizar un compañero de intensidad 10^5 más débil que su estrella huésped brillante a una separación angular de 0.2 arcsec.

List of acronyms

4QPM	Four Quadrant Phase Mask
AB Dor	AB Doradus
ADC	Atmospheric Dispersion Compensator
ADI	Angular Differential Imaging
AO	Adaptive Optics
APLC	Apodized Pupil Lyot Coronagraph
CAOS	Code for Adaptive Optics System
CDR	Critical Design Review
CLC	Classical Lyot Coronagraph
CRC	Classical Roddier Coronagraph
DDI	Double Differential Imaging
DM	Deformable Mirror
DZPM	Dual Zone Phase Mask
ESO	European Southern Observatory
FP1	First Focal Plane of FRIDA
FP2	Second Focal Plane of FRIDA
FP3	Third Focal Plane of FRIDA
FRIDA	inFraRed Imager and Dissector for the Adaptive optics system of the GTC
FFT	Fast Fourier Transform
FT	Fourier Transform
FWHM	Full Width at Half Maximum
GTC	Gran Telescopio Canarias
GTCAO	Gran Telescopio Canarias Adaptive Optics system
GPI	Gemini Planet Imager
IA-UNAM	Instituto de Astronomía de la Universidad Nacional Autónoma de México
IFU	Integral Field Unit
IFS	Integral Field Spectroscopy
IRE	Integrated Residual Energy
LAM	Laboratory of Astrophysics of Marseilles
MFT	Matrix Fourier Transform
ORM	Observatorio del Roque de los Muchachos
PDR	Preliminary Design Review
PP0	GTC aperture Pupil Plane

PP1	First Pupil Plane of FRIDA
PP2	Second Pupil Plane of FRIDA
PSF	Point Spread Function
SDI	Simple Differential Imaging
VLT	Very Large Telescope
SLLC	Stop-less Lyot Coronagraph
SPHERE	Spectro-Polarimetric High-contrast Exoplanet REsearch
SSDI	Simultaneous Spectral Differential Imaging
WFS	Wavefront Sensor

Contents

Introduction

The quest and discovery of new worlds has always fascinated mankind and paved the way for the international astronomical community. In that context, the past decade was mainly remarkable for the first confirmed detections of exosolar planets via indirect methods.
More recently, direct images of substellar mass companions, like exosolar planets and brown dwarfs, have successfully been achieved, risen the expectations within the scientific community that direct imagery constitutes a promising approach. On the one hand, the astronomical data reached with indirect detection methods can be combined and completed with the information achieved by directly imaging the low-mass companions. On the other hand, direct imaging will allow access to spectral characterization and therefore, atmospheric composition analysis of the detected dim objects. Thus, the possible presence of life in exoplanets could be determined by detection of bio-signals (like water [H_2O], oxygen [O_2], ozone [O_3] and alike) present in their atmosphere.
However, imaging faint objects, like substellar mass companions close to nearby bright stars, appears to be very challenging; indeed, large flux ratios ($> 10^4$) at small angular separations (< 1 arcsec) have to be overcome. Hence, the precious photons coming from a close-by companion have to be very well isolated from the luminous halo formed by its host star. High contrast imaging techniques are required to remove the diffracted light of the parent star and complemented with sophisticated methods to image and characterize the faint substellar mass companions.

Since 2003, several instruments have been conceived specifically to obtain images and spectra of exoplanets. In particular, two of them are currently in the final design stages and close to be constructed and operated in 8 m-class telescopes in Chile: SPHERE (Spectro-Polarimetric High-contrast Exoplanet REsearch), a second-generation instrument for the Very Large Telescope; and GPI (Gemini Planet Imager), a facility scheduled for the Gemini South telescope. In both cases, extreme Adaptive Optics (AO) systems are built-in to accurately control the wavefront errors induced by the atmosphere above ground-based telescopes. Moreover, they rely on very efficient near infrared coronagraphic devices to reduce the diffraction peak of the parent star and features from the optics edges of telescope and instrument. Spectroscopic capabilities are also included in both planet imagers for the spectral characterization of the detected exoplanets. In particular, both instrument teams have recognized that Integral Field Spectroscopy (IFS) devices are potentially crucial for exoplanet detection. Indeed, true planetary companions can be distinguished from speckle artifacts of the instrument or background objects, thanks to data-analysis strategies independent of *a priori* knowledge or assumed features of the planet's spectrum.

In parallel, FRIDA, the inFraRed Imager and Dissector for the Adaptive optics system of the

Gran Telescopio Canarias, represents another very ambitious project with some characteristics in common to both instruments above, but different scientific goals. FRIDA is designed to work in the near infrared with requirements for direct imaging and Integral Field Spectroscopy. This is a second-generation instrument conceived for the Gran Telescopio Canarias (GTC), a 10.4 m equivalent diameter telescope which started operating in February 2009 in the Observatory of Roque de los Muchachos in La Palma Island, Spain. Given its collecting area, the GTC is currently the largest telescope in the world and, therefore, making FRIDA the most sensitive infrared instrument nowadays.
FRIDA will work in concert with the AO system of the GTC (GTCAO). FRIDA and GTCAO are also in the design stages, only a few months behind SPHERE and GPI. GTCAO+FRIDA are designed to address a wide range of astrophysical problems, but unlike SPHERE and GPI, none of these topics deal with the discovery of exoplanets by direct imaging. Moreover, GTCAO only has a quarter of actuators of the AO modules (about 400 in GTCAO against at least 1500 in GPI or SPHERE). This provides a lower image quality from GTCAO+FRIDA than with SPHERE or GPI. However, the GTC collecting area is 1.68 times larger, making FRIDA considerably more sensitive for spectroscopic studies than its competitors.

One of the design requirements scheduled for FRIDA is the ability to perform high contrast images. In order to reach this goal, the installation of focal and pupil plane masks is planned at strategic places of the optical assembly. In the same way, FRIDA shall have an adequate processing of the obtained images in IFS mode. The question is: what are the best instrument configurations to reach high contrast images with these mask devices and post-processing techniques?
This is the main goal of the present thesis: doing a feasibility study to provide a high contrast imaging capability for FRIDA and make it competitive, with the least possible drawbacks, to SPHERE and GPI.

Chapter I reviews the main coronagraphic solutions proposed during the past few years. In particular, we focus on techniques which prove to be the most convenient and promising for our study. FRIDA is then presented in Chapter II and different coronagraphic configurations are suggested. In Chapter III we describe the numerical tool implemented to compute and compare the behavior of the different coronagraphic devices. Laboratory tests are carried out with a Roddier & Roddier phase mask to validate our tool with experimental evidence. This constitutes the topic of a paper sent to a referred journal. We finally give a direct application of our numerical tool in FRIDA's case and evaluate the performance of the coronagraphic configurations in the context of a diffraction-limited approach. This preliminary study allows us to calibrate the star brightness attenuations reachable with suitable coronagraphs in the absence of aberrations produced by the atmospheric turbulence in any astronomical site. In Chapter IV, AO-compensated images considering the GTCAO characteristics are added to the model in order to estimate FRIDA's performance in the context of instruments equipped with coronagraphs and coupled to a ground-based telescope. Finally, in Chapter V we evaluate the reachable contrast gains and discuss the potential of additional post-processing techniques with an IFS system as planned for FRIDA. The analysis of all these results concludes the feasibility study of high contrast imaging with the FRIDA instrument.

Introducción

La búsqueda de nuevos mundos ha fascinado siempre a la humanidad y su descubrimiento ha abierto nuevos caminos para la comunidad astronómica internacional. En este contexto la década pasada ha sido remarcable, principalmente por las primeras detecciones confirmadas de planetas exosolares por medio de métodos indirectos.
Recientemente, se han logrado obtener imágenes directas de compañeros de masa sub-estelar, como son los planetas exosolares o las enanas marrón, y esto ha generado aún mas expectativa en la comunidad ya que constituye un método con mucho potencial. Por un lado, los datos astronómicos adquiridos mediante los métodos indirectos pueden ser combinados y completados con la información obtenida con los métodos de imagen directa de los compañeros de baja masa. Por otro lado, estos métodos de imagen directa pueden permitir el acceso a la caracterización espectral, y por tanto, a un análisis de la composición de la atmósfera de esos objetos estelares muy débiles. De esta manera, la posible presencia de vida en estos objetos podría ser determinada mediante una estimación de bio-marcadores (como agua [H_2O], oxigeno [O_2], ozono [O_3]...), presentes en su atmósfera.
Sin embargo, obtener imágenes de objetos estelares de muy débil luminosidad, como son estos compañeros de masa sub-estelar, que están situados muy cerca de estrellas brillantes, es todo un reto debido, indudablemente, a las dificultades que hay que superar por los grandes cocientes de los flujos ($> 10^4$) y de las separaciones angulares muy pequeñas (< 1 arcsec). Para esto, los preciosos fotones provenientes de un compañero cercano, deben de ser muy bien aislados del halo luminoso de su estrella huésped. Técnicas de muy alto contraste son requeridas para remover la luz difractada proveniente de la estrella, además de las técnicas para obtener las imágenes y caracterizar los débiles objetos de masa sub-estelar.

De 2003 a la fecha, algunos instrumentos han sido concebidos específicamente para obtener imágenes y espectros de planetas exosolares. Dos de ellos se encuentran en las etapas finales de diseño y en las primeras etapas de su construcción. Estos son SPHERE (*Spectro-Polarimetric High-contrast Exoplanet REsearch*), un instrumento de segunda generación para uno de los telescopios de 8 m del *Very Large Telescope* de la *European Southern Observatory* (ESO) en Chile y GPI (*Gemini Planet Imager*), un instrumento para el telescopio Gemini-Sur de 8 m, también en Chile. En ambos casos, los instrumentos están equipados con sistemas de Óptica Adaptativa (AO, por sus siglas en inglés) extrema, para un control muy preciso de la corrección de los frentes de onda distorsionados por la atmósfera encima de los telescopios. Además cuentan con dispositivos coronográficos muy eficientes para reducir la luz de la estrella principal y eliminar el halo producido por la difracción de los bordes de la óptica tanto del telescopio como del instrumento mismo. Para la caracterización del espectro de los exo-planetas ambos instrumentos cuentan con uno o más sistemas espectrográficos.

En especial los equipos de trabajo de los instrumentos han reconocido que es potencialmente crucial para la detección de exo-planetas la utilización de dispositivos de Espectroscopía Integral de Campo (IFS, por sus siglas en inglés). Esto es debido a que los compañeros planetarios pueden ser distinguidos de speckles producidos inevitablemente por la óptica del instrumento o por objetos de fondo, gracias a estrategias de análisis de imágenes que no dependen de un conocimiento *a priori* de características particulares del espectro del planeta.

Paralelamente a estos dos proyectos, FRIDA (in**F**ra**R**ed **I**mager and **D**issector for the **A**daptive optics system of the Gran Telescopio Canarias) representa otro proyecto muy ambicioso con algunas de las características comunes a ambos instrumentos, pero objetivos científicos diferentes. FRIDA es un instrumento que trabaja en el cercano infrarrojo con requerimientos de formación de imagen directa y de espectroscopía integral de campo. Es un instrumento de segunda generación para el Gran Telescopio Canarias (GTC), telescopio de 10.4 m de diámetro equivalente, que ha sido puesto en operación en febrero de 2009 en el observatorio del Roque de los Muchachos en La Palma, Islas Canarias, España. El área colectora de GTC hace que este telescopio sea, por el momento, el más grande del mundo y, en consecuencia FRIDA el instrumento infrarrojo más sensible del mundo.
FRIDA trabajará en concierto junto con el sistema de Óptica Adaptativa del GTC (GTCAO). Tanto FRIDA como GTCAO están en las etapas finales de diseño, unos meses detrás de SPHERE y GPI. GTCAO+FRIDA están diseñados para abordar problemas astrofísicos muy amplios pero ninguno de ellos es el descubrimiento por imagen directa de exo-planetas como es el caso de SPHERE y GPI. Además, GTCAO tiene solamente una cuarta parte del número de actuadores de los módulos de AO de esos instrumentos (alrededor de 400 en GTCAO contra 1500 en GPI y SPHERE). Esto hace que la calidad de imagen de GTCAO+FRIDA sea menor a la que se va a obtener con SPHERE y GPI. Sin embargo, para estudios de espectroscopía el área colectora de GTC es 1.68 veces más grande, haciendo que sea un instrumento más sensible que los otros dos para espectroscopía.

Uno de los requerimientos de diseño de FRIDA es poder obtener imágenes de alto contraste. Para esto, se ha especificado que se puedan instalar máscaras de plano focal y de pupila en algunas partes de su tren óptico. De la misma manera, se ha previsto que debe de haber un procesamiento adecuado de las imágenes obtenidas en el modo de espectroscopía integral de campo. La pregunta que surge es: ¿cuales son las mejores configuraciones del instrumento para que estos dispositivos y técnicas de procesamiento permitan obtener imágenes de muy alto contraste?
Esta es la motivación principal de este trabajo de tesis: hacer un estudio de factibilidad para proveer a FRIDA de la capacidad de obtener imágenes de alto contraste y competir, al menos no con muchas desventajas, con SPHERE y GPI.

En el Capítulo I, se hace una revisión de las principales soluciones coronográficas que se han propuesto en los años recientes. En particular se dirige la atención a técnicas que parecen ciertamente ser las más favorables. Se presenta luego FRIDA en el Capítulo II y se sugieren diferentes configuraciones coronográficas para este instrumento. En el Capítulo III, se describe la herramienta numérica implementada para comparar el comportamiento de los diferentes dispositivos coronográficos. Se hace también una verificación experimental con una máscara de fase de Roddier & Roddier para comprobar que la herramienta es valida. Este es el tema del artículo enviado a una revista arbitrada. Se da una aplicación directa de nuestra herramienta numérica tratando el caso de

FRIDA: se evalúa el desempeño de las configuraciones coronográficas considerando en una primera aproximación a GTC+FRIDA como un instrumento limitado en calidad de imagen por la difracción. Con esto, se pueden calibrar las atenuaciones del brillo de la estrella principal obtenidas con los coronógrafos propuestos, en ausencia de aberraciones producidas por la turbulencia de la atmósfera del sitio astronómico. Después en el Capítulo IV, imágenes parcialmente corregidas de la turbulencia atmosférica, características del sistema GTCAO, son introducidas en el modelo para estimar el desempeño de FRIDA en el contexto de instrumentos provistos de coronógrafos instalados en un telescopio terrestre. Finalmente en el Capítulo V, se evalúan los contrastes de imagen alcanzables y se discute el potencial de técnicas adicionales de post procesamiento de imágenes con un sistema de Espectroscopía Integral de Campo como el que está provisto en FRIDA. El análisis de todos estos resultados permite concluir el estudio de factibilidad de imagen de alto contraste con el instrumento FRIDA.

Chapter I

Context of stellar coronagraphy

I.1 Coronagraphy in contemporary astronomy and astrophysics

I.1.1 The quest for faint substellar mass companions: indirect detection methods

To date, the count of known exoplanet candidates stands at more than 300[1] and major part of these planetary objects was found thanks to indirect detection methods. These techniques are based on the detection of perturbations induced by the substellar mass companion on its parent star. Different approaches have been proposed these past few years to discern the presence of an extrasolar planet for instance. They have been largely reviewed and detailed in many papers that can be found in the literature. For instance, a general description of these schemes can be found in Quirrenbach (2006). In the following, we briefly present the main concepts.
Until now, the **method of radial velocity measurements** is the most powerful and efficient technique to detect extrasolar planets. This approach is based on the Doppler effect: it consists in analyzing the radial velocity fluctuations of an observed star to deduce the presence or not of a companion in its vicinity. The **photometric transit technique** is also an interesting method based on accurate measurements of a star luminous flux. The possible secondary eclipses produced by the transit of an object allows to conclude about the presence of an orbiting substellar mass companion around the observed star. The **gravitational micro-lensing technique** represents another elegant approach: when a star and its companion pass in front of another far away star, the luminosity of this last is amplified thanks to a gravitational effect similar to that of a "magnifying glass". The analysis of the far away star brightness profile and the possible observation of secondary amplifications lead to the detection of a companion close to the lensing star. Finally, **very accurate astrometric measurements** allow to presume the presence of an exoplanet by analyzing the oscillation movement of a star.
With indirect detection methods, we can have access to different substellar mass companion data like its orbital period P, its orbital eccentricity e, its semi-major axis a, its angular velocity ω, its minimum mass $M_2 \sin i$ assuming the star mass M_1 (i denotes the inclination angle of the orbital plane) or the radii of the star and its companion R_1 and R_2. The association of several techniques

[1] J. Schneider, "The Extrasolar Planets Encyclopedia", http://exoplanet.eu/

helps to achieve a better and more complete characterization of the detected object.
In a recent conference, Chauvin (2007) synthesized the discoveries made with the indirect methods. He showed that radial velocity, photometric transit and gravitational micro-lensing methods had enabled the detection of several substellar companions at distances smaller than 5 A.U.[2] from the host star. He also underlined the fact that large sky surveys had allowed to detect about 10 companions at distances greater than 500 A.U. from their host brown dwarfs, pointing out the absence of substellar mass companions detected at distances between 5 and 500 A.U. from the host star. Astronomers hope completing this missing link thanks to high contrast imaging techniques.

I.1.2 Expectations from high contrast imaging

Imaging faint substellar mass companions, like exosolar planets or brown dwarfs, is a very exciting but challenging issue. Contrary to the indirect approach, the direct detection consists in distinguishing the radiation which comes from the faint companion against the halo of the adjacent and enormously brighter parent star.
Imaging directly substellar mass companions will allow having access to their spectrum. The spectral characterization of these dim objects will provide data about their atmospheric composition. The detection of bio-signals (like water [H_2O], oxygen [O_2], ozone [O_3]...) will bring elements of response about the eventual presence of life (Woolf and Angel, 1998). With images of faint companions, it will also be possible to better understand mechanisms of planetary formation (Burrows and Sharp, 1999) and calibrate the current atmospheric evolution models (Marley et al., 1999). Hence, direct detection appears very promising to approach these issues. However, even companions like exosolar giant planets are predicted to be very faint compared to their host star: for instance, the planet-to-star flux ratio for a Jupiter-like planet with an age of 5 billion years orbiting a Sun-like star at 4 A.U. is estimated to be about 10^{-9} in the optical and near-infrared bands (Burrows et al., 2004). Therefore, reduction of the stellar diffracted light is required to image and thereafter characterize faint substellar mass companions.
Removing a star image can be assimilated to the creation of an artificial stellar eclipse. A similar problem was tackled about one century ago by Bernard Lyot (1932) to artificially eclipse the Sun. In the following, we propose to narrate the case and relate it to our current challenge of astronomical instrumentation: the direct imaging of substellar mass companions present in the vicinity of bright stars.

I.1.3 Goals of the chapter

This chapter constitutes a preamble about coronagraphy. In Section I.2, we briefly recall the origins of coronagraphy reminding the context of the solar coronagraph birth. After a transition between solar and stellar coronagraphy, we shortly review the different diffraction suppression systems developed during this past decade in Section I.3. A large number of technical solutions have been proposed to attenuate the brightness of a star image. However, within the context of coronagraph feasibility studies for FRIDA, we will focus on concepts named Lyot-style coronagraphs and remind the corresponding formalism in Section I.4. Several definitions will also be given in this part and

[2] A.U.: Astronomical Unit. 1 A.U. corresponds to the mean distance between the Sun and our planet Earth, it means about $1.50 \cdot 10^8$ km.

will prove to be very useful all along our analysis concerning high contrast imaging feasibility with FRIDA.

I.1 Coronografía en la astronomía y la astrofísica contemporanea

I.1.1 La busqueda de compañeros de masa sub-estelar de baja luminosidad: métodos de detección indirecta

Hasta la fecha, el número de candidatos conocidos de exoplanetas es superior a 300[3] y la mayor parte de estos objetos planetarios fue encontrado gracias a métodos de detección indirecta. Estas técnicas están basadas en la detección de perturbaciones inducidas por el compañero de masa sub-estelar sobre la estrella pariente. Diferentes métodos han sido propuestos estos últimos años para detectar la presencia de un planeta extrasolar por ejemplo. Estos han sido ampliamente revisados y detallados en diferentes artículos que se pueden encontrar en la literatura. Por ejemplo, se puede encontrar una descripción general de estos métodos en Quirrenbach (2006). En lo que sigue, vamos a presentar brevemente los principales conceptos.

Hasta ahora, el **método de medición de velocidades radiales** es la técnica más poderosa y eficiente para detectar planetas extrasolares. Este método está basado en el efecto Doppler: consiste en analizar las fluctuaciones de la velocidad radial de una estrella observada para deducir la presencia o ausencia de un compañero en su vecindad. La **técnica de transito fotométrico** es igualmente un método interesante basado en la medición precisa del flujo luminoso de una estrella. Los eventuales eclipses secundarios producidos por el transito de un objeto permite concluir acerca de la presencia de un compañero de masa sub-estelar girando alrededor de la estrella observada. La **técnica de micro-lente gravitacional** representa otro método elegante: cuando una estrella y su compañero pasa enfrente de una estrella más alejada, la luminosidad de esta última es amplificada gracias a un efecto gravitacional similar al efecto amplificador de una lupa. El análisis del perfil de luminosidad de la estrella lejana y la observación eventual de amplificaciones secundarías lleva a la detección de un compañero cerca de la estrella-lente. Finalmente, **mediciones astrométricas muy precisas** permiten imaginar la presencia de un exoplaneta con la análisis del movimiento oscilatorio de una estrella.

Con los métodos de detección indirecta, se puede tener acceso a diferentes características del compañero de masa sub-estelar, como su periodo orbital P, su excentricidad orbital e, su semieje mayor a, su velocidad angular ω, su masa mínima $M_2 \sin i$ suponiendo una estrella huésped de masa M_1 (i denota el angulo de inclinación del plano orbital) o los radios de la estrella R_1 y de su compañero R_2. Asociar varias técnicas ayuda a obtener una caracterización mejor y más completa del objeto detectado.

En una conferencia reciente, Chauvin (2007) sintetiza los descubrimientos hechos con los métodos indirectos. Mostró que los métodos de velocidad radial, de tránsito fotométrica y de micro-lente gravitacional, habían favorecido la detección de varios compañeros sub-estelares a distancias inferiores a 5 U.A.[4] de la estrella huésped. Subrayó también que gracias a amplios sondeos del cielo, se había podido detectar alrededor de 10 compañeros a distancias superiores a 500 U.A. de sus enanas marrón huésped, y señaló al mismo tiempo la ausencia de compañeros de masa sub-estelar detectados a distancias entre 5 y 500 U.A. de la estrella huésped. Los astrónomos esperan completar este vínculo ausente gracias a las técnicas para obtener imágenes de alto contraste.

[3] J. Schneider, "The Extrasolar Planets Encyclopedia", http://exoplanet.eu/

[4] U.A.: Unidad Astronómica. 1 U.A. corresponde a la distancia promedio entre el sol y nuestro planeta tierra, es decir aproximadamente $1.50 \cdot 10^8$ km.

I.1.2 Expectativas con las imágenes de alto contraste

Obtener imágenes de compañeros de masa sub-estelar y de baja luminosidad, como exoplanetas o enanas marrón, representa una problemática muy apasionante pero es también todo un reto. Al contrario de los métodos indirectos, la detección directa consiste en distinguir la radiación proveniente de un compañero de baja luminosidad inmerso en el halo de la estrella huésped de un brillo extremadamente muy intenso.
Con la formación directa de imágenes de los compañeros de masa sub-estelar, se podrá tener acceso a su espectro. La caracterización espectral de estos objetos de baja luminosidad proporcionará datos acerca de su composición atmosférica. La detección de bio-marcadores (como agua [H_2O], oxígeno [O_2], ozono [O_3]...) brindará elementos de respuesta sobre la eventual presencia de vida (Woolf and Angel, 1998). Con imágenes de compañeros débiles, se podrá también acceder a un mejor entendimiento de los mecanismos de formación planetaria (Burrows and Sharp, 1999) y calibrar los módelos actuales de evolución atmosférica (Marley et al., 1999). Por lo tanto, la detección directa es muy prometedora para abordar estos temas. Sin embargo, se predice una luminosidad muy débil para los compañeros, como por ejemplo los planetas extrasolares gigantes, con respeto a la de su estrella huésped: por ejemplo, la razón de flujo planeta/estrella para un planeta de tipo Júpiter con una edad de 5 mil millones de años girando alrededor de una estrella de tipo Sol y a una distancia angular de 4 U.A. está estimado a 10^{-9} en el óptico e infrarojo (Burrows et al., 2004). Por eso, se requiere reducir la luz estelar difractada para formar la imagen y luego caracterizar los compañeros de masa sub-estelar y de baja luminosidad.
Retirar la luz de la imagen de una estrella dejando intacta la imagen del compañero débil se puede asimilar a la creación de un eclipse estelar artificial. Un problema similar fue abordado hace un siglo por Bernard Lyot en 1932 para eclipsar artificialmente el sol. En lo que sigue, se va a relatar esta historia y a enlazarlo con nuestro reto de instrumentación astronómica actual: la formación de imagen directa de los compañeros de masa sub-estelar presentes en la vecindad de las estrellas brillantes.

I.1.3 Objetivos del capítulo

Este capítulo constituye un preámbulo acerca de la coronografía. En la Sección I.2, se recuerdan las orígenes de coronografía subrayando el contexto del nacimiento del coronógrafo solar. Luego de hacer una transición entre la coronografía solar y estelar, se revisarán brevemente los diferentes sistemas de supresión de difracción desarrollados durante la última década en la Sección I.3. Se ha propuesto un amplío número de soluciones para atenuar el brillo de la imagen de una estrella huésped. Sin embargo, en el contexto de los estudios de factibilidad de coronógrafos para FRIDA, se centrará el trabajo en los llamados coronógrafos de tipo Lyot y se recordará el formalismo correspondiente en la Sección I.4. Se darán igualmente varias definiciones en esta parte que resultarán muy útiles a lo largo de nuestro estudio de factibilidad para formar imágenes de alto contraste con FRIDA.

I.2 From solar to stellar coronagraphy

Eclipses are natural phenomena which have always fascinated mankind. Several ancient civilizations were able to determine the occurrence of eclipses and most of them had a mythological, religious or symbolical interpretation. In particular, most of the prehispanic cultures in Mexico could predict when an eclipse was to occur thanks to accurate reports of previous occulting astronomical phenomena (Aveni, 2005). Nowadays, eclipses go on calling our attention as it can be attested each time this kind of event occurs.
During the past century, an astronomer started designing instruments to recreate eclipses for scientific goals; we propose here to relate this chapter of astronomical instrumentation.

I.2.1 Natural solar eclipses

At the beginning of the 20^{th} century, astronomers were getting interested in the observation of the solar corona. Unfortunately, the study of the Sun's corona could only be done when a total solar eclipse occurred. Indeed, the main difficulty is the brightness of the solar corona, which is less than one millionth (10^{-6}) that of the Sun, see Figure I.1. Blocking the light of the solar disk allows to observe the corona of our star and a total eclipse of the Sun represents a good way to reach this goal.
However, the frequency of solar total eclipses is about once every 18 months on average somewhere on Earth, and it has been estimated that it recurs about 3 times per millenium at any given place[5]. Moreover, the maximum duration of totality is about 7 minutes, but it succeeds less than 10 times in a millennium! These data allow to realize how difficult it was to observe and study the solar corona one century ago, since an eclipse is a very rare and short event.

I.2.2 Generation of artificial eclipses with the solar coronagraph

At the beginning of the 1930s, the French astronomer Bernard Lyot (1897-1952) invented an optical instrument to make artificial eclipses of the Sun: the **coronagraph** (Lyot and Marshall, 1933; Lyot, 1933), which name derives from the word **corona**. A schematic representation of the coronagraph designed by Lyot is shown in Figure I.2. It deals with the use of an opaque mask to block the solar disk and a diaphragm to remove the light diffracted by the mask. One of the Bernard Lyot's merits consisted in understanding the importance of using a downstream diaphragm: it suppresses the diffuse light created by the reflections between the optics within his system and eliminates the light diffracted by the opaque mask. As a tribute, nowadays this diaphragm is named "Lyot stop".
With his invention, Bernard Lyot could observe the corona without having to wait for a solar eclipse. In 1931, thanks to his optical setup, he took the first picture of the solar corona in the absence of a natural eclipse and in 1939, he recorded a movie named *Les flammes du Soleil* (flames of the Sun). It dealt with the movements of the solar protuberances and was realized thanks to his coronagraph and some filters. Figure I.3 shows Bernard Lyot during the installation of his coronagraph in the *Pic du Midi* Observatory where he worked.
Nowadays, SoHO (Solar and Heliospheric Observatory), launched on December 1995, is equipped

[5] See NASA Eclipse website: http://eclipse.gsfc.nasa.gov/eclipse.html

with a Lyot coronagraph to take pictures of the solar corona and until now, it has detected more than 1500 comets[6]. A picture captured by SoHO is shown in Figure I.4.

I.2.3 Extension of the solar coronagraph principle to point sources

The Lyot coronagraph was originally conceived to eclipse the Sun and thus, observe the solar corona. The analogy with one of the most exciting challenge of current astronomy, the imaging of faint substellar mass companions close to bright stars, is clear. A device is also required here to suppress the image of a bright stellar point source and ease the observation of dim objects in its vicinity. An optical layout similar to the solar coronagraph and dedicated to eliminate the diffracted stellar light, appears naturally as a first step to tackle the problem.
In the following, we review the techniques mainly developed during the last decade to attenuate the luminous flux coming from an observed star. Devices based on interferometry or apodization will be analyzed and thereafter, our attention will be focused on concepts deriving from the Lyot coronagraph.

[6] Visit the SoHO webpage: http://sohowww.nascom.nasa.gov/home.html

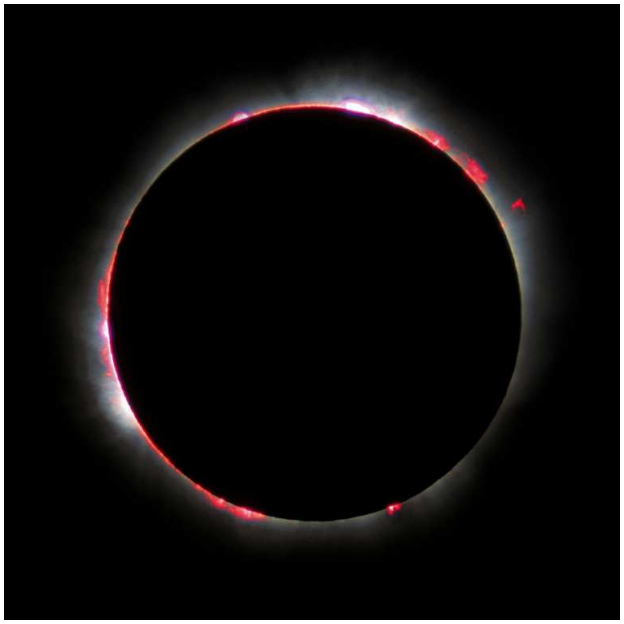

Figure I.1: Total solar eclipse of 1999 in France (©Luc Viatour).

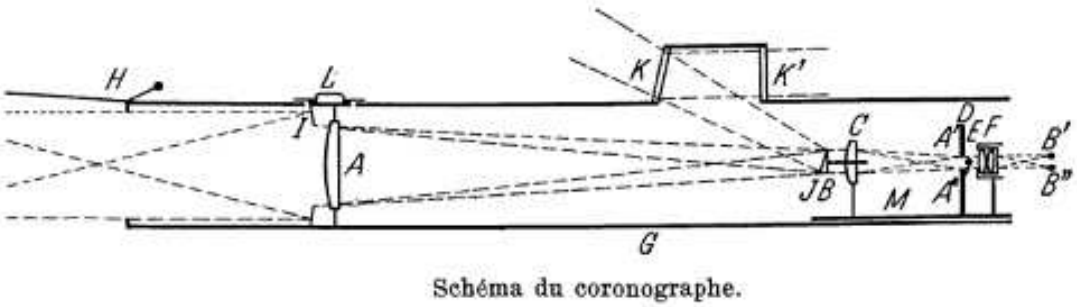

Figure I.2: Original scheme of the coronagraph designed by Bernard Lyot in 1932 (extracted from Lyot (1932)).

Figure I.3: Bernard Lyot during the installation of his solar coronagraph in the *Pic du Midi* Observatory (France) in 1939 (©American Museum of Natural History).

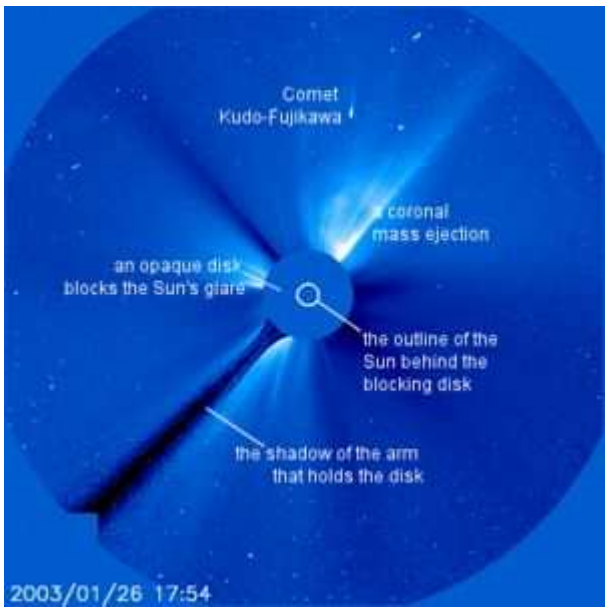

Figure I.4: Example of coronagraphic image of the solar corona and different astronomical events detected around it, with SoHO in 2003 (©NASA).

I.3 Brief review of the diffraction suppression systems

Several coronagraphic concepts have been proposed to suppress the diffracted light of a star. A classification scheme in the form of a coronagraphic tree of life was proposed by Quirrenbach (2005); we reproduce his scheme in Figure I.5. Most of them are reviewed in Guyon et al. (2006) or in Guyon (2007).
In the following, we propose to summarize the main techniques and describe in more details those of interest for the high contrast imaging feasibility study with FRIDA.

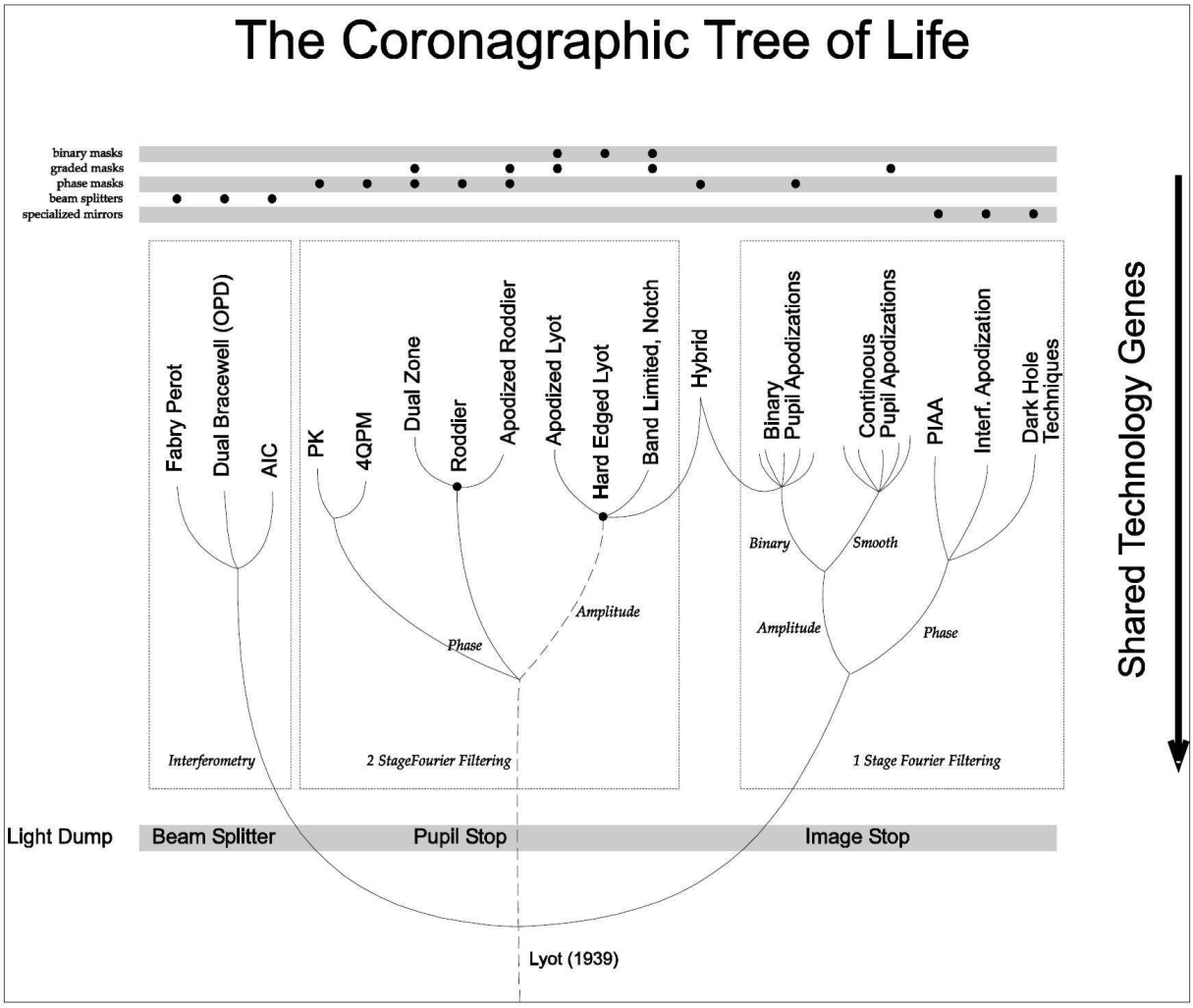

Figure I.5: Classification of coronagraphic concepts; this coronagraph tree of life was extracted from Quirrenbach (2005).

I.3.1 Coronagraphs based on nulling interferometry

Some coronagraphic designs based on nulling interferometry were suggested to achieve cancellation of the image of an observed bright star. They consist of creating at least two beams from a single telescope beam. The adequate recombination of these beams allow to produce on-axis destructive and off-axis constructive interferences in the re-imaged telescope focal plane where the star image is formed.
The Achromatic Interferometric Coronagraph (Gay and Rabbia, 1996) was the first nulling interferometer to be proposed, followed by several studies or improvements of this original device (Baudoz et al., 2000b, 2005; Tavrov et al., 2005). Tests on the sky have already carried out (Baudoz et al., 2000a,c).
The Visible Nuller coronagraph (Mennesson et al., 2003) and the Pupil Swapping Coronagraph (Guyon and Shao, 2006) are other examples of coronagraph interferometers recently invented to increase image contrast. These devices are based on beam shearing to yield destructive interference and therefore nulling in the following re-imaged pupil plane.

I.3.2 Pupil apodization coronagraphs

Another coronagraphic approach considers the concentration of stellar light within the central peak of the star image, rather than its elimination. It deals with pupil apodization[7] which consists in a modification of the entrance pupil transmission function. This concept was largely developed in Jacquinot and Roizen-Dossier (1964) and studied hereafter. Figure I.6 shows examples of light transmission for a circular pupil, before and after the use of an apodizer.
The goal here consists of smoothing the diffraction rings (or *pieds*, feet in French) of the stellar Point Spread Function (PSF[8]) to increase the contrast in the substellar mass companion search area. To achieve this result, a reduction or cancellation of the spatial frequencies corresponding to the PSF rings is realized thanks to an apodizer placed in the upstream pupil plane.
This can be done by using shaped/binary pupils (Kasdin et al., 2003; Vanderbei et al., 2003b,a, 2004; Aime, 2005a), continuous/smoothed pupils (Nisenson and Papaliolios, 2001; Gonsalves and Nisenson, 2003; Aime, 2005a) or with pupil remapping techniques (e. g. Guyon, 2003; Traub and Vanderbei, 2003). We can also mention the Pupil phase apodization (Yang and Kostinski, 2004) and the Phase Induced Zonal Zernike Apodization (Martinache, 2004) as alternative solutions proposed in the field of apodization for high contrast imaging. The diffraction rings of the stellar point spread function (PSF) are considerably reduced, resulting in higher contrast in the search area.

I.3.3 Coronagraphs using focal plane masks

The vast majority of the stellar coronagraphs are inherited from the original Lyot coronagraph. They consist of placing a mask at the telescope aperture focal plane in which the star image is formed. Focal plane masks can be split into two categories: the amplitude and the phase masks.

[7] The word "Apodization" comes from ancient greek and means "without feet".
[8] Point Spread Function: Impulse response of an optical system, here it represents the image of the observed star, considered as a punctual source in a first approximation, at the telescope focal plane

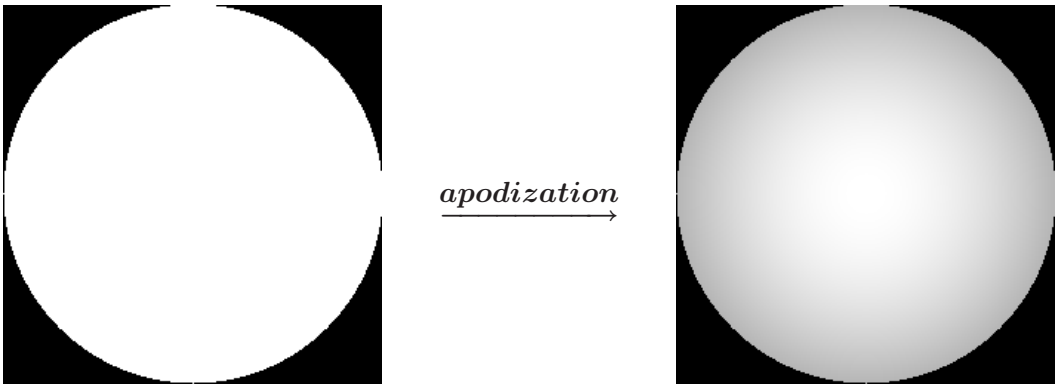

Figure I.6: Example of light transmission for a circular pupil before and after using an apodizer. Images are represented here in gray scale, where white represents a total light transmission whereas black symbolizes a total absence of transmission.

I.3.3.1 Coronagraphs using focal plane amplitude masks

Amplitude masks are opaque disks used to directly block the image of an observed on-axis bright star at the telescope focal plane. Thereafter, a diaphragm, usually named Lyot stop, is placed in the re-imaged pupil plane. It stops the light diffracted by the mask, present outside the re-imaged pupil. Star attenuation is therefore achieved and the coronagraphic image can be observed at the detector placed in the re-imaged focal plane. Images at each plane of the coronagraphic device are represented in Figure I.7. This concept is usually called **Classical Lyot Coronagraph** (CLC). Let us mention the band-limited mask, an improved design of the basic amplitude mask proposed to increase the contrast and to be well-adapted to the telescope geometry (Kuchner and Traub, 2002; Kuchner et al., 2005). Here, we will limit our study to CLC, for the simplicity of the mask design.

I.3.3.2 Coronagraphs using focal plane phase mask

On the other hand, phase masks use part of the starlight to create destructive interferences and hence remove the stellar luminous flux. The original concept was proposed by Roddier and Roddier (1997). A circular phase mask of diameter approximately equal to half the Airy disk is placed in the telescope focal plane, see Figure I.9(a). Part of the wavefront coming from an observed on-axis bright star goes through the mask and is phase shifted by π radians whereas the other part is not affected. The recombination of these two complex amplitudes leads to the rejection of the stellar light outside the re-imaged pupil. The Lyot stop placed there allows to block the rejected starlight, removing it from the following re-imaged focal plane. In Figure I.8, we represent the images obtained in each plane of this coronagraphic setup. This device is usually called **Classical Roddier Coronagraph** (CRC) and could allow to search substellar mass companions at closer distances of the star than CLC, since the phase mask is much smaller than the opaque one.
Unfortunately, CRC suffers from a double problem of chromatism: the phase mask radius is wavelength dependant (size chromatism) and the π-phase shift is optimized at just one wavelength (phase chromatism). Let us notice that CLC does not present the problem of phase chromatism. The Roddier & Roddier phase mask (RRPM) coronagraph was largely improved by the develop-

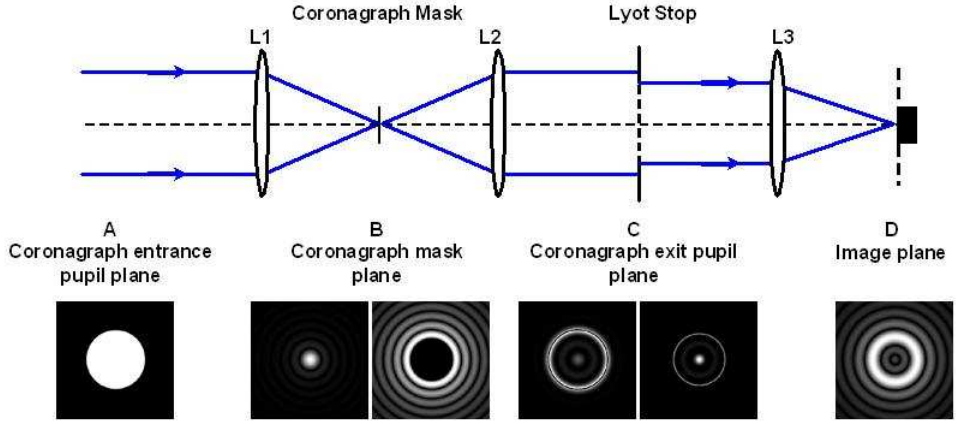

Figure I.7: Coronagraph assembly using an opaque mask. L1, L2 and L3 symbolize the lenses of the optical layout. L1 represents the telescope, L2 a collimator and L3 a camera. L2 and L3 could be an afocal system. At the bottom, from left, we represent the images in each plane. We work with a clear circular pupil in plane A. In the following focal plane B, the star PSF is formed and after then, partially blocked by an opaque mask (images before and after using an opaque mask). In the exit pupil plane C, we can notice the formation of a bright ring, result of the diffraction due to the mask; this ring is thereafter blocked by the lyot stop (images represented before and after Lyot stop). Finally, in the re-imaged focal plane D, we obtain the final coronagraphic image. The contrast of images was enhanced here for a better visibility.

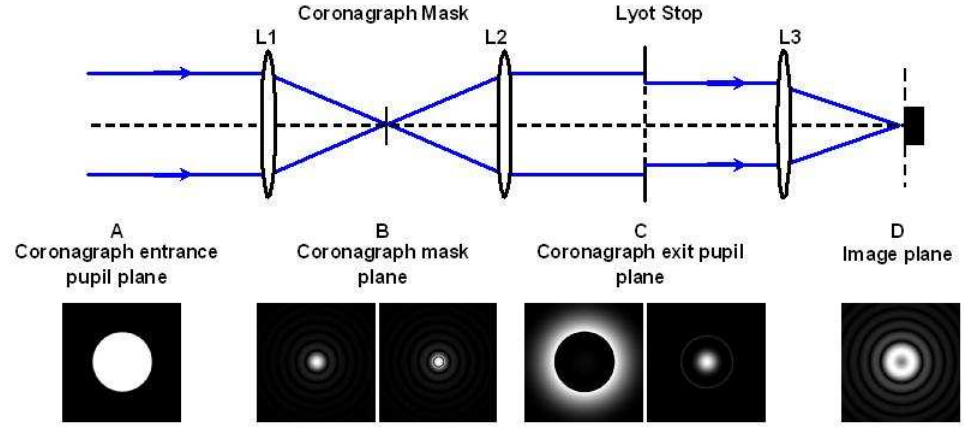

Figure I.8: Same as Figure I.7 but here, the opaque mask is replaced by a Roddier & Roddier phase one. We can notice the stellar light rejection outside the exit pupil in plane C. This light is thereafter blocked by a Lyot stop placed in the same plane. The final result is a star image in the re-imaged focal plane D fainter than in the coronagraph mask one (B). The contrast of images was enhanced here for a better visibility.

ment of other phase mask supports over the past few years (Rouan et al., 2000; Soummer et al., 2003b; Mawet et al., 2005; Palacios, 2005; Foo et al., 2005; Oti et al., 2005; Swartzlander, 2006).
Let us mention the **Four Quadrant Phase Mask** (4QPM): this mask does not present a circular but a 4 quadrant geometry. This design allows to solve the size chromatism problem of RRPM since 4QPM splits the focal plane into four identical parts, ensuring that half of the star energy will effectively cross the π-phase shift areas. Indeed, a π-phase shift is provided in opposite quadrants whereas the other quadrants present a null phase shift. The 4QPM is illustrated in Figure I.9(b). However, 4QPM is much more sensitive to the aperture design (for instance, the presence of a central obstruction). In our further studies, our work will mainly focus on centrally obstructed apertures and in particular, the Gran Telescopio Canarias (GTC), on which FRIDA will be installed. Hence, we decided to not include the 4QPM coronagraph in our further studies. However, this solution remains interesting as reference of the coronagraph feasibility since it has already been tested and validated on bench and on sky (Riaud et al., 2003; Boccaletti et al., 2004; Gratadour et al., 2005).
Let us mention also the **Dual Zone Phase Mask** (DZPM) proposed by Soummer et al. (2003b): this mask presents the advantage of being achromatic and allows to solve the double chromatism problem of RRPM. DZPM is a doughnut-shaped phase mask surrounding the original Roddier & Roddier phase disk; a schematic representation is given in Figure I.9(c). Two different phase shifts φ_1 and φ_2 are attributed to this dual-zone phase mask. Therefore, the coronagraphic amplitude at the re-imaged pupil plane will appear as the summation of three complex components. The first term represents the wavefront crossing the DZPM central disk, the second one comes from the wavefront going through the DZPM doughnut area and the third one is due to the wavefront surrounding the mask in the aperture focal plane (see Figure I.10 from Soummer et al. (2003b)). The DZPM coronagraph is a very promising device but is not studied in details here. Later, we will show that DZPM could constitute an interesting solution for high contrast imaging with FRIDA when working in Integral Field Spectroscopy (IFS) mode.
Concerning the coronagraphs involving phase masks, we will limit our studies to the RRPM and just consider CRC, its corresponding coronagraphic device.

I.3.3.3 Coronagraphs combining pupil apodizer & focal plane mask

Pupil apodizers and focal plane masks can also be combined to enhance companion image (Aime et al., 2001, 2002; Soummer et al., 2003a; Aime, 2005b; Soummer, 2005). With the association "pupil apodizer + focal plane mask", we can benefit from the advantages of each device. On the one hand, the focal plane mask allows to partially remove the PSF central peak and therefore, avoid an eventual detector saturation in the coronagraphic plane. On the other hand, the apodization of the entrance pupil (a re-imaged telescope aperture) allows to reduce the intensity of the PSF rings and increase the contrast in the companion search area. This kind of coronagraph will be considered in our further coronagraph feasibility studies for FRIDA.
For instance, **Apodized Pupil Lyot Coronagraph** (APLC) is a combination of a pupil apodizer, a focal plane opaque mask and a Lyot stop in the re-imaged pupil plane (Aime et al., 2001, 2002; Soummer et al., 2003a) and its performance will be evaluated. This coronagraph is a promising solution since it can be well designed to work with centrally obstructed apertures (Soummer, 2005).
We will also propose a modified version of APLC, the **Stop-less Lyot Coronagraph** (SLLC), which is an association of an apodization and a focal plane opaque mask, but no Lyot stop is used

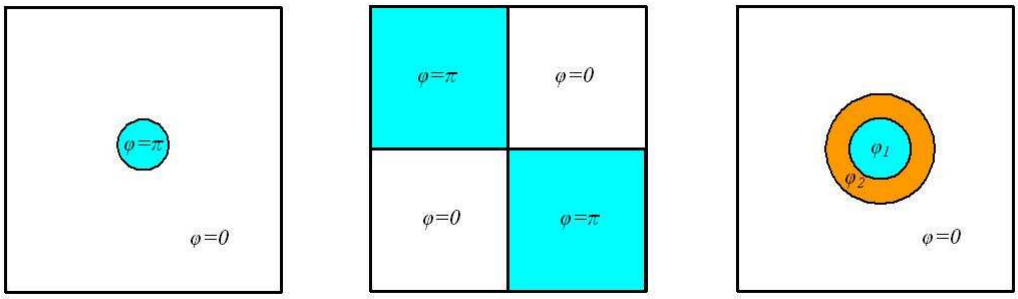

(a) Roddier & Roddier Phase Mask

(b) Four Quadrant Phase Mask

(c) Dual Zone phase mask

Figure I.9: Schematic representation of phase masks.

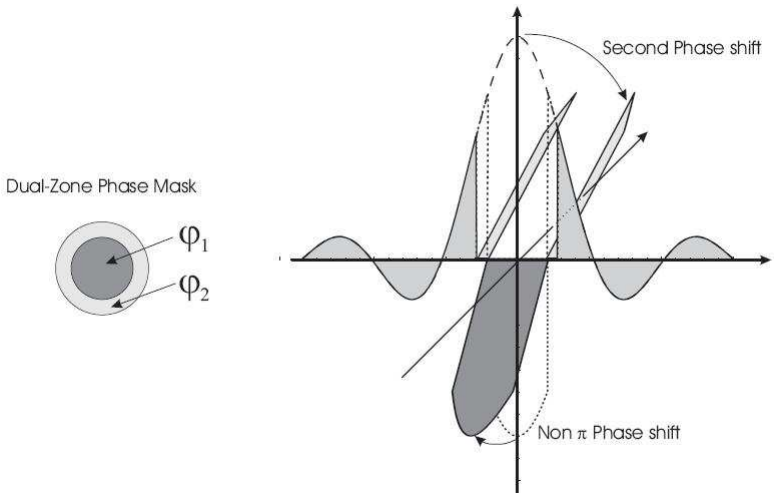

Figure I.10: On the left, scheme of the Dual Zone Phase Mask and on the right, representation in a three dimensional space of the three amplitude waves reached after crossing the mask. The sum of these components will result in a perfect cancelation of the star image in the re-imaged focal plane. This sketch was extracted from Soummer et al. (2003b) (©ESO 2003).

in this case (N'Diaye et al., in prep.). We will discuss the interest of this coronagraphic solution for FRIDA and instruments for which the insertion of a diaphragm is made impossible.
In fact, the Apodized Pupil Phase Mask Coronagraph first suggested by Guyon and Roddier (2000) cannot be inserted within the FRIDA optical assembly, because of some mechanical issues.
In the following section, we expose the formalism of Lyot-style coronagraphs, i.e. those involving a focal plane mask, a Lyot stop and possibly an entrance pupil apodizer. This formalism allows to describe all the coronagraphic concepts that will be considered in our further studies, even those which do not involve a Lyot stop in their scheme like SLLC.

I.4 Formalism of Lyot-style coronagraphs and performance criteria

I.4.1 General formalism

The principle of a coronagraphic experiment, with focal plane mask and apodization, is exposed in Aime et al. (2002) and Soummer et al. (2003a), and generalized in Soummer (2005) to the case of arbitrary telescope apertures. We briefly review the common formalism, following the notations of Aime et al. (2002). Fig. I.11 gives an illustration of the coronagraphic setup.

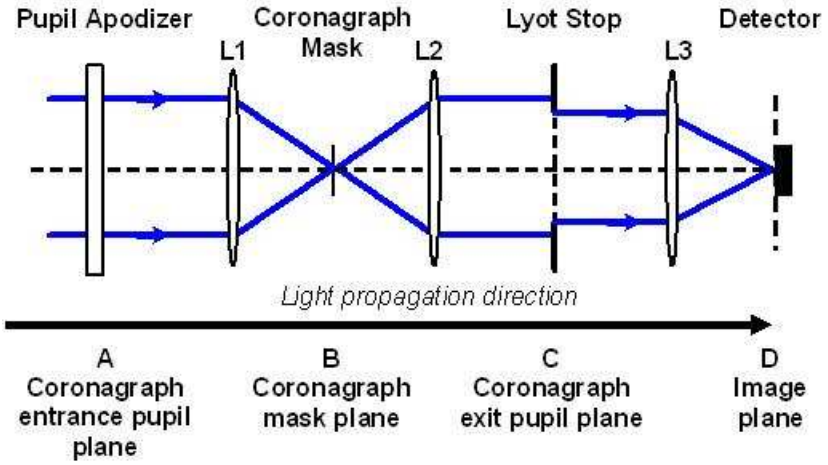

Figure I.11: Schematic illustration of the coronagraph assembly.

Planes A, B, C and D denote respectively the entrance pupil plane, the coronagraphic focal plane, the exit pupil plane and the detector plane. Here, the usual approximations of paraxial optics are made. Moreover, the quadratic phase terms associated with the propagation of the waves are neglected. Therefore, the coronagraph can be described using classical Fourier optics: a Fourier transform exists between each of the four planes. We denote $\mathbf{r}$ the position vector respectively and r its modulus. $\hat{f}$ is the Fourier transform of the function f and $\otimes$ denotes the convolution product. P and ϕ are the telescope aperture function and the apodizer transmission. The wavefront complex amplitude in plane A (Ψ_A) can be expressed as follows:

$$\Psi_A(\mathbf{r}) = P(\boldsymbol{r})\,\phi(\boldsymbol{r})\,. \tag{I.1}$$

In the focal plane B, the coronagraph mask is applied. Its transmission is given by $1 - \epsilon\, M(\boldsymbol{r})$ ($M(\boldsymbol{r})$ is equal to 1 inside the coronagraphic mask and 0 outside). The parameter ϵ is equal to 1 for an opaque mask (Lyot coronagraph) and 2 for a Roddier & Roddier phase mask. The complex amplitude becomes:

$$\Psi_B(\boldsymbol{r}) = \hat{\Psi}_A(\boldsymbol{\rho}) \times [1 - \epsilon\, M(\boldsymbol{r})]\ , \tag{I.2}$$

where $\boldsymbol{\rho}$ symbolizes the spatial frequency in the Fourier domain: $\boldsymbol{\rho} = \boldsymbol{r}/\lambda f$, λ and f denote the wavelength and the telescope focal length.
In the exit pupil plane C, Ψ_C denotes the complex amplitude. The pupil stop present there removes

the starlight diffracted by the mask outside the exit pupil. L is the index function of the Lyot stop and can be chosen exactly equal to the entrance pupil shape. Therefore, the complex amplitude can be written as:

$$\Psi_C(\boldsymbol{r}) = \hat{\Psi}_B(\boldsymbol{\rho}) \times P(\boldsymbol{r}) = \left[\Psi_A(\boldsymbol{r}) - \epsilon\, \Psi_A(\boldsymbol{r}) \otimes \hat{M}(\boldsymbol{\rho})\right] \times L(\boldsymbol{r})\,, \tag{I.3}$$

and in plane D, the coronagraphic complex amplitude is given by:

$$\Psi_D(\boldsymbol{r}) = \hat{\Psi}_C(\boldsymbol{\rho}) = \left[\hat{\Psi}_A(\boldsymbol{\rho}) - \epsilon\, \hat{\Psi}_A(\boldsymbol{\rho}) \times M(\boldsymbol{r})\right] \otimes \hat{L}(\boldsymbol{\rho})\,. \tag{I.4}$$

The intensity I_i at a given plane i is obtained as follows:

$$I_i(\boldsymbol{r}) = |\Psi_i(\boldsymbol{r})|^2\,. \tag{I.5}$$

Hence, the residual intensity I_D in the detector plane for an on-axis star is:

$$I_D(\boldsymbol{r}) = |\Psi_D(\boldsymbol{r})|^2\,. \tag{I.6}$$

Eq. (I.3) makes apparent the effect of the coronagraph. Indeed, the complex amplitude in C is the sum of two terms: the direct wavefront corresponding to the entrance pupil and the wavefront diffracted by the mask. Complete starlight extinction is achieved if these two wavefronts are identical. An appropriate choice of the apodizer profile leads to theoretical perfect cancellation. Both wavefronts match perfectly in the case of the Apodized Pupil Phase Mask Coronagraph (Roddier and Roddier, 1997; Aime et al., 2002; Soummer et al., 2003a). In the case of the Apodized Pupil Lyot Coronagraph (APLC), the coronagraphic amplitude is minimized and proportional to the apodizer function. Considering a non trivial pupil geometry, the apodizer shape depends both on the central obstruction of the telescope aperture and the mask size (Soummer, 2005; Martinez et al., 2007).

I.4.2 Focus on the centrally obstructed circular apertures

The formalism, presented above, can be applied to any arbitrary telescope geometry. In this section, focus is made on the case of centrally obstructed circular entrance apertures. The telescope secondary mirror and its mount project their shadow on the primary mirror, what implies a central obscuration within the entrance pupil. Hereafter, the effects produced by the secondary mirror mount, usually called "spider arms", are neglected.

The main results of Fourier Optics are well described in several books: Born and Wolf (1999), Goodman (1996) or Shroeder (2000). Here, we briefly review the expression of the PSF corresponding to an obstructed circular aperture in the following lines, but more details can be found in these reference books.

Let us consider an aperture diameter D and a central obstruction size γD (with $0 \leq \gamma < 1$). The circular symmetry of the problem suggests that the position vector $\boldsymbol{r}$ can be substituted by the radial coordinate r. Therefore, the telescope aperture function can be written as:

$$P(r) = \Pi\left(\frac{r}{D}\right) - \Pi\left(\frac{r}{\gamma D}\right)\,, \tag{I.7}$$

where $\Pi(r) = 1$ for $|r| < 1/2$ and 0 elsewhere.
In the case neither the pupil apodizer ($\phi(\boldsymbol{r}) = 1$) nor the mask ($\epsilon = 0$) are used, the amplitude distribution in the focal plane B is seen to be:

$$\Psi_B(r) = \frac{\pi D^2}{4}\left[\frac{2J_1(Z)}{Z} - \gamma^2\frac{2J_1(\gamma Z)}{\gamma Z}\right], \tag{I.8}$$

where J_1 is a Bessel function of the first kind and $Z = \pi Dr/\lambda f$. The ratio $J_1(Z)/Z$ approaches one as Z approaches zero, hence $\Psi_B(0) = \pi D^2(1-\gamma^2)/4$. For a clear aperture ($\gamma = 0$), the PSF characterizes the so-called Airy diffraction pattern, otherwise the Fraunhoffer diffraction pattern is the term to be employed.
These classical expressions will be useful to check the numerical simulations of the coronagraph setup that we will present in the following chapters. Indeed, in the absence of coronagraph, the complex amplitude in the image plane is characterized by Eq. (I.8). Let us remind that we omit in the previous expressions, the quadratic phase terms, the scale factor $1/i\lambda f$ and the factor e^{ikf}, where $k = 2\pi/\lambda$, which represents the constant phase delay suffered by all plane-wave components traveling between two parallel planes separated by a normal distance f (Goodman, 1996). In the approach of polychromatic point sources, we will be very careful to not forget the impact of these terms since a wavelength dependence appears in these expressions.

I.4.3 Estimate of the coronagraph performance

Quantifying the coronagraph performance is required if we want to estimate the extinction level of a star image achieved by a given coronagraph and therefore, evaluate the possibility of detecting a dim object close to a nearby bright star. Several metrics have been proposed to measure the gain reached by a given coronagraph. We review the criteria presented by Abe (2004) or Boccaletti (2004), and described again in Cavarroc (2007):

- The **total rejection** $\mathcal{R}_{total}$ represents the ratio between the residual energy obtained after coronagraph application and the total energy in the absence of mask:

$$\mathcal{R}_{total} = \frac{\iint I_D(\mathbf{r})_{with\,mask}\, d\mathbf{r}}{\iint I_D(\mathbf{r})_{w/o\,mask}\, d\mathbf{r}}. \tag{I.9}$$

- The **maximum rejection** $\mathcal{R}_{max}$ defines the ratio between the maximum coronagraphic intensity and the intensity in the absence of mask:

$$\mathcal{R}_{max} = \frac{max\left(I_D(\mathbf{r})_{with\,mask}\right)}{max\left(I_D(\mathbf{r})_{w/o\,mask}\right)}. \tag{I.10}$$

- The **contrast** $\mathcal{C}$ defines the ratio between the mean intensity at a given angular separation α from the main optical axis and the maximum intensity in the absence of mask:

$$\mathcal{C}(\alpha) = \frac{\iint_{\mathcal{D}} I_D(\mathbf{r})_{with\,mask}\, d\mathbf{r}}{max\left(I_D(\mathbf{r})_{w/o\,mask}\right)}, \tag{I.11}$$

  where $\mathcal{D}$ denotes an area centered on the angular separation α and which corresponds to a range of angular radii.

- The **attenuation** $\mathcal{A}$ at a given angular separation α from the main optical axis is given by:

$$\mathcal{A}(\alpha) = \frac{\iint_{\mathcal{D}} I_D(\mathbf{r})_{w/o\,mask}\, d\mathbf{r}}{\iint_{\mathcal{D}} I_D(\mathbf{r})_{with\,mask}\, d\mathbf{r}}\,. \tag{I.12}$$

  The **contrast gain** Δm in stellar magnitudes is obtained using the following expression which involves the obtained attenuation $\mathcal{A}$:

$$\Delta m = 2.5 \log_{10}(\mathcal{A}(\alpha)) \tag{I.13}$$

- Another useful term, above all when we work in the presence of aberrations, is the **detectability** σ. This standard deviation is relied on the ability to extract the companion signal from the speckle halo at a given angular separation α (Boccaletti, 2004):

$$\sigma(\alpha) = \frac{\sigma\left(\iint_{\mathcal{D}} I_D(\mathbf{r})_{w/o\,mask}\, d\mathbf{r}\right)}{max\left(I_D(\mathbf{r})_{w/o\,mask}\right)}\,. \tag{I.14}$$

Several other criteria have been defined in the literature. In particular, we can cite the **Inner Working Angle** which is usually defined as the minimum angular distance at which the throughput for the companion is half the maximum throughput, the search area which represents the fraction of the focal plane image within which a companion can be detected or the throughput measured at large angular separation.
Guyon et al. (2006) also proposed a criteria, named the "useful throughput" and, which characterizes the area fraction in the focal plane image within which the companion flux is greater than the starlight amount. Lyon et al. (2003) and Martinez et al. (2007) also give interesting contributions to quantify the coronagraph performance.
However in the present work, we will mainly focus on the contrast gain and the detectability to quantify the performance of a coronagraph.

I.5 Conclusion of the first chapter

After a review of the context in contemporary astronomy and astrophysics, we have pointed out the importance and the interest of using high contrast imaging techniques. The solar coronagraph invented by Bernard Lyot, to reach images of the Sun corona despite the presence and brightness of the solar disk, was a precursor for stellar coronagraphy. We have noticed that most of the stellar coronagraphic designs developed these past few years derive essentially from the original Lyot coronagraph.
In a first step, the different diffraction suppression systems recently proposed have been summarized. Afterwards, we have focused on the devices we will study in the context of high contrast imaging with FRIDA instrument: the Lyot-style coronagraphs which involve a focal plane mask, a Lyot stop and possibly an entrance pupil apodizer. The formalism of these concepts were reviewed and useful definitions given to characterize the performance of a coronagraph. In the following, these criteria will be of great importance in our coronagraph feasibility studies for FRIDA.
In the following chapter, we present FRIDA and describe its main capabilities. An analysis of its optical setup will be carried out to determine some feasible coronagraphic configurations.

I.5 Conclusión del primer capítulo

Después de una revisión del contexto en astronomía y astrofísica, se ha subrayado la importancia y el interés de utilizar técnicas para formar imágenes de alto contraste. El coronógrafo solar, inventado por Bernard Lyot para obtener imágenes de la corona solar a pesar de la presencia y del brillo del disco solar, fue un precursor para la coronografía estelar. Se ha hecho notar que la mayoría de los diseños coronográficos estelares desarrollados estos últimos años provienen esencialmente del coronógrafo original de Lyot.
En una primera etapa, se ha hecho un resumen de los diferentes sistemas de supresión de difracción recientemente propuestos. Luego, se ha centrado en los dispositivos que se van a estudiar en el contexto de la formación de imágenes de alto contraste con el instrumento FRIDA: los coronógrafos de tipo Lyot que involucran una máscara de plano focal, un diafragma de Lyot y eventualmente, una apodización pupilar de entrada. Se revisó el formalismo de estos conceptos y se dieron definiciones útiles para caracterizar el desempeño de un coronógrafo. En lo que sigue, estos criterios serán de mayor importancia en nuestros estudios de factibilidad de coronógrafos para FRIDA.
En el próximo capítulo, se presenta FRIDA y se describen sus principales características. Se llevará a cabo una análisis de su esquema óptico para determinar las configuraciones coronográficas que pueden ser factibles.

I.6 References

L. Abe. Numerical Simulations in Coronagraphy. Part I. In C. Aime and R. Soummer, editors, *EAS Publications Series*, volume 12 of *EAS Publications Series*, pages 157–164, 2004.

C. Aime. Radon approach to shaped and apodized apertures for imaging exoplanets. *A&A*, 434, 785–794, 2005a.

C. Aime. Principle of an Achromatic Prolate Apodized Lyot Coronagraph. *Public. of the Astron. Soc. Pac.*, 117, 1012–1019, 2005b.

C. Aime, R. Soummer, and A. Ferrari. Interferometric apodization of rectangular apertures. Application to stellar coronagraphy. *A&A*, 379, 697–707, 2001.

C. Aime, R. Soummer, and A. Ferrari. Total coronagraphic extinction of rectangular apertures using linear prolate apodizations. *A&A*, 389, 334–344, 2002.

A. F. Aveni. *Observadores del Cielo en el México Antiguo*. Observadores del Cielo en el México Antiguo, Edition: 2nd ed., Publisher: México D.F., Fondo de Cultura Económico, 2005, ISBN: 9 68 167293 3, 2005.

P. Baudoz, D. Mouillet, J.-L. Beuzit, D. Mékarnia, Y. Rabbia, J. Gay, and J.-L. Schneider. First Results of the Achromatic Interfero Corono-graph at CFHT. *Bulletin d'information du telescope Canada-France-Hawaii*, 42, 17–19, 2000a.

P. Baudoz, Y. Rabbia, and J. Gay. Achromatic interfero coronagraphy I. Theoretical capabilities for ground-based observations. *A&AS*, 141, 319–329, 2000b.

P. Baudoz, Y. Rabbia, J. Gay, R. Burg, L. Petro, P. Bely, B. Fleury, P.-Y. Madec, and F. Charbonnier. Achromatic interfero coronagraphy. II. Effective performance on the sky. *A&AS*, 145, 341–350, 2000c.

P. Baudoz, A. Boccaletti, Y. Rabbia, and J. Gay. Stellar Coronagraphy: Study and Test of a Hybrid Interfero-Coronagraph. *Public. of the Astron. Soc. Pac.*, 117, 1004–1011, 2005.

A. Boccaletti. Numerical Simulations for Coronagraphy. part II. In C. Aime and R. Soummer, editors, *EAS Publications Series*, volume 12 of *EAS Publications Series*, pages 165–176, 2004.

A. Boccaletti, P. Riaud, P. Baudoz, J. Baudrand, D. Rouan, D. Gratadour, F. Lacombe, and A.-M. Lagrange. The Four-Quadrant Phase Mask Coronagraph. IV. First Light at the Very Large Telescope. *Public. of the Astron. Soc. Pac.*, 116, 1061–1071, 2004.

M. Born and E. Wolf. *Principles of optics, Electromagnetic theory of propagation, interference and diffraction of light*. Principles of optics, Edition: 7nd (expanded) ed., Publisher: Cambridge, Cambridge University Press, 1999, ISBN: 0 52 164222 1, 1999.

A. Burrows and C. M. Sharp. Chemical Equilibrium Abundances in Brown Dwarf and Extrasolar Giant Planet Atmospheres. *ApJ*, 512, 843–863, 1999.

A. Burrows, D. Sudarsky, and I. Hubeny. Spectra and Diagnostics for the Direct Detection of Wide-Separation Extrasolar Giant Planets. *ApJ*, 609, 407–416, 2004.

C. Cavarroc. *Caractérisation d'un coronographe pour la détection d'exoplanètes avec MIRI/JWST*. PhD thesis, Université de Paris VII - Denis Diderot, 2007.

G. Chauvin. Direct Imaging Detection of Planets and Brown Dwarfs. In P. Kalas, editor, *In the Spirit of Bernard Lyot: The Direct Detection of Planets and Circumstellar Disks in the 21st Century*, 2007.

G. Foo, D. M. Palacios, and G. A. Swartzlander, Jr. Optical vortex coronagraph. *Optics Letters*, 30, 3308–3310, 2005.

J. Gay and Y. Rabbia. An interferometric method for coronography. *Academie des Science Paris Comptes Rendus Serie B Sciences Physiques*, 322, 265–271, 1996.

R. Gonsalves and P. Nisenson. Calculation of Optimized Apodizers for a Terrestrial Planet Finder Coronagraphic Telescope. *Public. of the Astron. Soc. Pac.*, 115, 706–711, 2003.

J. W. Goodman. *Introduction to Fourier Optics*. Introduction to Fourier Optics, Edition: 2nd ed., Publisher: New York, The McGraw-Hill companies, 1996, ISBN: 0 07 024254 2, 1996.

D. Gratadour, D. Rouan, A. Boccaletti, P. Riaud, and Y. Clénet. Four quadrant phase mask K-band coronagraphy of NGC 1068 with NAOS-CONICA at VLT. *A&A*, 429, 433–437, 2005.

O. Guyon. Phase-induced amplitude apodization of telescope pupils for extrasolar terrestrial planet imaging. *A&A*, 404, 379–387, 2003.

O. Guyon. The Coronagraph Tree of Life. In P. Kalas, editor, *In the Spirit of Bernard Lyot: The Direct Detection of Planets and Circumstellar Disks in the 21st Century*, 2007.

O. Guyon and F. J. Roddier. Direct exoplanet imaging possibilities of the nulling stellar coronagraph. In P. J. Lena and A. Quirrenbach, editors, *Proc. SPIE Vol. 4006, p. 377-387, Interferometry in Optical Astronomy, Pierre J. Lena; Andreas Quirrenbach; Eds.*, volume 4006 of *Presented at the Society of Photo-Optical Instrumentation Engineers (SPIE) Conference*, pages 377–387, 2000.

O. Guyon and M. Shao. The Pupil-swapping Coronagraph. *Public. of the Astron. Soc. Pac.*, 118, 860–865, 2006.

O. Guyon, E. A. Pluzhnik, M. J. Kuchner, B. Collins, and S. T. Ridgway. Theoretical Limits on Extrasolar Terrestrial Planet Detection with Coronagraphs. *ApJS*, 167, 81–99, 2006.

P. Jacquinot and B. Roizen-Dossier. *Apodisation*, pages 31–186. Progress in Optics volume III, Edition: E. Wolf, Publisher: Amsterdam, North-Holland Publishing Company, 1964, 1964.

N. J. Kasdin, R. J. Vanderbei, D. N. Spergel, and M. G. Littman. Extrasolar Planet Finding via Optimal Apodized-Pupil and Shaped-Pupil Coronagraphs. *ApJ*, 582, 1147–1161, 2003.

M. J. Kuchner and W. A. Traub. A Coronagraph with a Band-limited Mask for Finding Terrestrial Planets. *ApJ*, 570, 900–908, 2002.

M. J. Kuchner, J. Crepp, and J. Ge. Eighth-Order Image Masks for Terrestrial Planet Finding. *ApJ*, 628, 466–473, 2005.

R. G. Lyon, J. M. Hollis, and J. E. Dorband. Comparative optical analysis of extrasolar planetary imaging techniques. In A. B. Schultz, editor, *High-Contrast Imaging for Exo-Planet Detection. Edited by Alfred B. Schultz. Proceedings of the SPIE, Volume 4860, pp. 251-265 (2003).*, volume 4860 of *Presented at the Society of Photo-Optical Instrumentation Engineers (SPIE) Conference*, pages 251–265, 2003.

B. Lyot. Étude de la couronne solaire en dehors des éclipses. Avec 16 figures dans le texte. *Zeitschrift fur Astrophysik*, 5, 73–95, 1932.

B. Lyot. The Study of the Solar Corona without an Eclipse (with Plate V). *Journal of the Royal Astron. Soc. of Canada*, 27, 265–280, 1933.

B. Lyot and R. K. Marshall. The Study of the Solar Corona without an Eclipse. *Journal of the Royal Astron. Soc. of Canada*, 27, 225–234, 1933.

M. S. Marley, C. Gelino, D. Stephens, J. I. Lunine, and R. Freedman. Reflected Spectra and Albedos of Extrasolar Giant Planets. I. Clear and Cloudy Atmospheres. *ApJ*, 513, 879–893, 1999.

F. Martinache. PIZZA: a phase-induced zonal Zernike apodization designed for stellar coronagraphy. *Journal of Optics A: Pure and Applied Optics*, 6, 809–814, 2004.

P. Martinez, A. Boccaletti, M. Kasper, P. Baudoz, and C. Cavarroc. Optimization of apodized pupil Lyot coronagraph for ELTs. *A&A*, 474, 671–678, 2007.

D. Mawet, P. Riaud, O. Absil, and J. Surdej. Annular Groove Phase Mask Coronagraph. *ApJ*, 633, 1191–1200, 2005.

B. P. Mennesson, M. Shao, B. M. Levine, J. K. Wallace, D. T. Liu, E. Serabyn, S. C. Unwin, and C. A. Beichman. Optical Planet Discoverer: how to turn a 1.5-m class space telescope into a powerful exo-planetary systems imager. In A. B. Schultz, editor, *High-Contrast Imaging for Exo-Planet Detection. Edited by Alfred B. Schultz. Proceedings of the SPIE, Volume 4860, pp. 32-44 (2003).*, volume 4860 of *Presented at the Society of Photo-Optical Instrumentation Engineers (SPIE) Conference*, pages 32–44, 2003.

M. N'Diaye, K. Dohlen, and S. Cuevas. Stop-less Lyot Coronagraphs. In preparation, 2010.

P. Nisenson and C. Papaliolios. Detection of Earth-like Planets Using Apodized Telescopes. *ApJL*, 548, L201–L205, 2001.

J. E. Oti, V. F. Canales, and M. P. Cagigal. The Optical Differentiation Coronagraph. *ApJ*, 630, 631–636, 2005.

D. M. Palacios. An optical vortex coronagraph. In D. R. Coulter, editor, *Techniques and Instrumentation for Detection of Exoplanets II. Edited by Coulter, Daniel R. Proceedings of the SPIE, Volume 5905, pp. 196-205 (2005).*, volume 5905 of *Presented at the Society of Photo-Optical Instrumentation Engineers (SPIE) Conference*, pages 196–205, 2005.

A. Quirrenbach. Coronographic Methods for the Detection of Terrestrial Planets. *ArXiv Astrophysics e-prints*, 2005.

A. Quirrenbach. Detection and Characterization of Extrasolar Planets. In D. Queloz, S. Udry, M. Mayor, W. Benz, P. Cassen, T. Guillot, and A. Quirrenbach, editors, *Saas-Fee Advanced Course 31: Extrasolar planets*, pages 1–242, 2006.

P. Riaud, A. Boccaletti, J. Baudrand, and D. Rouan. The Four-Quadrant Phase Mask Coronagraph. III. Laboratory Performance. *Public. of the Astron. Soc. Pac.*, 115, 712–719, 2003.

F. Roddier and C. Roddier. Stellar Coronagraph with Phase Mask. *Public. of the Astron. Soc. Pac.*, 109, 815–820, 1997.

D. Rouan, P. Riaud, A. Boccaletti, Y. Clénet, and A. Labeyrie. The Four-Quadrant Phase-Mask Coronagraph. I. Principle. *Public. of the Astron. Soc. Pac.*, 112, 1479–1486, 2000.

D. J. Shroeder. *Astronomical Optics*. Astronomical Optics, Edition: 2nd ed., Publisher: San Diego, Academic Press, 2000, ISBN: 0 12 629810 6, 2000.

R. Soummer. Apodized Pupil Lyot Coronagraphs for Arbitrary Telescope Apertures. *ApJL*, 618, L161–L164, 2005.

R. Soummer, C. Aime, and P. E. Falloon. Stellar coronagraphy with prolate apodized circular apertures. *A&A*, 397, 1161–1172, 2003a.

R. Soummer, K. Dohlen, and C. Aime. Achromatic dual-zone phase mask stellar coronagraph. *A&A*, 403, 369–381, 2003b.

G. A. Swartzlander, Jr. Achromatic optical vortex lens. *Optics Letters*, 31, 2042–2044, 2006.

A. V. Tavrov, Y. Kobayashi, Y. Tanaka, T. Shioda, Y. Otani, T. Kurokawa, and M. Takeda. Common-path achromatic interferometer-coronagraph: nulling of polychromatic light. *Optics Letters*, 30, 2224–2226, 2005.

W. A. Traub and R. J. Vanderbei. Two-Mirror Apodization for High-Contrast Imaging. *ApJ*, 599, 695–701, 2003.

R. J. Vanderbei, D. N. Spergel, and N. J. Kasdin. Spiderweb Masks for High-Contrast Imaging. *ApJ*, 590, 593–603, 2003a.

R. J. Vanderbei, D. N. Spergel, and N. J. Kasdin. Circularly Symmetric Apodization via Star-shaped Masks. *ApJ*, 599, 686–694, 2003b.

R. J. Vanderbei, N. J. Kasdin, and D. N. Spergel. Checkerboard-Mask Coronagraphs for High-Contrast Imaging. *ApJ*, 615, 555–561, 2004.

N. Woolf and J. R. Angel. Astronomical Searches for Earth-Like Planets and Signs of Life. *Annual Review of Astron and Astrophys*, 36, 507–538, 1998.

W. Yang and A. B. Kostinski. One-sided Achromatic Phase Apodization for Imaging of Extrasolar Planets. *ApJ*, 605, 892–901, 2004.

Chapter II

FRIDA and stellar coronagraphy

II.1 Context

II.1.1 FRIDA, the future Imager and IFU spectrograph for the GTC

In the first chapter, we reminded the context of stellar coronagraphy and reviewed the formalism of the most promising concepts. In the following, the coronagraphic devices previously presented are now considered in the approach of FRIDA, a second-generation instrument for the Gran Telescopio Canarias (GTC).
FRIDA (in**F**ra**R**ed **I**mager and **D**issector for the **A**daptive optics system of the GTC) is being designed as a diffraction limited instrument with broad and narrow band imaging and integral field spectroscopy (IFS) capabilities to operate in the wavelength range 0.9–2.5 μm (López et al., 2006a,b, 2007a,b; Cuevas et al., 2006, 2008). The imaging and IFS observing modes will use the same single 2048×2048 Hawaii II Teledyne detector. FRIDA will be installed at the Nasmyth A platform behind GTCAO, the Adaptive Optics system of the GTC. The thermal emission produced by the optics at wavelengths larger than 2 μm imposes FRIDA to be a fully cryogenic instrument

II.1.2 Coronagraphic capability for FRIDA

FRIDA is planned to address a wide range of astrophysical issues with its capabilities. Design specifications clearly mentioned that FRIDA shall be able to perform high contrast imaging and therefore, coronagraphic paths shall be scheduled and provided to FRIDA. To reach this goal, the GTC scientific community expressly required the presence of reserved sites in the FRIDA optical assembly to allow the insertion of focal plane masks, diaphragms or pupil apodizers.

II.1.3 Possible coronagraph configurations for FRIDA

The FRIDA opto-mechanical design was thought to facilitate some upgrades. Here, we are getting interested in the reachable coronagraphic paths for FRIDA. Indeed, we want to allow FRIDA to produce high contrast images at high angular resolutions. In Section II.2, we present FRIDA and give a detailed description of this instrument. An analysis of the FRIDA optical layout will be led

in Section II.3 in order to suggest different coronagraphic devices that could be introduced within this GTC instrument.

II.1 Contexto

II.1.1 FRIDA, el futuro instrumento de segunda generación para el GTC

En el primer capítulo, se expuso el contexto de la coronografía estelar y se revisó el formalismo de los conceptos más prometedores. En lo que sigue, se consideran ahora los dispositivos coronográficos anteriormente presentados en el enfoque de FRIDA, un instrumento de segunda generación para el Gran Telescopio Canarias (GTC).
FRIDA (in**F**ra**R**ed **I**mager and **D**issector for the **A**daptive optics system of the GTC) está siendo diseñado como un instrumento con calidad de imagen limitada por difracción con capacidades de imagen de banda ancha y angosta y espectroscopía integral de campo (IFS, por sus siglas en inglés) para operar en el intervalo de longitudes de onda 0.9–2.5 μm (López et al., 2006a,b, 2007a,b; Cuevas et al., 2006, 2008). Los modos de observación imagen y IFS usarán el mismo detector Hawaii II Teledyne de tamaño 2048×2048 en pixeles. FRIDA será instalado en la plataforma Nasmyth A detrás de GTCAO, el sistema de Óptica Adaptativa del GTC. Debido a la emisión de la óptica a longitudes de onda mayores a 2 μm, FRIDA es un instrumento criogénico.

II.1.2 Capacidad coronográfica para FRIDA

FRIDA está planeado para tratar un amplio intervalo de problemas astrofísicos. Además, las especificaciones de diseño de FRIDA mencionan que este instrumento debe ser capaz de formar imágenes de alto contraste y por lo tanto, se deben planear opciones coronográficas. Para alcanzar esta meta, la comunidad científica de GTC pidió expresamente la presencia en el montaje óptico de FRIDA de sitios reservados para permitir la inserción de máscaras de plano focal, diafragmas o apodizaciones de pupila.

II.1.3 Posibles configuraciones coronográficas para FRIDA

El diseño opto-mecánico de FRIDA fue pensado para permitir algunas mejoras futuras. Aquí, nos interesamos en los caminos coronográficos factibles para FRIDA. De hecho, se quiere introducir en FRIDA la posibilidad de formar imágenes de alto contraste a muy altas resoluciones angulares. En la Sección II.2, se presenta FRIDA y se da una descripción detallada de este instrumento. Luego, se llevará a cabo un análisis del esquema óptico de FRIDA en la Sección II.3 con el objetivo de sugerir diferentes dispositivos coronográficos que se podrán insertar en este instrumento del GTC.

II.2 FRIDA: the future science instrument for the GTC

FRIDA has been largely presented and developed in several papers (e.g. López et al., 2006a,b, 2007a,b; Cuevas et al., 2006, 2008). In the following, we propose a brief summary of the main FRIDA characteristics. To get more information about this GTC instrument, we invite the reader to report to the corresponding literature.

II.2.1 Introduction

The Gran Telescopio Canarias (GTC) obtained its "first light" on July 2007 and is currently the single largest operating optical / infrared telescope in the world (see Figure II.1). Since the angular resolution of a telescope scales as λ/D, once the Adaptive Optics system is operating, GTC will have the finest resolution of any infrared telescope. Furthermore, when observing point sources in the background limit, the combination of light grasp and diffraction limit will give GTC a D^4 advantage over smaller telescopes. Consequently, FRIDA has been designed with diffraction limited optics to avoid degrading the high image quality that will be delivered by the Adaptive Optics system. FRIDA will be sensitive in the near infrared regime, for which the highest Strehl ratios are achieved. FRIDA is a collaborative project between the main GTC partners, namely Spain, Mexico and USA-Florida.

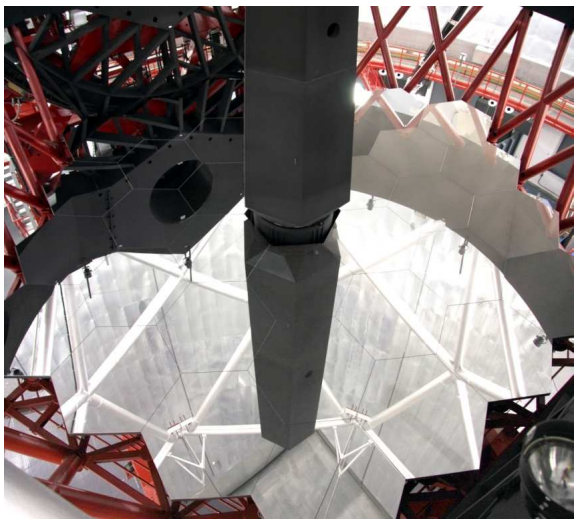

Figure II.1: GTC with its 36 mirrors. View inside the dome in La Palma island, Spain.

In the diffraction limited imaging mode, FRIDA will provide a comprehensive set of broad and narrow band filters. The same detector (Teledyne Hawaii II) will be used for Imaging and Integral Field Spectroscopy (IFS) modes. Mode switching will be easily performed and the larger field of view in imaging mode (see Table II.1) will facilitate field recognition for the IFS mode, where the field of view is small. The integral field spectrograph will provide a wide range of spectral resolutions, from low $R \sim 1000$ and medium $R \sim 4000$ to high $R \sim 30000$. Upgrade paths for high contrast imaging using Lyot or phase spots and pupil masks have also been considered in the design. In addition of Table II.1 parameters, there are other functional parameters. The most important is

the stability of the image and spectra on the detector with or without mode configuration changes. The image or the spectra shall be stable less than 1/10 detector pixel without configuration changes and 1 pixel with configuration changes.
FRIDA will be able to tackle a large number of astrophysical problems, thanks to the characteristics of its operating wavelength range. There is a large interest for FRIDA in the GTC community, indeed, the scientific cases range from solar system bodies to high redshifts galaxies, including resolved stellar populations, close binary systems, young stellar objects and star formation environments, circumstellar phenomena in advanced stages of stellar evolution and active galactic nuclei.

Table II.1: Summary of the main parameters for FRIDA

	Summary of the main parameters for FRIDA
Working location	Nasmyth A platform, after GTCAO system
Wavelength range	0.9 to 2.5 μm, performance optimized for 1.1 to 2.4 μm
Observing modes	Imaging and Integral Field Spectroscopy
Array format	2048×2048 HgCdTe Hawaii II, Teledyne
Imaging mode	
Scales	0.010 and 0.020 arcsec /pixel (5 % tolerance, goal 2 %)
Field of view	20.48×20.48 arcsec^2 and 40.96×40.96 arcsec^2
Image quality	Strehl ratio better than 90 % (goal 95 %) from 1.1 to 2.4 μm and better than 80 % from 0.9 to 2.5 μm
Field distortion	Less than 2 % (goal 1 %) over the whole field
Throughput	Better than 50 % (goal 70 %), excluding filters and detector
IFS mode	
Scales	0.010 arcsec /pixel $\times$0.020 arcsec /slice 0.020 arcsec /pixel $\times$0.040 arcsec /slice
Field of view	0.66×0.60 arcsec^2 and 1.32×1.20 arcsec^2
Spectral resolution	$R \sim 1000$ covering H & K bands $R \sim 4000$ over each of the Z, J, H & K bands and $R \sim 30000$ over selectable windows of $\sim \lambda/30$ from 1.4 to 2.4 μm
Image quality	Strehl degradation less than 20 % (goal 15 %) from 1.1 to 2.4 μm and less than 20 % from 0.9 to 2.5 μm

II.2.2 FRIDA basic layout

Basic conceptual designs of FRIDA are shown in Figures II.2(a) and II.2(b) for respectively the imaging and IFS modes. Light from the GTC adaptive optics (GTCAO) system (Devaney et al., 2004) enters from the left through a circular IR grade fused silica window. The optics forms a dual re-imaging system using a classical refractive collimator-camera configuration (pre-optics module) to select the spatial scale and a refractive double-pass spectrograph. The spatial scale is selected changing the pre-optics camera. In imaging mode, the beam avoids entering the integral field unit and spectrograph by a fold mirror and goes directly to the Hawaii II detector. For the IFS mode, the beam is directed into the Integral Field Unit (IFU) before continuing to the spectrograph. The

spectrograph is a double pass optical system in which the collimator and the camera are performed by the same lenses.
Three pre-optics cameras, dubbed coarse, medium and fine camera, are included to select the desired plate scale. Each camera provides the selected scale in both observing modes (imaging and IFS) and within the full wavelength range. The use of CaF_2 / S-FMT16 glass combination provides well corrected achromatic doublets for both, the pre-optics collimator and cameras and the spectrograph lenses. Filters and pupil masks are placed at the pre-optics pupil plane. Diffraction gratings are placed on a selectable carousel. All the FRIDA subsystems are mounted inside the cryostat to operate at a nominal temperature of 80 K.
GTCAO and FRIDA are mounted in a fixed position on the Nasmyth station. A field rotator is provided by GTCAO to compensate for the field rotation. Hence, the gravity vector is constant for both GTCAO and FRIDA, and the stability functional conditions can be reached. Furthermore, GTCAO provides an Atmospheric Dispersion Compensator (ADC).

II.2.3 FRIDA Imaging mode

Figure II.2(a) shows the conceptual design of FRIDA in imaging mode. FRIDA will perform broad-band and narrow-band imaging at two selectable spatial scales. These provide adequate Nyquist sampling over the entire wavelength range with scales of 0.010 arcsec /pixel (fine camera) and 0.020 arcsec /pixel (medium camera), with corresponding fields of view of respectively, 20.48×20.48 arcsec^2 and 40.96×40.96 arcsec^2. The finer scale will provide adequate sampling of the almost limited core in J and H bands and the coarser one will give adequate sampling in K band. Additionally over-sampling in K band can be performed with the fine camera. A 0.040 arcsec /pixel (coarse camera) is also provided but this will work only for small fields and for the IFS mode.
The medium camera is based on a two separated doublets and the fine camera is a tele-objective based on two separate doublets. The Pre-optics collimator is a separated doublet. The collimator and both cameras are designed using the CaF_2 /S-FTM16 glass matching.
The design strategy has been to simplify and optimize the design at K band, for which the GTCAO system has its optimal performance. Thus, the collimator - medium camera were designed with the minimum number of components to obtain the highest throughput. The fine camera, suited for better sampling at shorter wavelengths, was designed adapted to the coarse camera space. Figure II.3 shows the optical configuration in imaging mode for the medium camera. Moreover, spot diagrams for FRIDA in imaging mode are given in Figure II.4. The presented images present a Strehl ratio around 0.95 for the complete field for wavelengths $\lambda > 1.4\,\mu$m.

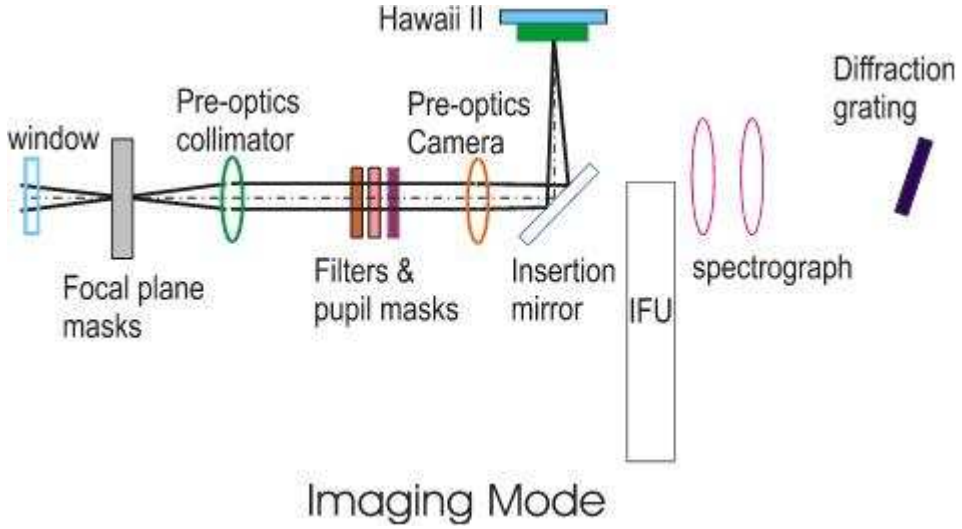

(a) Imaging mode

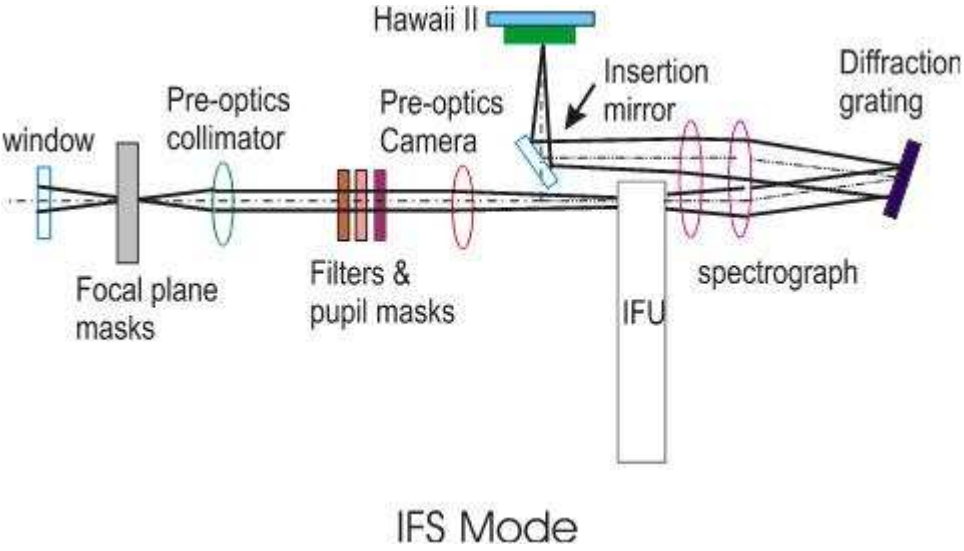

(b) IFS mode

Figure II.2: FRIDA conceptual designs

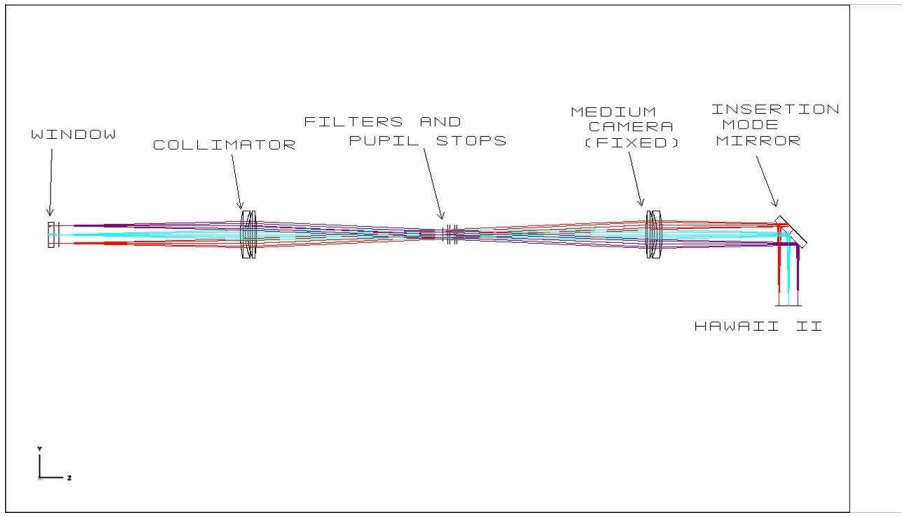

Figure II.3: FRIDA optical layout for the Imaging mode with the Medium Camera. Image courtesy of S. Cuevas and FRIDA team.

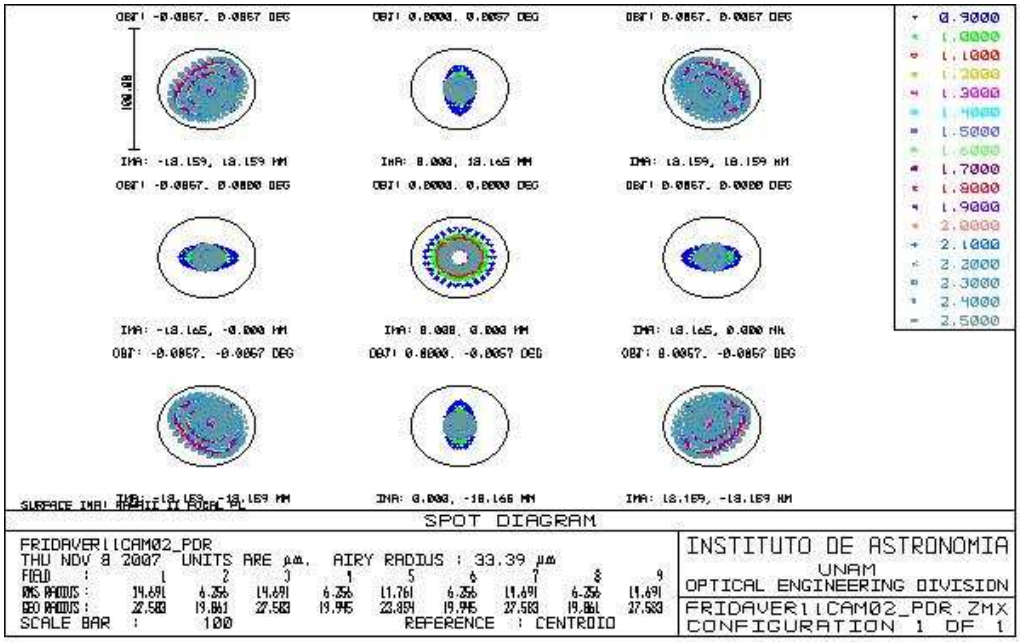

Figure II.4: Image quality along the field for the FRIDA whole wavelength band. Imaging mode for medium camera configuration. The circle has the size of the Airy disc for 1.7 μm. Image courtesy of S. Cuevas and FRIDA team.

II.2.4 FRIDA IFS mode

Figure II.2(b) shows the conceptual design of FRIDA in IFS mode. FRIDA will provide an integral field spectroscopy (IFS) mode using an image slicer IFU. The IFU slices the image in 30 slices and conforms a "pseudoslit" for the spectrograph. The IFU design is based on FISICA (Eikenberry et al., 2004), a monolithic mirrors array. FISICA design is based on the "bolt-and-go" philosophy that was successfully applied at the University of Florida to T-ReCS, CanariCam. Under this approach, the reflective mirror surface of an optic and its mechanical mount are cut from a single piece of metal. Advanced diamond-turning techniques are used to cut mechanical alignment references into the mirror mounts in the same cutting process used to finish the optical surface.
The selectable spatial scales parallel to the slices are: 0.010 arcsec /pixel (Fine), 0.020 arcsec/pixel (Medium) and 0.040 arcsec /pixel (Coarse). The corresponding scales perpendicular to the slices are 0.020 arcsec /slice, 0.040 arcsec /slice and 0.080 arcsec /pixel. Each slice will be projected onto two pixels in the spectral direction. Thus the spatial resolution in the spectral direction is 2 pixels and in the perpendicular direction is 1 pixel. The spatial resolution element is named "spaxel". So, the spaxel size is 0.010×0.020 arcsec^2, 0.020×0.040 arcsec^2 and 0.040×0.080 arcsec^2. The plate scale on the IFU slices is provided by the IFU relay optics. The FRIDA IFU format is 30 slices, 66 pixels long each. This format allows some 2 to 4 pixels of separation between the spectra projected on the Hawaii II detector. These scales translate into field of views 0.66×0.60 arcsec^2 and 1.32×1.20 arcsec^2 for the Fine and Medium Cameras.
The available spectral resolutions will be $R \sim 1400$ (low), 4000 (medium), 30000 (high). For all spectral resolutions the spectrograph operates with classical, plane diffraction gratings. The combination of high spectral and spatial resolution will be a unique capability of FRIDA.
FRIDA spectrograph is a double pass optics. The collimator and the camera are performed by the same lenses. The lenses are designed with a two separated doublets in an achromatic configuration. The glasses are CaF_2/S-FTM16 and CaF_2/Fused quartz. The effective focal length is 650 mm and the lenses diameter is 150 mm. The long focal distance is imposed by the high spectral resolution power requirement. Figure II.5 shows FRIDA in IFS mode.
The IFU has its own relay optics that introduces linear amplification and a slice optics that performs a linear de-amplification. The $\times$11.1144 relay optics amplification adapts the pre-optics scale plate to the slice width (400 μm). This is performed by a Schwarzschild relay, a concentric two spherical mirrors system working in off axis configuration. The slice optics performs the $\times 1/11.1144$ (de-)amplification in two stages. The first stage introduces a 1/4 deamplification imaging a pupil in each of the IFU Pupil Mirrors. The pupil mirrors image the slice images on the Field mirrors. A second stage de-amplifies by 1/2.77. This is performed by an afocal system composed by two off axis parabolic mirrors. Thus, the total IFU amplification is $\times 1$ making it compatible with the pre-optics and the spectrograph in image mode.
The Schwarzschild relay mirror based system has been adopted in this case to provide high amplification power, and can deliver anastigmatic, diffraction limited image quality. The slice optics has been designed to introduce reduced aberrations.
Figure II.6 shows a front view of the IFU with Non Sequential Components Zemax modeling. It is shown a ray tracing for the central slices, the extreme slices and the slices at intermediate locations of the IFU. The beam enters through the relay optics, located at the top left in Figure II.6. It then reaches the slicer stack located at the right in Figure II.6. The sliced beam is redirected to

thirty off axis spherical mirrors, where the telescope pupil is imaged. These are the Pupil mirrors. After the pupil mirrors, the beam is directed on another 30 mirror stack where the pseudo-slit is produced. This is the field mirrors stack. The off axis afocal system is indicated by TMA1 and TMA2. Finally, a flat mirror inserts the optical beam toward the spectrograph. Each of the mirrors stack are manufactured on a single block of aluminum. The three mirrors blocks, the Schwarzschild relay mirrors and the parabolic off axis mirrors, are bolted on an aluminum base.
An important item about the IFU is that it has a real pupil plane in each of the pupil mirrors and an input focal plane were it could be introduced a mask (Lyot or phase).
The IFU pre-optics PSF is sliced by, approximately, λ/D and $\lambda/2D$ for the coarse and fine camera respectively. This introduces diffraction effects on the IFU mirrors and on the diffraction gratings of the spectrograph. Both, the IFU mirrors diameter and the spectrograph gratings dimensions were calculated to prevent the loss of energy and avoid introducing additional diffraction effects on the resulting PSF on the Hawaii II detector.

II.2.5 FRIDA milestones

A design review for the FRIDA optics was held in Florida on May 2006. The FRIDA Preliminary Design Review (PDR) was held in Mexico City on August 2007. The Critical Design Review (CDR) will be effectuated in 2009. When the CDR is approved, the team will have the authorization to manufacture. FRIDA is scheduled to be delivered at the GTC La Palma site on December 2010. The GTCAO+FRIDA commissioning will start afterward.

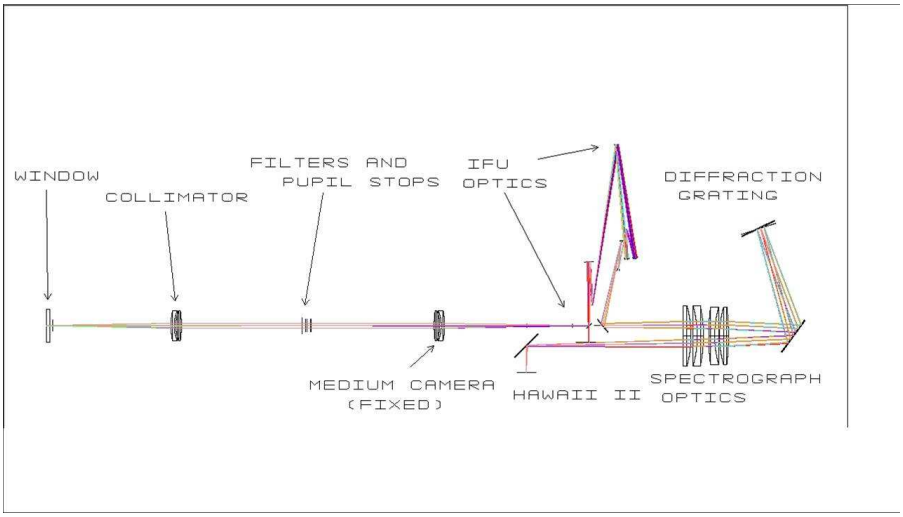

Figure II.5: FRIDA optical layout for the IFS mode with the Medium Camera. Image courtesy of S. Cuevas and FRIDA team.

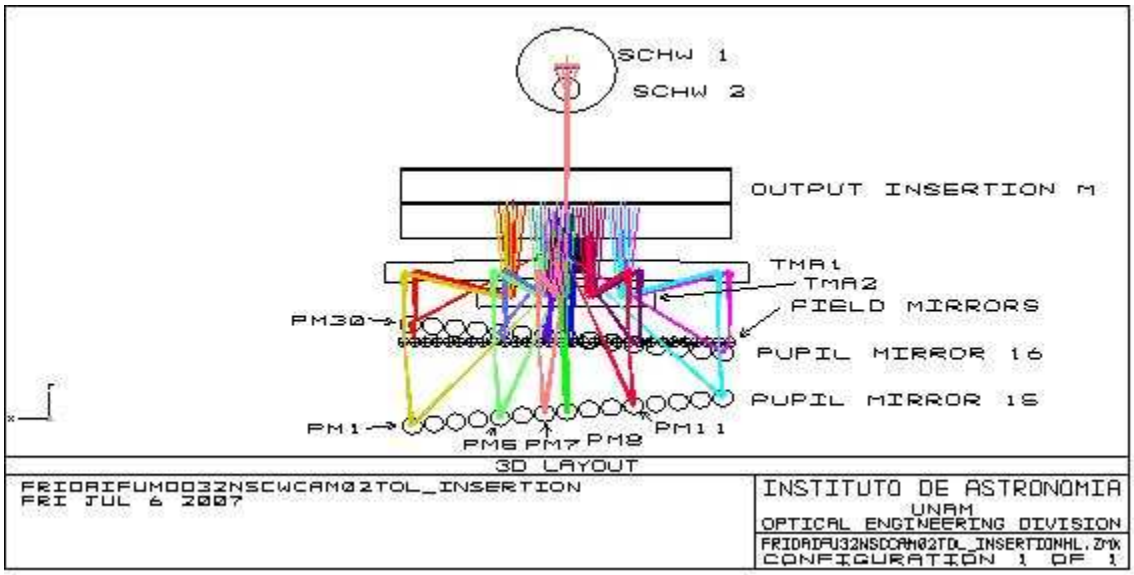

Figure II.6: Zoom to the FRIDA IFU in Figure II.5 in direction through the optical axis. It is shown some beam trajectories correspondent to the center of slices 1, 5, 7, 8, 11, 15, 16, 20, 23, 24, 26, 30 and their corresponding pupil mirrors and field mirrors. Image courtesy of S. Cuevas and FRIDA team.

II.3 Coronagraphic paths for FRIDA

II.3.1 Upgrade paths scheduled for FRIDA

FRIDA will be an imager and IFU spectrograph for the GTC. Let us remind that this is not an instrument mainly designed to perform high contrast imaging contrary to SPHERE (Beuzit et al., 2006) or Gemini Planet Imager (Macintosh et al., 2006). However, FRIDA capabilities coupled to additional coronagraphic paths could offer to GTC community the possibility of imaging and characterizing some substellar mass companions close to nearby bright stars.
Upgrade paths for high contrast imaging using Lyot or phase masks and pupil apodizers have been considered in the FRIDA design. Hence, different coronagraphs could be inserted within the FRIDA optical assembly. In a first time, our goal is to propose several coronagraphic configurations for FRIDA and thereafter, estimate the reachable starlight attenuation with each one of them. In the present, our approach will be carried out in the context of a diffraction-limited system.

II.3.2 FRIDA technical considerations for coronagraphy

Figure II.7 gives a schematic representation of the FRIDA optical layout for coronagraph insertion studies. This simplified version of the FRIDA conceptual design (see Figure II.2(b)) helps to establish where the focal plane masks, apodizations or diaphragms can be collocated. In addition, mechanical considerations allows to determine the feasible coronagraphic configurations for FRIDA. When this chapter was written, it was not clear that some pupil stops could be introduced in some of the pupil mirrors of the IFU. Consequently, excluding the IFU optics a quick analysis of the FRIDA optical schemes enables the identification of three focal and two pupil planes accessible for technical coronagraphic solutions.
Image of the GTC aperture is given in Figure II.8(a). Let us note that this is not a circular aperture. We assume the aperture to be situated in a pupil plane called PP0. It has to be noticed that this plane does not belong to FRIDA. Light from the telescope goes through the FRIDA pre-optics system which aims to select the spatial scale.
The 1^{st} focal plane (FP1) denotes the telescope focal plane. Figure II.9 shows the focal plane wheel located in FP1. In its configuration, two holders are planed for coronagraphic masks (Lucero et al., 2008). Hence, an opaque and a phase masks can be inserted in this wheel.
The 1^{st} pupil plane (PP1) is met between the collimator and the camera optics of the pre-optics system. A pupil wheel takes place in this plane and is shown in Figure II.10. It presents space for 3 cold pupil stops of up to 26 mm useful aperture and 3 holders for upgrade coronagraphic pupil masks (Lucero et al., 2008). So, there is no stress for inserting a pupil stop and 2 more pupil apodizers in the pupil wheel located in PP1. In the following, we assume that the eventual Lyot stop is a circular diaphragm which diameter is equal to the size of the inscribed circle of the GTC re-imaged pupil. Moreover, this pupil stop presents a 29 % central obscuration: indeed, the central stop size is chosen equal to the size of the circumscribed circle of the GTC re-imaged central obstruction. A representation of the pupil shape is shown in Figure II.8(b).
In Imaging mode, the beam is directly sent to the Hawaii II detector which is thus situated in the 2^{nd} focal plane (FP2). As it is shown in Figure II.5, the IFU input focal plane is accessible. The light from this focal plane is relayed by the IFU optics and the spectrograph optics to the Hawaii II detector, where is located the 3^{rd} focal plane (FP3). Furthermore the spectrograph pupil plane

is imaged on the diffraction grating. Here is located the 2^{nd} pupil plane (PP2).
Image slicer seems to constitute an obstacle for the insertion of a mask in FP2. In reality, the slicing device is slightly defocused out of this plane. Hence, introducing a mask there represents something reachable. The spectrograph location represents a mechanical stress for pupil mask insertion since it prevents the insertion of a conventional Lyot stop in the 2^{nd} pupil plane.

II.3.3 Presentation of the coronagraphic configurations for FRIDA

First of all, let us note that our study is limited to IFS mode for FRIDA: therefore, a spectra is supposed to be observed in the detector. However with the data cube obtained by FRIDA, it will be possible to recover the complete image at a given wavelength and without loss of information. We explain it in more details in Chapter V. Hence, our computations will be done assuming a monochromatic and on-axis point source.
Afterward, our study is focused on Lyot-style coronagraphs and classical pupil apodizations. Lyot or phase masks can be inserted in FP1 and FP2 while apodization or Lyot stop can be introduced in PP1. Let us remind that pupil apodizer has to be located in the upstream pupil plane with respect to the focal plane mask place. Classical Lyot Coronagraph (CLC), Classical Roddier Coronagraph (CRC) and Apodized Pupil Lyot Coronagraph (APLC) were the first diffraction suppression systems analyzed at the beginning of our study. Afterward, technical aspects forced us to reconsider the insertion of APLC within FRIDA.
Since the stresses for the introduction of a Lyot stop in PP2 is assumed too hard to overcome, we propose to replace the traditional APLC by either APLC working without Lyot stop or an original coronagraph design: the Stop-less Lyot Coronagraph (SLLC). These diffraction suppression systems consist of using a pupil apodizer in the entrance pupil plane and an opaque mask in the following focal plane. However, contrary to APLC case, no Lyot stop is used in the re-imaged pupil plane with these coronagraphic concepts. In the following, we estimate the star brightness attenuation that can be provided by the apodizers of APLC working without Lyot stop and SLLC. The SLLC apodizer is an optimized version of the previous coronagraph and its design will be presented in the next chapter. We do not simulate the presence of the opaque mask in FP2: since no Lyot stop is present in plane PP2, the spot will block starlight in FP2 and only residual light due to diffraction will be present in its re-imaged area in FP3, depending on the size of the geometric exit pupil in plane PP2.
Table II.2 summarizes the different coronagraphic configurations for FRIDA. For each solution, we specify the location of each coronagraphic element within the different planes of FRIDA. Moreover, schemes of each coronagraphic paths are given in Figure II.11 for CLC or CRC and in Figure II.12 for APLC without Lyot stop and SLLC. In the following section, we estimate the contrast gains reached by these coronagraphs. Let us remind that the present study is carried out in the approach of a diffraction-limited system.

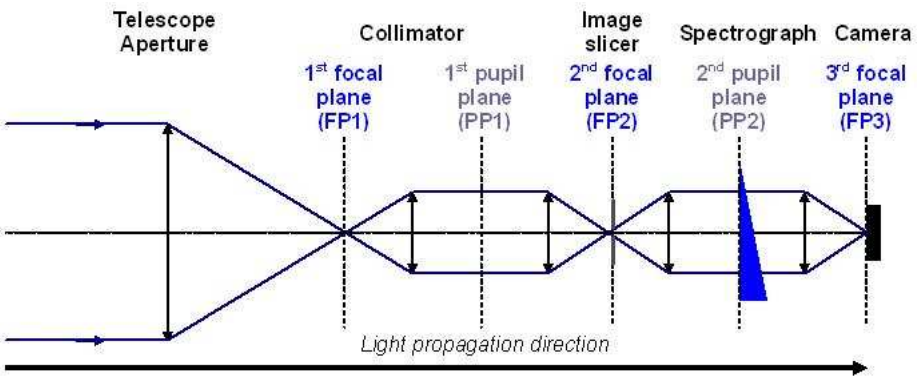

Figure II.7: Schematic representation of the FRIDA optical layout for coronagraphy studies.

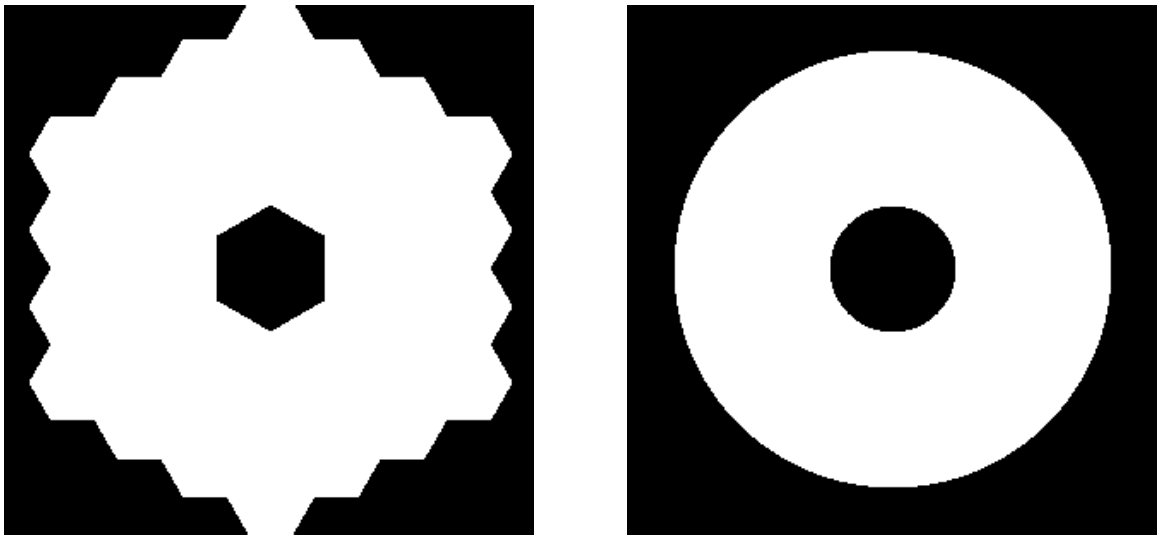

(a) Aperture of the Gran Telescopio Canarias.

(b) Geometric pupil in FRIDA plane PP1.

Figure II.8: Pupil shapes in FRIDA planes PP0 and PP1.

Table II.2: Suitable coronagraphic configurations for FRIDA.

Coronagraph	**FRIDA planes**				
	FP1	PP1	FP2	PP2	FP3
CLC	Lyot mask	Lyot stop	–	–	–
CRC	R&R phase mask	Lyot stop	–	–	–
APLC without Lyot stop	–	Apodizer	Lyot mask	–	–
SLLC	–	Apodizer	Lyot mask	–	–

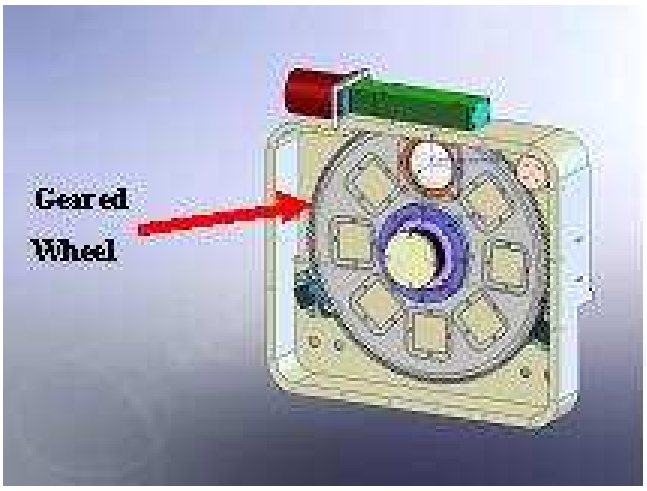

Figure II.9: Focal plane wheel. Picture courtesy of FRIDA team and extracted from Lucero et al. (2008).

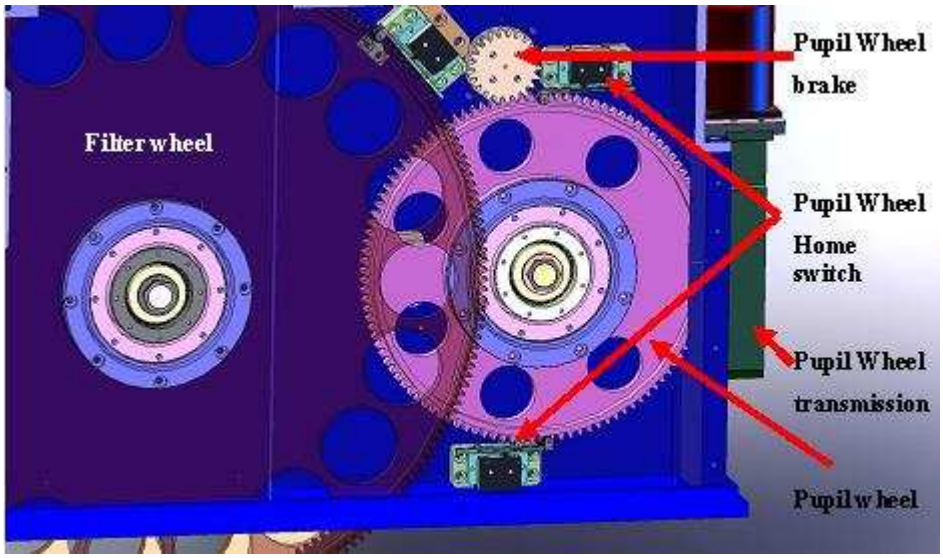

Figure II.10: Pupil wheel. Picture courtesy of FRIDA team and extracted from Lucero et al. (2008).

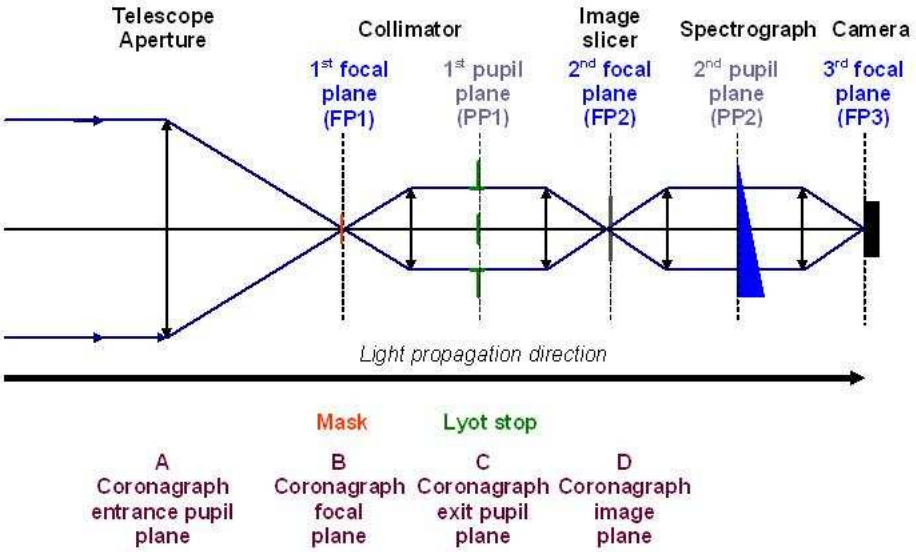

Figure II.11: Simplified representation of the FRIDA optical assembly in IFS mode. The coronagraph mask can be either an opaque mask or a Roddier & Roddier phase mask. In this scheme, the elements of the Classical Lyot or Roddier Coronagraph are inserted in the 1^{st} pupil and focal planes of FRIDA.

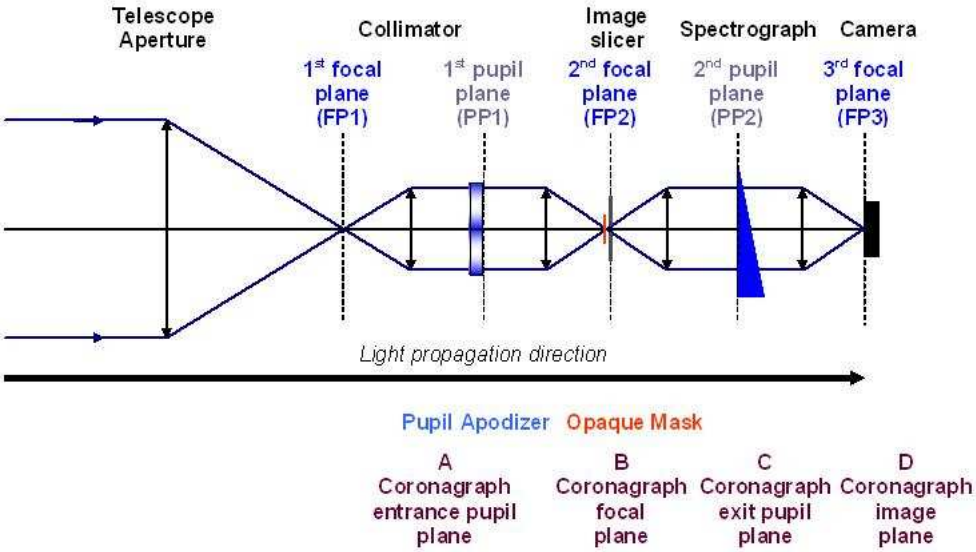

Figure II.12: Same as Figure II.11, but here, the Classical Lyot or Roddier Coronagraph is replaced by the Stop-less Lyot Coronagraph or APLC working without Lyot stop. Note that this time, the eventual coronagraph mask takes place in the 2^{nd} FRIDA focal plane while it is located the first one in the previous configurations.

II.4 Conclusion of the second chapter

In this chapter, FRIDA was presented and we analyzed its optical layout to determine which coronagraphs are feasible for FRIDA. Four suitable coronagraphic paths were proposed for FRIDA instrument: the Classical Lyot Coronagraph (CLC), the Classical Roddier Coronagraph (CRC), the Apodized Pupil Lyot coronagraph (APLC) without Lyot stop and the Stop-less Lyot Coronagraph (SLLC).
Numerical simulations are now required to quantify the star brightness attenuation achieved by each coronagraph configurations for FRIDA. In the following, we will describe the numerical tool implemented to compute the behavior of Lyot-style coronagraphs and pupil apodizers. Our coronagraph computations will find a direct application: the realization of a coronagraph feasibility study for FRIDA by estimating the contrast gains that can be reached with each coronagraphic solution. In the next chapter, our studies will be restrained to the diffraction-limited case. This preliminary approach allows to calibrate the performance of coronagraphs in the absence of aberrations. Thereafter in the following chapters, atmospheric wavefront phase errors will be taken into account.

II.4 Conclusión del segundo capítulo

En este capítulo, se presentó FRIDA y se analyzó su esquema óptico para determinar cuales son los coronógrafos factibles para FRIDA. Cuatro soluciones coronográficas realizables fueron propuestas para el instrumento FRIDA: el Coronógrafo de Lyot Clásico (CLC), el Coronógrafo de Roddier Clásico (CRC), el Coronógrafo de Lyot con pupila apodizada (APLC, por sus siglas en inglés) y sin diafragma de Lyot y el Coronógrafo de Lyot sin diafragma (SLLC, por sus siglas en inglés).
Se requiere ahora hacer simulaciones numéricas para cuantificar la atenuación de la luminosidad estelar alcanzable para cada una de las configuraciones coronográficas propuestas. En lo que sigue, se describirá la herramienta numérica implementada para evaluar el comportamiento de los coronógrafos de tipo Lyot y las apodizaciones pupilares. Nuestras simulaciones de coronógrafo tendrán una aplicación directa: la realización de un estudio de factibilidad de coronógrafos para FRIDA con una estimación de las ganancias de contraste que se puede alcanzar con cada solución coronográfica. En el próximo capítulo, nuestros estudios se retringirán al caso del límite de difracción. Este estudio preliminar tiene por objetivo la calibración del desempeño para cada coronógrafo en ausencia de aberraciones. Luego en los capítulos siguientes, se tomarán en cuenta los errores de frente de onda introducidos por la turbulencia atmosférica.

II.5 References

J.-L. Beuzit, M. Feldt, K. Dohlen, D. Mouillet, P. Puget, J. Antici, A. Baruffolo, P. Baudoz, A. Berton, A. Boccaletti, M. Carbillet, J. Charton, R. Claudi, M. Downing, P. Feautrier, E. Fedrigo, T. Fusco, R. Gratton, N. Hubin, M. Kasper, M. Langlois, C. Moutou, L. Mugnier, J. Pragt, P. Rabou, M. Saisse, H. M. Schmid, E. Stadler, M. Turrato, S. Udry, R. Waters, and F. Wildi. SPHERE: A 'Planet Finder' Instrument for the VLT. *The Messenger*, 125, 29–34, 2006.

S. Cuevas, J. A. López, S. Eikenberry, B. Sánchez, A. Watson, F. Garzón, A. Prieto, J. Fuentes, J. J. Díaz, C. Espejo, R. Flores, V. Bringas, and O. Chapa. FRIDA: The infrared imager and integral field spectrograph for the adaptive optics system of GTC. *New Astronomy Review*, 50, 389–391, 2006.

S. Cuevas, S. S. Eikenberry, B. Sánchez, O. Chapa, C. Espejo, R. Flores-Meza, G. Lara, L. C. Álvarez, and C. Keiman. Optical design of FRIDA, the integral-field spectrograph and imager for the AO system of the Gran Telescopio Canarias. In *Society of Photo-Optical Instrumentation Engineers (SPIE) Conference Series*, volume 7014 of *Society of Photo-Optical Instrumentation Engineers (SPIE) Conference Series*, 2008.

N. Devaney, D. Bello, B. Femenia, J. Castro, A. Villegas Lopez, M. Reyes, and J. J. Fuensalida. Preliminary design and plans for the GTC adaptive optics system. In D. Bonaccini Calia, B. L. Ellerbroek, and R. Ragazzoni, editors, *Advancements in Adaptive Optics. Edited by Domenico B. Calia, Brent L. Ellerbroek, and Roberto Ragazzoni. Proceedings of the SPIE, Volume 5490, pp. 913-923 (2004).*, volume 5490 of *Presented at the Society of Photo-Optical Instrumentation Engineers (SPIE) Conference*, pages 913–923, 2004.

S. S. Eikenberry, R. Elston, R. Guzman, J. Julian, S. N. Raines, N. Gruel, G. Boreman, P. E. Glenn, C. G. Hull-Allen, J. Hoffman, M. Rodgers, K. Thompson, S. Flint, L. Comstock, and B. Myrick. FISICA: the Florida image slicer for infrared cosmology and astrophysics. In A. F. M. Moorwood and M. Iye, editors, *Ground-based Instrumentation for Astronomy. Edited by Alan F. M. Moorwood and Iye Masanori. Proceedings of the SPIE, Volume 5492, pp. 1264-1273 (2004).*, volume 5492 of *Presented at the Society of Photo-Optical Instrumentation Engineers (SPIE) Conference*, pages 1264–1273, 2004.

J. A. López, V. Bringas, S. Cuevas, J. J. Díaz, S. Eikenberry, C. Espejo, R. Flores, F. J. Fuentes, J. Gallego, F. Garzón, P. L. Hammersley, R. Pelló, A. Prieto, B. Sánchez, and A. Watson. FRIDA: Diffraction limited imaging and integral field spectroscopy with GTC. In *Revista Mexicana de Astronomia y Astrofisica Conference Series*, volume 26 of *Revista Mexicana de Astronomia y Astrofisica*, pages 151–152, 2006a.

J. A. López, V. Bringas, S. Cuevas, J. J. Díaz, S. S. Eikenberry, C. Espejo, R. Estrada, R. Flores-Meza, F. J. Fuentes, F. Garzón, P. L. Hammersley, J. M. Montoya, A. Prieto, B. Sánchez, R. Toral, and A. Watson. FRIDA: integral-field spectrograph and imager for the adaptive optics system of the Gran Telescopio Canarias. In *Ground-based and Airborne Instrumentation for Astronomy. Edited by McLean, Ian S.; Iye, Masanori. Proceedings of the SPIE, Volume 6269, pp. 62693R (2006).*, volume 6269 of *Presented at the Society of Photo-Optical Instrumentation Engineers (SPIE) Conference*, 2006b.

J. A. López, V. Bringas, S. Cuevas, J. J. Díaz, S. Eikenberry, C. Espejo, R. Flores, F. J. Fuentes, J. Gallego, F. Garzón, P. Hammersley, R. Pelló, A. Prieto, B. Sánchez, and A. M. Watson. FRIDA: Near Infrared Imager and Integral Field Spectroscopy for GTC. In *Revista Mexicana de Astronomia y Astrofisica Conference Series*, volume 28 of *Revista Mexicana de Astronomia y Astrofisica*, pages 69–72, 2007a.

J. A. López, V. Bringas, S. Cuevas, J. J. Díaz, S. S. Eikenberry, C. Espejo, R. Flores, F. J. Fuentes, J. Gallego, F. Garzón, P. Hammersley, R. Pelló, A. Prieto, B. Sánchez, and A. Watson. FRIDA: The first instrument for the adaptive optics system of GTC. In *Revista Mexicana de Astronomia y Astrofisica Conference Series*, volume 29 of *Revista Mexicana de Astronomia y Astrofisica*, pages 18–20, 2007b.

D. Lucero, S. Pacheco, V. Bringas, C. Espejo, and S. Cuevas. FR/DD-MC/133: Mechanical design. Frida technical note, Instituto de Astronomía - Universidad Nacional Autónoma de México, 2008.

B. Macintosh, J. Graham, D. Palmer, R. Doyon, D. Gavel, J. Larkin, B. Oppenheimer, L. Saddlemyer, J. K. Wallace, B. Bauman, J. Evans, D. Erikson, K. Morzinski, D. Phillion, L. Poyneer, A. Sivaramakrishnan, R. Soummer, S. Thibault, and J.-P. Veran. The Gemini Planet Imager. In *Advances in Adaptive Optics II. Edited by Ellerbroek, Brent L.; Bonaccini Calia, Domenico. Proceedings of the SPIE, Volume 6272, pp. 62720L (2006).*, volume 6272 of *Presented at the Society of Photo-Optical Instrumentation Engineers (SPIE) Conference*, 2006.

Chapter III

Coronagraph performance study for FRIDA in a diffraction-limited approach

III.1 Introduction

III.1.1 From the formalism to numerical simulations for FRIDA

In Chapter I, we reviewed the formalism of Lyot-style coronagraphs. It allowed to remind that the expressions of the complex amplitudes of the electric field, in two successive planes of the coronagraphic setup, were Fourier transforms (FTs). Hence, the intensity profile of a coronagraphic image can be determined numerically by properly defining the following parameters: the entrance pupil shape, the possible apodization transmission function, the nature and dimensions of the focal plane mask and finally the Lyot stop aperture size.
In addition, FRIDA was presented in Chapter II and four suitable coronagraphic configurations were proposed to provide high contrast imaging capability to this instrument. Our purpose consists now in performing numerical simulations to evaluate the levels of starlight extinction that can be achieved by each one of them. Therefore, we have to compute the images and estimate the contrast gains reached by the feasible diffraction suppression systems for FRIDA. This requires the implementation of a tool which allows to calculate and optimize the star brightness attenuation of different Lyot-style coronagraphs and pupil apodizers.

III.1.2 Approach for a diffraction-limited system

As a first step, we consider a diffraction-limited system for the implementation of our tool. Therefore, no optical aberrations will be introduced in our simulations and then, our study will correspond to that of an ideal instrument working in space. This approach allows to quantify the performance of a coronagraph in the absence of wavefront distortions and thus, calibrate its starlight attenuation thresholds. Once the coronagraph simulator has been implemented, we will work in the context of a ground-based instrument. Our tool will be associated with another software to get closer to the real life where phase aberrations have to be considered: atmospheric turbulence, distortion of

the wavefronts and their correction by an Adaptive Optics system will be taken into account. This combination will be detailed and analyzed later in the next chapter.

III.1.3 Goals of the chapter

In the following sections, we will review the assumptions made for the implementation of our simulator: computational results will be given in the context of a diffraction-limited approach. In Section III.2, critical points about spatial sampling problems will be discussed. In section III.3, we will detail the methodology finally used for our numerical tool and check the consistency of its results by studying the behavior of a CRC with laboratory tests. The experimental results are compared with our simulations. This will allow to validate experimentally the numerical tool. In section III.4, we will expose the algorithms used for the calculation of the different apodization transmission profiles. In Section III.5, other important aspects of the numerical simulations for coronagraphy will be analyzed: chromatism, stellar angular size and selection of the mask size. Finally in Section III.6, we will report the contrast gain results reached by each suitable coronagraph for FRIDA.

III.1 Introducción

III.1.1 Del formalismo a las simulaciones numéricas para FRIDA

En el Capítulo I, se revisó el formalismo de los coronógrafos de tipo Lyot. Eso nos permitió recordar que las expresiones de las amplitudes complejas del campo eléctrico, en dos planos sucesivos del montaje coronográfico, están relacionadas con una simple transformada de Fourier (FT, por sus siglas en inglés). Por lo tanto, se puede determinar numéricamente el perfil de intensidad de una imagen coronográfica definiendo de manera apropiada los siguientes parámetros: la forma de la pupila de entrada, la función de transmisión de una eventual apodización, la naturaleza y las dimensiones de la máscara de plano focal y finalmente, el tamaño de apertura del diafragma de Lyot.
Además, se presentó FRIDA en el Capítulo II y se propusieron cuatro configuraciones coronográficas factibles para proveer a este instrumento la capacidad de formar imágenes de alto contraste. Nuestro objetivo consiste ahora en desarrollar simulaciones numéricas para evaluar los níveles de extincción de luz estelar que se puede alcanzar con cada uno de ellos. Por lo tanto, se tienen que simular las imágenes y estimar las ganancias de contraste alcanzadas por los sistemas de supresión de difracción factibles con FRIDA. Todo eso requiere la implementación de una herramienta que permita calcular y optimizar la atenuación de brillo estelar de los diferentes coronógrafos de tipo Lyot con las apodizaciones de pupila.

III.1.2 Estudio para un sistema limitado por la difracción

Como primera etapa, se considera un sistema al límite de difracción para la implementación de nuestra herramienta. Por lo tanto, no se introducirá ninguna aberración óptica en nuestras simulaciones así que nuestro estudio será equivalente a la de un instrumento perfecto ubicado en el espacio. Este enfoque permite cuantificar el desempeño de un coronógrafo en ausencia de distorción del frente de onda y asi, calibrar los umbrales de atenuación de luz estelar. Una vez implementado nuestro simulador de coronógrafo, trabajaremos en el contexto de un instrumento terrestre. Nuestra herramienta será asociada con otro software para acercarse más de la realidad en donde se deben considerar las aberraciones de fase: se tomarán en cuenta la turbulencia atmosférica, la distorción de los frentes de onda y su corrección por un sistema de Óptica Adaptativa. Esta combinación se detallará y se analyzará más adelante en el próximo capítulo.

III.1.3 Objetivos del capítulo

En las siguientes secciones, se revisarán las hipótesis hechas para la implementación de nuestro simulador: se proporcionarán resultados computacionales en el contexto de un sistema limitado por la difracción. En la Sección III.2, se discutirán algunos puntos críticos acerca de los problemas de muestreo. En la Sección III.3, se detallará la metodología adoptada para nuestra herramienta numérica y se verificará la consistencia de los resultados con el estudio del comportamiento del CRC en laboratorio. Se compararán los resultados experimentales con las simulaciones. Esto permitirá validar de manera experimental la herramienta. En la Sección III.4, se expondrán los algoritmos usados para determinar los perfiles de transmisión para las apodizaciones. En la Sección III.5, se analyzarán otros aspectos importantes de las simulaciones numéricas para coronografía:

cromatismo, tamaño angular de una estrella y selección del tamaño de la máscara. Finalmente en la Sección III.6, se reportarán los resultados de ganancía a nivel de contraste alcanzados por cada uno de los coronográfos factibles para FRIDA.

III.2 Sampling problem

Several important points have to be considered to simulate the coronagraphic behavior. They mainly deal with the spatial sampling problem that Abe (2004) mentioned in his paper. How to correctly sample a continuous and curved shape such as coronagraphic mask or entrance pupil? What are the unwanted effects and how to overcome them? And what is the consistency of the result?
Here, some comments are developed for the coronagraph setup computation. We expose our choices and the compromises we decide to make hereafter. Notions of signal sampling and Nyquist-Shannon sampling theorem are briefly reviewed in Annexe A.

III.2.1 Compromise between pupil and image planes

The Lyot-style coronagraphic setup (see Figure I.11) was presented and described in Chapter I. We reminded that the expressions of complex amplitudes between two successive planes of the coronagraphic device are simply relied on a Fourier Transform. Lyot-type coronagraphic computations involve finite size arrays and multiple Fourier transform operations, therefore the result can only be an approximation of the theory. To simulate these coronagraphs numerically, a first option consists in using the Fast Fourier Transform (FFT) between two successive planes. Naturally, numerical round-offs occur in the FFT for the Fourier Transform computation what leads to a result which is an approximation of the theory. Our purpose is to limit as much as possible the effects of the other parameters intervening in our numerical calculation and achieve results close to the theoretical predictions.
There is a two-fold sampling requirement for simulation of Lyot-style coronagraphs:
— a pupil size sampling large enough to allow the calculation of the aperture transmission function when an entrance pupil apodizer is considered in the coronagraphic device,
— a resolution element in the focal plane (λ/D) sampling large enough for an adequate sampling of the PSF and coronagraph mask in the focal plane.
Hence, a good sampling is required as well in the focal as in the pupil plane to avoid "step effects" (or aliasing) on the mask and pupil borders. A compromise has to be found between two successive planes, since a pupil size represented with a large number of points in a finite size array implies few points per resolution element in another equivalent array and conversely.
In our computation, we decide to work with 1024×1024 size arrays with double precision float or complex format. A rapid analogy can be realized with the previous equations describing the sampling theory: the sampling interval is given by $\tau = 1/1024$ and therefore, the sampling rate $\nu_s = 1024$. We also choose to work with 81 points across the pupil diameter, what leads to $\lambda/D = 12.64$ points in the following focal plane (λ/D is the frequency in the Fourier domain). Roddier & Roddier phase mask represents the smallest mask involved in our numerical simulations: its diameter is about $1.06\,\lambda/D$ for a clear circular aperture, what corresponds to 13.40 points. These pupil and mask size values allow to well simulate the coronagraph behavior, simultaneously in the different pupil and focal planes.
However, the aliasing effects are not completely removed in both planes. For instance, when we observe the Airy diffraction pattern achieved with a clear circular aperture (see Figure III.1(a)), Airy rings start to blur not very far away from the center, as shown in Figure III.2(a). An additional

solution is required if we want to obtain more accurate results at largest angular separations.

III.2.2 Super sampling of the pupils and masks

To mitigate the aliasing effect at a given plane, a common technique consists in applying the "super sampling" trick in the upstream plane. The method is described in Abe (2004) in the context of coronagraphy: instead of designing a spot with binary values, the edge of a mask is computed using gray-pixel approximation. Thus, values on the spot edge are given using different levels of gray scale. We give in Figure III.1 a representation of a circular entrance pupil before and after super sampling trick.
This image processing technique is equivalent to generate a signal with a band-limited spectrum. Indeed, considering a smoothed rectangular function is equivalent to a convolution of the rectangular function with a Gaussian or a sinc function. The result in the domain frequency will be a spectrum filtered respectively with a Gaussian or a rectangular function and the aliasing effects will be greatly removed.
In Figure III.2, we can observe the Airy diffraction patterns obtained with or without the application of the super sampling trick on the entrance pupil. It results in more distinguishable rings in the diffraction pattern achieved with a smoothed entrance pupil, at larger separations from the central intensity peak.

III.2.3 Representation of the telescope central obstruction and its spider arms

Obscuration can be computed in a binary way to represent the central obstruction of a telescope. For instance, Gran Telescopio Canarias (GTC) presents a 29% central obstruction: for an aperture size of 81 points, the numerical representation leads to a pupil obscuration diameter of 23.49 points. The super sampling trick can also be used to implement the telescope secondary mirror shadow within the entrance pupil and avoid some aliasing effects again.
Spider arms and segment gaps should be taken into account to achieve a more complete representation of a telescope aperture. However, for instance, the projected image of the spider arms in the entrance pupil is very narrow: in the case of GTC, a width of 3.6 cm is expected, what corresponds to 0.32 point! We decide to not introduce the spider arms in our coronagraphic simulator and renounce to temporarily study the diffraction effects induced by their presence within the input pupil. A similar conclusion is obtained for the gaps between each segments of the GTC.
In the following, we present an alternative to the approach we initially use for computing behaviors of Lyot-style coronagraphs.

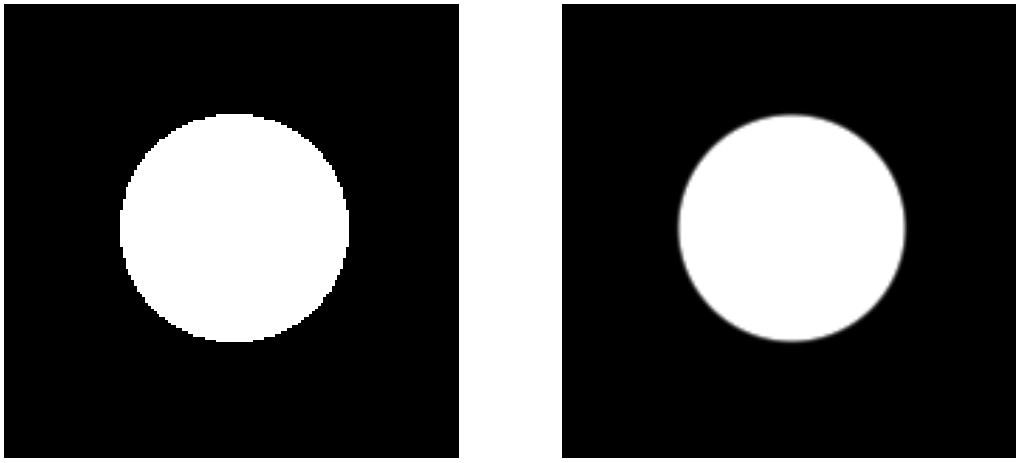

(a) A binary pupil (b) A smoothed pupil

Figure III.1: Zoom on the pupil before and after the super sampling trick. Pupils have a diameter of 81 points and we worked here with 1024×1024 size arrays. The gray scale symbolizes the pupil transmission. It is linear ranging from 1 (white) to 0 (black).

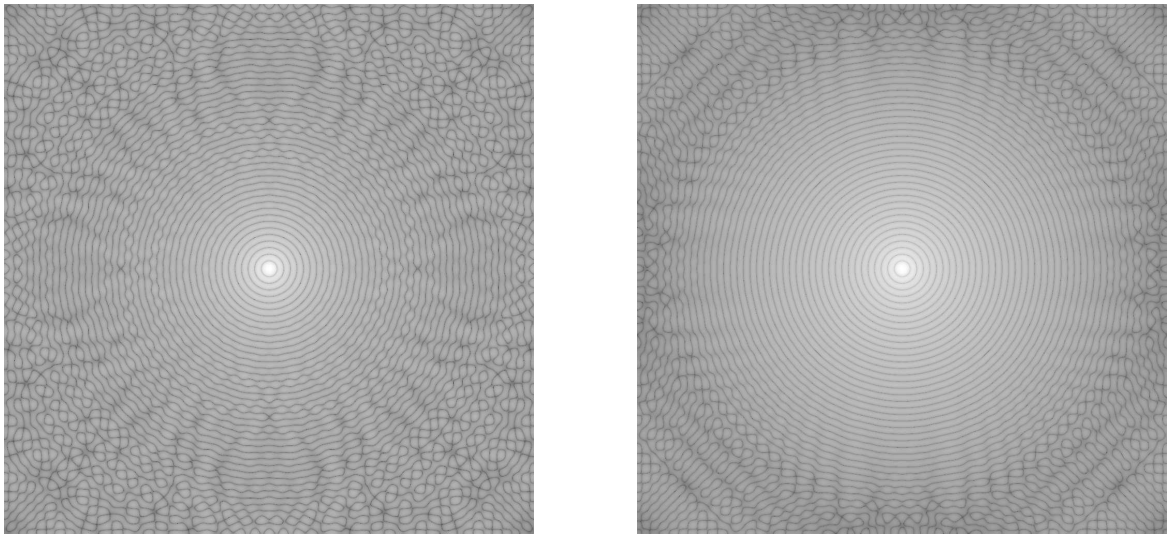

(a) A binary pupil (b) A smoothed pupil

Figure III.2: Image of the Airy diffraction pattern obtained before (left) and after (right) supersampling trick applied on the entrance pupil. Images are represented in log scale and enhanced for a better visualization of the rings. To obtain these pictures, we initially worked with a pupil diameter of 81 points and all original array dimensions are 1024×1024 points, what gives a linear range of $81\,\lambda/D$ for each image.

III.3 Semi-analytical approach: a powerful method to compute coronagraph numerically

III.3.1 Description

Several issues have been evoked in the previous section to point out the main obstacles for a correct numerical computation of coronagraphs. The key point of coronagraph simulations results in the compromise to realize in order to reach a satisfying resolution both in the focal and pupil planes. Until now, our simulations involved several FFTs to represent the coronagraphic behavior. It implied very large arrays and therefore, staggering demands on memory and computing power.
Soummer et al. (2007) propose a semi-analytical method to compute coronagraphic behavior, allowing a very sensitive gain of time and memory. It consists in considering another approach for the expression of the field in the Lyot plane, given in Eq. (I.3). This equation can be simply re-written as:

$$\Psi_C(\boldsymbol{r}) = (\Psi_A(\boldsymbol{r}) - \epsilon\,\mathcal{F}\left[\mathcal{F}\left[\Psi_A(\boldsymbol{r})\right] M(\boldsymbol{r})\right]) L(\boldsymbol{r})\,, \tag{III.1}$$

where $\mathcal{F}$ denotes the Fourier Transform (FT) operator. This expression underlines the fact that the first FT of the pupil field amplitude $\mathcal{F}\left[\Psi_A(\boldsymbol{r})\right]$ is truncated by the mask $M(\boldsymbol{r})$ and the second FT is truncated by the Lyot stop $L(\boldsymbol{r})$. Hence, we are only interested in the knowledge of the FT inside the limited mask and Lyot stop area. This remark allows to avoid calculating FTs of large arrays with small pupil or mask area.
Therefore, we can work with large pupil and mask sizes contained in arrays of same dimensions. As mentioned by Soummer et al. (2007), the semi-analytical approach consists of computing these limited-area FTs numerically and subtracting the result from the pupil complex amplitude, according Eq. (III.1). The different FTs of the analytical expression are computed using a Matrix Fourier Transform (MFT), which expression is given in Soummer et al. (2007) and recalled in Annexe B, and does not involve any additional approximation. MFT is in practice slower than FFT but this apparently drawback is largely compensated by the fact that with MFT, we only need to calculate FTs inside the pupil or mask area.
It can already be noticed in Figure III.3 that a better image sampling of Airy diffraction pattern seems to be achieved, compared with that of the images displayed in Figure III.2. In the following, we will confirm this result by plotting the corresponding intensity profiles.

III.3.2 Consistency of the results

In Figure III.4, we give the profiles achieved with a Classical Roddier Coronagraph (mask radius $r = 0.525\,\lambda/D$) and Classical Lyot Coronagraph for two different spot sizes (mask radii $r_1 = 0.850\,\lambda/D$ and $r_2 = 1.850\,\lambda/D$).
In Figure III.4 top plot, the intensity profiles are computed with the traditional FFT method and using the super sampling trick for each focal plane mask. We work with 1024×1024 size arrays and the pupil diameter is chosen equal to 81 points. In Figure III.4 bottom plot, the curves are computed with the semi-analytical approach. In this context, we use 256×256 size arrays for the input and exit pupil planes and aperture of 256 points in diameter. For the mask size, we work with 128×128 size arrays and 128 points in diameter for the spot size. Finally, a 512×512 size array is considered for the representation of the diffraction patterns in the image plane D and we

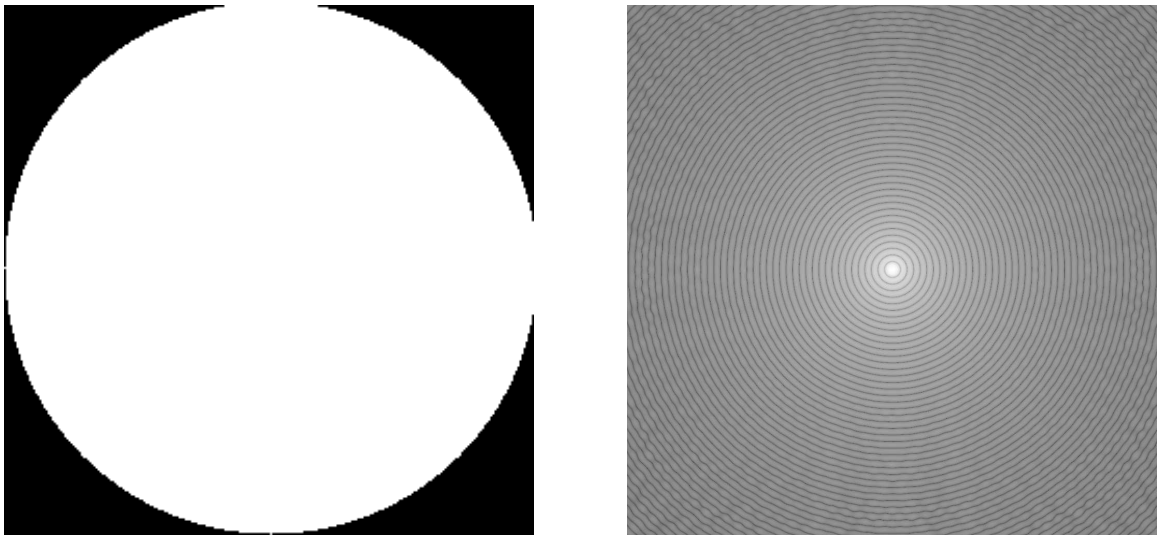

Figure III.3: Left: Image of a clear circular pupil. The original array dimensions are 256×256 points. **Right**: Image of the Airy diffraction pattern obtained with a MFT of the clear circular pupil function. This image is represented in log scale and enhanced for a better visualization of the rings. The original array dimensions are 1024×1024 points and we choose here a linear range of $81\,\lambda/D$ to allow the visual comparison with the images of Figure III.2.

arbitrary choose a linear range of $14\,\lambda/D$. Let us note that all array dimensions are expressed in power of 2 but this is not a requirement for the efficiency of MFT algorithm.
It can be noticed that both results are in good agreement with the solutions provided in Figure 3 of Aime and Soummer (2003), see Figure III.5. To realize these simulations, we choose the same parameters than those referred by the authors in their paper (Aime and Soummer, 2003). This example allows to underline the consistency of the results provided by our simulator with the semi-analytical method using MFT. On the one hand, we note that successive FFTs and semi-analytical approach using MFT give the same profiles. On the other hand, these results are congruent with those found in the literature (Aime and Soummer, 2003).
From now one, we will use the method recently proposed by Soummer et al. (2007) to simulate more quickly and accurately the behavior of Lyot-style coronagraphs and therefore study the behavior of suitable coronagraphs for FRIDA.

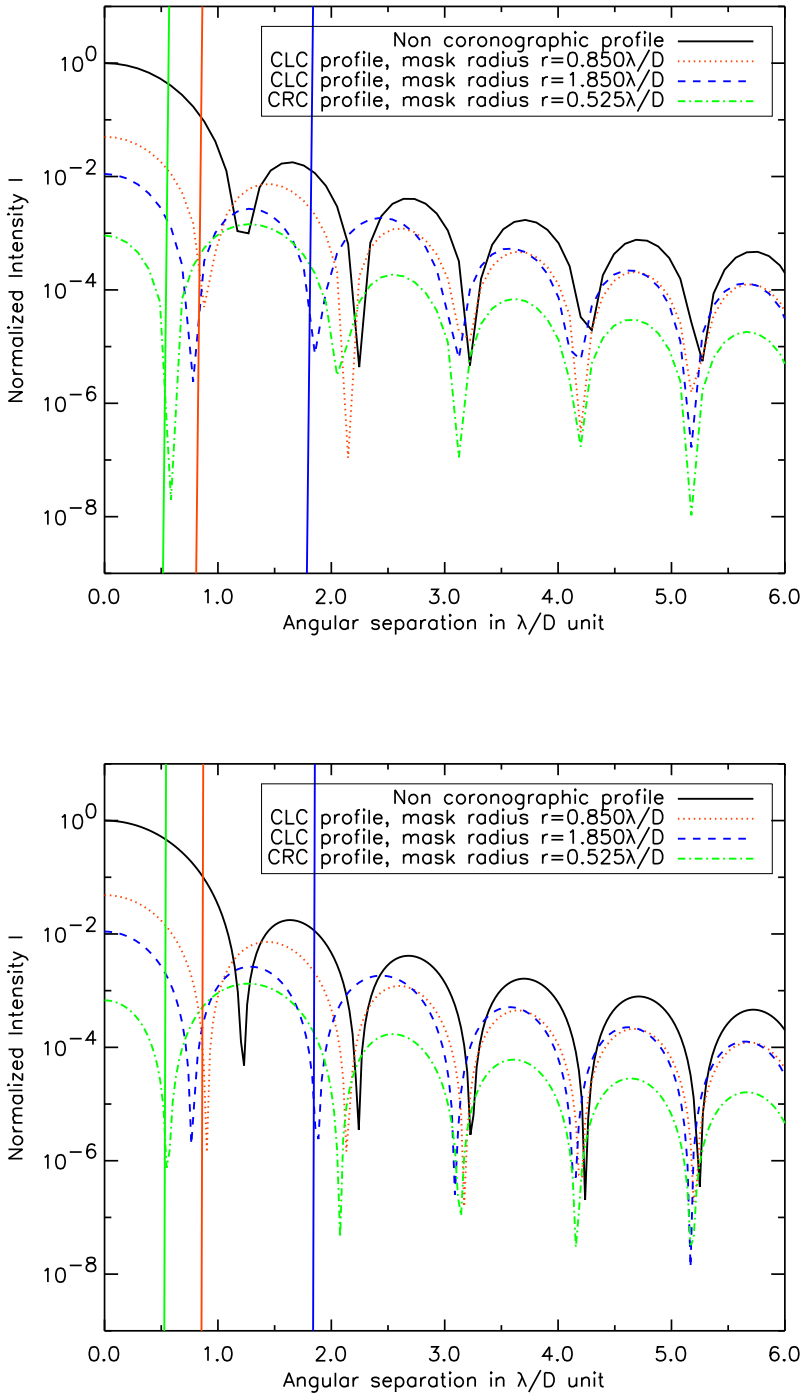

Figure III.4: Radial profiles of the non coronagraphic PSF (Airy pattern) and coronagraphic images obtained with different coronagraphic devices, for a clear circular aperture. A monochromatic point source is considered here. These results are obtained in the context of a diffraction-limited system. In top plot, results are achieved with successive FFTs whereas in bottom plot, they are obtained with the semi-analytical approach using MFT.

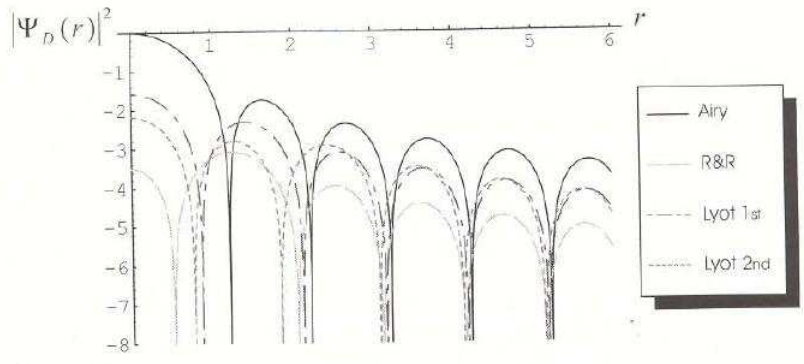

Fig. 3. Residual intensity for an on-axis monochromatic point source (in log scale) and a circular aperture (radial cuts). From top to bottom: without coronagraph (Airy pattern), Lyot for $a = 1.7\lambda/D$ (first minium of Fig. 4), Lyot for $a = 3.7\lambda/D$ (second minimum of Fig. 4), R&R for $a = 1.05\lambda/D$. The coronagraphic effect is in the whole field. The mask sizes correspond to Figure 2.

Figure III.5: Radial profiles of the non coronagraphic PSF (Airy pattern) and coronagraphic images obtained with different coronagraphic devices, for a clear circular aperture. This plot is extracted from Aime and Soummer (2003).

III.3.3 Experimental validation

The simulator, based on the semi-analytical method using MFT, allows to accurately compute the behavior of coronagraphs predicted by the theory. Our simulations are in good agreement with the formalism of Lyot-style coronagraphs. However, they require a validation in laboratory to consider realistic and feasible the numerical results achieved with our tool. The experimental proof is essential in the context of coronagraph feasibility studies for FRIDA. In the following, we propose to give a laboratory test validation relying us on the case of the Classical Roddier Coronagraph (CRC).

III.3.3.1 Coronagraphy and laboratory tests: context

Let us remind that CRC is a concept proposed by Claude and François Roddier (Roddier and Roddier, 1997). Some first laboratory tests were carried out by Guyon et al. (1999) to demonstrate experimentally the theoretical predictions made by Roddier and Roddier (1997). While the results of the experiment clearly validate the principles of this new coronagraphic concept, it achieved only a modest peak intensity attenuation of 16. Theoretically, adjusting carefully the size of the mask to the size of the diffraction pattern (or vice-versa, by the aid of a variable iris entrance pupil), a peak intensity attenuation of infinity could have been achieved. The modest attenuation achieved with this spot was explained by the rounded edges of this first-generation mask, see Figure III.6.
At the beginning of this research project, Kjetil Dohlen and the Laboratory of Astrophysics of Marseilles (LAM) ordered the fabrication of a new, second-generation, Roddier & Roddier phase mask (RRPM) to Fanny Chemla and the Pole of Instrumentation of the Observatory of Paris. An alternative method to photo-lithographic deposition was investigated in order to achieve a better mask thickness profile: the phase dot is machined into the substrate by the aid of photo-lithographic ion beam etching. In Figure III.7, we can see the thickness profiles of the new mask fabricated by the Pole of Instrumentation of the Observatory of Paris: at first sight, it seems much closer to the required profile than that of 1999. While a slight rounding of the edges can be seen, a very good uniformity of the mask depth can be appreciated.
To evaluate the coronagraphic gain reachable with this second-generation RRPM, I did a three week practice to work in laboratory with Kjetil Dohlen, in Marseilles on October-November 2007. The goal of this work was to probe the efficiency of the fabricated mask, compare it with the previous results achieved with the first-generation RRPM and validate experimentally our numerical results.

III.3.3.2 Experimental setup and protocol

The optical design of the coronagraphic assembly is given in Figure III.8. A picture of the optical bench can also be seen in Figure III.9(a). The source is spatially filtered through a $5\,\mu$m pinhole and collimated by the lens L1. A variable iris (P1) allows to define the entrance pupil (A) of the system. To avoid having excessive bench dimensions while providing an appropriate beam of $F/80$, a pupil size of 1–2 mm is used.
The lens L3 provides an intermediate image (B) in which the RRPM is placed (see picture of the mask in Figure III.9(b)) and then projects a pupil image in the exit pupil plane (C) in which the Lyot stop is located. While this setup appears ideal in the sense of minimizing optics, hence aberrations, it does not provide a telecentric beam to the coronagraph, but this does not appear to be

of importance for this concept.
The following lens L4 images the coronagraphic image (D) onto the camera (a CMOS PixelLink device). It also projects the pupil onto a plane (E) some 100 mm behind the image plane, allowing rapid switching between image and pupil plane observations by sliding the camera between these positions.
Focal mask and Lyot stop are mounted on xyz micro-positioning stages, allowing both lateral and focus adjustment of these components. Once optimal positioning has been determined, the only adjustments necessary to perform the measurement protocol described below are a lateral (x) movement of the mask to remove or replace it onto the stellar image (a displacement of a few 100 μm is sufficient), and diameter of the entrance pupil and the Lyot stop. A picture of the optical bench can be seen in Figure III.9(a).
Images were recorded using an 8-bit camera. To obtain acceptable dynamic range, 3 images were taken at different exposure times from 0.04 ms to 1 s, and composite images were created by extracting annular zones from each image. For each exposure time, a corresponding dark image was taken and subtracted from the scientific images. The resulting image quality proved sufficient for this experiment.
The coronagraphic mask has a fixed size. We want to observe the coronagraph behavior in the re-imaged pupil and focal planes as a function of the RRPM radius. Therefore, to simulate various mask sizes, we operate on the entrance pupil diameter thanks to the variable iris and acquire images for each aperture size. The camera is placed respectively in planes D and E to acquire images in the focal and pupil planes.
For each experimental image acquisition, obtained at a given integration time, a corresponding dark image is taken. Thus, the dark current noise source of the detector and some additional parasite light can be removed from the experimental image by subtracting it with the dark image.

III.3.3.3 Experimental results in the image plane

Azimuthally averaged profiles of the coronagraphic and non coronagraphic images have been calculated, see Figs. III.10(a), III.10(b) and III.10(c). The non coronagraphic profile is compared with the theoretical Airy pattern, indicating a very good correspondence. This comparison turned out to be useful in optimizing the image analysis approach, allowing to understand some unexpected features of the camera such as exposure-time saturation for the shortest exposure times, leading us to implement a non-linear exposure-time correction.
Theoretical coronagraph images were calculated using the semi-analytic method based on matrix Fourier transforms (Soummer et al., 2007). The measured coronagraphic profile corresponds well with the theoretical prediction down to a contrast of around 10^{-6}, both for the $0.455\,\lambda/D$ mask (Fig. III.10(a)) and the $0.516\,\lambda/D$ case (Fig. III.10(b)). For the $0.741\,\lambda/D$ case (Fig. III.10(c)), however, the correspondence with theory is less good. Still, the contrast performance in the field is clearly better than in the other cases.
In order to investigate the effect of varying mask size, we have calculated the intensity at different distances from the star, plotted as a function of mask radius, both for theoretical and measured profiles. Figure III.11 displays these results. We considered six distances from the main optical axis, corresponding to the central peak and the first five bright rings of the Airy diffraction pattern (see Table III.1). At each of these positions, we averaged the intensity of the coronagraphic image over

an annulus of width λ/D. Theoretical results are plotted as lines, and experimental data are plotted as points. All results are normalized with respect to the central intensity of the non coronagraphic image, averaged in the same way.
The theoretical curves clearly show that the mask giving the optimal peak attenuation, seen here to reach beyond 10^4, does not correspond to the optimal performance in terms of contrast in the field. At the 5^{th} Airy ring, an improvement by a factor of about 10 can be expected by increasing the mask radius to around $0.65\,\lambda/D$. The experimental measurements confirm this result in spite of some loss of performance in the case of larger mask sizes. Indeed, the measurements fit very well with theory for mask radii smaller than $0.55\,\lambda/D$, with an average difference between experimental and theoretical intensity less than 0.21 magnitudes, see Table III.2. For larger masks, differences up to 1.7 magnitudes are observed.

III.3.3.4 Discussion

The main goal of our experiment, demonstrating that improved technology was capable of providing a significant improvement of coronagraphic performance compared with the original RRPM demonstrator of 1999, has clearly been reached. In particular, while the original experiment was limited to a peak attenuation of 16, we have measured attenuation as high as 216. It is believed that the main improvement is in the mask profile, where our device has been seen to have a very sharp edge.
We believe the main reasons for this deterioration are linked to features of our experimental setup, combined with the high peak intensity and increased aperture size corresponding to the larger mask diameters. In particular, a family of ghosts are observed along the vertical axis, probably due to internal reflections between the detector surface and the double detector window. Deficiencies in terms of optical quality of the bench also become more important in the case of the larger mask size, where the entrance pupil was enlarged so as to reduce the focal ratio. This stresses the optical setup both in terms of source uniformity, optical aberrations, and surface quality. Other error sources include mechanical stability and adjustment accuracy. All adjustments are manual, with direct TV images as the only aid to alignment. Slight mis-adjustments cause spillage of light back into the pupil, hence reduced coronagraphic efficiency.
Despite the limitations of our laboratory tests, we clearly show and underline the good agreement between the experimental results, the simulations made with semi-analytical method and the theoretical predictions. This is a very important point: it means that our further coronagraph feasibility studies for FRIDA will be consolidated with this experimental proof. The main results of this work are reported in our referred paper, see Annexe C.

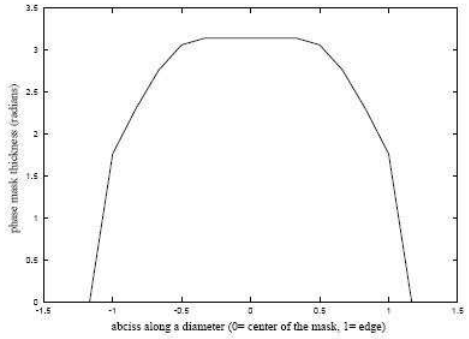

FIG. 8.—Simulated thickness profile of our experimental phase mask. This profile has been chosen to fit the results of our experiment, as shown in Fig. 9. It is also in good agreement with the observation of the thickness profile of the mask we have carried out by inserting the mask in one arm of a Michelson interferometer, which showed that the mask had "bent" edges. The phase is in radians (thus peaking at π), and the distance from the center of the mask is in mask radius units.

Figure III.6: Simulated thickness profile of the first Roddier & Roddier phase mask. This figure is extracted from Guyon et al. (1999). ©The Astronomical Society of the Pacific 1999.

Table III.1: Angular separations of the intensity peak and first five bright rings of the Airy diffraction pattern.

	Intensity peak	1^{st} bright ring	2^{nd} bright ring	3^{rd} bright ring	4^{th} bright ring	5^{th} bright ring
Angular separation in λ/D	0.00	1.64	2.68	3.70	4.71	5.71

Table III.2: Averaged difference between the experimental and theoretical intensity values for different mask radii. We exclude the central peak values from the averages.

Mask radius in λ/D	0.294	0.304	0.338	0.359	0.455	0.516
$\overline{\Delta I}$ in stellar magnitudes	0.12	0.21	0.06	0.07	0.07	0.09
Mask radius in λ/D	0.645	0.656	0.741	0.851	0.930	
$\overline{\Delta I}$ in stellar magnitudes	1.67	1.72	1.54	1.54	1.66	

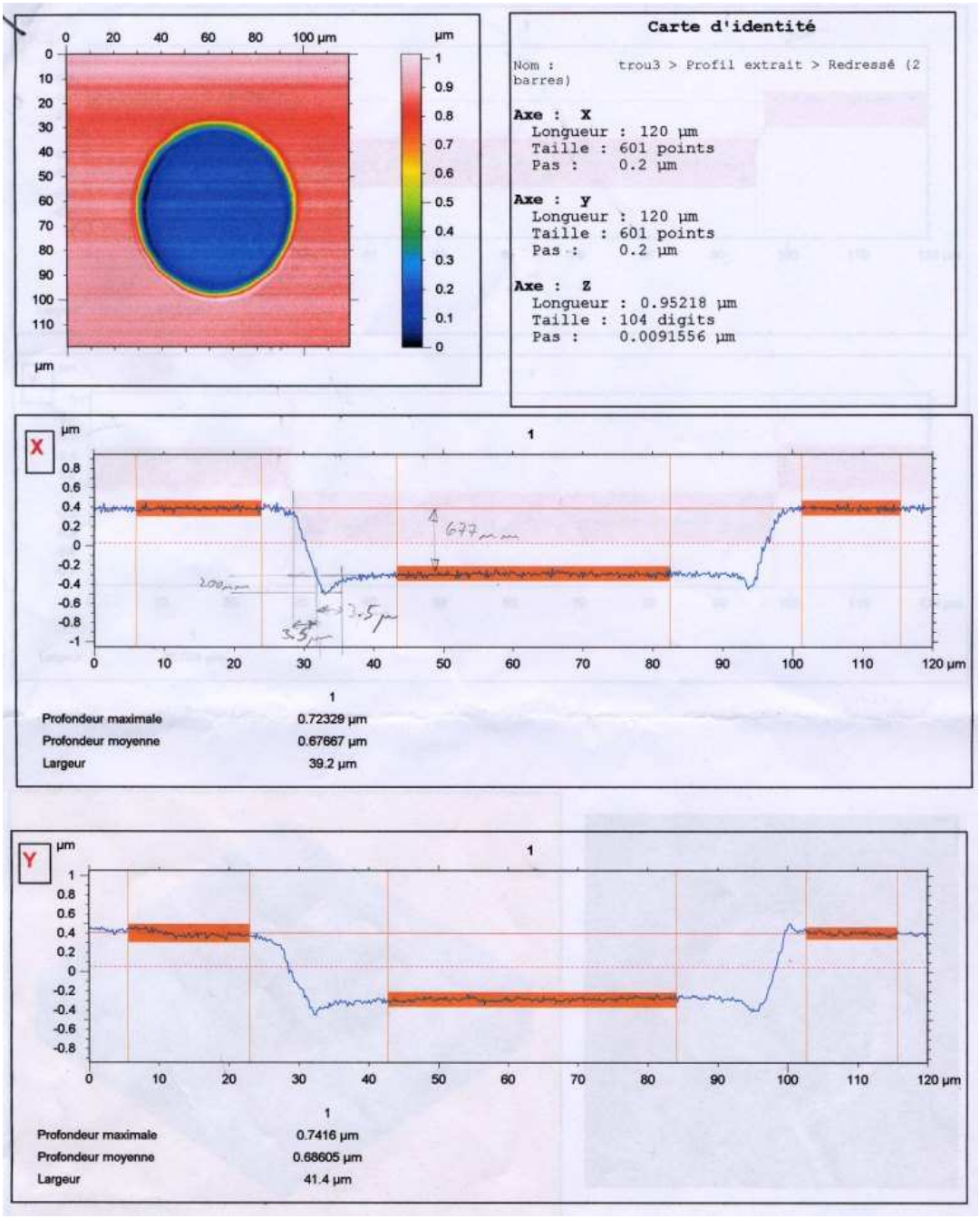

Figure III.7: Document giving the thickness profile of the mask fabricated in 2007. This mask was ordered by the Laboratory of Astrophysics of Marseilles and fabricated by the Pole of Instrumentation of the Observatory of Paris.

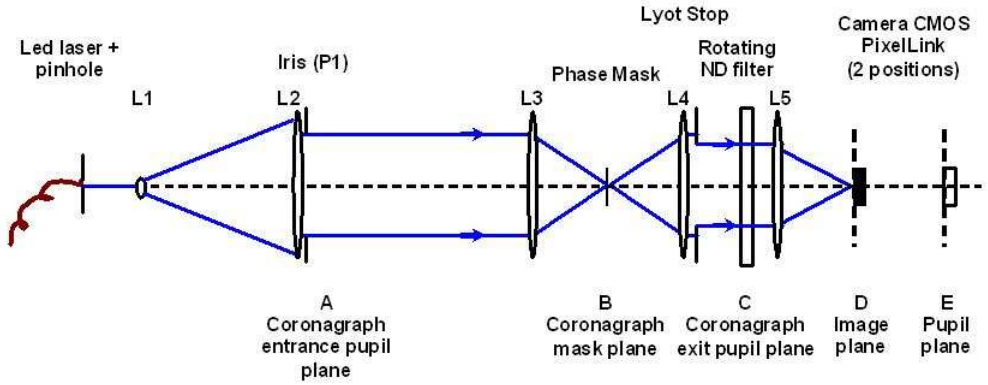

Figure III.8: Scheme of the optical assembly of the experiment.

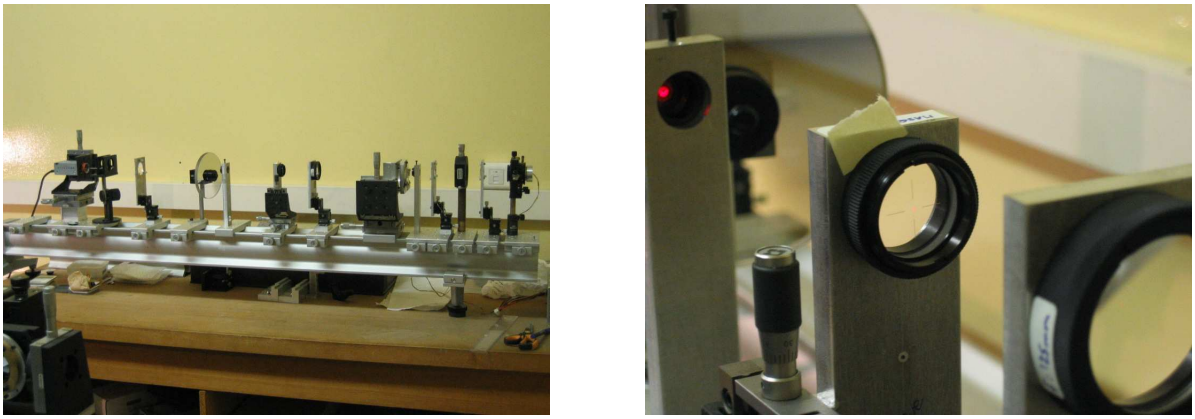

(a) Picture of coronagraphic bench

(b) Zoom on the Roddier & Roddier phase mask

Figure III.9: Pictures of the optical assembly taken by Kjetil Dohlen.

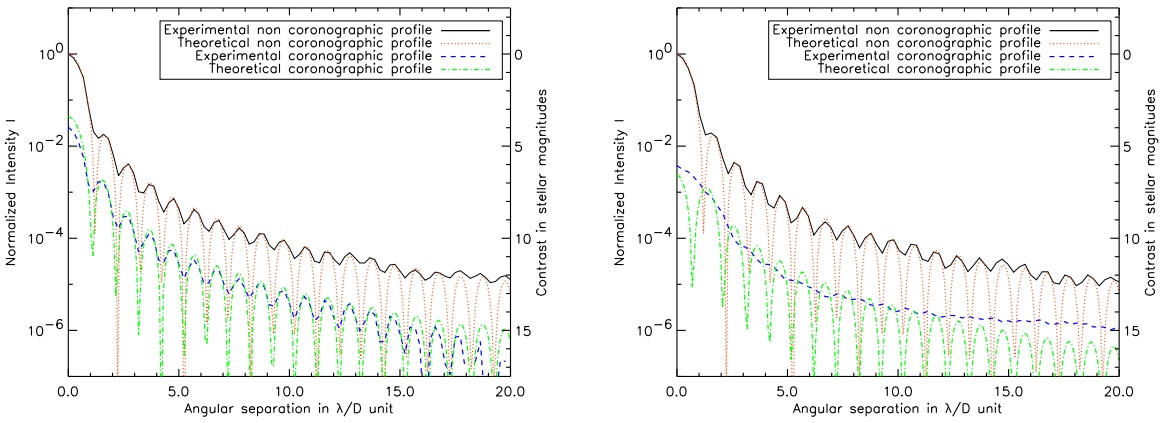

(a)

(b)

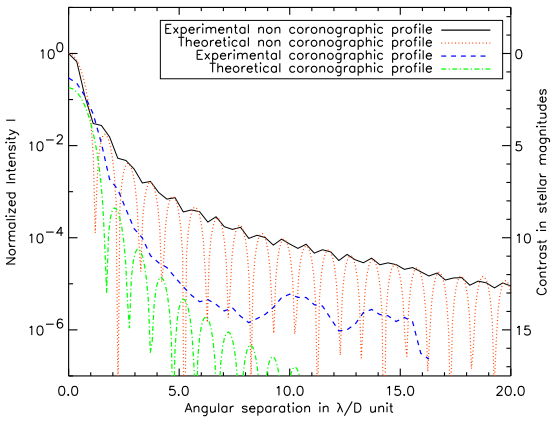

(c)

Figure III.10: Radial profiles of the experimental and theoretical images achieved in the presence or not of the RRPM. Mask radii are estimated to be $0.455\,\lambda/D$ (a), $0.516\,\lambda/D$ (b) and $0.741\,\lambda/D$ (c), respectively.

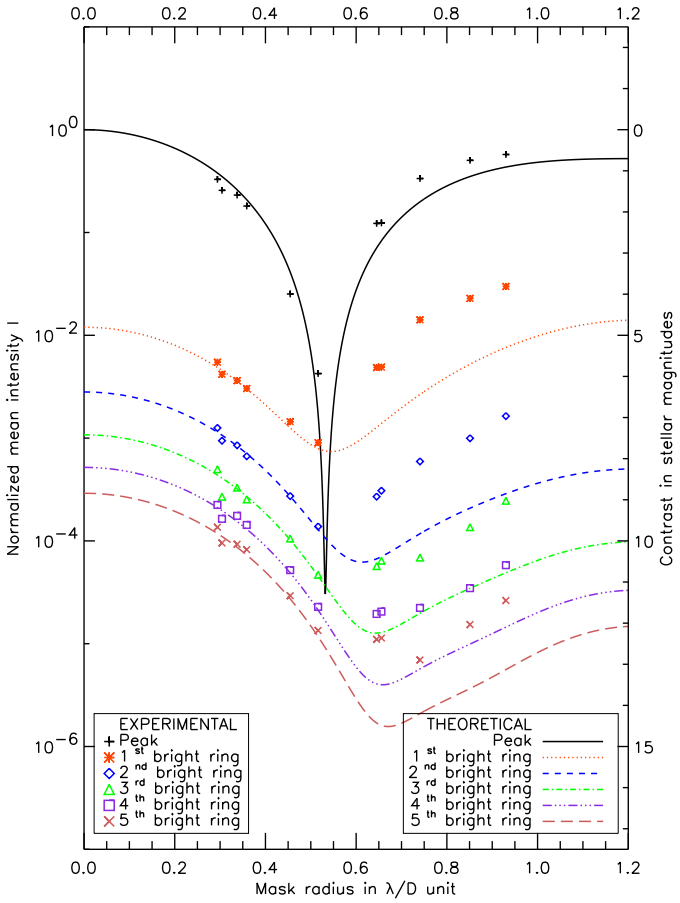

Figure III.11: Normalized image plane intensity at different field positions as a function of RRPM mask radius. The field positions considered correspond to bright rings in the non coronagraphic image, whose radial distances from the central star are given in Table III.1. Theoretical intensities are shown as lines, experimental values are shown as points. See text for a detailed description of this plot.

III.4 Algorithms for computing apodization profiles

In this section are presented the algorithms used to compute the different apodizer profiles of our study. First of all, we consider the design of classical pupil apodizers. Thereafter, we examine the case of the apodizers involved in Lyot-style coronagraphs.

III.4.1 Method for general purpose

III.4.1.1 Description of the algorithm

Gonsalves and Nisenson (2003) presented an algorithm for the calculation of apodizer transmission profiles. Their approach allows to optimize the design of a classical pupil apodizer in order to reduce the diffraction rings of an on-axis bright star PSF and increase the contrast of images in the search area. The method is quite general since it can be utilized for any telescope aperture geometry. However, the authors did not expose the case of entrance pupils with central obscuration in their paper. In the following, we review Gonsalves and Nisenson's algorithm and illustrate it by computing the apodizer shape for GTC geometry.
In Figure III.12, we scheme the algorithm for computing the best apodization. $\phi^{(n)}$ denotes the apodizer transmission function at iteration n. The complex amplitude of the electric field in the entrance pupil plane a can be expressed as follows:

$$\Psi_a^{(n)}(\boldsymbol{r}) = P(\boldsymbol{r})\,\phi^{(n)}(\boldsymbol{r})\,. \tag{III.2}$$

where P is the telescope aperture function.
Hence, the PSF is obtained with a Fourier transform of the previous expression. Since it deals with apodization, we aim to smooth the PSF so as to achieve a starlight concentration in its peak and a luminosity reduction of its bright rings. To reach this goal, a filter is applied in this plane: a mask W which transmission is non null inside the mask area and 0 outside. Therefore, the complex amplitude in the following focal plane b can be written as:

$$\Psi_b^{(n)}(\boldsymbol{r}) = \hat{\Psi}_a^{(n)}(\boldsymbol{\rho}) \times W(\boldsymbol{r})\,. \tag{III.3}$$

It can be noticed that the Fourier Transform calculus of $\Psi_a^{(n)}$ is only required inside the mask area. This remark outlines the possible use of the MFT for this algorithm. Finally, with a reverse Fourier transform of the previous expression, we achieve the apodizer transmission function at the iteration $n+1$:

$$\phi^{(n+1)}(\boldsymbol{r}) = \hat{\Psi}_b^{(n)}(\boldsymbol{\rho}) \times \Omega(\boldsymbol{r})\,. \tag{III.4}$$

where Ω represents a possible filter to smooth the apodizer shape. The operations described before are repeated iteratively n times until reaching a satisfying apodizer. An initial apodizer shape $\phi^{(0)}$ can also be introduced in the algorithm as suggested by Gonsalves and Nisenson (2003). Indeed, a good choice of this initial function allows to improve the algorithm efficiency and compute an optimal apodizer profile with relatively few iterations.

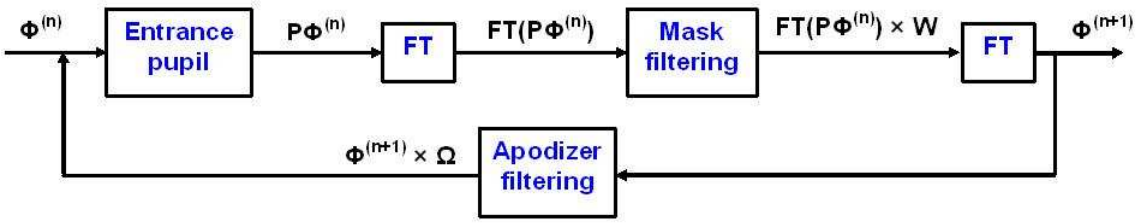

Figure III.12: Schematic illustration of the basic algorithm proposed by Gonsalves and Nisenson (2003) for computing the apodization profile.

III.4.1.2 Results

Here, we decide to work with a mask which expression is given by $W = M$. We remind that $M(\boldsymbol{r})$ is equal to 1 inside the mask area and 0 outside. No apodizer shape filter is used in our computations, thus $\Omega(\boldsymbol{r}) = 1$. Moreover, we decide to stop the iterations at $n = 200$: at this level, the difference in terms of attenuation gain between two successive iterations is no longer significant.
First of all, we check our algorithm computation. To realize this operation, we reproduce the result achieved in Figure 6 of Gonsalves and Nisenson's paper, see Figure III.13. The involved parameters are a clear circular aperture and mask area radius $r_W = 3.50\,\lambda/D$. We decided to start the iterations with an initial Gaussian function $\phi^{(0)}(\boldsymbol{r}) = \exp(-17.5\,r^2)$. Figure III.14 shows the apodizer profile reached with our simulator: we obtain the same result than that of the paper. This test validates our algorithm computation.
Afterward, we apply the algorithm to the case of FRIDA, considering a 29% centrally obstructed circular aperture and work with a mask area radius $r_W = 4.00\,\lambda/D$. Different initial apodizer profiles $\phi^{(0)}$ were examined: APLC apodizer profile (which computation algorithm is detailed below) and decentered Gaussian functions. In both cases, we did not notice relevant differences between the reached solution and that achieved in the absence of initial apodizer shape. Above all, discrepancy in contrast gains and apodizer throughput were no longer noted. The final profile is represented in Figure III.15. This apodizer associated with a focal plane opaque mask will be named Stop-less Lyot Coronagraph (SLLC).

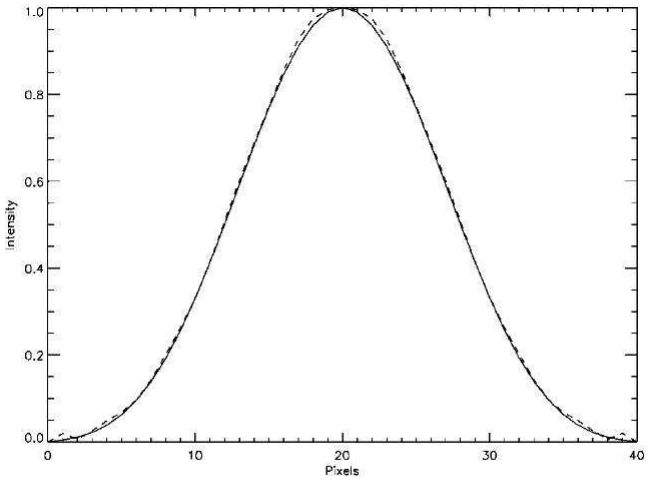

FIG. 6.—CB apodizer (*solid line*) and modified CB apodizer (*dashed line*).

Figure III.13: Transmission profile of the optimized apodization (solid line) computed for a clear circular aperture with the algorithm proposed by Gonsalves and Nisenson's algorithm. This plot is extracted from Gonsalves and Nisenson (2003).

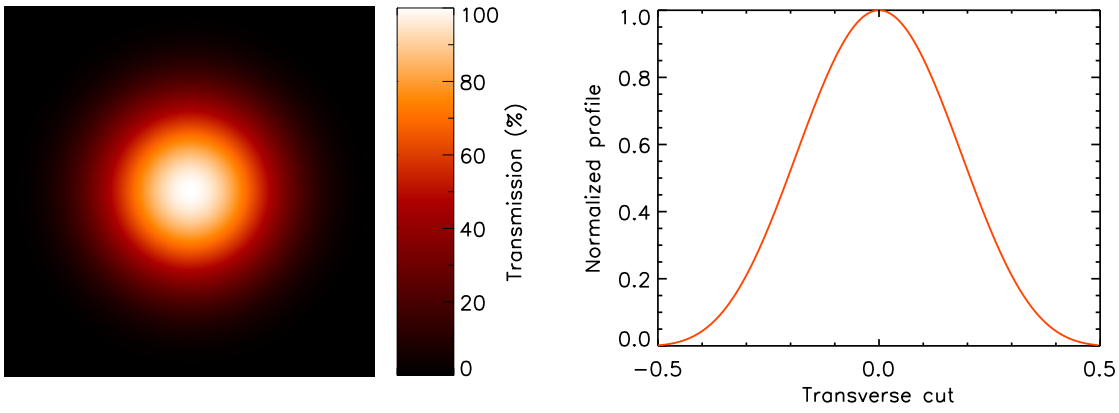

Figure III.14: Optimal apodization computed for a clear circular aperture and optimized with an opaque mask of radius $r_W = 3.50\,\lambda/D$. Total throughput is 12.07%. On the left, image of the apodizer and on the right, the corresponding transmission profile. Note that these results were obtained with 200 iterations.

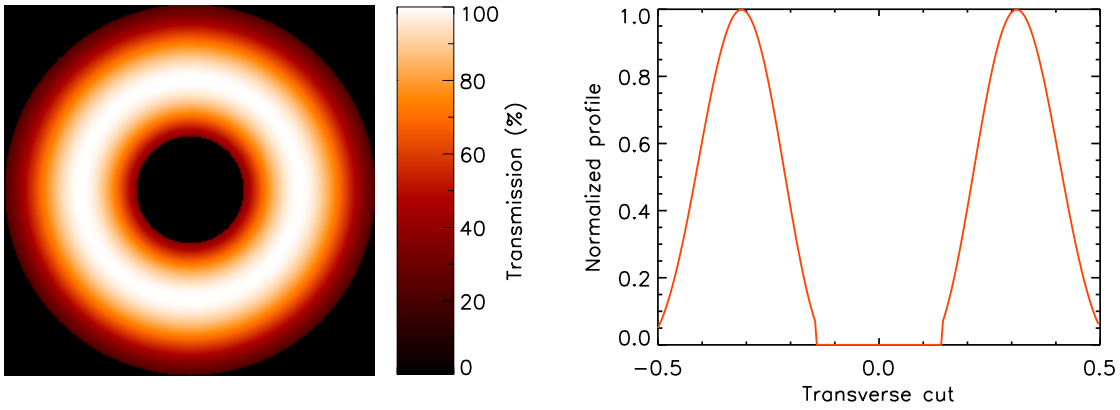

Figure III.15: Optimal apodization computed for the geometry of GTC (29% central obscuration) and optimized with an opaque mask of radius $r_W = 4.00\,\lambda/D$. Total throughput is 41.68%. On the left, image of the apodizer and on the right, the corresponding transmission profile. Note that these results were obtained with 200 iterations.

III.4.2 Algorithm for generating apodizer shape of Lyot-style coronagraphs

III.4.2.1 Description of the algorithm

Lyot-style coronagraphs are some of the considered diffraction suppression systems here which can involve an apodization in their scheme. A correct computation of their pupil apodizer profile is therefore required. The approach is quite different from that developed in Gonsalves and Nisenson (2003), in which an apodization in the input pupil plane is seen as a unique coronagraphic device. In that context, the use of an opaque mask in the following focal plane just represents an additional option for this coronagraphic technique: the spot helps to avoid detector saturation.
In the following, we work with Lyot-style coronagraphs. Our goal consists to achieve an entrance pupil apodizer profile taking into account parameters like mask size and Lyot stop aperture diameter. Hence, the apodization transmission function depends both on the entrance pupil shape and the coronagraphic mask, contrary to the previous method where only aperture shape is considered.
In the case of the Roddier & Roddier phase mask, Soummer et al. (2003) showed that the circular prolate spheroidal functions to apodize clear circular apertures provide a theoretical total starlight extinction. Furthermore, the authors also demonstrate that these functions for apodization also give optimal starlight rejections, when it deals with the Lyot opaque mask. The apodization shape becomes even more sophisticated if we consider an arbitrary telescope aperture (Soummer, 2005; Aime, 2005). Computing analytically the ideal pupil apodizer profile is not evident since several non trivial equations are involved in the generation of the optimal apodization function.
To reach the optimal apodization profile, we follow the numerical algorithm proposed by Guyon and Roddier (2000), and used again in Guyon and Roddier (2002), Abe (2004) or Soummer (2005). Let us note that this method was demonstrated analytically by Soummer et al. (2003). It consists of subtracting the residual Lyot stop wave amplitude Ψ_C from the aperture wave amplitude Ψ_A in an iterative loop. A schematic representation of the algorithm is given in Figure III.16. With few iterations, the optimal apodizer profile is achieved.
With this algorithm, the ideal apodization transmission function is generated for a given mask size and aperture shape. A possible way to improve this algorithm consists of optimizing the mask size applying a second intern iterative loop (Guyon and Roddier, 2000). Here, we decide to work with the basic version of the algorithm, optimizing first the mask size before generating the apodization with the obtained mask radius.

III.4.2.2 Results

To check the relevance of the results provided by our algorithm computation, we decide to reproduce the apodizer profile for the Roddier & Roddier phase mask coronagraph in the case of a clear circular aperture (Soummer et al., 2003). In this context, the mask radius is equal to $r = 0.53\,\lambda/D$. Figure III.18 shows the result of our simulation: it is in good agreement with the solution yielded by Soummer et al. (2003) and displayed in Figure 1B of their paper, see Figure III.17. Moreover, we obtain an apodizer throughput $T = 72.7\%$ which corresponds to the value given by Soummer et al. (2003): $T = 72.6\%$. These tests allow to validate our computation of the algorithm for generating apodizer shape of Lyot-style coronagraphs.
Afterward, we decide to generate the apodizer profile of Apodized Pupil Lyot Coronagraph (APLC) with a mask radius $r = 2.42\,\lambda/D$ and for a 29% centrally obstructed circular aperture. Indeed,

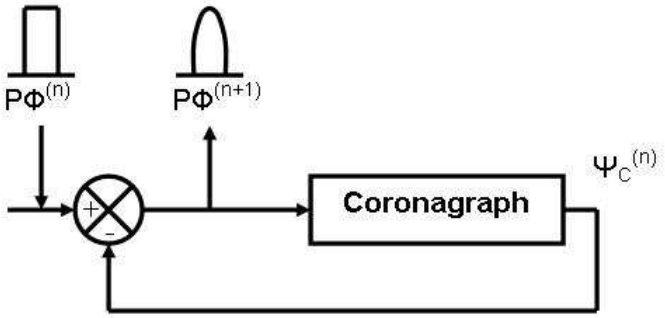

Figure III.16: Schematic representation of the algorithm suggested by Guyon and Roddier (2000) for the computation of pupil apodizer profile. In the original algorithm, a second loop is added to determine the optimal mask size at each iteration.

APLC working without Lyot stop is one of the coronagraphic configuration proposed for FRIDA. Figure III.20 shows the solution reached with our simulator. We achieve an apodizer throughput $T = 53.5\%$: this result is congruent with the values given in Figure 3 of Martinez et al. (2007), who plot the apodizer throughput as a function of the mask radius for different obscuration sizes, see Figure III.19.

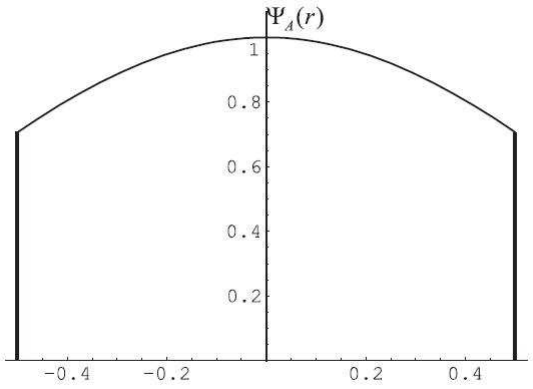

Figure III.17: Transmission profile of the optimized apodization computed for a clear circular aperture and Apodized Pupil Roddier Coronagraph with a Roddier & Roddier phase mask of radius $r = 0.53\,\lambda/D$. This plot is extracted from Soummer et al. (2003).

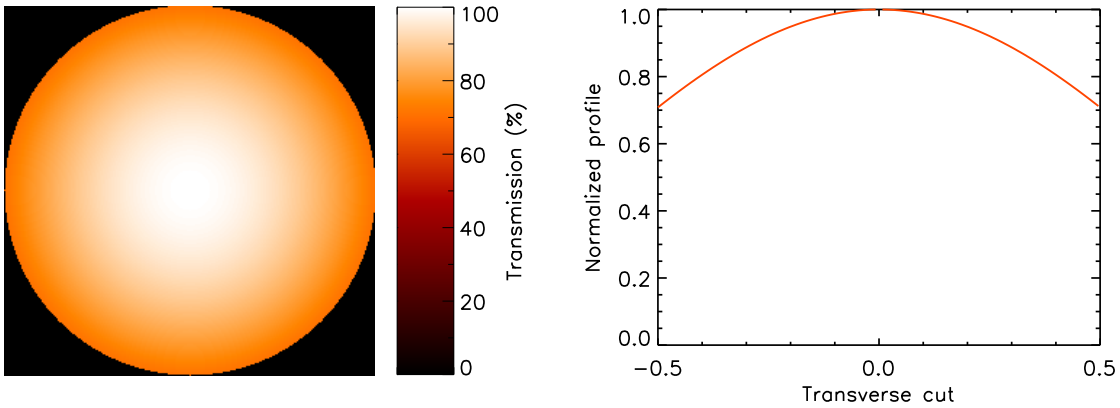

Figure III.18: Optimal apodization computed for a clear circular aperture and Apodized Pupil Roddier Coronagraph with a Roddier & Roddier phase mask of radius $r = 0.53\,\lambda/D$. Total throughput is 72.73%. On the left, image of the apodizer and on the right, the corresponding transmission profile. Note that these results were obtained with only 10 iterations.

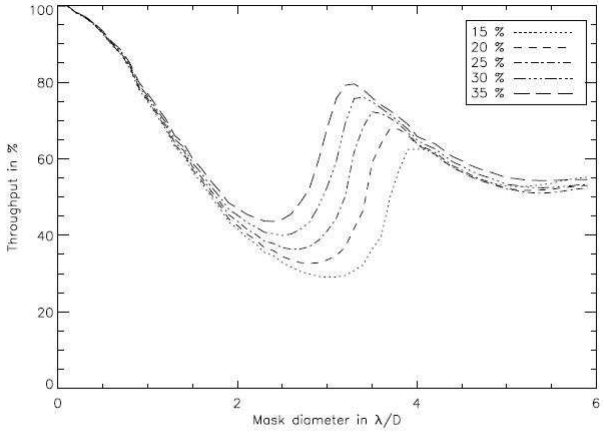

Fig. 3. Apodizer throughput (relative to full transmission of the telescope pupil) as a function of FPM diameter for different obscuration sizes.

Figure III.19: Apodizer throughput as a function of the opaque mask diameter for different obscuration sizes. This plot is extracted from Martinez et al. (2007).

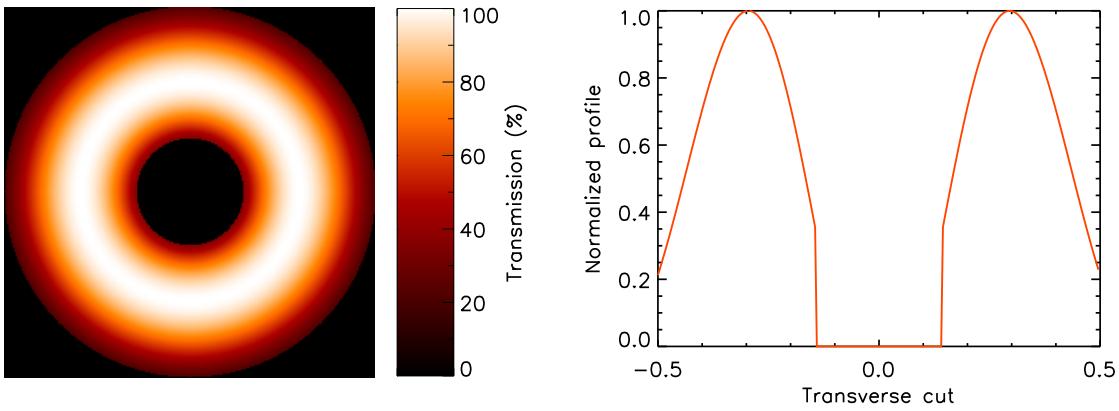

Figure III.20: Optimal apodization computed for the geometry of GTC (29% central obscuration) and APLC with an opaque mask of radius $r = 2.42\,\lambda/D$. Total throughput is 53.53%. On the left, image of the apodizer and on the right, the corresponding transmission profile. Note that these results were obtained with 20 iterations.

III.5 Other aspects of the numerical simulations for coronagraphs

III.5.1 Mono and polychromatic on-axis point source cases

Considering a monochromatic point source, the analysis of the coronagraph performance constitutes a first good and interesting approach. Working at just one wavelength allows to give a quick idea of the contrast gain reachable with a given coronagraph.
However, instruments are used to working with filters which never present null bandwidth. For instance, Table III.3, extracted from Tokunaga et al. (2002) and reproduced in Watson (2007), gives the central wavelength λ and widths $\Delta\lambda$ of the bandpass filters that will be used in FRIDA. On the one hand, the z, J, H, Ks and K filters represent the main FRIDA broadband filters. On the other hand, the Nz, NJ, NH and NK are representative 1.5% narrow-band filters located at the centers of z, J, H and K filters. Consequently, whatever the involved filter, the point source image provided at the system output will be polychromatic. Even with the narrowest filter NJ, which presents a $0.0024\,\mu$m bandwidth, the star image observed on the detector will be slightly polychromatic.
These remarks are in particular true in the context of FRIDA working in imaging mode. Since our study will be limited to FRIDA working in IFS mode, the images obtained with the data cube will be monochromatic. Hence, we will only compute monochromatic PSFs in our following simulations.

Table III.3: Characteristics of the filters that will be used by FRIDA with the central wavelength λ and the bandwidth $\Delta\lambda$.

Filter	z	J	H	Ks	K	Nz	NJ	NH	NK
λ in μm	1.015	1.250	1.635	2.150	2.200	1.015	1.250	1.635	2.200
$\Delta\lambda$ in μm	0.170	0.160	0.290	0.320	0.340	1.5%	1.5%	1.5%	1.5%

III.5.2 Star angular size

The stellar angular size may affect the performance of a coronagraph. Guyon et al. (2006) studied the effects of the stellar angular diameter over the coronagraphic performance and pointed out the sensitivity of several designs. This study was carried out in the context of Exosolar Terrestrial Planet imaging, therefore, they investigate a system capable of delivering 10^{10} contrast at less than 0.1 arcsec. For instance, they underline the high sensitivity to stellar radius of CRC, since this coronagraph could not maintain high contrast at small angular separations even with a $0.01\,\lambda/D$ stellar angular radius. On the other hand, they show that CLC and APLC will present a better but moderate robustness to stellar angular size.
However, our goal does not consist of achieving such levels of high contrast (10^{10}) at so small angular separations (< 0.1 arcsec), since FRIDA is not initially designed to detect Earth-like planets. Hence, and in order to reduce the complexity of the study, our numerical simulations will be made considering a point source.

III.5.3 Choice of the different mask sizes

The performance of Lyot-style coronagraphs depends on the focal plane mask diameter. Therefore, defining adequately the spot size is required for our work. A common criterion used to choose the mask size consists in plotting the Integrated Residual Energy (IRE) inside the Lyot aperture in plane C as a function of the spot radius (e.g. Aime and Soummer, 2003; Ferrari et al., 2007). In Figure III.21, we reproduce the graphs achieved with the Roddier & Roddier phase and Lyot opaque masks for a clear circular aperture. These profiles are in agreement with those found in Ferrari et al. (2007), see Figure III.22.

On the one hand, for the Lyot opaque mask, we can note the presence of several local maxima and minima in IRE profile: they simply correspond respectively to the bright and dark rings of the Airy diffraction pattern. Ferrari et al. (2007) underlined several points from this profile. First of all, the performance of Lyot-style coronagraphs is not strictly linear with the mask size. Afterward, a large amount of the star residual energy is located at the edges of the pupil and can be eliminated with a moderate reduction of the Lyot stop radius. Finally, the off-axis transmission of the coronagraph is important for the substellar-mass companion detection, therefore we have to take care about not selecting a too large opaque mask.

On the other hand, for the Roddier & Roddier phase mask, it can be noticed that a unique minimum exists at $r \simeq 0.53\,\lambda/D$. This value corresponds to the best central extinction of an on-axis bright star image. However, Ferrari et al. (2007) points out the fact that an extended phase mask would operate as an apodizer for the wave complex amplitude. Consequently, this graph no longer constitutes an absolute and valid criterion for selection of an optimal value of the radius. However, for the choice of the phase mask radius, we will pick out the minimum of IRE profile as we will see below in the case of FRIDA with CRC configuration.

In Figure III.21, we also represent the IRE profiles for a 29% centrally obstructed circular aperture. This allows to consider the case of a mask inserted in FRIDA plane FP2 in the case of an APLC working without Lyot stop, see Figure II.12. From this plot, we extract the values of the mask radius for our study. Concerning the configuration of APLC working without Lyot stop, we select the second local maximum for the opaque mask radius: $r = 2.42\,\lambda/D$. This choice is quite arbitrary but in agreement with the values generally found in the literature.

In Figure III.23, we plot the profiles of the IRE inside the Lyot aperture in FRIDA plane PP1 as a function of the spot radius. These profiles are computed for the Roddier & Roddier phase and Lyot opaque masks located in plane FP1 and in the FRIDA approach: it means a GTC aperture in the upstream plane PP0 and a circular pupil stop with 29% central obscuration in the downstream plane PP1, see Figure II.11. Pictures of the respective pupils have been given in Figure II.8. In addition, these profiles are normalized with respect to the energy present in the telescope aperture plane PP0. Concerning the Lyot coronagraph, we select the third local minimum for the opaque mask radius: $r = 2.69\,\lambda/D$. For the Roddier & Roddier phase mask, the radius corresponding to the unique minimum of IRE is chosen: $r = 0.60\,\lambda/D$.

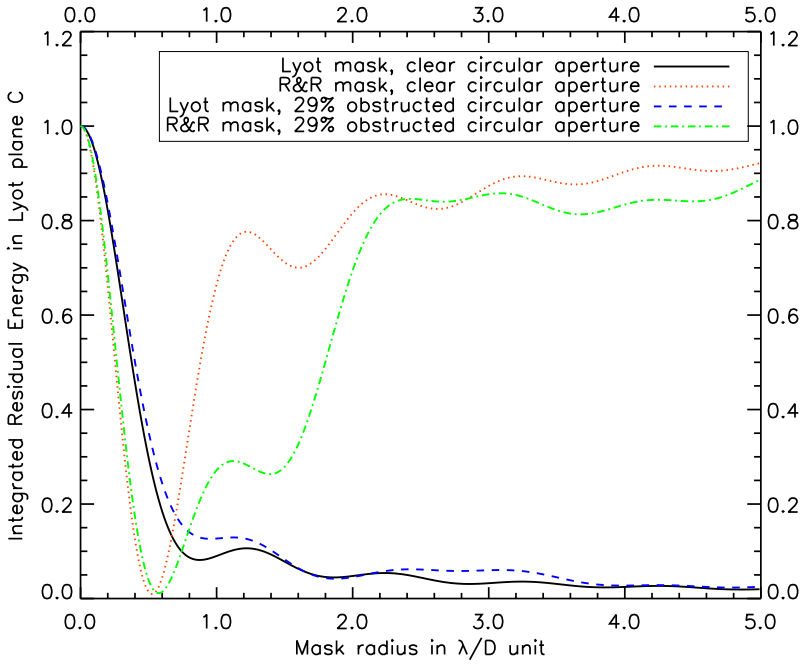

Figure III.21: Integral residual energy (IRE) in plane C as a function of the spot size for different entrance pupil geometry and mask nature.

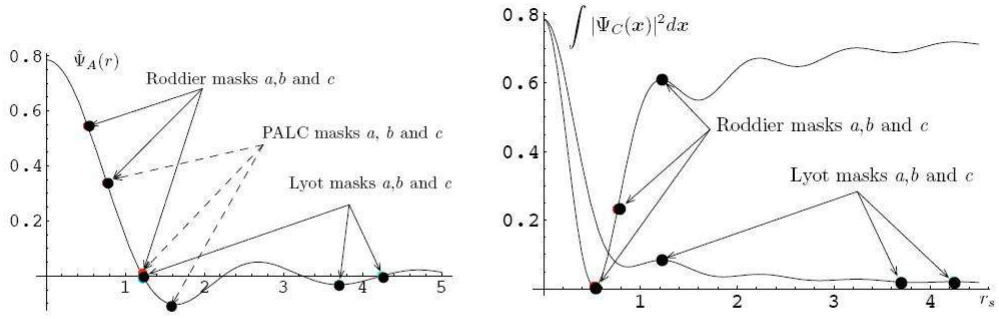

Figure 3. The left plot locates the different masks used in the simulation on the response of an on-axis point source. The right plot gives the integrated intensity in C for $r_s = R$ as a function of the mask size.

Figure III.22: On the right, Integral residual energy (IRE) in plane C as a function of the spot size for different entrance pupil geometry and mask nature. This plot is extracted from Ferrari et al. (2007).

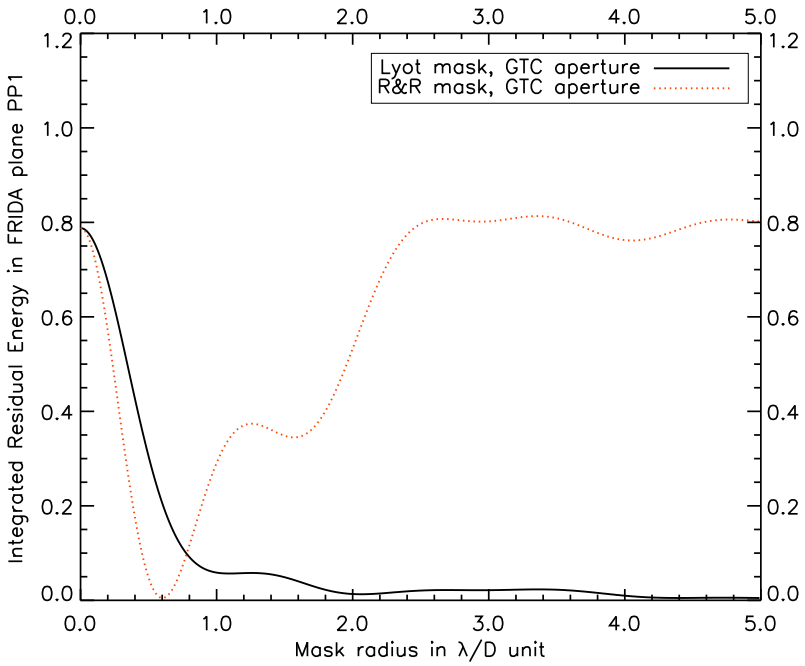

Figure III.23: Integral residual energy (IRE) in plane PP1 as a function of the spot size for GTC pupil geometry and different mask nature.

III.6 Application for FRIDA in a diffraction-limited approach

III.6.1 Numerical results obtained with CLC and CRC

Figure III.24 gives the profiles achieved for suitable coronagraphic configurations for FRIDA. Here, we analyzed the cases of CLC and CRC represented in top plot. Indeed, FRIDA can be equipped with these coronagraphic paths since a coronagraphic mask and Lyot stop can be inserted respectively in FP1 and PP1 of FRIDA optical assembly, see Figure II.11. The coronagraphic image obtained with CLC is not perfectly symmetric and therefore, we decide to compute its azimuthal average to represent CLC radial intensity profile. Brightness attenuations reached by CLC and CRC at different separations are reported on Table III.4. Numerical results show that CRC yields better contrast gains than CLC at all separations: in some cases, it provides starlight attenuations better 5 mag and above all, at the smallest angular distances from the observed on-axis point source.

III.6.2 Numerical results obtained with APLC without Lyot stop and SLLC

Since we started our coronagraph feasibility study for FRIDA, we have investigated the possibility of inserting a coronagraph which involves pupil apodizer, focal plane mask and Lyot stop. Indeed, this kind of coronagraph is expected to provide better starlight attenuations than CLC or CRC and constitutes a very promising solution for high contrast imaging at small angular separations. In the context of FRIDA operating in IFS mode, APLC was firstly considered for this GTC instrument. An apodization and coronagraph mask can be introduced respectively in the 1^{st} pupil and focal planes. However, no Lyot stop can be included in PP2. We therefore propose an original coronagraphic concept to overcome the FRIDA stresses: the Stop-less Lyot Coronagraph (SLLC), a combination of pupil and focal masks. Hereafter, we estimate the star brightness attenuation that can be obtained with this innovating approach.
Figure II.12 gives an illustration of the optical scheme of FRIDA equipped with SLLC or APLC working without Lyot stop. Let us remind that we do not simulate the presence of the opaque mask in FP2: since no Lyot stop is present in plane PP2, the spot will block starlight in FP2 and only residual light due to diffraction will be present in its re-imaged area in FP3, depending on the size of the geometric exit pupil in plane PP2. The intensity profiles of these apodizer solutions are reported in Figure III.24 bottom plot. Table III.4 summarizes the contrast gain results that can be reached with the apodizers of APLC working without Lyot stop and SLLC at different angular separations. The SLLC apodizer can yield brightness attenuations greater than 3.50 mag. These values are very promising and allow to point out the relevancy of using this coronagraph. SLLC proves to be a very interesting option for instruments for which the insertion of a pupil is made impossible.

III.6.3 Discussion

Hereafter, we propose to synthesize the results achieved numerically with all the coronagraphic configurations of our study. In addition, we decide to report the results obtained with APLC. It aims to compare the performance of APLC and suitable coronagraphs and determine the best coronagraphic option for FRIDA in the approach of a diffraction-limited system.
The APLC option was studied assuming that a Lyot stop could be inserted in the 2^{nd} pupil plane

of FRIDA. This is not realistic at all but gives us a good idea about the capabilities of APLC if its insertion could be technically feasible. The entrance pupil geometry for APLC is circular with a 29 % central obscuration, therefore we use the characteristics of APLC already computed and presented in the present chapter. Since APLC is not a suitable coronagraph for FRIDA, we decide to not sketch its intensity profile in the respective plots of Figure III.24.
Table III.4 summarizes the contrast gains that can be reached with all the coronagraphic devices at different angular separations.
CRC is the only coronagraph able to provide observations at an angular separation of $2\,\lambda/D$ or 0.100 arcsec at $\lambda = 2.200\,\mu$m (K-band). This is due to the small size of the mask ($r = 0.60\,\lambda/D$). At an angular separation of $4\,\lambda/D$ from the star (0.200 arcsec at $\lambda = 2.200\,\mu$m), it can be noticed that CRC and APLC provides the best contrast gains with respectively $\Delta m = 5.20$ and 12.66 in stellar magnitudes. These starlight attenuations are greatly better than those achieved with SLLC apodizer ($\Delta m = 4.27$) and CLC ($\Delta m = 1.72$). We can also note the large difference of contrast between APLC and apodizer of APLC working without Lyot stop: this underlines the interest in using a Lyot stop for a coronagraph which involves an apodizer and a mask.
At larger angular distances from the on-axis star, APLC represents the best coronagraphic option with contrast gains usually greater than 10 mag. Thereafter, SLLC followed by CRC constitute the best coronagraphic configurations for FRIDA, since it should provide gains better than 5 mag. SLLC deserves to be considered as a non negligible diffraction suppression concept. CLC and APLC working without Lyot stop present the weakest results in terms of contrast gain.
These numerical values give an accurate idea in terms of reachable contrast for FRIDA with the different coronagraphic configurations and in the absence of aberrations. Under this approach, APLC would be the best solution for FRIDA. However, since no Lyot stop can be included in PP2, APLC is not suitable and therefore, SLLC becomes the more encouraging option, followed by CRC.

Table III.4: Contrast gains reached by suitable coronagraphs and APLC for FRIDA in a diffraction-limited approach. The present study is done considering a monochromatic on-axis point source.

Coronagraph	**Contrast gain in stellar mag. Δm at an angular separation (in λ/D):**						
	2.0	4.0	6.0	8.0	10.0	12.0	14.0
CLC		1.72	1.38	3.14	2.17	2.16	2.44
APLC without Lyot stop apodizer		4.27	3.32	1.48	2.12	2.90	3.13
CRC	5.16	5.20	2.68	4.00	5.83	3.59	2.52
SLLC apodizer			3.55	3.62	5.82	6.70	4.18
APLC		12.66	11.71	9.87	10.52	11.29	11.53

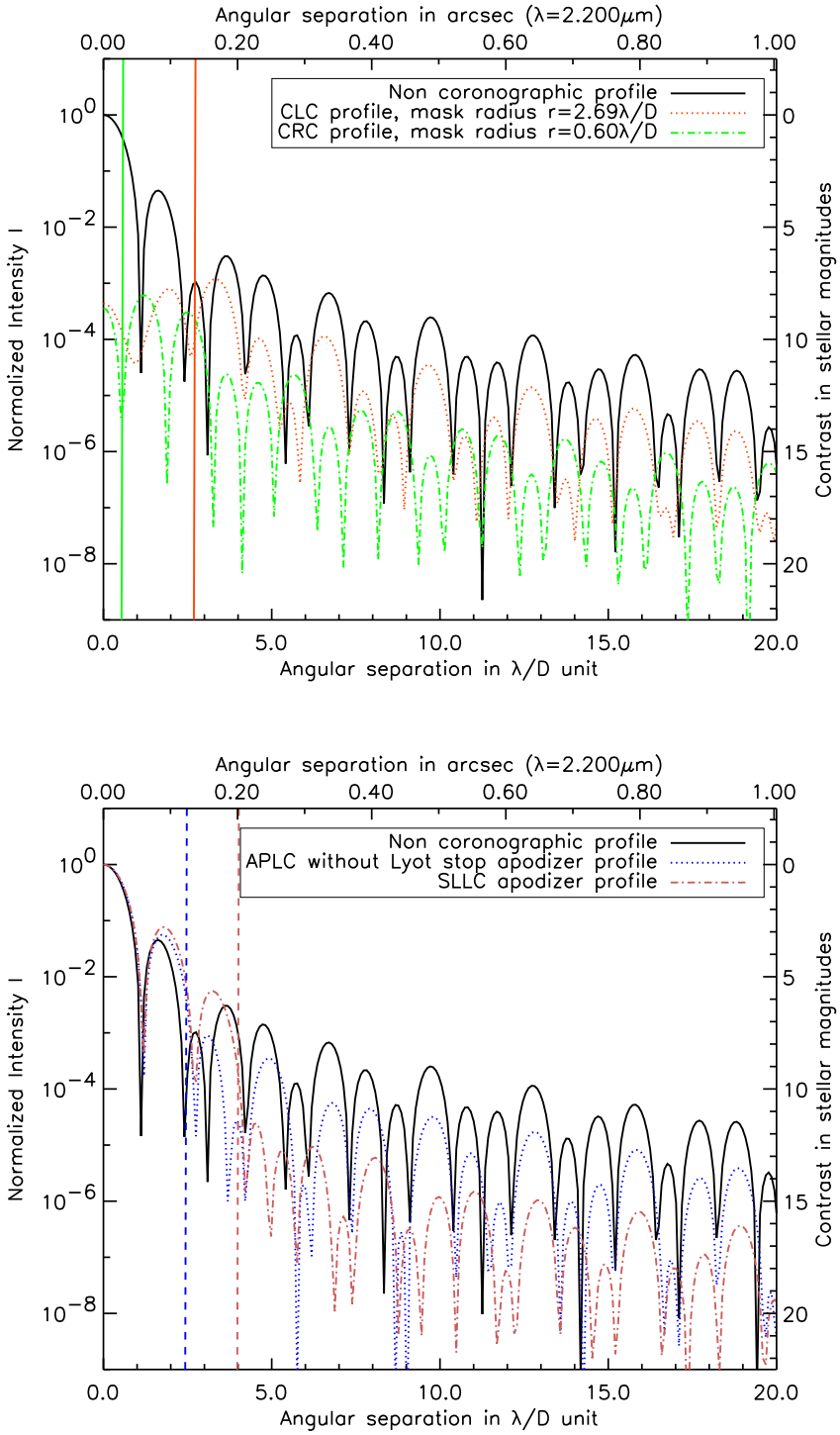

Figure III.24: Radial profiles of the non coronagraphic PSF and coronagraphic images obtained with suitable coronagraphic devices for FRIDA. A monochromatic point source is considered here in K-band. These results are obtained in the context of a diffraction-limited system. CLC and CRC are represented in top plot and their focal plane masks are delimited by a vertical line for each coronagraph. APLC without Lyot stop and SLLC apodizer profiles are represented in bottom plot and possible opaque masks are denoted by a dashed line for use with the respective apodizers.

III.7 Conclusion of the third chapter

In this chapter, we carried out the implementation of a numerical tool to simulate the behavior of different coronagraphic devices. The numerical tool was based on the Matrix Fourier Transform (MATF). The semi-analytical approach performed with MATF allows to compute efficiently and accurately coronagraphic intensity profiles. Furthermore, we described the algorithms used to generate apodizer transmission profiles and illustrated them with some examples. Some important computational aspects like chromatism or selection of the mask size were also reviewed. In all cases, we checked the consistency of the solutions yielded with our tool. It was showed that our simulations were in good agreement with the formalism of the stellar coronagraphs described in the first chapter. Moreover, we validated experimentally the theory and simulations through the laboratory tests made with a second-generation Roddier & Roddier phase mask. This aspect of the work was reported in a paper which was sent to a referred journal, accepted and presented in Annexe C. It allowed to point out the good consistency existing between numerical simulations and experimental results.
Afterward, we put our numerical tool into practice to evaluate the performance reachable by the suitable coronagraphic configurations for FRIDA. As a first step, the contrast gains were estimated in the context of a diffraction-limited system. We noticed that SLLC seemed to be the best option for FRIDA in terms of star brightness attenuation, followed by CRC, APLC working without Lyot stop and finally CLC.
In the next chapter, we will extend this study to the approach of ground-based instruments. Therefore, the atmospheric turbulence and its correction by the Adaptive Optics (AO) system of the GTC will be considered. Thus, perfect wavefronts coming into FRIDA equipped with a coronagraph will be replaced by AO corrected wavefronts. We will determine numerically the contrast gains provided by each coronagraph for FRIDA in this context.

III.7 Conclusión del tercer capítulo

En este capítulo, se llevó a cabo la implementación de una herramienta numérica para simular el comportamiento de diferentes dispositivos coronográficos. La herramienta está basada en la Transformada de Fourier Matricial (MAFT por sus siglas en inglés). El método semi-analítico realizado con MATF permite calcular de manera eficiente y con precisión los perfiles de intensidad coronográfica. Luego, se describieron los algoritmos adoptados para generar los perfiles de transmisión de las apodizaciones y se ilustraron con algunos ejemplos. Algunos aspectos importantes de computación como el cromatismo o la selección del tamaño de máscara fueron revisados. En todos los casos, se verificó que las soluciones producidas con nuestra herramienta fueran consistentes. Se mostró que nuestras simulaciones concordaban bien con el formalismo de los coronógrafos estelares descritos en el primer capítulo. Además, se validaron la teoría y las simulaciones de manera experimental a través de unas pruebas efectuadas en laboratorio con una máscara de fase de Roddier & Roddier de segunda generación. Este aspecto del trabajo se reporta en forma de un artículo que fue aceptado en una revista arbitrada y que se presenta en el anexo C. Se verificó la coherencia que existe entre las simulaciones numéricas y los resultados experimentales.
Luego, se utilizó nuestra herramienta numérica para evaluar el desempeño alcanzado por las confi-

guraciones coronográficas factibles para FRIDA. Como primera etapa, se estimaron las ganancias a nivel de contraste en el contexto de un sistema limitado por la difracción. Se notó que el SLLC es la mejor opción para FRIDA en términos de atenuación de brillo estelar, seguido por el CRC, el APLC sin diafragma de Lyot y finalmente el CLC.
En el próximo capítulo, se extenderá este estudio al caso de los instrumentos terrestres. Por lo tanto, se considerarán la turbulencia atmosférica y su corrección por un sistema de Óptica Adaptativa (AO por sus siglas en inglés). De tal forma, los frentes de onda perfectos que llegan a FRIDA equipado con un coronógrafo serán reemplazados por unos frentes de onda corregidos por AO. Se determinará numéricamente las ganancias a nivel de contraste que cada uno de los coronógrafos para FRIDA proveerá en este contexto.

III.8 References

L. Abe. Numerical Simulations in Coronagraphy. Part I. In C. Aime and R. Soummer, editors, *EAS Publications Series*, volume 12 of *EAS Publications Series*, pages 157–164, 2004.

C. Aime. Principle of an Achromatic Prolate Apodized Lyot Coronagraph. *Public. of the Astron. Soc. Pac.*, 117, 1012–1019, 2005.

C. Aime and R. Soummer. Introduction to stellar coronagraphy with entrance pupil apodization. In C. Aime and R. Soummer, editors, *EAS Publications Series*, volume 8 of *EAS Publications Series*, pages 79–92, 2003.

A. Ferrari, R. Soummer, and C. Aime. An introduction to stellar coronagraphy. *Comptes Rendus Physique*, 8, 277–287, 2007.

R. Gonsalves and P. Nisenson. Calculation of Optimized Apodizers for a Terrestrial Planet Finder Coronagraphic Telescope. *Public. of the Astron. Soc. Pac.*, 115, 706–711, 2003.

O. Guyon and F. Roddier. A nulling wide field imager for exoplanets detection and general astrophysics. *A&A*, 391, 379–395, 2002.

O. Guyon and F. J. Roddier. Direct exoplanet imaging possibilities of the nulling stellar coronagraph. In P. J. Lena and A. Quirrenbach, editors, *Proc. SPIE Vol. 4006, p. 377-387, Interferometry in Optical Astronomy, Pierre J. Lena; Andreas Quirrenbach; Eds.*, volume 4006 of *Presented at the Society of Photo-Optical Instrumentation Engineers (SPIE) Conference*, pages 377–387, 2000.

O. Guyon, C. Roddier, J. E. Graves, F. Roddier, S. Cuevas, C. Espejo, S. Gonzalez, A. Martinez, G. Bisiacchi, and V. Vuntesmeri. The Nulling Stellar Coronagraph: Laboratory Tests and Performance Evaluation. *Public. of the Astron. Soc. Pac.*, 111, 1321–1330, 1999.

O. Guyon, E. A. Pluzhnik, M. J. Kuchner, B. Collins, and S. T. Ridgway. Theoretical Limits on Extrasolar Terrestrial Planet Detection with Coronagraphs. *ApJS*, 167, 81–99, 2006.

P. Martinez, A. Boccaletti, M. Kasper, P. Baudoz, and C. Cavarroc. Optimization of apodized pupil Lyot coronagraph for ELTs. *A&A*, 474, 671–678, 2007.

F. Roddier and C. Roddier. Stellar Coronagraph with Phase Mask. *Public. of the Astron. Soc. Pac.*, 109, 815–820, 1997.

R. Soummer. Apodized Pupil Lyot Coronagraphs for Arbitrary Telescope Apertures. *ApJL*, 618, L161–L164, 2005.

R. Soummer, C. Aime, and P. E. Falloon. Stellar coronagraphy with prolate apodized circular apertures. *A&A*, 397, 1161–1172, 2003.

R. Soummer, L. Pueyo, A. Sivaramakrishnan, and R. J. Vanderbei. Fast computation of Lyot-style coronagraph propagation. *Optics Express*, 15, 15935–15951, 2007.

A. T. Tokunaga, D. A. Simons, and W. D. Vacca. The Mauna Kea Observatories Near-Infrared Filter Set. II. Specifications for a New JHKL'M' Filter Set for Infrared Astronomy. *Public. of the Astron. Soc. Pac.*, 114, 180–186, 2002.

A. M. Watson. FR/FR-SC/040: Signal and Noise estimates. Frida technical note, Centro de Radioastronomía y Astrofísica - Universidad Nacional Autónoma de México, 2007.

Chapter IV

Coronagraph performance in the presence of AO corrected wavefronts

IV.1 From diffraction-limited systems to ground-based instruments

IV.1.1 Interest of the diffraction-limited approach

In the previous chapter, our study was centered on the diffraction-limited approach and in that context, we quantified numerically the contrast gain reachable with different coronagraphic configurations for FRIDA. Our results were computed in the absence of aberrations. This approach proves to be very interesting when it deals with a space telescope. However, it remains limited in the case of a ground-based instrument: the wavefront errors, which deteriorate the coronagraph performance, have to be taken into account.

IV.1.2 Stellar coronagraphy in the context of ground-based instruments

In the context of a ground-based instrument, the presence of the atmosphere and its effects on the telescope performance have to be considered. Indeed, atmospheric turbulence distorts the wavefronts coming from a star: this implies a loss of resolution on the star image. Nowadays, an Adaptive Optics (AO) system represents the most spread and admitted solution to correct the wavefront errors due to the atmospheric turbulence. With AO, a ground-based telescope can get closer to its theoretical resolution limit. The quality of the AO correction depends both on the strength of the atmospheric perturbations and the characteristics of the AO system.
In the present study, we need first to compute the complex amplitude of the electric field yielded by a ground-based telescope with AO system. Afterward, we will be able to simulate different coronagraphs in the presence of AO compensated wavefronts and estimate their performance. Here, our study is focused on FRIDA. Hence, we will consider parameters of the Gran Telescopio Canarias (GTC) supplied with GTCAO, its Adaptive Optics system (Devaney et al., 2004), in our following computations since FRIDA is planned to work in concert with these instruments. Once "GTC+GTCAO+FRIDA" has been modeled numerically, it will be possible to quantify the contrast gains reached by different coronagraphic configurations for FRIDA.

IV.1.3 Goals of this chapter

In the present chapter, we propose to estimate numerically the contrast gains reachable with suitable coronagraphs for FRIDA. This study is now led in the presence of AO compensated wavefronts. Section IV.2 reviews the atmospheric turbulence and its implications on the image quality provided by a telescope. In Section IV.3, we briefly remind how an AO system works before giving the main characteristics of GTCAO. Afterward in Section IV.4, we shortly describe CAOS (Carbillet et al., 2005), the software we decide to use to model GTCAO and generate AO corrected wavefronts. Two GTCAO configurations are considered here: its current design and a possible future upgrade.
In Section IV.5, numerical simulations are realized combining our coronagraph simulator with the wavefronts computed with CAOS for both GTCAO models. We numerically evaluate and compare the starlight attenuation achieved with CLC, CRC, APLC without Lyot stop and SLLC respectively. Finally, a synthesis of the reachable contrast gains is given and thus, we discuss the relevance of equipping FRIDA with just a coronagraph to provide high contrast images.

IV.1 De sistemas limitados por la difracción a instrumentos terrestres

IV.1.1 Interés por el estudio de sistema limitado por la difracción

En el capítulo anterior, nuestro estudio se centró en sistemas limitados por la difracción y en ese contexto, se cuantificó de manera numérica la ganancia de contraste alcanzable con las diferentes configuraciones coronográficas de FRIDA. Nuestros resultados fueron efectuados en ausencia de aberraciones. Este estudio resulta ser muy interesante cuando se trata de un instrumento trabajando en el espacio. Sin embargo, no es el caso de un instrumento colocado en un instrumento terrestre.

IV.1.2 Coronografía estelar en el contexto de instrumentos terrestres

En el caso de un instrumento terrestre, se debe considerar la presencia de la atmósfera y sus efectos en el desempeño del telescopio. De hecho, la turbulencia atmosférica distorsiona los frentes de onda que provienen de una estrella observada: eso implica una perdida de resolución en la imagen de la estrella. Hoy en día, un sistema de Óptica Adaptativa (AO por sus siglas en inglés) representa la solución más difundida y admitida para corregir los errores de frente de onda producidos por la turbulencia atmosférica. Con AO, un telescopio terrestre puede acercarse de su límite de resolución teórico. La calidad de la corrección AO depende a la vez de la intensidad de las perturbaciones atmosféricas y de las características del sistema AO.
En el presente estudio, se necesita primero calcular la amplitud compleja del campo eléctrico obtenida con un telescopio terrestre equipado con un sistema AO. Luego, se podrá simular los diferentes coronógrafos en presencia de frentes de onda compensados por AO y estimar su desempeño. Aquí, nuestro estudio está enfocado en FRIDA. Por lo tanto, se considerarán parámetros del Gran Telescopio Canarias (GTC) equipado con GTCAO, su sistema de Óptica Adaptativa (Devaney et al., 2004), en nuestras simulaciones ya que FRIDA está planeado para trabajar en conjunto con estos instrumentos. Una vez modelado numéricamente "GTC+GTCAO+FRIDA", será posible cuantificar las ganancias en contraste alcanzadas por las diferentes configuraciones coronográficas de FRIDA.

IV.1.3 Objetivos del capítulo

En este capítulo, se propone estimar de manera numérica las ganancias en contraste alcanzables con los coronógrafos factibles para FRIDA. Este estudio se hace ahora en presencia de frentes de onda compensados por AO. Se revisa en la Sección IV.2 la turbulencia atmosférica y sus implicaciones en la calidad de imagen proporcionada por un telescopio. En Sección IV.3, se recuerda brevemente como funciona un sistema AO antes de dar las principales características de GTCAO. Luego en la Sección IV.4, se describe brevemente CAOS (Carbillet et al., 2005), el software que decidimos usar para modelar GTCAO y generar frentes de onda corregidos por AO. Se consideran dos configuraciones de GTCAO aquí: su diseño actual y una eventual actualización que se podría realizar en el futuro. En la Sección IV.5, se realizan simulaciones asociando nuestro simulador de coronógrafo con los frentes de onda calculados con CAOS y para ambos modelos de GTCAO. Se evalúan numéricamente y se comparan las atenuaciones alcanzadas con CLC, CRC, APLC sin diafragma de Lyot y SLLC respectivamente. Finalmente, se provee una síntesis de las ganancias en contraste alcanzables y así,

se discute acerca de la relevancia de equipar FRIDA con sólo un coronógrafo para proporcionar imágenes de alto contraste.

IV.2 Atmospheric turbulence and image quality

IV.2.1 Image resolution in the absence of aberrations

In this section, we review the criteria commonly used to characterize the image quality of a point source object formed by an optically perfect system. In the present study, an observed star symbolizes our point source and its image is described by the Point Spread Function (PSF), the impulse response of our optical system, in the focal plane of the telescope aperture.
Let us consider a clear circular aperture in the absence of aberrations. Hence, the PSF is characterized by the so-called Airy diffraction pattern. Following Lord Rayleigh's criterion, two stars of equal brightness are just resolved when the peak of one Airy disk falls on the first dark ring of the other Airy disk. Therefore, the **angular limit of resolution** α is given by the radius of the first dark Airy ring:

$$\alpha = 1.22\frac{\lambda}{D}\,, \tag{IV.1}$$

where D and λ denote respectively the telescope diameter and the wavelength of study.
The **angular Full Width at Half Maximum** (FWHM) is another typical parameter used in imagery. For a point source, the angular FWHM at a given direction is approximately the ratio between the wavelength and the width of the aperture in that direction:

$$FWHM \simeq \frac{\lambda}{D}\,. \tag{IV.2}$$

IV.2.2 Energy criteria

The Strehl ratio and encircled energy constitute other common measures to estimate the quality of an image. Both parameters are criteria of energy distribution within an image.
On the one hand, the **Strehl ratio** S represents the ratio of the peak intensity to that of a perfect optical system. In the absence of aberrations, $S = 1$.
On the other hand, the **encircled energy** EE is defined as the fraction of the total energy E in the image enclosed within a circle of radius r centered on the PSF peak.
In the following, we will see how the angular limit of resolution and the Strehl ratio evolve when atmospheric turbulence aberrations are considered.

IV.2.3 Atmospheric turbulence statistics

A brief physical description of the atmospheric turbulence is given here. We explain how the wavefront distorts and its implications on the image formation. Therefore, a part of this section is devoted to the statistics of the air refractive index fluctuations. A more detailed statistics description of the air refractive index fluctuations and wavefront distortions can be found in several papers (e.g. Roddier, 1981, 1989; Fried, 1994) and books (Roddier, 1999a; Tyson, 1998). Here, we summarize the main results given in Roddier (1999b) and review several notions and parameters that will be used latter.
Fluctuations in the air refractive index are essentially proportional to the fluctuations in the air temperature. The changes in temperature are due to wind shears which produces turbulence and mixes the air layers at different temperature. Therefore, temperature inhomogeneities appear,

what implies small changes in the atmospheric density and hence, to the index of refraction. The statistics of refractive index follows that of temperature inhomogeneities, which are governed by the Kolmogorov-Obukhov law of turbulence. Here, we deal with a non stationary random process. Let us evaluate the difference of the refractive index n between a point $\boldsymbol{r}$ and a nearby point at a distance $q = |\boldsymbol{q}|$ apart. Vectors $\boldsymbol{r}$ and $\boldsymbol{q}$ represent three dimensional positions and separations. The variance of the difference between the two values of the refractive index is given by:

$$D_n(\boldsymbol{q}) =< |n(\boldsymbol{r}) - n(\boldsymbol{r}+\boldsymbol{q})|^2 >= C_n^2\, q^{2/3}\,, \tag{IV.3}$$

where $D_n(\boldsymbol{q})$ is called the **index structure function** and the brackets <> represent an ensemble average. The constant C_n^2 is the **index structure coefficient** and it defines a measure of the turbulence strength. This amount varies with seasons as well as the geographic location and the altitude. Furthermore, the dependence of C_n^2 on altitude is called the turbulence profile. Table IV.1 gives the atmospheric layer model of the GTC location: the *Observatorio del Roque de Los Muchachos* (ORM) in Canary Islands, Spain, see Figure IV.1.

Eq. (IV.3) is a valid approximation as long as q is smaller than some value called the turbulence outerscale L_0. Indeed at longer distances, the fluctuations $n(\boldsymbol{r})$ and $n(\boldsymbol{r}+\boldsymbol{q})$ are expected to become eventually uncorrelated and therefore, the index structure function no longer depends on q.
Now, let us analyze the wavefront phase distortions caused by the atmospheric turbulence. The wavefront complex amplitude ψ is defined as follows:

$$\psi = A\exp(i\varphi)\,, \tag{IV.4}$$

where A and φ are real numbers which respectively represent the amplitude and the phase of the field fluctuation. A surface over which φ takes the same value is called a wavefront surface. Before entering the atmosphere, light from stars forms plane waves. However, inside the atmosphere the speed of light will vary as the inverse of the refractive index. Parts of the wavefront surface will enter in regions of higher refractive index and will be delayed compared to other parts of the wavefront through other regions, see Figure IV.2. It implies a deformation of the wavefront surface. The deformation is given by the optical path fluctuation δ:

$$\delta = \int n(z)\, dz\,, \tag{IV.5}$$

where n represents the refractive index fluctuation along the light propagation axis.
The phase φ, at the wavelength λ, can be expressed as:

$$\varphi = \frac{2\pi\delta}{\lambda}\,. \tag{IV.6}$$

To study the phase fluctuations between a point $\boldsymbol{r}$ of the telescope aperture and a nearby point at a separation $q = |\boldsymbol{q}|$, we estimate the phase structure function D_φ which represents the variance of the phase difference:

$$D_\varphi(\boldsymbol{q}) =< |\varphi(\boldsymbol{r}) - \varphi(\boldsymbol{r}+\boldsymbol{q})|^2 > \ . \tag{IV.7}$$

Using Eqs. (IV.3), (IV.5) and (IV.6), the previous equation can be rewritten as:

$$D_\varphi(\boldsymbol{q}) = 2.91\, k^2\, q^{5/3} \int C_n^2(z)\, dz\,, \tag{IV.8}$$

Table IV.1: Seven layer model of the *Observatorio del Roque de los Muchachos* turbulence variation. Table extracted from Devaney et al. (2002).

Altitude h (m)	500	1500	2500	7000	10000	15000	17000
C_n^2 ($\times 10^{-14}\,\mathrm{m}^{-2/3}$)	32	28.5	5.62	2.93	2.43	2.82	48.7
Normalized weighted C_n^2	0.2602	0.2317	0.0457	0.0238	0.0198	0.0229	0.3959

Figure IV.1: GTC dome in the *Observatorio del Roque de los Muchachos* (ORM) at La Palma island, Spain.

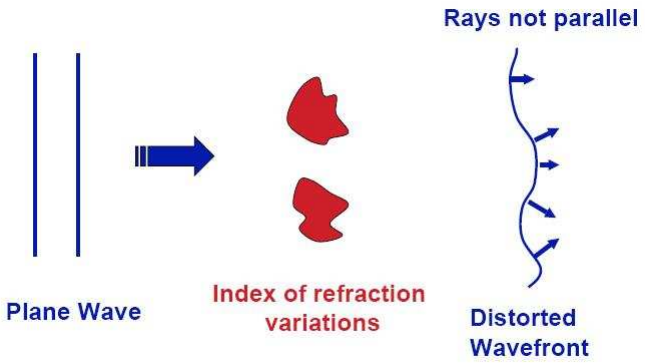

Figure IV.2: Illustration showing the distortion of initially plane wavefronts caused by air refractive index fluctuations. © Claire E. Max UCSC.

where k denotes the wave number ($k = 2\pi/\lambda$).
C_n^2 integral along the light propagation path gives a measure of the total amount of wavefront degradation or **seeing**. The atmosphere is generally considered to be stratified in plane parallel layers, therefore C_n^2 only depends on the height h above the ground. In this case, Eq. (IV.8) can be rewritten:

$$D_\varphi(\boldsymbol{q}) = 2.91\, k^2\, (\cos\gamma)^{-1} q^{5/3} \int C_n^2(h)\, dh\,, \tag{IV.9}$$

where γ represents the angular distance of the source from the zenith and $(\cos\gamma)^{-1}$ is called the air mass.
The Kolmogorov model of the turbulence distortions prescribes the specific form of the phase structure function:

$$D_\varphi(\boldsymbol{q}) = 6.88 \left(\frac{q}{r_0}\right)^{5/3}\,, \tag{IV.10}$$

with

$$r_0 = \left[0.423\, k^2\, (\cos\gamma)^{-1} \int C_n^2(h)\, dh\right]^{-3/5}\,. \tag{IV.11}$$

r_0 is a length called **Fried's parameter** (Fried, 1965) or coherence diameter. Inside a disk area of diameter r_0 within a wavefront, the optical phase distortion has a mean square value of 1 rad^2. The Fried's parameter gets smaller when turbulence is strong (large C_n^2). r_0 is usually given at $\lambda = 0.5\,\mu$m for reference purposes. Moreover, it has to be noticed that r_0 increases as the power 6/5 of the wavelength ($r_0 \propto \lambda^{6/5}$): r_0 gets bigger at longer wavelengths and therefore, AO is easier in the infrared than in the visible. Let us also note another important property: r_0 gets smaller quickly as telescope looks toward the horizon (larger zenith angle γ). At excellent observing sites such as Mauna Kea in Hawaii, r_0 is such as $15 < r_0 < 30\,$cm at $\lambda = 0.5\,\mu$m.

IV.2.4 Seeing

The Fried's parameter allows to define another important criteria: the **seeing**. The FWHM of an atmospheric PSF β or seeing is given by:

$$\beta = 0.98 \frac{\lambda}{r_0}\,. \tag{IV.12}$$

If we compare this expression with Eq. (IV.2), it can be noticed that in the presence of atmospheric turbulence, the FWHM given by a ground-based telescope of diameter D is equivalent to that of an ideal telescope of diameter r_0. Adaptive Optics systems aim to recover the resolution limit of an ideal telescope of diameter D. For a typical value $r_0 = 15\,$cm at $\lambda = 0.5\,\mu$m, we obtain a seeing value $\beta = 0.67$ arcsec.

IV.3 Adaptive Optics: review and simulations

IV.3.1 Principle of the Adaptive Optics

We briefly describe the basic and general scheme of **Adaptive Optics**, see Figure IV.3. A wavefront, coming from a **guide star** (either a natural guide star, NGS, or an artificial laser guide star, LGS) close to the science object, crosses several atmospheric layers before arriving into the telescope aperture and being analyzed by a **wavefront sensor** (WFS) which measures its aberrations. This information is sent to an algorithm control system which is going to generate the required shape of the **Deformable Mirror** (DM) to correct the wavefront errors. The WFS and the algorithm control system work in real time trying to obtain zero aberrations by continuously adjusting the DM shape. By this way, the science object wavefront is corrected by the DM thanks to the information obtained by the guide star wavefront. Figure IV.4 gives an example of images obtained before and after AO correction.
Our present study is focused on FRIDA, an instrument planned to work in concert with GTC and its AO system, namely GTCAO. Therefore, we will base us on GTCAO characteristics to simulate the AO corrected wavefronts that will be seen by FRIDA.

IV.3.2 Formation of the AO residual speckles

This part is devoted to the speckle formation in the image plane when we deal with the presence of atmospheric turbulence. First of all, the uncompensated image of a stellar point source is analyzed. Afterward, we will explain the effects of AO correction on the star image yielded by a telescope aperture of diameter D. Many descriptions of speckle formation can be found in the literature. Here, we mainly follow and summarize the explanation given by Racine et al. (1999).
Firstly, let us consider a circular patch of diameter r_0 within an atmospheric distorted wavefront coming from an observed star. Since r_0 denotes the coherence diameter, the beam derived from this sub-pupil generates a PSF of width $\sim \lambda/r_0$ imposed by the diffraction, in the image plane.
Secondly, if we consider two such patches separated by a distance $\sim D$, they can be seen as a two-beam interferometer. Therefore, we obtain a PSF of width $\sim \lambda/D$ and which intensity is modulated by a system of linear interference fringes. The movement of the fringe pattern within the PSF envelop results from the randomly varying phase difference between the two subapertures. Now, we extend the approach to three patches which are assumed to be non collinear. Thus, considering that there are three non redundant pairs of subpupils, three moving patterns of fringes are obtained in the image plane. It will carry out to the mix of these fringes in the telescope focal plane. Where constructive interferences occur, an enhanced bright speckle of width λ/D appears.
Finally, if we consider that the D-diameter pupil is filled with r_0-size subpupils, the interferences resulting from all the beams will produce the full speckle pattern. There is a room for $\kappa(D/r_0)^2$ adjacent speckles of size $\sim \lambda/D$ within the seeing disk of width $\sim \lambda/r_0$. Roddier (1981) and Roddier et al. (1982) show that when $D/r_0 \gg 1$ or $S \ll 1$, the filling factor κ has a value 0.342. Until now, we have contemplated the case of a short exposure integration time. If a long exposure integration time is considered, the speckle pattern will be time-averaged and a blurred star image of width $\sim \lambda/r_0$ will be obtained as we evoked previously, see Figure IV.4 middle frame.
The use of the AO correction leads to an enhancement of the original star diffraction pattern. In addition, this image will get closer to that obtained with a diffraction-limited system in the absence

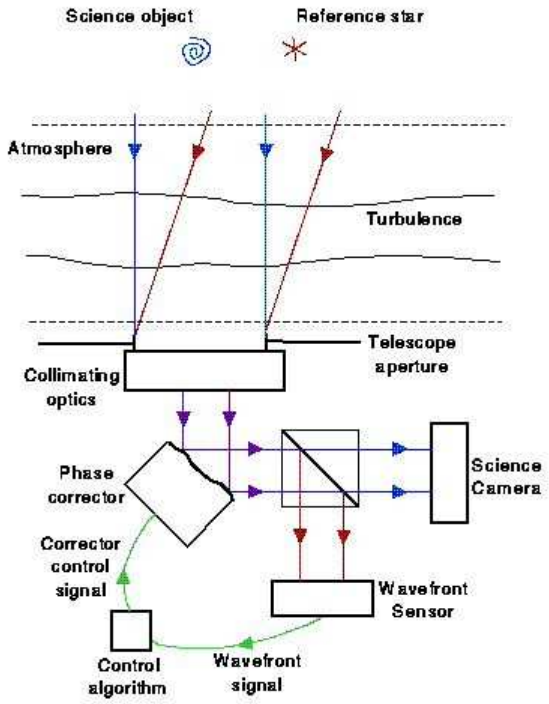

Figure IV.3: General scheme of an Adaptive Optics system. Extracted from the AO tutorial at CTIO, see: www.ctio.noao.edu/∼ atokovin/tutorial/intro.html, ©Imperial College.

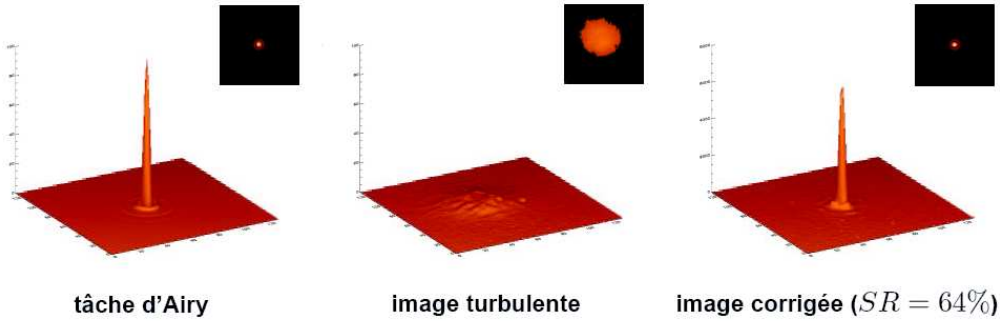

Figure IV.4: Impulse response of the Nasmyth Adaptive Optics System (NAOS) on the Very Large Telescope (VLT) for $r_0 = 1\,\mathrm{m}$, $D = 8\,\mathrm{m}$ and $\lambda = 2.2\,\mu\mathrm{m}$. **Left**: Airy diffraction pattern corresponding to the impulse response obtained with a clear circular aperture. **Middle**: Long exposure image obtained in the presence of atmospheric turbulence. **Right**: Correction of the previous image with the Adaptive Optics system. The achieved Strehl ratio is $S = 0.64$ in this case. ©ESO.

of aberrations. Indeed, the PSF central core and some of the first bright rings arise thanks to the AO compensation which increases the coherence (an effective increase in r_0), see Figure IV.4 right frame. This PSF contains a fraction S of the star luminous energy, where S denotes the Strehl ratio. The other part $1 - S$ is found within the speckles described before, namely here the AO residual speckles. Hence, by time-averaging, the final image formed in the telescope focal plane results in the sum of the PSF obtained with a diffraction-limited system and a smooth long-exposure halo due to the speckle pattern. These two contributions are respectively balanced with S and $1 - S$. Depending on the AO system efficiency and the Strehl ratio reached with the AO compensation, the Fraunhoffer diffraction pattern of an ideal telescope free of aberrations will be more or less recovered.

IV.3.3 GTCAO: current characteristics and performance

The Gran Telescopio Canarias is installed at ORM on La Palma island. The Fried's parameter is $r_0 = 15\,\mathrm{cm}$ at $\lambda = 0.5\,\mu\mathrm{m}$ and the wind velocity $v = 10\,\mathrm{m{\cdot}s^{-1}}$ for the standard seeing scenario.
GTCAO, the adaptive optics system of the GTC (Devaney et al., 2004), will offer high-order correction in the near-infrared while the tip-tilt correction will be provided by the secondary mirror of the GTC. The AO system will initially operate with a single deformable mirror conjugated to the GTC pupil. Moreover, GTCAO is planned to have a performance similar to the following deformable mirror geometry: 21 actuators placed across the long axis of the telescope pupil. In addition, the system will employ a Shack-Hartmann wavefront sensor.
"GTCAO+FRIDA" will be mounted on fixed positions at the Nasmyth station. However, they will not be attached to the GTC Nasmyth derotator. GTCAO will perform his own field derotation, therefore the GTC pupil image will rotate in the FRIDA pupil planes. In the following, the pupil masks are supposed circular in order to not introduce a pupil rotator.

IV.4 The CAOS software

IV.4.1 Presentation

The Code for Adaptive Optics Systems (CAOS, Fini et al., 2001; Carbillet et al., 2004, 2005) is properly said a Problem Solving Environment. Its original aim was to define and simulate as realistically as possible the behavior of a generic AO system, from the atmosphere propagation of light to the sensing of the wavefront aberrations and the correction through a deformable mirror. The different developments made these last years result in a very versatile numerical tool complete of a global graphical interface (The CAOS application builder) and different specialized scientific packages: the original one designed for AO system simulations (The Software Package CAOS), an image reconstruction package with interferometric capabilities (The Software Package AIRY) and a more recent one being built and dedicated to multi-conjugate AO (The software Package MAOS). In the following, we use the CAOS application builder and the Software Package CAOS. A screen capture is given in Figure IV.5. This tools allow to design an AO system with the proposed modules, generate the corresponding AO corrected wavefronts and predict the AO system performance.
Here, our goal consists in computing the AO compensated wavefronts performed by GTCAO and thereafter provided to FRIDA. Thus, it will be possible to quantify the contrast gain reached by

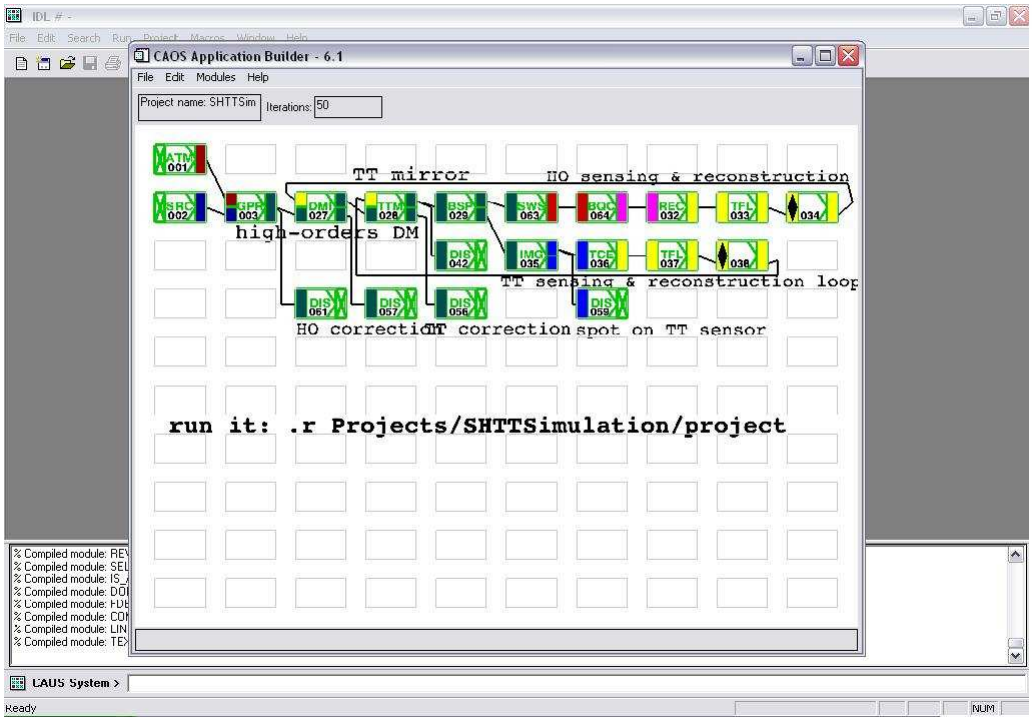

Figure IV.5: Screen capture of the CAOS operative system. This tool allows to account for the atmospheric turbulence characteristics and implement the Adaptive Optics system to correct them. Here, we can observe the graphic interface and the use of some modules. This configuration and the corresponding parameters will be adapted here to the GTCAO case.

suitable coronagraph configurations for FRIDA in the presence of AO compensated wavefronts. CAOS was provided by courtesy of Marcel Carbillet and can be downloaded from the following websites: http://www-luan.unice.fr/caos/ and http://lbtwww.arcetri.astro.it/CAOS/.

IV.4.2 Association CAOS+coronagraph simulator

In the previous chapters, we presented the tool developed to compute coronagraphic behaviors and the numerical results obtained with it. Our simulator allowed to estimate numerically the brightness attenuation reached by different coronagraph configurations for FRIDA. However, this study was done in the context of a diffraction-limited system and therefore, incoming wavefronts were assumed to be plane.
In the approach of a ground-based instrument, the imperfect AO correction causes residual artifacts within the compensated wavefronts. CAOS helps us to implement these more realistic wavefronts. By combining CAOS and our coronagraph simulator, we plan to characterize the coronagraph performance in the presence of wavefronts with residual errors. The contrast gains reachable with the suitable coronagraphs for FRIDA are quantified thereafter.

IV.4.3 Parameters of our simulations

In the present approach, we work with characteristics of an inscribed disk pupil inside the GTC pupil (diameter $D = 9.039\,\mathrm{m}$, central obstruction: 29%). Let us remind that the parameters of ORM are considered here: the standard seeing scenario gives a Fried parameter $r_0 = 15\,\mathrm{cm}$ at $\lambda = 0.5\,\mu\mathrm{m}$ (or equivalently a seeing $\beta \simeq 0.67$ arcsec) and a wind velocity $v = 10\,\mathrm{m{\cdot}s^{-1}}$. Two GTCAO configurations are modeled with the CAOS software and studied hereafter. In both cases, the wavefront sensor measurements are assumed to be perfect (ideal detector) and 200 independent AO corrected phase screens are generated.
First of all, we model the current GTCAO design with a number of actuators across the pupil diameter $N_{act} = 20$. We achieve Strehl ratios $S = 0.414$ and 0.603 at respectively $\lambda = 1.635\,\mu\mathrm{m}$ (H-band) and $2.200\,\mu\mathrm{m}$ (K-band). It corresponds respectively to residual wavefront variances $\sigma^2_\varphi = 0.881\ \mathrm{rad}^2$ and $0.506\ \mathrm{rad}^2$ based on the approximation $S \simeq \exp(-\sigma^2_\varphi)$ and valid for $S > 0.1$. These values are in good agreement with those expected for the current GTCAO system: $S = 0.415$ and $S = 0.610$ for a seeing $\beta = 0.65$ arcsec (Femenia et al., 2006). Simulation and contrast gain results are reported in section IV.5.1.
In addition, we consider a possible upgrade for GTCAO system with $N_{act} = 40$ instead of 20 for the deformable mirror. This allows us to predict the behavior of suitable coronagraphic devices for FRIDA in the presence of an improved AO system. We now achieve Strehl ratios $S = 0.813$ and 0.892 at respectively $\lambda = 1.635\,\mu\mathrm{m}$ and $2.200\,\mu\mathrm{m}$. Values of the reachable brightness attenuations are given in section IV.5.2
To avoid an accumulation of graphs, we only expose the numerical results achieved in K-band. Let us remind that AO performs better at larger wavelengths, what leads to a better correction of the incoming wavefronts for FRIDA in K-band rather than in H-band. Moreover, since FRIDA is planned to work in a cryogenic way, the radiative emission of its components in K-band is negligible.

IV.4.4 Operative mode

Let us describe the operative mode which allows to yield the numerical results reported hereafter. First of all, AO corrected wavefronts are implemented with CAOS accounting for the ORM site and GTCAO parameters. Thereafter, we save the corresponding phase screens into a file. Secondly, the archived file is opened and the wavefronts are inserted into the entrance pupil plane of the coronagraph simulator describing FRIDA optical assembly and equipped with a given coronagraph. For each phase screen, all the steps of the coronagraphic system are computed to obtain a coronagraphic PSF in the image plane. After realizing this operation for all the called phase screens, we sum and average the achieved coronagraphic images to reach a mean one. In the following, we report the azimuth averaged intensity and the azimuth standard deviation 5σ profiles derived from this mean coronagraphic image. The corresponding graphs are obtained for each coronagraphic configuration of our analysis.

IV.4.5 Profiles shoulders

In the following, it will be noticed that our profiles present a shoulder: at $\sim 5.5\,\lambda/D$ for $N_{act} = 20$ and $\sim 11\,\lambda/D$ for $N_{act} = 40$. They delimit the area of AO partial correction extending to the shoulder from the center of the image. Outside this plateau, AO correction does not improve the

image. Let us remind that the cutoff frequency of the AO filter cannot be higher than the spatial Nyquist frequency of the actuator spacing, $k_{AO} = N_{act}/2D$ (Sivaramakrishnan et al., 2001). At a given wavelength λ, this spacing corresponds to an angle $\theta_{AO} = N_{act}\lambda/2D$. Hence, $\theta_{AO} = 10\,\lambda/D$ for $N_{act} = 20$ and $\theta_{AO} = 20\,\lambda/D$. Several reasons can be advanced to explain the sharpness of the cutoff observed in our profiles: the DM actuator influence functions that extend the neighboring actuators' positions or an imperfect DM calibration can cause a reduction of the efficacy of the high spatial frequency wavefront correction.

IV.5 Simulations for a ground-based instrument equipped with a coronagraph

IV.5.1 Numerical results obtained for FRIDA with the current GTCAO

IV.5.1.1 Results obtained with CLC and CRC

Figure IV.6 gives on the top plot, the azimuth averaged intensity profiles reached with CLC or CRC and on the bottom plot, the 5σ detectability graphs for each one of these profiles. On the top plot, the profiles represent the AO corrected image, the CLC and CRC images. On the bottom plot, the 5σ value gives us an idea about the detectability of a faint substellar companion in the presence of residual speckles.
As seen in Figure IV.6 top plot, some intensity attenuations can be reached with CLC or CRC. With CLC and CRC, magnitude differences $\Delta m = 0.55$ and 0.49 can respectively be achieved at an angular separation 0.200 arcsec from the star (or equivalently, $4.0\,\lambda/D$ from the main optical axis). Moreover, a contrast gain $\Delta m = 1.26$ can also be reached at an angular distance 0.100 arcsec from the star (or equivalently $2.0\,\lambda/D$ from the main optical axis) with CRC. Table IV.2 summarizes the contrast gain results that can be obtained with CLC or CRC at different angular separations.

IV.5.1.2 Results obtained with APLC without Lyot stop and SLLC

Figure IV.7 is similar to Figure IV.6 but here, apodizers of APLC without Lyot stop and SLLC are the computed coronagraphs for the simulation. Let us remind that we do not simulate the presence of the opaque mask in FP2: since no Lyot stop is present in plane PP2, the spot will block starlight in FP2 and only residual light due to diffraction will be present in its re-imaged area in FP3, depending on the size of the geometric exit pupil in plane PP2.
As shown in Figure IV.7, some additional intensity attenuations can be reached with apodizer of APLC without Lyot stop. A magnitude difference $\Delta m = 0.38$ is quantified with apodizer of APLC without Lyot stop. This value is estimated at an angular separation 0.200 arcsec (or equivalently $4.0\,\lambda/D$ from the main optical axis). In the case of SLLC apodizer, we do not obtain brightness attenuation. This can be explained by the fact that SLLC apodizer profile, as well as that of APLC without Lyot stop, does not reach the halo profile of speckles as we expected. After several tests, we did not find the reasons of this behavior. The case is discussed at the end of the present chapter. Table IV.2 summarizes the numerical results reached with apodizers of APLC without Lyot stop or SLLC, at different angular separations.

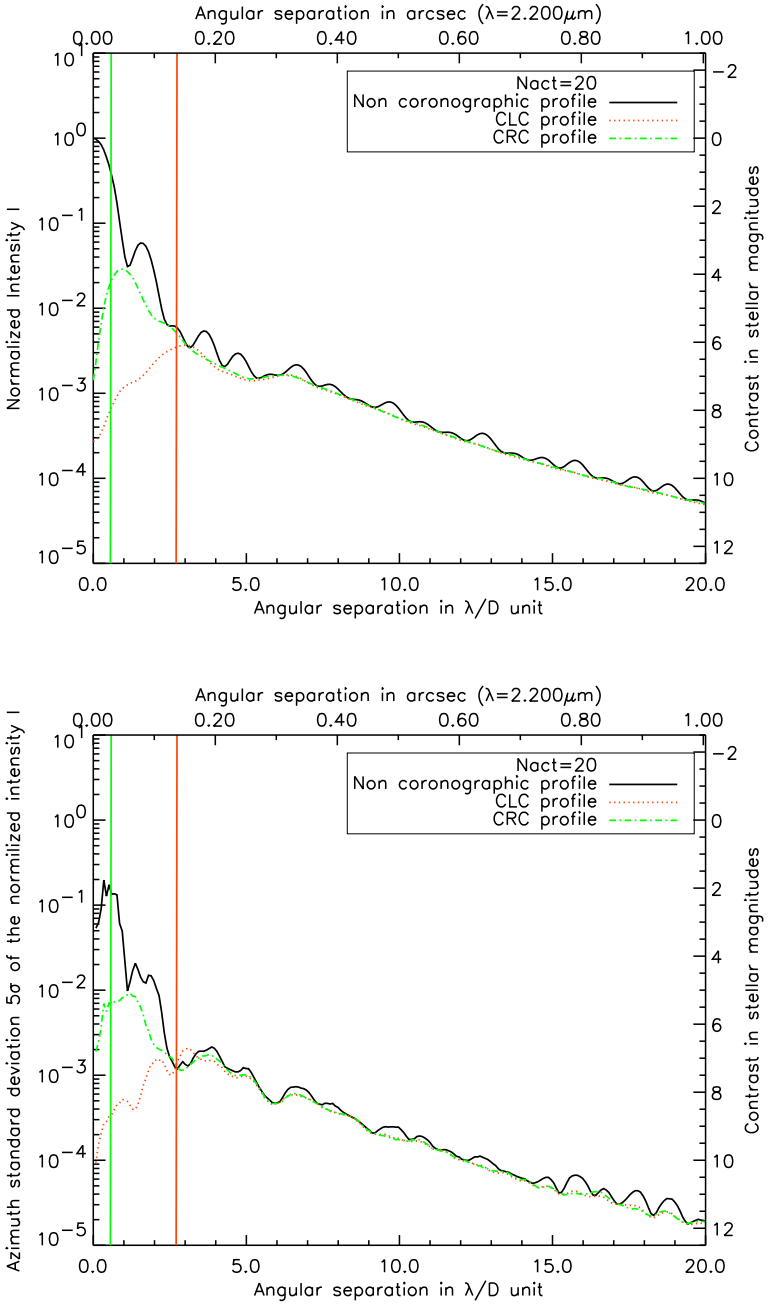

Figure IV.6: **Top**: Azimuth averaged profiles of the non coronagraphic PSF and images obtained with CLC and CRC, for a 29% centrally obstructed telescope (GTC case), in K-band ($\lambda = 2.200\,\mu$m) and for $N_{act} = 20$. **Bottom**: Profiles of the azimuth standard deviation 5σ of the normalized intensities I. Focal plane masks are delimited by a vertical line.

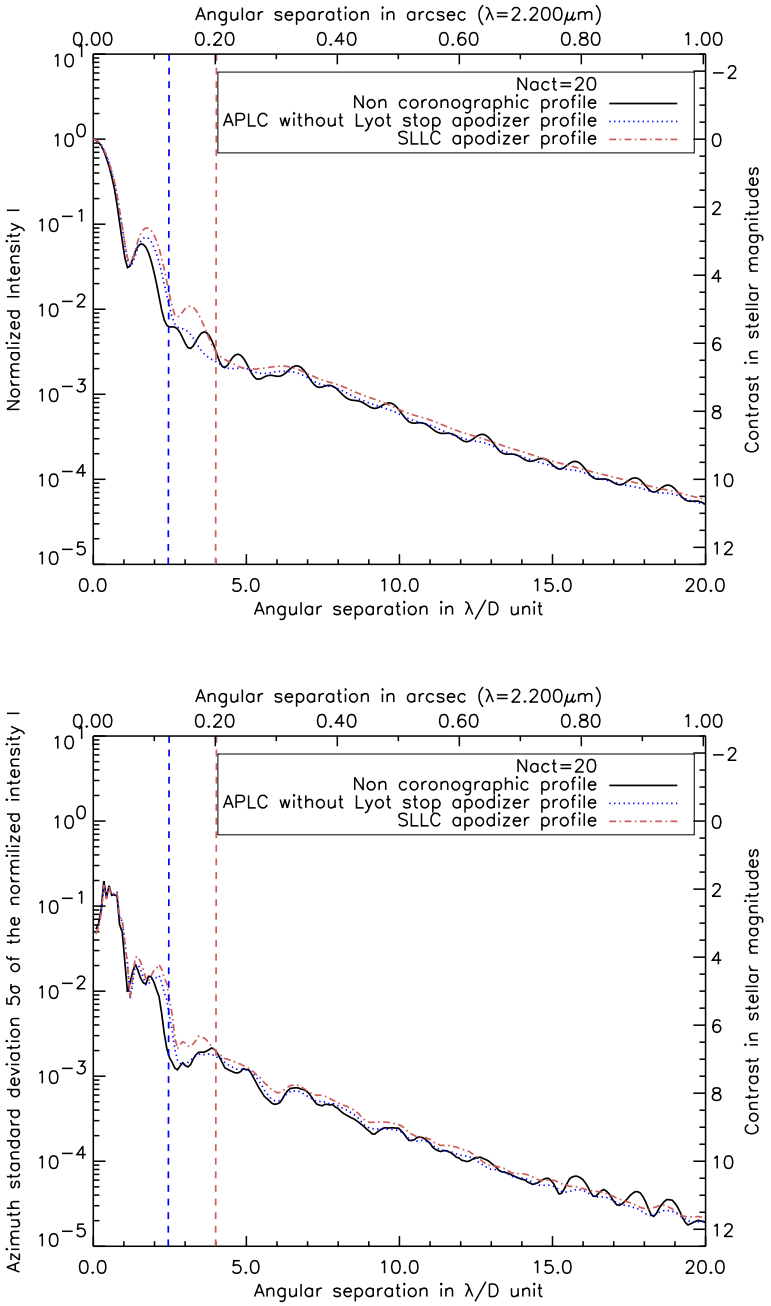

Figure IV.7: **Top**: Azimuth averaged profiles of the non coronagraphic PSF and images obtained with APLC without Lyot stop and SLLC, for a 29% centrally obstructed telescope (GTC case), in K-band ($\lambda = 2.200\,\mu$m) and for $N_{act} = 20$. **Bottom**: Profiles of the azimuth standard deviation 5σ of the normalized intensities I. Possible opaque masks are delimited by a dashed vertical line for use with apodizers of APLC working without Lyot stop and SLLC.

IV.5.2 Numerical results obtained for FRIDA with an improved GTCAO

IV.5.2.1 Results obtained with CLC and CRC

Figure IV.8 is similar to Figure IV.6 but here, we work with $N_{act} = 40$ instead of 20. Let us remind that we do not simulate the presence of the opaque mask in FP2: since no Lyot stop is present in plane PP2, the spot will block starlight in FP2 and only residual light due to diffraction will be present in its re-imaged area in FP3, depending on the size of the geometric exit pupil in plane PP2.
As seen in Figure IV.8 top plot, better intensity attenuations are reached with CLC or CRC, and $N_{act} = 40$ instead of 20. With CLC and CRC, magnitude differences $\Delta m = 1.32$ and 1.99 can respectively be achieved at an angular separation 0.200 arcsec (corresponding to $4.0\,\lambda/D$ from the main optical axis). In addition, a contrast gain $\Delta m = 3.18$ can also be reached at an angular distance 0.100 arcsec from the star (or equivalently $2.0\,\lambda/D$ from the main optical axis) with CRC. Table IV.3 summarizes the contrast gain results that can be obtained with CLC or CRC, for different angular separations. It can be noticed that the contrast gain values obtained with an improved GTCAO configuration are greater than those obtained when we consider the current GTCAO design.

IV.5.2.2 Results obtained with APLC without Lyot stop and SLLC

Figure IV.9 is similar to Figure IV.7 but here, we work with $N_{act} = 40$ instead of 20.
As shown in Figure IV.9, some additional intensity attenuations can be reached with apodizers of APLC without Lyot stop or SLLC. A magnitude difference $\Delta m = 0.65$ or 0.49 is quantified with the apodizers of respectively APLC without Lyot stop and SLLC. These values are estimated at an angular distance 0.301 arcsec from the star (or equivalently $6.0\,\lambda/D$ from the main optical axis). At larger separations, contrast gains provided by SLLC apodizer are better than those of apodizer of APLC without Lyot stop. However, we notice again that APLC without Lyot stop and SLLC apodizer profiles are slightly above that of the non coronagraphic image. We discuss the case at the end of the chapter.
Table IV.3 summarizes the contrast gain results that can be reached with the apodizers of APLC without Lyot stop or SLLC, at different angular separations. Here again, it can also be noticed that the contrast gain values obtained with an improved GTCAO configuration are greater than those obtained when we consider the current GTCAO design.

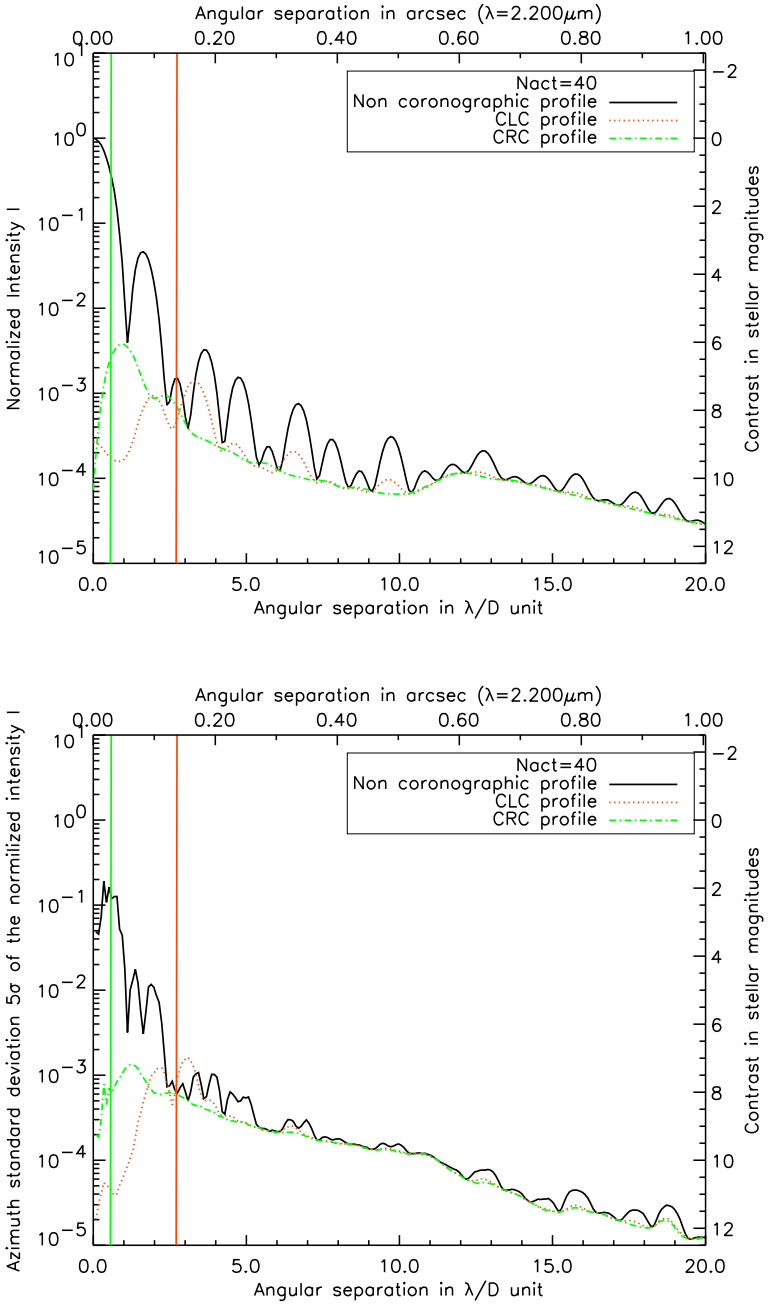

Figure IV.8: **Top**: Azimuth averaged profiles of the non coronagraphic PSF and images obtained with CLC and CRC, for a 29% centrally obstructed telescope (GTC case), in K-band ($\lambda = 2.200\,\mu$m) and for $N_{act} = 40$. **Bottom**: Profiles of the azimuth standard deviation 5σ of the normalized intensities I. Focal plane masks are delimited by a vertical line.

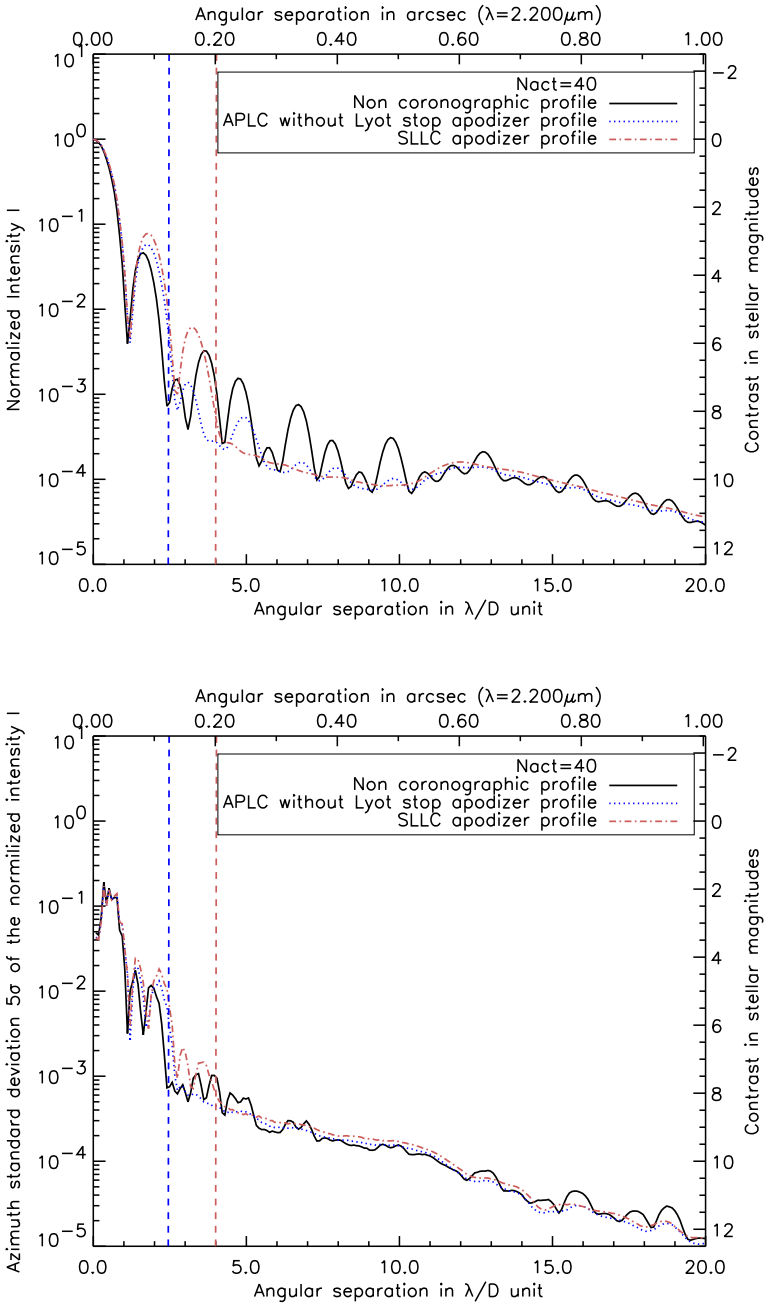

Figure IV.9: **Top**: Azimuth averaged profiles of the non coronagraphic PSF and images obtained with APLC without lyot stop and SLLC, for a 29% centrally obstructed telescope (GTC case), in K-band ($\lambda = 2.200\,\mu$m) and for $N_{act} = 40$. **Bottom**: Profiles of the azimuth standard deviation 5σ of the normalized intensities I. Possible opaque masks are delimited by a dashed vertical line for use with apodizers of APLC working without Lyot stop and SLLC.

Table IV.2: Contrast gain reached with different coronagraphic configurations and $N_{act} = 20$. Results are given here in K-band.

Coronagraph	**Contrast gain in stellar mag. Δm at an angular separation (in λ/D):**						
	2.0	4.0	6.0	8.0	10.0	12.0	20.0
CLC		0.55	0.10	0.13	0.23	0.10	0.06
CRC	1.26	0.49	0.07	0.11	0.23	0.08	0.04
APLC without Lyot stop apodizer		0.38	−0.07	−0.05	0.09	−0.01	−0.02
SLLC apodizer			−0.22	−0.18	−0.05	−0.17	−0.17

Table IV.3: Contrast gain reached with different coronagraphic configurations and $N_{act} = 40$. Results are given here in K-band.

Coronagraph	**Contrast gain in stellar mag. Δm at an angular separation (in λ/D):**						
	2.0	4.0	6.0	8.0	10.0	12.0	14.0
CLC		1.32	0.54	0.84	0.94	0.19	0.08
CRC	3.18	1.99	0.68	0.84	1.15	0.20	0.08
APLC without Lyot stop apodizer		1.86	0.65	0.47	0.81	−0.01	−0.09
SLLC apodizer			0.49	0.59	0.86	−0.15	−0.24

IV.5.3 Consistency of the results

IV.5.3.1 Tests based on statistics

Some basic tests are used to check the relevance of our results. According to the Rician statistics (Aime and Soummer, 2004), for one snapshot image (that means a unique realization of speckles), its azimuth averaged intensity profile is expected to be equal to that of its azimuth standard deviation: $\bar{I} = \sigma$.
In the case of a long-exposure image, simulated by averaging N independent realizations of image and assuming that there is no static aberrations, we expect to find the following relationship in the area in which speckles are prevailing:

$$\frac{\bar{I}}{\sigma} = \sqrt{N}\,. \tag{IV.13}$$

In addition, we can deduce the following assertions. On the one hand, in the area where the diffraction residuals prevail on speckles, $\bar{I}$ will be larger and therefore, $\bar{I}/\sigma > \sqrt{N}$. On the other hand, when the diffraction term is not dominant but large enough to provide a substantial amount of pinned speckles (a detailed description of these speckles is given in Chapter VI), the standard deviation σ will increase. However, since the azimuth averaged intensity of the pinned speckles is null, their contribution do not appear within $\bar{I}$ and thus, $\bar{I}/\sigma < \sqrt{N}$. These considerations allow to understand the shape of the 5σ detectability profiles and in particular, their curious lobes at the angular separations corresponding to bright diffraction rings in the image.
For all our simulations, we considered 200 independent realizations and therefore, we expect a ratio $\bar{I}/5\sigma \simeq 2.83$, which corresponds to a magnitude difference $\Delta m = 1.12$, at angular separations in which the speckles prevail the other contributions in the star image. This value represents the difference of magnitudes to observe between the profiles of the azimuth averaged intensity and standard deviation for a given long-exposure image and where the speckles are prevailing. A quick observation of Figures IV.6 to IV.9 allows to note that considering the profiles at $20\,\lambda/D$, the magnitude difference between $\bar{I}$ and 5σ seems to be ~ 1.
This first approximation allows to be optimistic about the relevance of our results. Let us check if our wavefronts are independent. Another test consists in evaluating the averaged value at a given point of the phase screens. Firstly, we choose randomly a point of our phase screens and check if the average value at this point is null. The test is repeated for two different points of our phase screens and the result given in Figure IV.10 top and bottom plot for respectively $N_{act} = 20$ and 40. For both points, we obtained a null average. Secondly, we generalized our test to all the points of our wavefronts. A mean wavefront is calculated from the 200 AO corrected screens and thereafter, its azimuth average is estimated to reach its radial profile, see Figure IV.11. A null average is obtained for this mean wavefront. Moreover, we compare the variance of this mean wavefront and the sum of the variances for each wavefront divided by N and an equality is obtained as expected. We can conclude about the independence of our wavefronts and be confident about the relevance of our results.

IV.5.3.2 Analysis of profiles with apodizer

In the graphs in which APLC without Lyot stop and SLLC apodizer behaviors are displayed, it can have been noticed that their profiles find out slightly above the non coronagraphic one. A

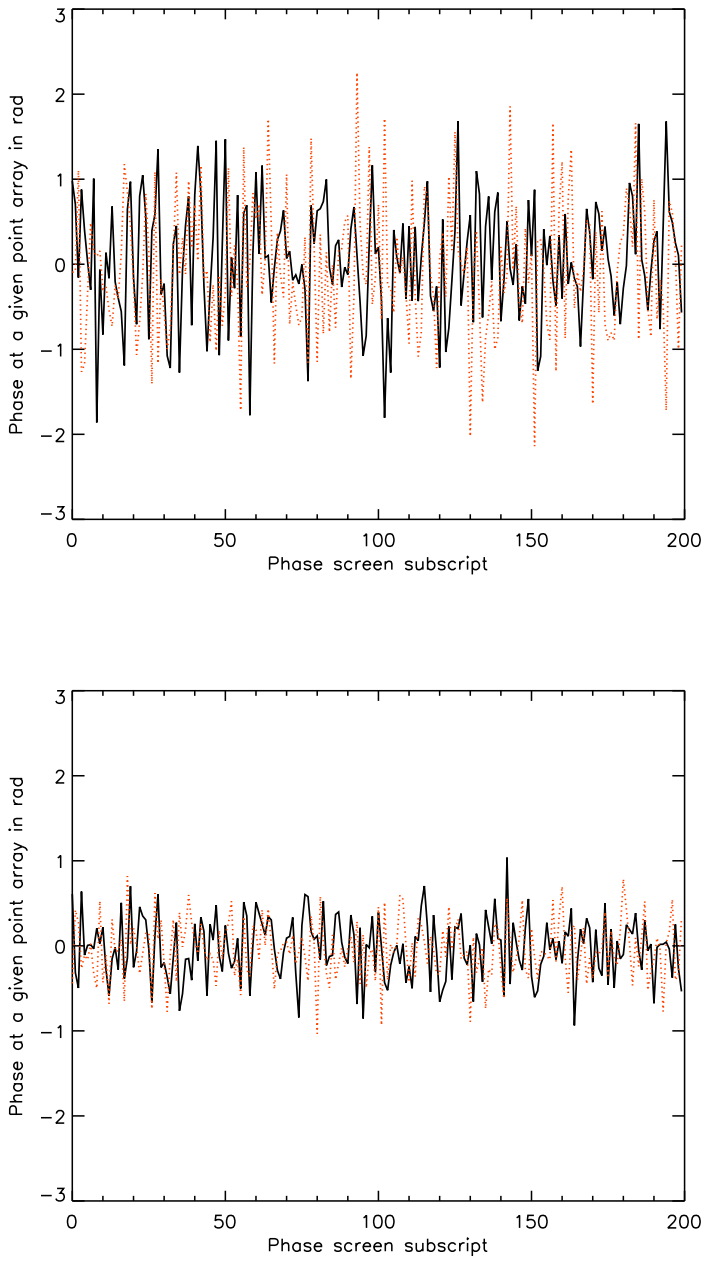

Figure IV.10: Phase profiles at a given point for two different points of our 200 AO corrected wavefronts in K-band ($\lambda = 2.200\,\mu$m). Profiles displayed for $N_{act} = 20$ and 40 in top and bottom plots respectively.

convergence of all our profiles to the speckle halo threshold was expected as in the case of CLC and CRC. The first reason that can be advanced to justify this curious result is an uncorrect normalization of the apodizer profiles. However, all these profiles are normalized to their respective intensity peak value, since no focal plane mask is considered here. Let us remind that an apodizer in the entrance pupil implies three main effects on the apodized PSF compared to a non coronagraphic PSF, in the following focal plane:
– a decrease of the intensity peak value of the apodized PSF
– an enlargement of the apodized PSF core
– a concentration of energy within the apodized PSF core.
The decrease of the intensity peak value of the apodized PSF cannot be observed in our curves; indeed, our profiles are normalized to their intensity peak value. On the opposite, the enlargement of the PSF core can be noticed in our represented profiles. The last point can be pointed out with a plot of the Encircled Energy profiles of the apodized and not apodized images.
Without normalization of our profiles, we no longer achieve the expected results since the halo of the apodized profile is far away from that of the non coronagraphic one. In a last test, we consider the normalization of our profiles with respect to their respective intensity peak value and divided them with the throughput value of the used apodizer. Within this approach, it can have been noted that all the profiles converge to the same speckle halo. However, the values at the centre are no longer equal to one for the apodized profiles. We did not succeed in determining if our apodizer profiles are correct or if we made a mistake in our simulations.

IV.5.4 Discussion about coronagraph usefulness for FRIDA

The numerical results have shown that a contrast gain can be reached in the presence of AO compensated wavefronts and whatever the used coronagraph. However, if we compare these results with those achieved in Chapter IV, we can notice a great difference of starlight attenuation. In the approach of a ground-based instrument, coronagraphs do not succeed in achieving contrast gains as good as those obtained in the case of a diffraction-limited system. This results from the limitation imposed by the residual speckles. Coronagraphs are restrained by the halo produced by the average of the speckles and therefore, cannot overcome this intensity threshold (Aime and Soummer, 2004). The coronagraphic efficiency depends on the intensity level of the halo. In our approach, we have showed that working with an improved GTCAO design rather than the current GTCAO design allows to increase the performance of all the suitable coronagraphs for FRIDA. Sivaramakrishnan et al. (2001) and Aime and Soummer (2004) show numerically and analytically respectively that the lower the halo (equivalently, the greater the Strehl ratio), the greater the coronagraphic efficiency. Hence, as they said, there is no use working with a very powerful coronagraph if the level of the halo created by the speckle average is too high. Our simulation results confirm their assertion with the difference that we yielded an end-to-end simulation of the complete GTCAO system with CAOS.
One can wonder therefore if there is a real interest in applying coronagraphy to a ground-based science instrument behind AO system. On the one hand, one of the main benefits of the coronagraph results in its ability to suppress the star PSF core and some first bright diffraction rings. In Figures IV.6 and IV.6 top plots, it can be noticed that CRC and CLC allow to reach at least a maximum rejection value of 10^2. The same comment is valid for APLC without Lyot stop and SLLC since an opaque mask can be used in the image plane and allow to avoid detector saturation. Hence,

risks of detector saturation are lower for instruments and in particular, FRIDA supplied with a coronagraph. It also carries out to an increase of the image dynamic range for these instruments and therefore FRIDA, if it is equipped with a coronagraph. On the other hand, the contrast gains in the search area are maybe small but not null. Consequently, they represent a first star brightness attenuation made with an optical processing technique. Since imaging an eventual faint substellar companion close to a bright star is extremely challenging, the PSF bright ring extinction yielded by coronagraphs constitutes above all a first encouraging star luminosity reduction. We have shown that with an improved AO system, it is possible to increase the contrast gain provided by a coronagraph for FRIDA.
These exposed points (PSF core suppression, intensity reduction of the first PSF bright rings) underline the usefulness of the coronagraph for a ground-based instrument in the presence of AO compensated wavefronts.

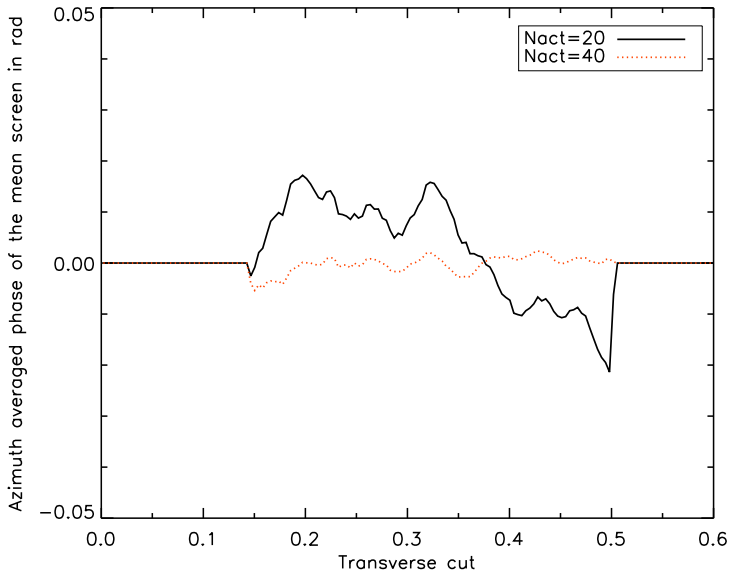

Figure IV.11: Azimuth averaged phase profiles of the mean wavefront in K-band ($\lambda = 2.200\,\mu$m) for $N_{act} = 20$ and 40.

IV.6 Conclusion of the forth chapter

In this chapter, we considered AO corrected wavefronts instead of perfect wavefronts. Under this approach, numerical results about the performance of different coronagraphs were exposed. To realize our simulations, the characteristics of the instrument "GTC+GTCAO+FRIDA" were involved using CAOS and our coronagraph simulator. We showed that coronagraphy is useful for a science instrument. Indeed, coronagraphic devices allow to increase the image dynamic range by eliminating the star PSF core and some first bright diffraction rings. The suppression of the PSF brightest components results in the avoidance of detector saturation. Furthermore, we quantified numerically the starlight attenuation provided by several coronagraph configurations (CLC, CRC, APLC without Lyot stop, SLLC) in the search area. From the analysis of these values, we concluded that coronagraphs perform a contrast increase in the regions of interest, it means where substellar mass companions could eventually be found and imaged.
However, the results we obtained also confirm that the combination "AO+Coronagraphy" will not be enough to produce high contrast images for FRIDA with the current GTCAO system. This assertion is true whatever the chosen coronagraph. Improving the GTCAO system allows FRIDA equipped with a coronagraph to reach better contrast gains but this remains insufficient to image faint substellar mass companions close to nearby bright stars. Removing the speckle noise is required to observe dim stellar objects.
To overcome the AO residual speckles, we propose to apply some additional post processing techniques to coronagraphic images in order to increase the image dynamic range of FRIDA. In the next chapter, we will estimate the starlight attenuation and analyze the results that could be yielded with the following association "AO+Coronagraphy+Post processing techniques" for FRIDA.

IV.6 Conclusión del cuarto capítulo

En este capítulo, se consideraron frentes de onda corregidos por AO en vez de frentes de onda perfectos. Con este nuevo enfoque, se expusieron los resultados numéricos del desempeño de los diferentes coronógrafos. Para realizar nuestras simulaciones, las características del instrumento "GTC+GTCAO+FRIDA" fueron introducidos usando CAOS y nuestro simulador de coronógrafo. Se mostró lo útil que podía ser la coronografía para un instrumento. De hecho, los dispositivos coronográficos permiten aumentar el intervalo dinámico de imagen ya que llevan a la eliminación del núcleo y de algunos de los primeros anillos brillantes de difracción de la PSF de una estrella observada. De tal forma, con la supresión de las componentes más brillantes de la PSF, se evita saturar el detector. Además, se cuantificó de manera numérica la atenuación de luz estelar alcanzada por varias configuraciones coronográficas (CLC, CRC, APLC sin diafragma de Lyot, SLLC) en la zona de búsqueda. Del análisis de estos valores, se llegó a la conclusión de que los coronógrafos ofrecían un cierto aumento de contraste en las regiones de interés, es decir en donde los compañeros de masa sub-estelar podrían estar para luego formar su imagen.
Sin embargo, los resultados que se obtuvieron confirman que la combinación "AO+Coronagrafía" no será suficiente para que FRIDA produzca imágenes de alto contraste con el sistema GTCAO actual. Esta afirmación es cierta sea cual sea el coronógrafo escogido. Con un mejoramiento del sistema GTCAO, se podrían alcanzar mejores ganancias en contraste pero no lo suficiente como

para formar imágenes de compañeros de baja luminosidad cerca de estrellas brillantes. Se requiere quitar el ruido de speckles para poder observar estos objetos estelares.
Para eliminar los speckles residuales de AO, se propone aplicar técnicas adicionales de post procesamiento a las imágenes coronográficas para aumentar el intervalo dinámico de imagen de FRIDA. En el próximo capítulo, se estimará la atenuación de luz estelar y se analyzarán los resultados que se pueden obtener con la asociación "AO+Coronografía+Técnicas de post procesamiento" para FRIDA.

IV.7 References

C. Aime and R. Soummer. The Usefulness and Limits of Coronagraphy in the Presence of Pinned Speckles. *ApJL*, 612, L85–L88, 2004.

M. Carbillet, C. Verinaud, M. Guarracino, L. Fini, O. Lardiere, B. Le Roux, A. T. Puglisi, B. Femenia, A. Riccardi, B. Anconelli, S. Correia, M. Bertero, and P. Boccacci. CAOS: a numerical simulation tool for astronomical adaptive optics (and beyond). In D. Bonaccini Calia, B. L. Ellerbroek, and R. Ragazzoni, editors, *Advancements in Adaptive Optics. Edited by Domenico B. Calia, Brent L. Ellerbroek, and Roberto Ragazzoni. Proceedings of the SPIE, Volume 5490, pp. 637-648 (2004).*, volume 5490 of *Presented at the Society of Photo-Optical Instrumentation Engineers (SPIE) Conference*, pages 637–648, 2004.

M. Carbillet, C. Vérinaud, B. Femenía, A. Riccardi, and L. Fini. Modelling astronomical adaptive optics - I. The software package CAOS. *MNRAS*, 356, 1263–1275, 2005.

N. Devaney, J. M. Rodriguez Espinosa, A. Cardwell, P. Hammersley, J. M. Filgueira, J. A. Marrero, and B. Femenia. GEN/OPTI/0077-L: Adaptive Optics for the GTC - Conceptual Design. GTC Project Office document, Gran Telescopio Canarias - Instituto de Astrofísica de Canarias, 2002.

N. Devaney, D. Bello, B. Femenia, J. Castro, A. Villegas Lopez, M. Reyes, and J. J. Fuensalida. Preliminary design and plans for the GTC adaptive optics system. In D. Bonaccini Calia, B. L. Ellerbroek, and R. Ragazzoni, editors, *Advancements in Adaptive Optics. Edited by Domenico B. Calia, Brent L. Ellerbroek, and Roberto Ragazzoni. Proceedings of the SPIE, Volume 5490, pp. 913-923 (2004).*, volume 5490 of *Presented at the Society of Photo-Optical Instrumentation Engineers (SPIE) Conference*, pages 913–923, 2004.

B. Femenia, D. Bello, P. Hammersley, J. Castro, and P. Alvarez. Adaptive Optics. GTCAO System Error Budgets RPT/OPTI/0252-R, Gran Telescopio Canarias, 2006.

L. Fini, M. Carbillet, and A. Riccardi. The CAOS Application Builder. In F. R. Harnden, Jr., F. A. Primini, and H. E. Payne, editors, *Astronomical Data Analysis Software and Systems X*, volume 238 of *Astronomical Society of the Pacific Conference Series*, pages 253–256, 2001.

D. L. Fried. Statistics of a Geometric Representation of Wavefront Distortion. *Journal of the Optical Society of America (1917-1983)*, 55, 1427–1435, 1965.

D. L. Fried. Atmospheric Turbulence Optical Effects: Understanding the Adaptive-Optics Implications. In *NATO ASIC Proc. 423: Adaptive Optics for Astronomy*, 1994.

R. Racine, G. A. H. Walker, D. Nadeau, R. Doyon, and C. Marois. Speckle Noise and the Detection of Faint Companions. *Public. of the Astron. Soc. Pac.*, 111, 587–594, 1999.

F. Roddier. The Effects of Atmospheric Turbulence in Optical Astronomy. *Prog. Optics, Volume 19, p. 281-376*, 19, 281–376, 1981.

F. Roddier. Optical Propagation and Image Formation Through the Turbulent Atmosphere. In D. M. Alloin and J.-M. Mariotti, editors, *NATO ASIC Proc. 274: Diffraction-Limited Imaging with Very Large Telescopes*, pages 33–52, 1989.

F. Roddier. *Adaptive optics in astronomy*. Adaptive Optics in Astronomy, Edition: François Roddier, Publisher: Cambridge, Cambridge University Press, 1999, ISBN: 0 521 55375 X, 1999a.

F. Roddier. *Imaging through the atmosphere*, pages 9–22. Adaptive Optics in Astronomy, Edition: François Roddier, Publisher: Cambridge, Cambridge University Press, 1999, ISBN: 0 521 55375 X, 1999b.

F. Roddier, J. M. Gilli, and G. Lund. On the origin of speckle boiling and its effects in stellar speckle interferometry. *Journal of Optics*, 13, 263–271, 1982.

A. Sivaramakrishnan, C. D. Koresko, R. B. Makidon, T. Berkefeld, and M. J. Kuchner. Ground-based Coronagraphy with High-order Adaptive Optics. *ApJ*, 552, 397–408, 2001.

R. K. Tyson. *Principles of adaptive optics*. Principles of adaptive optics, Edition: 2nd ed., Publisher: Boston, Academic Press, 1998, ISBN: 0127059024, 1998.

Chapter V

Post-processing methods for ground-based instruments equipped with a coronagraph

V.1 Introduction

V.1.1 Speckle noise limitation

To expect imaging close-in companions with a ground-based instrument (telescope + Adaptive Optics system + coronagraphy), residual speckles have to be removed first. The performance of a coronagraph is mainly limited by this noise source as shown in the previous chapter. In the context of a diffraction-limited system, coronagraphy can provide relevant starlight extinction results. However, when dealing with ground-based instruments, coronagraphs are restrained by the presence of residual speckles. A coronagraph allows to avoid detector saturation since it eliminates the star PSF core. Hence, it implies an increase of the image dynamic range. Unfortunately, the brightness attenuation of the PSF rings, also performed by this same coronagraph, is too weak to enhance faint substellar mass companions. Speckle noise prevents coronagraphs from increasing significantly the image contrast in the search area.

V.1.2 Post-processing methods

Additional image processing techniques are required to suppress the speckle halo and thus, maximize the achieved contrast. Reducing the speckle noise could allow to directly detect dim substellar mass companions with ground-based instruments.
Several techniques have already been suggested to overcome the speckles (e.g. Marois et al., 2000; Sparks and Ford, 2002; Guyon, 2004; Marois et al., 2006; Lafrenière et al., 2007) and prove to be very encouraging to solve this problem. In Section V.2, we briefly review the main post-processing methods. In our approach, we consider above all the AO residual speckles, indeed residuals due the non common instrumental path errors are weaker in comparison. Consequently, our following study is focused on two techniques: the removal of the azimuth symmetric component (Thatte et al., 2007) to go on increasing the coronagraphic image dynamic range and the Simultaneous Spectral

Differential Imaging (SSDI) method (Marois et al., 2000) which aims to eliminate the AO residual speckles. These image processing methods constitute some promising steps to reach our goal: the detection and characterization of eventual substellar mass companions present in the halo of an observed bright star. Furthermore, these computational techniques can be generalized and relied on more sophisticated methods proposed in the literature (e.g. Sparks and Ford, 2002).
Several science instruments offer the possibility of working in Integral Field Spectroscopy (IFS) mode, like SINFONI for the Very Large Telescope. FRIDA will soon belong to this category. In IFS mode, it will be possible to select images at the wanted wavelengths. The extracted frames can thereafter be combined numerically with differential imaging techniques. Here, we underline the interest of using the SSDI method for FRIDA (or other instruments) supplied with a coronagraph and working in IFS mode.

V.1.3 Numerical simulations, results and analysis

In Section V.3, computational results about post-processing methods are exposed. Halo free removal and SSDI techniques will be applied to coronagraphic images. We consider images obtained numerically with the suitable coronagraphs for FRIDA. Finally, in Section V.4, we discuss the contrast gain provided by the association "coronagraphy+azimuth symmetric component removal+SSDI technique". From a concrete case, an analysis will be carried out to determine the potential of this combination for FRIDA.

V.1 Introducción

V.1.1 limitación por el ruido de speckles

Para poder esperar formar imágenes de compañeros con un instrumento terrestre (telescopio + sistema de Óptica Adaptativa + coronografía), primero se deben eliminar los speckles residuales. El desempeño de un coronógrafo está limitado por esta fuente de ruido como se mostró en el capítulo anterior. En el contexto de un instrumento limitado por la difracción, la coronografía puede proveer resultados relevantes de extincción de luz estelar. Sin embargo, cuando se trata de instrumentos terrestres, los coronógrafos están limitados por la presencia de speckles residuales. Un coronógrafo permite evitar la saturación del detector ya que elimina el núcleo de la PSF de una estrella observada. Por lo tanto, eso implica un incremento del intervalo dinámico de imagen. Desgraciadamente, la atenuación de brillo de los anillos de la PSF, también efectuados por el mismo coronógrafo, es demasiado débil para re-alzar la imagen de los compañeros de masa sub-estelar. El ruido de speckle impide a los coronógrafos aumentar de manera significante el contraste de una imagen en el campo útil del coronógrafo.

V.1.2 métodos de post procesamiento

Se requieren técnicas adicionales de procesamiento de imagen para poder suprimir el halo formado por los speckles y maximizar el contraste alcanzado. Reducir el ruido de speckle podría permitir la detección de manera directa de compañeros de masa sub-estelar con telescopios terrestres.
En los recientes años, se han sugerido diferentes técnicas para superar los speckles (e.g. Marois et al., 2000; Sparks and Ford, 2002; Guyon, 2004; Marois et al., 2006; Lafrenière et al., 2007) y resultan todas muy prometedoras para resolver este problema. En la Sección V.2, se revisan brevemente los principales métodos de post procesamiento. En este enfoque, se consideran sobre todo los speckles residuales AO. Esto es porque los errores de corrección AO de frente de onda debidos a las aberraciones estáticas del instrumento científico son comparativamente más débiles. Por lo tanto, el estudio que sigue está enfocado en dos técnicas: el retiro de la componente simétrica azimutal (Thatte et al., 2007) para seguir aumentando el intervalo dinámico de la imagen coronográfica y el método de imagen diferencial espectral simultaneada (SSDI por sus siglas en inglés Marois et al., 2000) que tiene por objetivo la eliminación de los speckles residuales AO. Estos métodos de procesamiento de imagen constituye algunas etapas prometedoras para alcanzar nuestra meta: la detección y la caracterización de eventuales compañeros de masa sub-estelar presentes en el halo de una estrella brillante observada. Además, se pueden generalizar estas técnicas de computación y relacionar con métodos más sofisticados propuestos en la literatura (e.g. Sparks and Ford, 2002). Varios instrumentos ya ofrecen la posibilidad de trabajar en modo Espectroscopía Integral de Campo (IFS por sus siglas en inglés), como SINFONI para el *Very Large Telescope*. FRIDA pronto pertenecerá a esta categoría. En modo IFS, será posible seleccionar imágenes a las longitudes de onda deseadas. Se podrá luego combinar las imágenes extraídas con técnicas de imagen diferencial. Aquí, se subraya el interés de usar el método SSDI para FRIDA (o otros instrumentos) equipado con un coronógrafo y trabajando en modo IFS.

V.1.3 Simulaciones numéricas, resultados y análisis

En la Sección V.3, se exponen resultados computacionales acerca de los métodos de post procesamiento. Se aplicarán técnicas de eliminación de halo y SSDI a las imágenes coronográficas. Se considerarán las imágenes obtenidas de manera numérica con los coronógrafos factibles para FRIDA. Finalmente en la Sección V.4, se discute la ganancia a nivel de contraste proporcionada por la asociación "coronagrafía+eliminación de la componente azimutal simétrica+técnica SSDI". A partir de un caso concreto, se llevará a cabo un análisis para determinar el potencial de esta combinación para FRIDA.

V.2 Post-processing methods

V.2.1 Defeating the AO residual speckles

V.2.1.1 AO residual speckles

Ground-based telescopes require very efficient Adaptive Optics (AO) systems to correct wavefront errors due to atmospheric turbulence. Even with a downstream diffraction suppression system, the faint source detection for current 8–10 m class telescopes remains limited by residual speckles (Racine et al., 1999). These speckles are due to limitations in the AO correction system, corresponding to atmospheric turbulence residuals and non-common path instrumental aberrations. The atmospheric turbulence residuals are short-lived, with lifetime of a few to a few hundred milliseconds (Macintosh et al., 2005). For total exposures times of tens of minutes, these speckles average down to a smooth halo. Non-common path instrumental aberrations originate from the differential optical path between wavefront sensor and science channels. They result in a mixture of static and slowly varying speckles, with lifetimes comparable to the exposure time. The resulting image therefore consists of a smooth halo onto which is superimposed a residual speckle pattern.

V.2.1.2 Usefulness and limits of coronagraphy

The final results obtained in the previous chapter confirmed the limits of coronagraphs evoked by Racine et al. (1999), Sivaramakrishnan et al. (2001) or Aime and Soummer (2004), when they worked in presence of AO corrected wavefronts. Coronagraphs are restrained by the presence of residual speckles which prevent these devices from increasing significantly the contrast of images. Nevertheless, coronagraphy is useful to partially tackle some particular speckles, namely the pinned speckles. In the following lines, we explain how coronagraphy allows to reduce some of the speckles present within the diffraction pattern as shown previously by Aime and Soummer (2004).
For the sake of clarity, the coordinates are omitted. The notations follow those given in the first chapter and which are relied on the coronagraphic scheme (see Fig. I.11). We remind that $\hat{f}$ defines the Fourier transform of the function f and the intensity I_i of an image in plane i is the absolute square of the complex amplitude of the electromagnetic wave Ψ_i: $I_i = |\Psi_i|^2$. Let us consider the complex amplitude in the entrance pupil plane A:

$$\Psi_A = P e^{i\varphi}\,, \tag{V.1}$$

where P and φ denote respectively the real aperture illumination function and a residual phase term. P is considered null outside the aperture, furthermore, we assume a phase term $\varphi \ll 1$ rad. Bloemhof et al. (2001) developed a first-order theory of PSF structure for symmetric, clear aperture telescopes, Sivaramakrishnan et al. (2002) developed the complete second-order expansion of the PSF of a well-corrected image taken with an arbitrarily shaped and apodized pupil, and Perrin et al. (2003) developed a full expansion of the partially corrected PSF in an infinite Taylor-like series. Here, we decide to limit to a first-order expansion of the term $e^{i\varphi}$, hence a substitution of it by $1 + i\varphi$ into Eq. (V.1) gives:

$$\Psi_A = P(1 + i\varphi)\,. \tag{V.2}$$

In the following focal plane B, the field can be written as:

$$\Psi_B = \hat{P} + i\hat{P} \otimes \hat{\varphi}\,. \tag{V.3}$$

The phase term φ present in the pupil plane can be decomposed in its even and odd parts $\varphi_e + \varphi_o$, hence in the Fourier domain, we will obtain: $\hat{\varphi} = \hat{\varphi}_e + i\hat{\varphi}_o$. Using these developments, Eq. (V.3) can be re-ordered as follows:

$$\Psi_B = (\hat{P} - \hat{P} \otimes \hat{\varphi}_o) + i(\hat{P} \otimes \hat{\varphi}_e)\,. \tag{V.4}$$

Using Eq. (V.4) and introducing the variables $\hat{Q}_o = \hat{P} \otimes \hat{\varphi}_o$ and $\hat{Q}_e = \hat{P} \otimes \hat{\varphi}_e$, we write the intensity I_B as:

$$I_B = (\hat{P} - \hat{Q}_o)^2 + (\hat{Q}_e)^2\,, \tag{V.5}$$

which can be expanded as:

$$I_B = \hat{P}^2 - 2\hat{P} \cdot \hat{Q}_o + \hat{Q}_o^2 + \hat{Q}_e^2\,. \tag{V.6}$$

The first term $\hat{P}^2$ describes the Fraunhauffer diffraction pattern in the absence of aberrations. It would give an Airy diffraction pattern if a clear circular aperture with plane wavefronts emerging from it was considered. The other contributions represent the speckles. They can be split into two categories:
-those which are pinned to the rings of the diffraction pattern ($2\hat{P} \cdot \hat{Q}_o$), namely the **pinned speckles**,
-those which are more general ($\hat{Q}_o^2 + \hat{Q}_e^2$), that will be called here **higher order speckles**.
At this point, the introduction of a coronagraph is considered. We will distinguish two cases: first of all the ideal coronagraph and thereafter the non perfect coronagraph.

- Let us apply an **ideal coronagraph**, therefore, in the re-imaged pupil plane C, the corresponding complex amplitude Ψ_C can be written as:

$$\Psi_C = \Psi_A - P\,. \tag{V.7}$$

It can be noticed that the absence of aberrations in the entrance pupil plane ($\varphi = 0$) carries out to $\Psi_A = P$. Since an ideal coronagraph is used, it naturally leads to a complete extinction in the coronagraph exit pupil C, what means $\Psi_C = 0$. However in the present case, some residual phase terms are considered. Hence, substituting Eqs. (V.2) into (V.7) gives:

$$\Psi_C = iP\varphi\,, \tag{V.8}$$

and in the re-imaged focal plane D, the amplitude becomes:

$$\Psi_D = i\hat{Q}_e - \hat{Q}_o\,. \tag{V.9}$$

The coronagraphic intensity I_D is therefore given by:

$$I_D = \hat{Q}_o^2 + \hat{Q}_e^2\,. \tag{V.10}$$

A comparison between Eq. (V.6) and (V.10) allows to notice that the terms relied on diffraction pattern and pinned speckles were eliminated by the ideal coronagraph. Hence, coronagraphy allows to remove the diffraction pattern of a star, but also the pinned speckles when we work in the presence of phase errors in the entrance pupil plane.

- Now, let us consider a **non perfect coronagraph**. Hence, the complex amplitude Ψ_C will not be null in the absence of aberrations, but will be written as:

$$\Psi_C = \Psi_A - P(1-\xi)\,, \tag{V.11}$$

where $0 < \xi \leq 1$ ($\xi = 1$ means absence of coronagraph whereas $\xi = 0$ would correspond to the ideal coronagraph). Using Eq. (V.2), the last expression becomes:

$$\Psi_C = iP\varphi - \xi P\,. \tag{V.12}$$

Applying a Fourier transform to Eq. (V.12) and using the variables $\hat{Q}_o$ and $\hat{Q}_e$, the complex amplitude in the re-imaged focal plane D will be given by:

$$\Psi_D = -\xi\hat{P} + i\hat{Q}_e - \hat{Q}_o\,, \tag{V.13}$$

what carries out to the following expression of the coronagraphic intensity:

$$I_D = \xi^2\hat{P}^2 - 2\xi\hat{P}\cdot\hat{Q}_o + \hat{Q}_o^2 + \hat{Q}_e^2\,. \tag{V.14}$$

The terms corresponding to the diffraction pattern and the pinned speckles are respectively modulated by a factor ξ^2 and ξ. Hence, a non perfect coronagraph will decrease the intensity of the diffraction pattern but also of the pinned speckles when working in the presence of aberrations in the entrance pupil plane.

These remarks point out the role of the coronagraph in the presence of pinned speckles. This device allows to reduce these residuals. It eliminates them completely if the coronagraph is an ideal diffraction suppression system. A coronagraph helps to avoid detector saturation and increase the image dynamic range. However, it remains inefficient to eliminate the other sources of speckles. For the direct detection of faint substellar companions, additional methods to coronagraphy are required.

V.2.2 Image processing techniques

In the context of ground-based instruments, the use of just a coronagraph is not enough to expect imaging faint substellar mass companions close to nearby bright stars. A downstream method is required to remove the speckle noise and therefore, increase the image dynamic range. Image processing techniques represent very promising solutions to reduce this main noise source (Racine et al., 1999) and push back the limit for the direct detection of dim stellar objects. For instance, differential imaging methods were designed to allow ground-based instruments to reach the photon noise limit. In the following lines, we briefly review the techniques developed these past ten years. Thereafter, focus is made on the image processing methods we will compute numerically.

V.2.2.1 Brief review

Marois (2007) reviewed the techniques recently developed to attenuate the speckle noise. These post-processing algorithms aim to enhance the image of possible faint substellar mass companions drowned in the halo of a bright star PSF. Here, we propose to remind the principle of the main

speckle suppression methods: a brief summary is given for each one of them. A more complete description of these different specialized observation schemes can be found in the literature and papers mentioned hereafter.
The Simultaneous Spectral Differential Imaging (SSDI) method was first suggested by Racine et al. (1999) before being formally described and extended by Marois et al. (2000). This technique aims to reduce the AO residual speckles: it takes advantage of the chromaticity of the speckle location while keeping intact the image of the faint substellar mass companions. It consists in the combination of two or three images taken at the same time and close wavelengths. These simultaneous images are selected in and out of a deep absorption feature of the companion spectrum (e.g. CH_4 in H-band). After scaling and subtracting the images, it results in a removal of the residual starlight while leaving the companion light intact. A generalization of this technique to a larger spectral bandwidth was proposed by Sparks and Ford (2002) and after then improved by Thatte et al. (2007). Here, we consider the SSDI technique as a particular case of an algorithm proposed by Sparks and Ford (2002). SSDI formalism will be detailed in the following section since we decide to implement numerically this method.
The Angular Differential Imaging (ADI) method (Marois et al., 2006; Lafrenière et al., 2007) is a technique proposed to remove the quasi-static speckles. Several images are acquired at the same wavelength but with different field angles to subtract the quasi-static speckles. This technique is only limited by the quasi-static speckle time evolution. We will discuss the impact of the non common path instrumental aberrations in Section V.4.1.
On the other hand, Perrin et al. (2003) analyzed the structure of high Strehl ratio PSFs and pointed out the symmetries present within them. From their description, a strategy was suggested: taking advantage of a possible dominant symmetry within the speckle pattern to reduce this noise source. Indeed, at high Strehl ratios and with coronagraphy, some speckle symmetry is expected and hence, could be exploited to partially suppress the speckle noise. Consequently, the acquisition of an image and its combination with a π-rotated version of itself allows to reduce the symmetric terms of the speckle pattern. A similar idea based on halo symmetry was proposed by Thatte et al. (2007): it consists in removing the azimuth symmetric component of a PSF.
In the present work, we decide to focus on the removal of the PSF azimuth symmetric component and the SSDI method.

V.2.2.2 Removal of the azimuth symmetric component

A first image processing method can be computed before the application of the SSDI method. It consists in removing the azimuth symmetric component from the coronagraphic images (Thatte et al., 2007).
An azimuth average of a coronagraphic image is estimated to obtain a radial profile. Thereafter, this calculated component is extended azimuthally to obtain an image of the halo and subtract it from the coronagraphic image. This operation allows to provide a halo free coronagraphic image and reach a first contrast gain. The halo free coronagraphic profile is simply obtained by azimuthally averaging the intensity of the halo free coronagraphic image.
Figures V.1 and V.2 illustrate the application of this concept. In these examples, after eliminating the azimuth symmetric component, a suppression of the residual PSF core and bright rings can be noted. Subtraction of the halo results in a decrease of the PSF brightness and a gain in contrast.

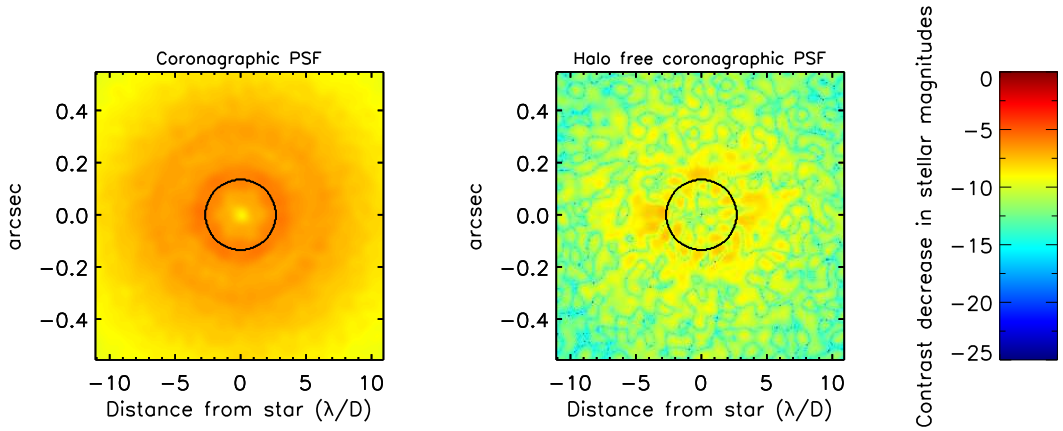

Figure V.1: Illustration of the azimuth symmetric component removal application. Here, the technique is computed numerically to a coronagraphic image obtained with CLC. Images are normalized with the intensity peak of the non coronagraphic PSF. Left and right images represent the coronagraphic image respectively before and after the use of the processing method. A brightness difference can be observed between the two images. The Lyot opaque mask of radius $r = 2.69\,\lambda/D$ is delimited by a black circle.

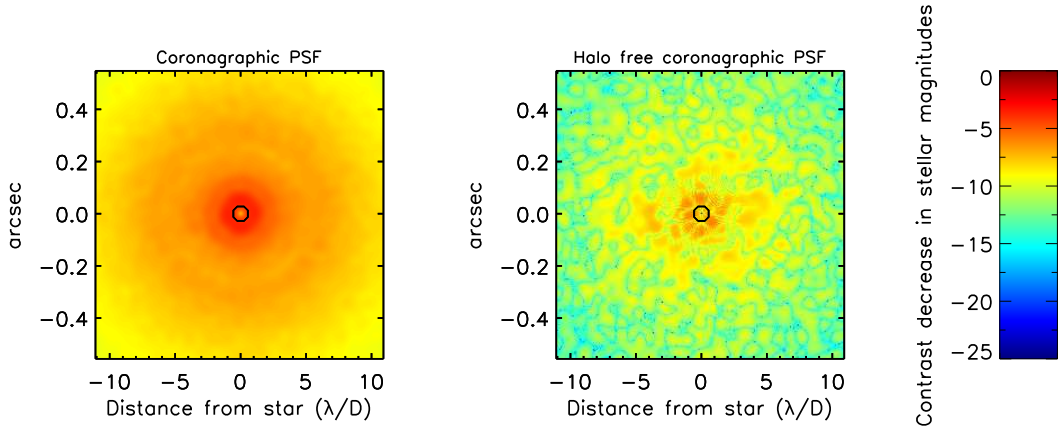

Figure V.2: Same as Figure V.1 but here CLC is replaced by CRC. The R&R phase mask of radius $r = 0.60\,\lambda/D$ is delimited by a black circle.

V.2.2.3 SSDI method: presentation of the formalism

The SSDI method (Marois et al., 2000) aims to overcome AO residual speckles and enhance the companion image. It consists in the combination of two or three images taken at the same time and three close wavelengths. These simultaneous images are taken in and out of a deep absorption feature of the companion spectrum (e.g. CH_4 in H-band). After scaling and subtracting the images, it results in a removal of the residual starlight while leaving the companion light intact.
Here, we briefly review the formalism given by Marois et al. (2000). Let us name I_1, I_2 and I_3 the three halo free coronagraphic images at λ_1, λ_2 and λ_3 in the coronagraphic focal plane D, rescaled and resized with respect to the wavelength. The simple differential imaging (SDI) can be expressed by:

$$d_{12} = I_1 - I_2\,, \tag{V.15}$$

and the double differential imaging (DDI) can be written as:

$$dd = (I_1 - I_2) - k_I \times (I_1 - I_3)\,. \tag{V.16}$$

Marois et al. (2000) explain that the constant factor k_I which applies to each pixel of d_{13} is the mean ratio of d_{12}/d_{13}. The global trend in the evolution of the PSF will, on the average, obey a same $\Delta I/I$ relationship at all radii. This global trend will be completely removed by the double difference when

$$k_I = \frac{S_1 - S_2}{S_1 - S_3}\,, \tag{V.17}$$

where S_i denotes the Strehl ratio of the image I_i. A schematic representation of the SSDI method is given in Figure V.3.
Marois et al. (2000) also show that the theoretical attenuation $\mathcal{A}_{SDI}$ reachable with SDI technique can be expressed as follows:

$$\mathcal{A}_{SDI} \sim (2\,\sigma_\varphi^2\,\Delta\lambda/\lambda)^{-1}\,, \tag{V.18}$$

where $\Delta\lambda$ denotes the bandpass separation between two successive wavelengths. In the case of the DDI approach, Marois et al. (2000) demonstrate with a crude estimate of $\Delta^2 I/I$ that the attenuation $\mathcal{A}_{DDI}$ is given by:

$$\mathcal{A}_{DDI} \sim \mathcal{A}_{SDI}^2\,. \tag{V.19}$$

It can be noticed that these attenuation expressions slightly differ from those given by Marois et al. (2000), since we decide to be homogeneous with the criteria definition given by Abe (2004).
In the following, the attenuation values are obtained estimating the azimuth averaged intensity over an annulus of width $1.0\,\lambda/D$ centered around a given angular distance from the main optical axis.

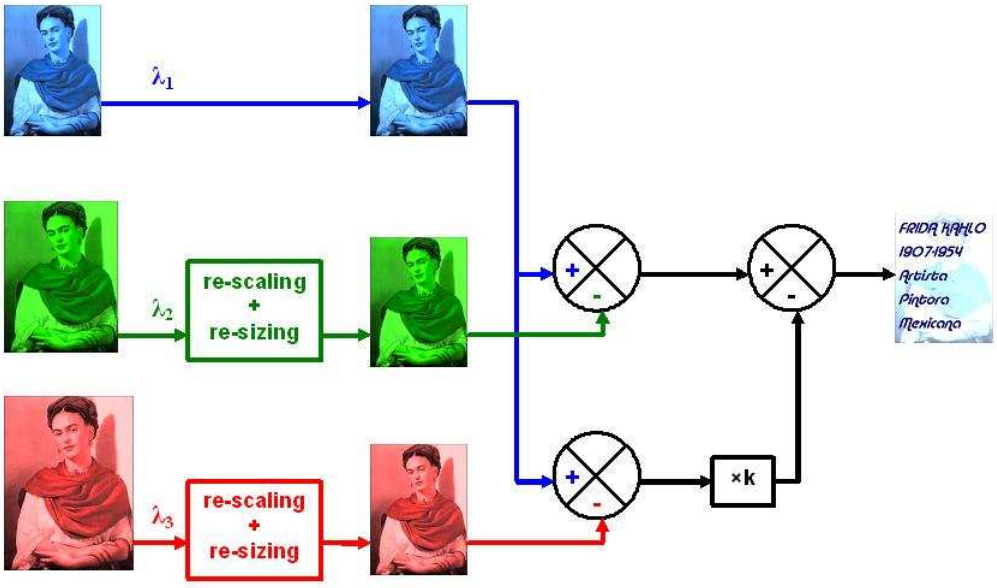

Figure V.3: Simplified representation of the SSDI method.

V.2.3 Feasibility of these techniques with FRIDA

V.2.3.1 Data cube provided by FRIDA in IFS mode

FRIDA should be able to provide a data cube of images when it works in IFS mode. In the following, we briefly review the IFS technique using an image slicer as it does in the case of FRIDA, see Figure V.4. An area of the AO corrected image is first selected. This new image is thereafter divided into several slices thanks to the image slicer. The obtained slices are then re-ordered linearly thanks to optical devices before going through a pseudo-slit. Thus, the light coming from this slit is sent to the spectrograph to be analyzed. Hence, each image slice will provide a spectrum and this will carry out to a spectrogram at the spectrograph output detector with the spectra obtained for all the image slices. Spectral images are finally reconstructed at each wavelength and the achieved set of frames constitutes an image data cube presenting two spatial and one spectral components.
Thanks to its Integral Field Unit spectrograph, FRIDA should give several simultaneous and wide field images of the observed stellar object at different wavelengths. Several image processing could be applied to extract new astronomical data about the images. In particular, extracting three images at different wavelengths from the FRIDA data cube will be possible.

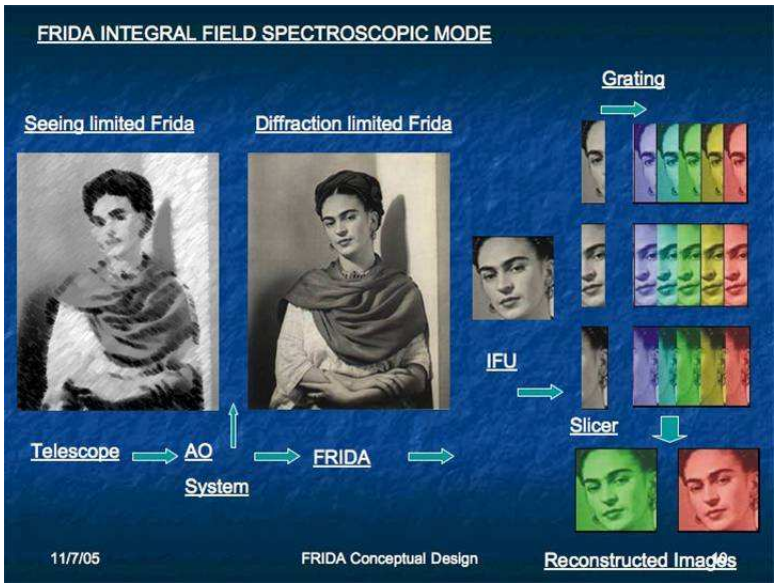

Figure V.4: Illustration of the FRIDA Integral Field Spectroscopy mode working with image slicer.

V.2.3.2 Possible use of the post-processing techniques with FRIDA

Therefore, applying azimuth symmetric component removal and SSDI methods with FRIDA is something perfectly reachable and realistic. It raises hope for imaging of high contrast with FRIDA. The idea is to obtain three simultaneous coronagraphic images, at different but close wavelengths and with a given coronagraph. The next step consists in combining them with the evoked post-processing techniques. In the following section, we present the simulation results obtained in this configuration.

V.3 Numerical results

V.3.1 Working hypothesis

The strategy is the following: we first remove the azimuth symmetric component from the coronagraphic images and after then we compute the SSDI technique with the obtained halo free coronagraphic images. The present approach is applied considering the characteristics of "GTC+GTCAO+ FRIDA equipped with a coronagraph" . However, we limit our study to two coronagraphic configurations for FRIDA: CLC and CRC.
We make the following assumption: FRIDA is supplied with a coronagraph and works in IFS mode. FRIDA should provide a data cube of images at several wavelengths and it will be possible to select those of our interest. Furthermore, FRIDA is supposed to work in its low spectral resolution mode ($R \sim 1500$) in K-band. Three coronagraphic images are extracted from the FRIDA data cube in and out of one companion absorption feature, at the respective wavelengths $\lambda_1 = 2.2000\,\mu$m (feature of the target's object spectrum), $\lambda_2 = 2.2015\,\mu$m and $\lambda_3 = 2.2030\,\mu$m. Thereafter, halo is removed from each of the coronagraphic frames.
The Strehl ratio values S_1, S_2 and S_3 of the images are respectively: 0.603132, 0.603540 and 0.603948, considering the AO compensated wavefronts provided by the current GTCAO design. They were calculated using the following approximation $S \simeq \exp(-\sigma_\varphi^2)$ valid for $S > 0.1$ and therefore, we obtain $k_I = 0.5$. Mean attenuations $\mathcal{A}_{SDI} = 1.26 \cdot 10^3$ and $\mathcal{A}_{DDI} = 1.59 \cdot 10^6$ are expected, what corresponds respectively to contrast gains in stellar magnitudes $\Delta m = 7.75$ and 15.51.

V.3.2 Results obtained with CLC

V.3.2.1 Analysis of the results

Figure V.5 gives on the top plot, the azimuth averaged intensity profiles reached after each step and on the bottom plot, the 5σ detectability graphs for each one of these profiles. On the top plot, the profiles represent successively from the top: the AO corrected image, the CLC images before and after removal of the azimuth symmetric component, and the halo free CLC images after application of SDI or DDI technique. On the bottom plot, the 5σ value gives us an idea about the detectability of a faint substellar mass companion in the presence of residual speckles. The different images are displayed in Figure V.6.
As seen in Figure V.5 top plot, some additional intensity attenuations can be reached after SDI or DDI application about halo free CLC images. With CLC and the post-processing techniques, magnitude differences $\Delta m = 8.99$ (with SDI) or 14.65 (with DDI) can be achieved at 0.200 arcsec from the star (or equivalently $4.0\,\lambda/D$ from the main optical axis). Table V.1 summarizes the contrast gain results that can be obtained with CLC associated with image processing techniques, for different angular separations.
At $4\,\lambda/D$ from the main optical axis, the contrast gains provided by SDI and DDI are respectively 5.61 and 11.64 stellar magnitudes. At larger separations, for instance $14\,\lambda/D$, these values down to 4.01 and 8.35 stellar magnitudes. The achieved results are slightly lower than the theoretical predictions (7.75 and 15.51 stellar magnitudes), essentially at very small angular separations. However, these attenuations are large enough to expect reaching the photon noise.

V.3.2.2 Discussion

CLC associated with post-processing methods represents a promising solution for ground-based instruments to do high contrast imaging. The characterization of faint substellar mass companions could also be done if we work with a not too large spectral bandwidth. Indeed, the Lyot opaque mask is size-chromatic. Hence, the coronagraphic PSFs slightly differ for each wavelength of work. This can explain why we do not achieve the theoretical contrast gains with SDI or DDI. This stress can represent a limit if we want to extend this combination of techniques to all the data cube. Further studies are required to analyze the size chromatism effect of the opaque mask and its impact when we want to rescale and resize all the frames of an IFS data cube, as suggested by Sparks and Ford (2002) or Thatte et al. (2007).

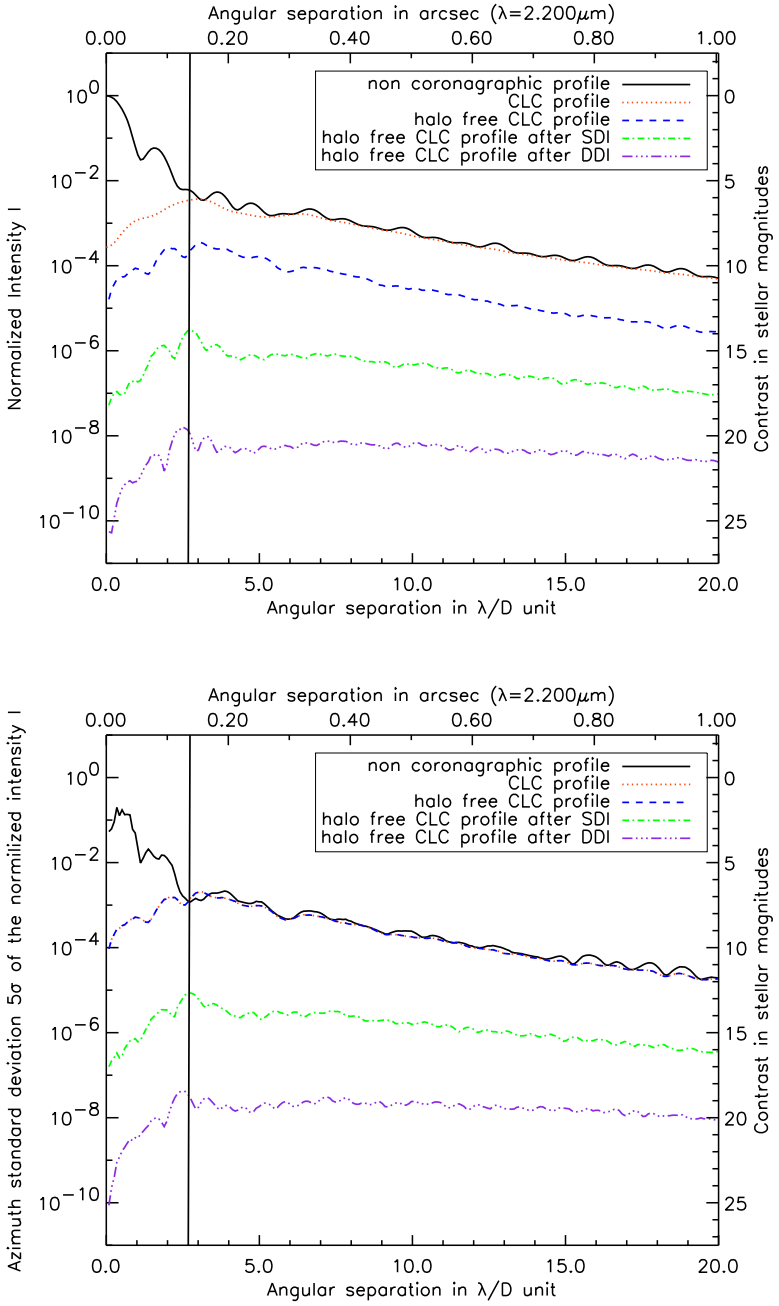

Figure V.5: Top: Azimuth averaged profiles of the non coronagraphic PSF and images obtained with CLC and different image processing techniques, for a 29% centrally obstructed telescope (GTC case), in K-band. **Bottom**: Profiles of the azimuth standard deviation 5σ of the normalized intensities I. The opaque mask of radius $2.69\,\lambda/D$ is delimited by a vertical line.

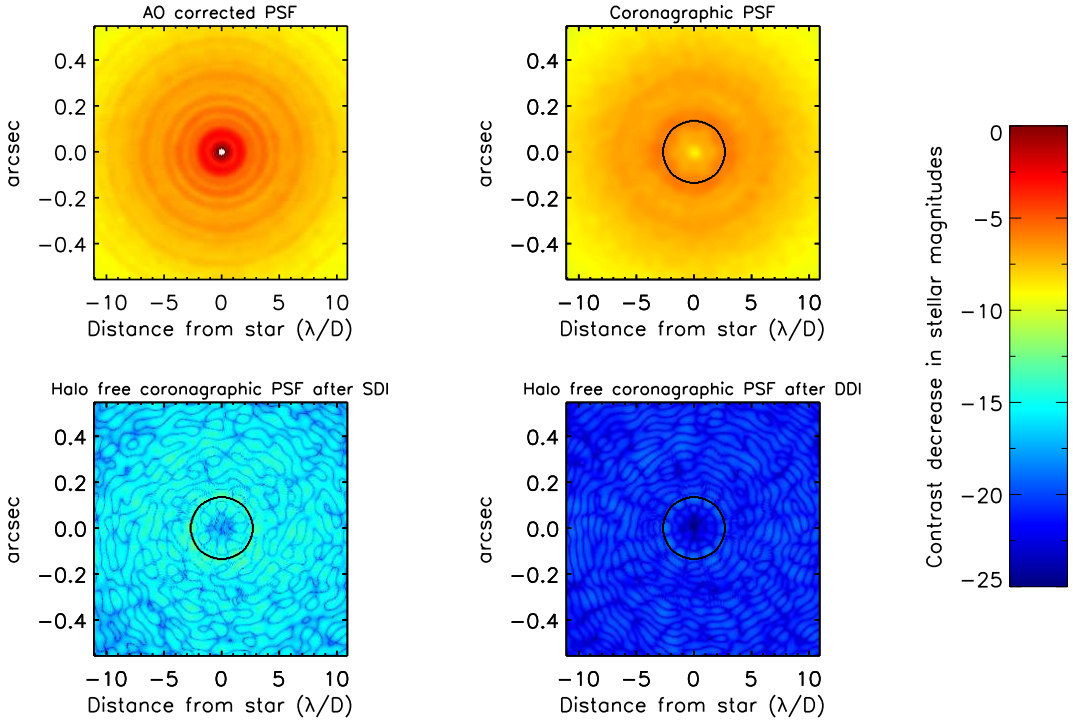

Figure V.6: Illustration of the azimuth symmetric component removal+SSDI method application on coronagraphic images. Here, the technique is computed numerically to halo free coronagraphic images obtained with CLC. On the top, left and right images represent the coronagraphic image respectively before and after the use of the halo free removal method. On the bottom, left and right images represent the halo free coronagraphic image respectively after SDI or DDI method. A brightness difference can be observed after each operation. The Lyot opaque mask of radius $r = 2.69\,\lambda/D$ is delimited by a black circle.

Table V.1: Contrast gain reached with CLC configuration and additional image processing techniques for FRIDA.

Profile	**Contrast gain in stellar mag. Δm at an angular separation (in λ/D):**					
	4.0	6.0	8.0	10.0	12.0	14.0
CLC profile	0.55	0.10	0.13	0.23	0.10	0.06
Halo free CLC profile	3.01	3.30	3.17	3.35	3.17	3.21
Halo free CLC profile after SDI	8.99	8.37	7.97	7.80	7.49	7.22
Halo free CLC profile after DDI	14.65	13.70	13.00	12.53	12.02	11.56

V.3.3 Results obtained with CRC

V.3.3.1 Analysis of the results

Figure V.7 reproduces the same scheme than Figure V.5, but with the difference that CLC is replaced by CRC. The different images are displayed in Figure V.8.
Figure V.7 top plot confirms that some additional intensity attenuations can be reached after SDI or DDI application about halo free CRC images. A contrast gain $\Delta m = 10.39$ (with SDI) or 16.47 (with DDI) can be achieved with the combination "CRC+azimuth symmetric component removal+SSDI method". These values are obtained at the angular distance of 0.100 arcsec from the star (or equivalently $2.0\,\lambda/D$ from the main optical axis). Table V.2 summarizes the brightness attenuations that can be reached with CRC associated with image processing techniques, for different angular separations.
At $2\,\lambda/D$ from the main optical axis, the contrast gains provided by SDI and DDI are respectively 5.97 and 12.05 stellar magnitudes. At larger separations, for instance $14\,\lambda/D$, these values down to 4.01 and 8.35 stellar magnitudes. The achieved results are again slightly lower than the theoretical predictions (7.75 and 15.51 stellar magnitudes). However, these attenuations are enough to reach the photon noise.

V.3.3.2 Discussion

Due to its small size ($r = 0.60\,\lambda/D$), the Roddier & Roddier phase mask (RRPM) is the only spot of our study which allows observation very close to the parent star (angular separation $2\,\lambda/D$). Its association with other image processing techniques results in a very interesting contrast gain at very small angular distances from an observed host star. This combination seems to be the best option for FRIDA to achieve high contrast imaging at small angular separations.
However, on the one hand, its fabrication is a technical challenge to overcome: at $\lambda = 2.200\,\mu$m and since GTC focal ratio presents an average value $f/17$, the mask diameter is about $44.9\,\mu$m. A quick comparison with the spot size of our experiment (about $70\,\mu$m) allows to underline that the required RRPM diameter for FRIDA is equal to about 2/3 of that of our experiment. We have to demonstrate that it is possible to manufacture a $44.9\,\mu$m diameter RRPM with the available technology. However, recent developments and improvements about the RRPM fabrication allows to be optimistic about the ability to build smaller masks.
On the other hand, the RRPM presents a double dependence in chromaticity. For SSDI method, only three CRC images at very close wavelengths were involved in the process. In FRIDA IFS mode, it will be possible to work with the complete data cube. Hence, if we want to work with a set of coronagraphic images spanning the H+K-bands, an achromatic phase mask is required to minimize the attenuation differences between all the coronagraphic frames. In the first chapter, we reviewed several techniques proposed these past few years. The ability of FRIDA to image and characterize eventual substellar mass companions over large spectral bands will depend on the development of these new concepts.

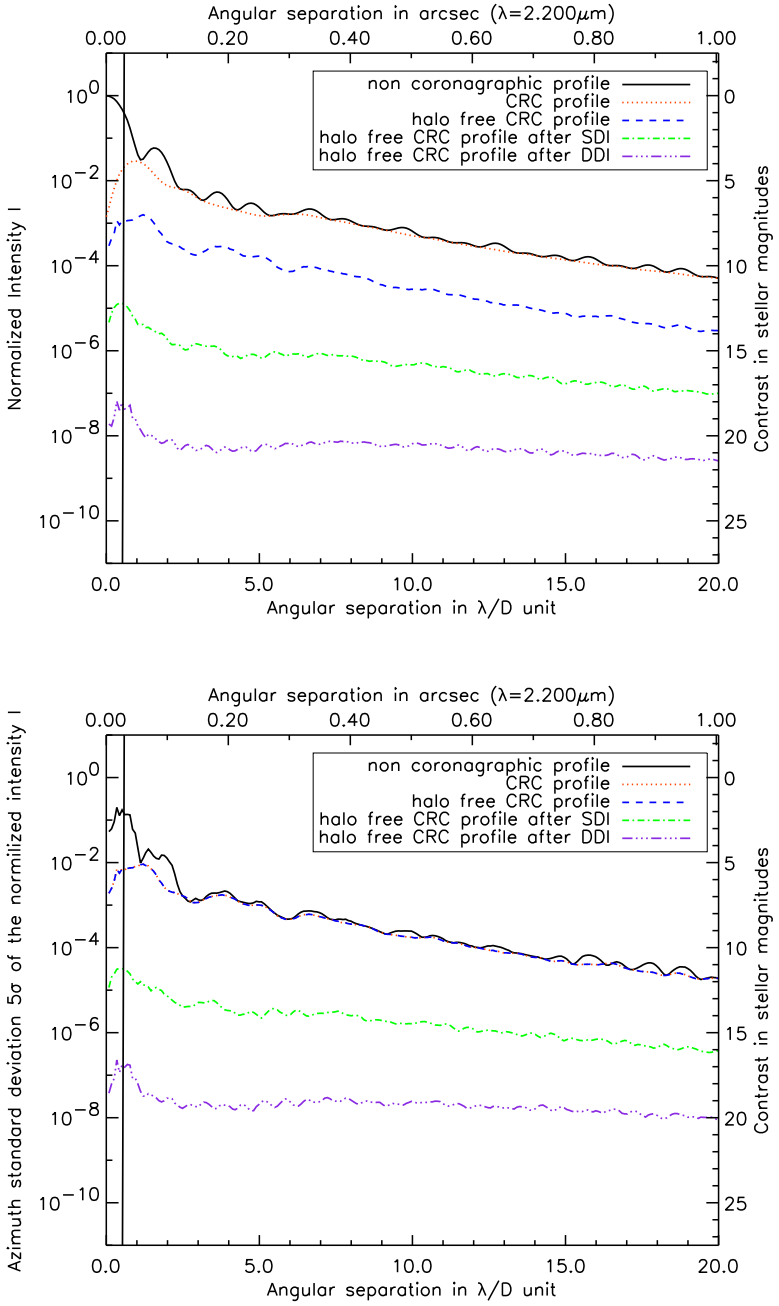

Figure V.7: Top: Azimuth averaged profiles of the non coronagraphic PSF and images obtained with CRC and different image processing techniques, for a 29% centrally obstructed telescope (GTC case), in K-band. **Bottom**: Profiles of the azimuth standard deviation 5σ of the normalized intensities I. The Roddier & Roddier phase mask of radius $0.60\,\lambda/D$ is delimited by a vertical line.

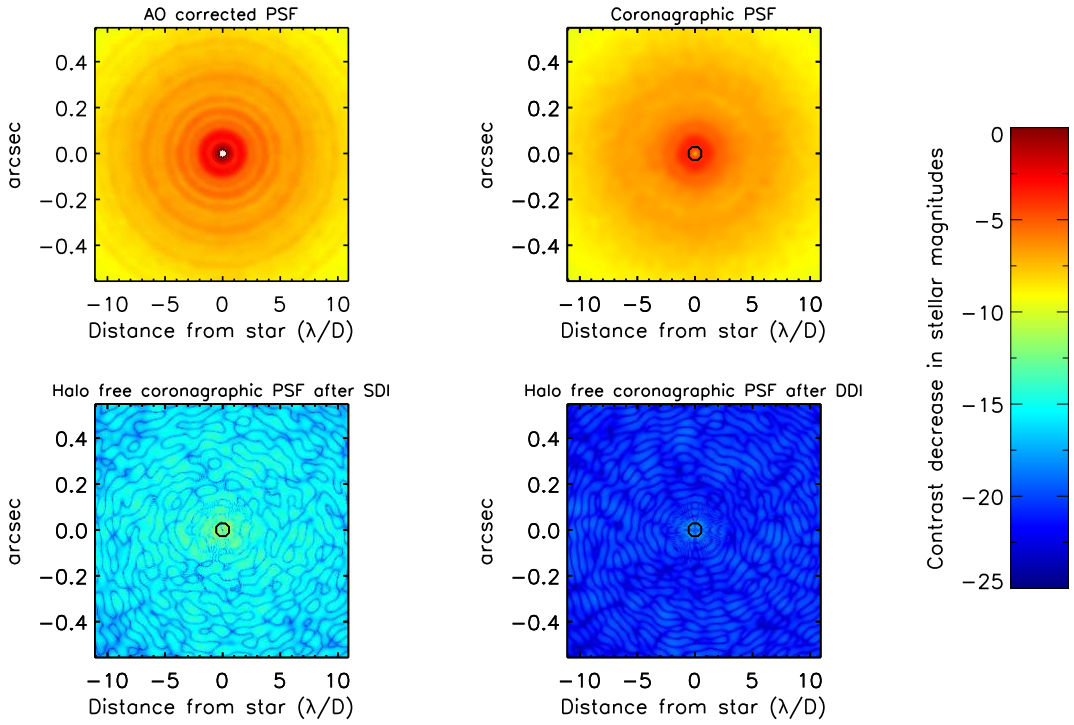

Figure V.8: Same as Figure V.6 but here, CLC is replaced by CRC. The Roddier & Roddier phase mask of radius $r = 0.60\,\lambda/D$ is delimited by a black circle.

Table V.2: Contrast gain reached with CRC configuration and additional image processing techniques for FRIDA.

Profile	**Contrast gain in stellar mag. Δm at an angular separation (in λ/D):**						
	2.0	4.0	6.0	8.0	10.0	12.0	20.0
CRC profile	1.26	0.49	0.07	0.11	0.23	0.08	0.04
Halo free CRC profile	4.42	2.89	3.29	3.15	3.37	3.16	3.18
Halo free CRC profile after SDI	10.39	9.02	8.29	7.96	7.80	7.49	7.19
Halo free CRC profile after DDI	16.47	14.65	13.64	12.96	12.54	11.98	11.53

V.4 Discussion

V.4.1 Non common path instrumental aberrations

These first results are very encouraging for the direct detection of dim substellar mass companions close to bright stars. However, in our numerical simulations, we consider AO residual speckles but quasi-static residual speckles were not taken into account. Quasi-static residual speckles are due to the non-common path errors present within an instrument.
In the case of FRIDA, the non common phase errors are estimated to be equal to 50 nm what corresponds to a variance of these quasi-static speckles $\sigma^2_{\varphi_2} = 0.020$ rad^2 at $\lambda = 2.200\,\mu$m. In comparison, the variance of the AO residual speckles is $\sigma^2_{\varphi_1} = 0.506$ rad^2. Considering the optical aberrations present within FRIDA would naturally carry out to a re-adjustment of the Strehl ratio of their images: $S = 0.591$ instead of 0.603 at $\lambda = 2.200\,\mu$m. The difference is negligible at level of image quality.

V.4.2 A concrete case...

Numerical results about the achievable contrast gains with "coronagraphy+image processing methods" are very promising. However, they have to be relativized: a comparison with the different noise source thresholds is required to validate them. A more realistic analysis would allow to determine accurately the magnitude of faint sources we can hope to image. In the following approach, we decide to consider a more concrete case. It aims to give a first idea about the potential of these techniques, in particular for FRIDA. Figure V.9 refers to Figure V.5 but here, the normalized intensity values have been replaced by those of a 4.60 mag star in K-band and are now expressed in amount of photons (or photo-electrons). Moreover, photon noise and readout noise thresholds have also been added. We have worked with 200 independent phase screens which correspond therefore to 200 decorrelated speckle patterns in the image plane. Macintosh et al. (2005) estimated that the decorrelation time scale for residual post coronagraph PSF speckles caused by atmospheric error sources is $0.6\,D/v$ irrespective of r_0 or the detailed behavior of the AO system. Let us remind that D denote the telescope diameter and v the wind turbulence and here, we deal with $D = 9.039$ m and $v = 10\,\mathrm{m{\cdot}s^{-1}}$. Thus, our simulation represents a 108.5 s time exposure and this is the value that has been considered to plot the different profiles and we assume that this total exposure time is split in 4 to allow dithering and sky subtraction.
The characteristics of the FRIDA optics (throughput, spectral resolution) and the Hawaii II detector (Watson, 2007) allow to determine the FRIDA image dynamic range $\Delta m = 10.75$ mag. In the context of high contrast imaging, we want to fully benefit from this range of values. In FRIDA IFS mode at $R = 1500$ and working with fine scale (0.01 arcsec /pixel in the spatial direction), the limiting magnitude (or readout noise) in K-band will be equal to 19.7, in the presence of a bright natural guide star. Hence, a 8.95 mag star is the brightest one observable by FRIDA without risk of detector saturation while reaching the limiting magnitude. The interest of the coronagraph results in its ability to increase this value and therefore, simultaneously study stars brighter than those of 8.95 mag and observe their close-in companions without detector saturation. In the following, we choose to work with CLC. Its application will mainly consist in reducing the PSF diffraction core. Here, since we consider a 4.60 mag star, the application of CLC allows to down to a $\sim$ 11 mag

intensity maximum level. This value is observed in Figure V.9, with the red dot-line CLC profile close to the mask delimitation ($r = 2.69\,\lambda/D$).
We work in IFS mode at $R = 1500$ therefore, images present in the FRIDA data cube are separated by a bandwidth $\Delta\lambda \simeq 1\,\text{nm}$. In this mode, it is assumed that each slice projects to two pixels which can be identified as a resolution element (resel). At $R = 1500$, the covered bands are H+K or equivalently 1.4–2.4 μm in bandpass and therefore, the width is equal to 1 μm. Since the detector format is 2048×2048, we will obtain $1000\,resel$ of bandwidth 1 nm. In the presence of CLC, the maximum number of photo-electrons is $\sim 3 \cdot 10^5$ while the maximum number of photo-electrons per exposure is 10^5. Therefore, 3 exposures are required to achieve the presented result. It gives an integration time $t_{int} = 36\,\text{s}$ per exposure for a full well of 100,000 electrons. Fig. V.9 bottom plot allows to notice that with the association "CLC+azimuth symmetric component removal+SDI", it would be possible to reach the photon or readout noise limit and detect a 16 mag substellar mass companion at a 0.2 arcsec angular distance from a 4.6 mag brilliant star at 5σ. At a 0.2 arcsec angular separation (or equivalently, $4\,\lambda/D$ from the main optical axis), the limit is imposed by the photon noise. With an increase of the integration time, the photon noise will drop to the read noise level and we can expect to image fainter substellar mass companions, reasonably up to 18 mag.
A quick comparison can be done with the study made by Thatte et al. (2007) about AB Doradus (AB Dor) A. In their approach, they use some image processing techniques but no coronagraph. Figure V.10 is extracted from their paper. AB Dor A and AB Dor C are respectively a 4.6 mag star and its 9.6 mag low-mass companion in K-band. Their angular separation is about 0.2 arcsec. The SINFONI AO system provided a mean Strehl ratio $S = 0.36$. In our computational results, we have assumed a parent star with the same magnitude than AB Dor A but here, $S = 0.60$. Hence, the star halo presents a ~ 11.5 mag threshold at 0.2 arcsec instead of 10 mag. So, an eventual 9.6 mag low-mass companion in K-band would be already detectable with the current design of GTCAO. The addition of coronagraphy and image processing methods would facilitate the enhancement of AB Dor C or also allow to detect fainter companions at the same angular separation with FRIDA. These predictions allow to be optimistic about the ability of FRIDA to perform high contrast imaging.

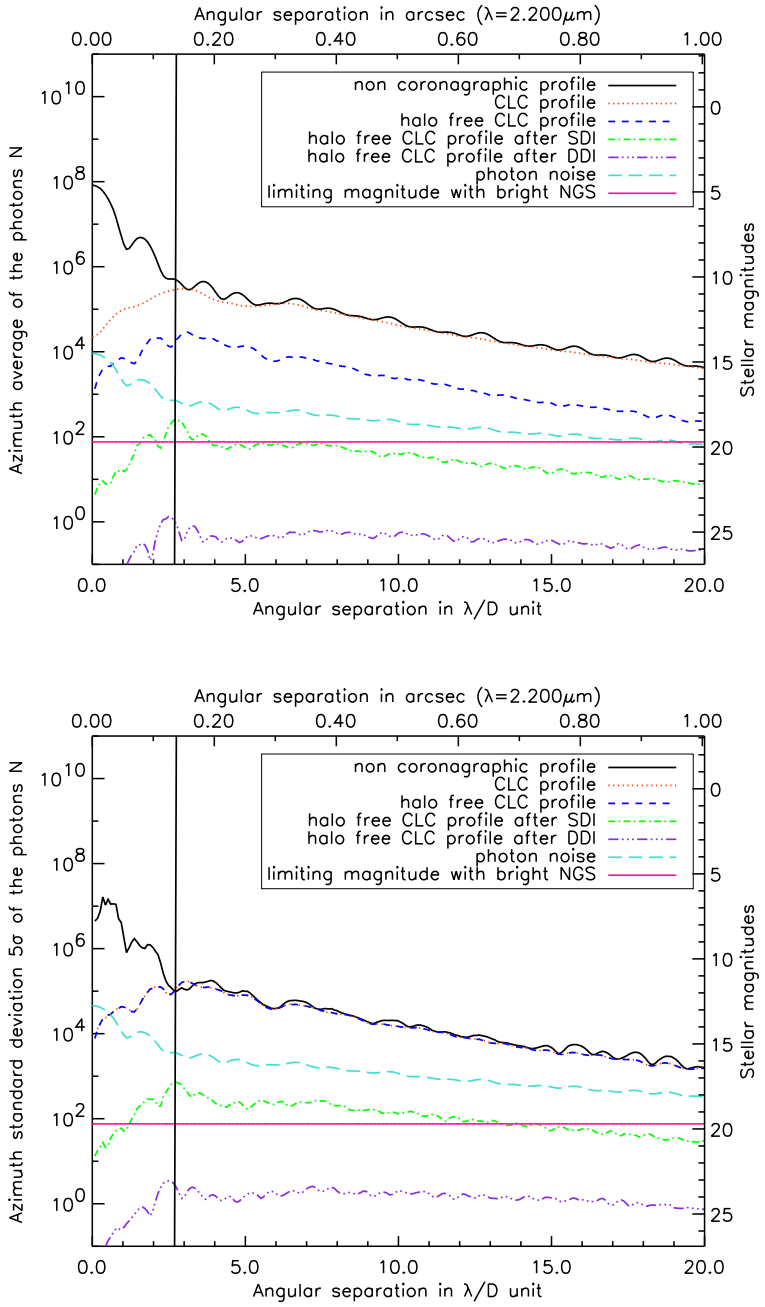

Figure V.9: Same as Fig. V.5 but here, the normalized intensity values were replaced by those of a 4.60 mag star in K-band and are now expressed in amount of photons. Furthermore, photon noise and readout noise thresholds were also added.

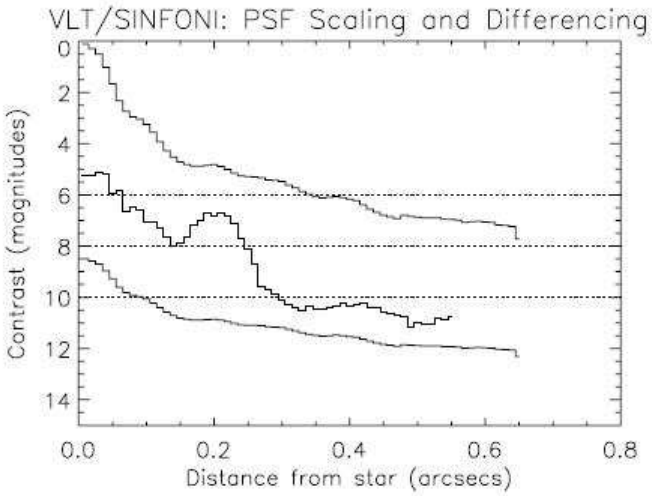

Figure 5. The plot shows three curves – the top curve is the radial profile of AB Dor A. The bottom curve is the square root of the top curve, so it represents the photon noise limit. The middle curve is the standard deviation in the SD result frame, so it is a measure of the residual noise. The horizontal lines at 6, 8 and 10 mag are for reference. The large bump at 0.2 arcsec in the SD result frame is due to AB Dor C. The achieved contrast is 9 mag at 0.2 arcsec, and 11 mag at 0.5 arcsec, in 20 min exposure time at $R_{\rm eff} = 400$. As no coronagraph is used, very high contrasts can be obtained at small inner working radii.

Figure V.10: Figure extracted from Figure 5 of Thatte et al. (2007).

V.5 Conclusion of the fifth chapter

In the present study, we have implemented numerically two post-processing methods to coronagraphic images. On the one hand, azimuth symmetric component removal method allows to keep on increasing the image dynamic range after coronagraphic use. On the other hand, differential imaging methods allow ground-based instruments to overcome the AO residual speckles present in the halo free coronagraphic images and reach the photon or readout noise limit of an instrument.
In the context of FRIDA instrument, we have estimated numerically the achievable contrast gains that these post coronagraphic methods can provide before concluding our analysis with a more concrete case. The numerical results achieved with this approach have showed that it is possible and feasible to perform high contrast imaging with FRIDA. With a good AO correction, a coronagraph and some downstream image processing techniques, FRIDA could be able to detect and characterize some possible substellar mass companions.
A complete characterization of the detected object can be imagined by replacing the SSDI method with a more generalized one as that proposed by Sparks and Ford (2002) and after then, improved by Thatte et al. (2007). Indeed, SSDI is limited in its application to just one intrinsic feature of the substellar mass companion spectrum. Spectral Deconvolution method (Sparks and Ford, 2002) allows to work over the whole spectral bandwidth of the data cube provided for instance by FRIDA in IFS mode. Thus, a follow-up spectroscopy of the detected candidate object could be done with FRIDA to confirm its nature and characterize it in details.

V.5 Conclusión del quinto capítulo

En este estudio, se implementaron numéricamente dos métodos de post procesamiento de imágenes coronográficas. Por un lado, el método para eliminar la componente simétrica azimutal permite seguir aumentando el intervalo dinámico de imagen después de usar un coronógrafo. Por otro lado, los métodos de imagen diferencial permiten a los instrumentos terrestres superar los speckles residuales AO presentes en las imágenes coronográficas libres ya del halo y alcanzar el límite del ruido de fotones o de lectura de un instrumento.
En el contexto del instrumento FRIDA, se estimaron numéricamente las ganancias de contraste alcanzables que pueden proveer estos métodos post coronográficos antes de concluir nuestra análisis con un caso más concreto. Los resultados numéricos alcanzados con este enfoque ponen en evidencia la posibilidad y la factibilidad de formar imágenes de alto contraste con FRIDA. Con una buena corrección AO, un coronógrafo y técnicas de procesamiento de imagen, FRIDA podrá detectar y caracterizar eventuales compañeros de masa sub-estelar. Se puede imaginar una caracterización completa del objeto detectado reemplazando el método SSDI por uno más general como el propuesto por Sparks and Ford (2002) y luego, mejorado por Thatte et al. (2007). De hecho, SSDI está limitado en su aplicación a solamente una característica intrínseca del espectro del compañero de masa sub-estelar. El método de deconvolución espectral (Sparks and Ford, 2002) permite trabajar en toda la banda espectral del cubo de datos proporcionado por ejemplo por FRIDA en modo IFS. De tal forma, se podría hacer un seguimiento espectroscópico seguida del objeto candidato detectado con FRIDA para confirmar su naturaleza y caracterizarlo con mejor detalle.

V.6 References

L. Abe. Numerical Simulations in Coronagraphy. Part I. In C. Aime and R. Soummer, editors, *EAS Publications Series*, volume 12 of *EAS Publications Series*, pages 157–164, 2004.

C. Aime and R. Soummer. The Usefulness and Limits of Coronagraphy in the Presence of Pinned Speckles. *ApJL*, 612, L85–L88, 2004.

E. E. Bloemhof, R. G. Dekany, M. Troy, and B. R. Oppenheimer. Behavior of Remnant Speckles in an Adaptively Corrected Imaging System. *ApJL*, 558, L71–L74, 2001.

O. Guyon. Imaging Faint Sources within a Speckle Halo with Synchronous Interferometric Speckle Subtraction. *ApJ*, 615, 562–572, 2004.

D. Lafrenière, C. Marois, R. Doyon, D. Nadeau, and É. Artigau. A New Algorithm for Point-Spread Function Subtraction in High-Contrast Imaging: A Demonstration with Angular Differential Imaging. *ApJ*, 660, 770–780, 2007.

B. Macintosh, L. Poyneer, A. Sivaramakrishnan, and C. Marois. Speckle lifetimes in high-contrast adaptive optics. In R. K. Tyson and M. Lloyd-Hart, editors, *Astronomical Adaptive Optics Systems and Applications II. Edited by Tyson, Robert K.; Lloyd-Hart, Michael. Proceedings of the SPIE, Volume 5903, pp. 170-177 (2005).*, volume 5903 of *Presented at the Society of Photo-Optical Instrumentation Engineers (SPIE) Conference*, pages 170–177, 2005.

C. Marois. Speckle Noise Attenuation in Coronagraphy and High-Contrast Imaging. In P. Kalas, editor, *In the Spirit of Bernard Lyot: The Direct Detection of Planets and Circumstellar Disks in the 21st Century*, 2007.

C. Marois, R. Doyon, R. Racine, and D. Nadeau. Efficient Speckle Noise Attenuation in Faint Companion Imaging. *Public. of the Astron. Soc. Pac.*, 112, 91–96, 2000.

C. Marois, D. Lafrenière, R. Doyon, B. Macintosh, and D. Nadeau. Angular Differential Imaging: A Powerful High-Contrast Imaging Technique. *ApJ*, 641, 556–564, 2006.

M. D. Perrin, A. Sivaramakrishnan, R. B. Makidon, B. R. Oppenheimer, and J. R. Graham. The Structure of High Strehl Ratio Point-Spread Functions. *ApJ*, 596, 702–712, 2003.

R. Racine, G. A. H. Walker, D. Nadeau, R. Doyon, and C. Marois. Speckle Noise and the Detection of Faint Companions. *Public. of the Astron. Soc. Pac.*, 111, 587–594, 1999.

A. Sivaramakrishnan, C. D. Koresko, R. B. Makidon, T. Berkefeld, and M. J. Kuchner. Ground-based Coronagraphy with High-order Adaptive Optics. *ApJ*, 552, 397–408, 2001.

A. Sivaramakrishnan, J. P. Lloyd, P. E. Hodge, and B. A. Macintosh. Speckle Decorrelation and Dynamic Range in Speckle Noise-limited Imaging. *ApJL*, 581, L59–L62, 2002.

W. B. Sparks and H. C. Ford. Imaging Spectroscopy for Extrasolar Planet Detection. *ApJ*, 578, 543–564, 2002.

N. Thatte, R. Abuter, M. Tecza, E. L. Nielsen, F. J. Clarke, and L. M. Close. Very high contrast integral field spectroscopy of AB Doradus C: 9-mag contrast at 0.2arcsec without a coronagraph using spectral deconvolution†. *MNRAS*, 378, 1229–1236, 2007.

A. M. Watson. FR/FR-SC/040: Signal and Noise estimates. Frida technical note, Centro de Radioastronomía y Astrofísica - Universidad Nacional Autónoma de México, 2007.

Conclusion

In the context of direct imaging and characterization of substellar mass companions, we led a feasibility study to perform high contrast imaging with the FRIDA instrument. FRIDA, an infrared imager and integral field spectroscopy (IFS) system, is a second-generation instrument conceived for Gran Telescopio Canarias (GTC) and planned to work in concert with its Adaptive Optics system (GTCAO). FRIDA is required to work as a high contrast imager. Our goal here was then to propose and evaluate several solutions to allow FRIDA to image dim low-mass companions close to nearby bright stars.

The main concepts of stellar coronagraphy were first reviewed. Coronagraphs aim to remove the diffraction pattern of an observed bright star and enhance the image of possible close-by companions. Numerous concepts have been investigated for a decade, in particular we decided to focus on Lyot-style coronagraphs and pupil apodizers, since they represent very promising solutions. Afterwards, the FRIDA instrument was presented, and its optical setup analyzed for the identification of several sites available for insertion of pupil apodizers and/or focal plane masks. Several coronagraphic configurations were then proposed: the Classical Lyot Coronagraph (CLC), the Classical Roddier Coronagraph (CRC), and the Apodized Pupil Lyot Coronagraph (APLC) without Lyot stop. Moreover, we suggested an original concept, the Stop-less Lyot coronagraph (SLLC), to overcome some mechanical stresses in the FRIDA design.
Secondly, coronagraph feasibility studies for FRIDA were carried out. For this purpose, we implemented a numerical tool based on a semi-analytical approach using Matrix Fourier Transform to compute the coronagraph behaviors of interest. Our methodologies and simulations were first verified with well defined test cases, and our results are consistent with other studies in the literature. In addition, our numerical results were validated in the laboratory through experiments led with a second-generation Roddier & Roddier phase mask coronagraph. Finally, we reported the contrast gains reachable with the coronagraphic configurations proposed for FRIDA.
We started our performance analysis considering FRIDA as a diffraction-limited system. This allowed us to calibrate the maximum star brightness attenuation yielded in the absence of aberrations and concluded that SLLC represents the best coronagraphic solution for FRIDA followed by CRC, APLC without Lyot stop, and CLC.
Later, we considered a more realistic approach with FRIDA working in concert with GTCAO. Therefore, AO-compensated wavefronts produced with the CAOS software were introduced in our simulations. We noticed that the insertion of suitable coronagraphs within FRIDA could help avoiding detector saturation, thanks to the suppression of the bright core in the star image. Furthermore, additional coronagraphs could allow a slight enhancement of the contrast in the field of view. These

devices would also increase the image dynamic range of FRIDA, which is essential for the imagery of low-mass companions. However, regardless of the coronagraph configuration used, GTCAO+FRIDA cannot perform high contrast imaging since coronagraphs are limited by the presence of AO residual speckles.
Finally, we analyzed the possibility of adding post-processing methods to coronagraphic techniques. Post-processing can be performed with FRIDA in IFS mode thanks to the data cube of images it will provide. These techniques allow to remove the AO residual speckles caused by the imperfect AO correction that cannot be overcome by coronagraphy. Two different approaches were studied here: the removal of the azimuth symmetric component and the Simultaneous Spectral Differential Imaging (SSDI) technique. We computed these methods assuming two or three simultaneous spectral coronagraphic images obtained with FRIDA coupled with GTCAO. Very encouraging contrast gain results were achieved: GTCAO+FRIDA can be able to image and characterize a companion 10^5 fainter than its parent bright star at a 0.2 arcsec angular separation. Therefore, post-processing methods added to coronagraphic techniques constitute a feasible and promising combination to perform high contrast imaging with GTCAO+FRIDA.

The potential of our solutions proposed for FRIDA exists and deserves consideration. However, non-common path errors have to be included in further simulations to be more realistic. Their effects on coronagraph behavior and post-processing methods performance have to be studied in order to determine if these optical aberrations significantly deteriorate the reachable contrast. Furthermore, our numerical results need to be completed with some system error budgets. Indeed, alignment errors of the focal plane mask, diaphragm or pupil apodizer may prove to be critical for the coronagraph performance. Acceptable tolerances of the coronagraphic devices also need to be estimated to reach images with satisfactory contrast in the field of view.
A wide range of solutions was not explored in this work. For instance, we can imagine generalizing the SSDI technique to spectral deconvolution method by considering the whole IFS data cube provided by FRIDA instead of two or three spectral images. This would lead to the complete characterization of companions possibly detected with FRIDA. Moreover, the introduction of more sophisticated phase masks for FRIDA could ease the application of spectral deconvolution method and improve its performance. In fact, working with achromatic masks may allow to achieve uniform star brightness attenuations over a wide wavelength range. Thus, the differences between all the coronagraphic PSFs of an observed star within a filter bandwidth could be reduced and potentially canceled. We believe that the Dual Zone phase mask, which is an achromatic version of the Roddier & Roddier one, constitutes a promising and feasible solution in this context.
Finally, it would be interesting to explore the potential of high contrast imaging capability for FRIDA, if GTCAO were upgraded with the same number of actuators as SPHERE (Very Large Telescope) or GPI (Gemini South telescope). Our work represents the first and essential steps towards contrast gain results if FRIDA were equipped with a coronagraph and coupled with an improved GTCAO system. Theses first tests revealed a considerable improvement of the coronagraphic performance even before the application of post-processing techniques. This powerful association of upgraded instruments is of significant relevance for the quest of direct imaging and characterization of substellar mass companions with the GTC, and represents an important first step for instrumentalists to acquired experience before considering the challenge of a future planet imager for GTC.

Conclusión

En el marco de formación de imagen directa y caracterización de compañeros de masa sub-estelar, se llevó a cabo un estudio de factibilidad para generar imágenes de alto contraste con FRIDA. FRIDA es un instrumento de segunda generación diseñado para el Gran Telescopio Canarias (GTC): este instrumento trabaja en el cercano infrarrojo con requerimientos de formación de imagen directa y de espectroscopía integral de campo (IFS), y está planeado para trabajar en concierto junto con el sistema de Óptica Adaptativa (AO por sus siglas en inglés) del GTC (GTCAO). Las especificaciones de diseño de FRIDA mencionaban que este instrumento tenía que ser capaz de proporcionar imágenes de alto contraste. Nuestro objetivo aquí consiste en proponer y evaluar diferentes soluciones que puedan beneficiar a FRIDA para obtener imágenes de compañeros de baja masa presentes en la vecindad de estrellas brillantes cercanas.

Primeramente, se revisaron los principales conceptos de coronografía estelar. Los coronógrafos tienen por objetivo eliminar el patrón de difracción de una estrella brillante observada y realzar la imagen de los eventuales compañeros cercanos. Varios conceptos han sido investigados desde hace una década: en el presente trabajo, se decidió centrarse en los coronógrafos de typo Lyot y las apodizaciones pupilares ya que representan soluciones muy prometedoras. Luego el instrumento FRIDA fue presentado y su esquema óptico fue analizado: se identificaron varios sitios disponibles para la inserción de apodizaciones pupilares y/o máscaras de plano focal. Partiendo de estas hipótesis, diferentes configuraciones coronográficas fueron propuestas: el Coronógrafo de Lyot Clásico (CLC), el Coronógrafo de Roddier Clásico (CRC) y el Coronógrafo de Lyot con Pupil Apodizada (APLC) sin diafragma de Lyot. Además, se sugirió un concepto original, el Coronógrafo de Lyot sin diafragma (SLLC) para superar algunos obstáculos mecánicos del diseño de FRIDA.
Después, se llevaron a cabo estudios de factibilidad de coronografía para FRIDA. Para este propósito, implementamos una herramienta numérica, basada en un método semi-analítico que usa una transformada de Fourier matricial, para determinar los comportamientos coronográficos de nuestro interés. Se verificó la consistencia de nuestros resultados y se mostró que nuestras simulaciones concordaban con las que se encuentran en la literatura. Además, nuestros resultados numéricos fueron validados en laboratorio, a través de experimentos realizados con un coronógrafo usando una máscara de fase de Roddier & Roddier de segunda generación. Finalmente, se hizo una comparación de las ganancias de contraste alcanzables con las configuraciones coronográficas propuestas para FRIDA.
A continuación, se inició el análisis de desempeño considerando a FRIDA como un sistema al límite de difracción. Esto nos permitió calibrar la atenuación máxima de flujo luminoso estelar alcanzable en ausencia de aberraciones. Para esta condición, el SLLC representa la mejor solución coronográ-

fica para FRIDA, seguido del CRC, el APLC sin diafragma de Lyot y el CLC.
Se consideró después un enfoque más realista, con FRIDA trabajando en concierto junto con GTCAO, el sistema AO del telescopio GTC. Por lo tanto, los frentes de onda compensados por AO y producidos con el software CAOS fueron entonces introducidos en nuestras simulaciones. Se notó que la inserción de coronógrafos adecuados en FRIDA ayudaba a evitar la saturación del detector, gracias a la supresión del núcleo brillante en la imagen de la estrella observada. Además, coronógrafos adicionales pueden permitir un ligero aumento del contraste en el campo útil del coronógrafo. Estos dispositivos pueden también permitir el aumento del intervalo dinámico de imágenes de FRIDA, lo cual es esencial para poder generar imágenes de compañeros de baja masa. Sin embargo, sea cual sea la configuración coronográfica usada, GTCAO+FRIDA no pueden realizar imágenes con un alto contraste. De hecho, los coronógrafos están limitados por la presencia de speckles residuales de AO.
Se analizó entonces la posibilidad de aplicar métodos de post procesamiento después de técnicas coronográficas. Se pueden utilizar métodos de post procesamiento con FRIDA en modo IFS, gracias al cubo de datos de imágenes que el instrumento va a proporcionar. Estas técnicas permiten eliminar los speckles residuales que se deben a la corrección imperfecta de AO y que afectan el buen desempeño del coronógrafo. Dos métodos fueron estudiados aquí: la eliminación de la componente simétrica azimutal y la técnica de imágenes diferenciales espectrales simultáneas (SSDI). Implementamos estos dos métodos considerando dos o tres imágenes coronográficas espectrales y simultáneas obtenidas numéricamente con FRIDA acoplado a GTCAO. Se alcanzaron resultados de ganancia en contraste muy prometedores: GTCAO+FRIDA puede ser capaz de formar la imagen y de caracterizar un compañero de intensidad 10^5 más débil que su estrella huésped brillante con una separación angular de 0.2 arcsec. Métodos de post procesamiento añadidos a técnicas coronográficas constituyen por lo tanto una combinación completamente factible y prometedora para realizar imágenes de alto contraste con GTCAO+FRIDA.

El potencial de las soluciones propuestas para el instrumento FRIDA existe y merece ser considerado. Sin embargo, los errores de corrección de la diferencia de camino óptico entre GTCAO y FRIDA deben ser incluidos en futuras simulaciones para ser más realistas. Se deben estudiar sus efectos sobre el comportamiento de los coronógrafos y el desempeño de los métodos de post procesamiento para determinar si estas aberraciones ópticas implican una deterioración significante del contraste alcanzable. Además, se requiere completar nuestros resultados numéricos con un presupuesto de errores del sistema. De hecho, los errores de alineación de la máscara de plano focal, del diafragma o de la apodización de pupila pueden resultar muy críticos en términos de desempeño coronográfico. Se requiere igualmente estimar las tolerancias aceptables de los dispositivos coronográficos si se quieren generar imágenes con un contraste satisfactorio en la zona de búsqueda.
Un amplio intervalo de soluciones no fue explorado en este trabajo. Por ejemplo, se puede imaginar una generalización de la técnica SSDI al método de deconvolución espectral, considerando el cubo de datos IFS entero proporcionado por FRIDA en vez de dos o tres imágenes espectrales. Esto nos llevaría a una caracterización completa de los compañeros posiblemente detectados con FRIDA. Además, la introducción de máscaras de fase más sofisticadas para FRIDA podría facilitar la aplicación del método de deconvolución espectral y mejorar su desempeño. De hecho, trabajar con máscaras acromáticas permitiría alcanzar atenuaciones uniformes de luminosidad estelar sobre un amplio intervalo de longitudes de onda. De tal forma, se podría reducir y tal vez cancelar las

diferencias entre todas las PSFs coronográficas de una estrella observada sobre todo el intervalo de longitudes de onda del filtro usado. Creemos que la máscara de fase de doble zona, que es una versión acromática de la de Roddier & Roddier, constituye una solución prometedora y factible en este contexto.

Finalmente, sería muy interesante explorar el potencial de formación de imágenes de alto contraste para FRIDA si GTCAO fuera actualizado con el mismo número de actuadores como es el caso de SPHERE para el *Very Large Telescope* o de GPI para el *Gemini South Telescope*. Se empezó a dar unos primeros resultados de ganancia en contraste considerando FRIDA equipado con un coronógrafo y acoplado con un sistema GTCAO mejorado. Las primeras pruebas revelaron una gran mejora del desempeño coronográfico antes de aplicar técnicas de post procesamiento. Esta asociación de instrumentos actualizados podría representar una primera etapa en la búsqueda de formación de imagen directa y caracterización de compañeros de masa sub-estelar con GTC: los instrumentistas podrán beneficiar de la experiencia adquirida con ella antes de investigar la realización de un nuevo instrumento para el GTC que se dedicará a la formación de imágenes de exoplanetas.

Appendix A

Nyquist-Shannon sampling theorem

We briefly review notions of signal sampling. To formalize these concepts, let us consider a continuous-time signal $x(t)$. In a simple and idealized case, sampling the signal $x(t)$ consists of multiplying it with a Dirac comb distribution, defined as:

$$\text{Ш}_{\delta_\tau}(t) = \sum_{n=-\infty}^{+\infty} \delta(t - n\tau)\,, \tag{A.1}$$

where n is an integer and τ stands for the sampling interval. δ denotes the Dirac delta distribution, a spike located at the origin with infinitesimal width and infinite height so that $\int_{-\infty}^{+\infty} \delta(t)\,dt = 1$. Therefore, the sampled signal $x_s(t)$ at a sampling frequency $\nu_s = 1/\tau$ can be written as:

$$x_s(t) = \text{Ш}_{\delta_\tau}(t)x(t), \tag{A.2}$$

or equivalently:

$$x_s(t) = \sum_{n=-\infty}^{+\infty} x(n\tau)\delta(t - n\tau). \tag{A.3}$$

A schematic representation of the signal and the sampling is given in Figure A.1. The terms $x(n\tau)$ form the sequence of the samples. Let us remind that $\hat{f}$ represents the Fourier transform of a function f and $\otimes$ denotes the convolution product. Hence, in the frequency domain, the previous equation becomes:

$$\hat{x}_s(\nu) = \left[\frac{1}{\tau}\text{Ш}_{\delta_{1/\tau}} \otimes \hat{x}\right](\nu)\,, \tag{A.4}$$

where the transform variable ν represents the ordinary temporal frequency, since the independent variable t symbolizes the time here. This expression points out the periodicity of the spectrum $x(\nu)$ with period $1/\tau$. Overlapping of the spectrum will occur in the frequency domain unless $\hat{x}_s(\nu > \nu_s/2) = 0$, where $\nu_s = 1/\tau$ is the sampling frequency. Accurate reconstruction of the original signal therefore relies on an adequate choice of this parameter. If this condition is not met, spurious information will appear due to the overlapping of the spectral replica. This effect, referred to as aliasing, is illustrated in Figure A.2.

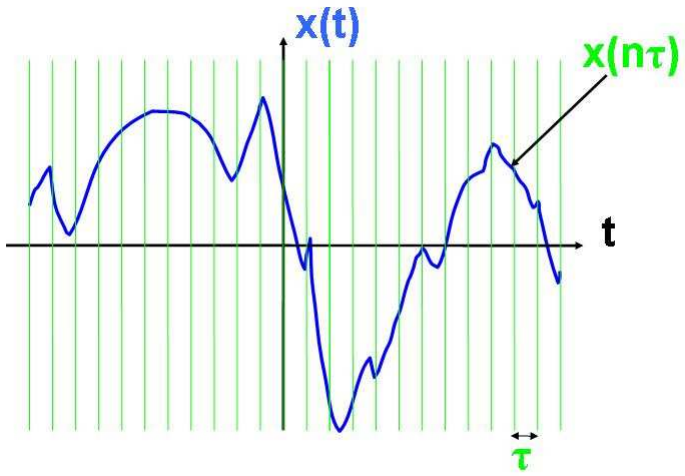

Figure A.1: Schematic representation of a signal $x(t)$, the sampling interval τ and one of the terms $x(n\tau)$.

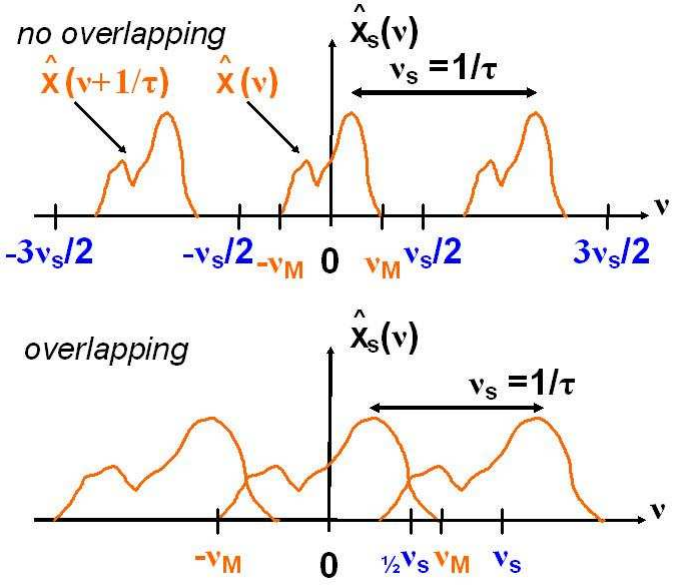

Figure A.2: Schematic representation of the spectrum $\hat{x}_s(\nu)$, the sampling interval τ, the frequency ν_M and the sampling rate ν_s. At the top, no overlapping succeeds. At the bottom, a bad sampling of the original signal $x(t)$ carries out to overlapping in the frequency domain and therefore, aliasing effects. It has to be noticed that the represented spectrum $\hat{x}_s(\nu)$ cannot correspond to the signal $x(t)$ sketched in Figure A.1. Indeed, if x is a real signal then $\hat{x}_s$ is hermitian i.e. the real part of $\hat{x}_s$ is real and symmetric and the imaginary part of $\hat{x}_s$ is real and antisymmetric.

Correct sampling therefore requires that the signal $x(t)$ has a band-limited spectrum, i.e. it exists a frequency ν_M such that $|\hat{x}(\nu)| = 0$ for all $\nu \geq \nu_M$ and that $1/\tau \geq 2\nu_M$. If this is not the case, then we should apply an adequate low-pass filter (e.g. a rectangular function):

$$\hat{x}(\nu) = \Pi\left(\frac{\nu}{2\nu_M}\right)\hat{x}(\nu)\,, \tag{A.5}$$

with $\Pi(\nu) = 1$ for $|\nu| \geq 1/2$ and 0 elsewhere. Hence, extracting $\hat{x}(\nu)$ from $\hat{x}_s(\nu)$, it becomes possible to recover the signal $x(t)$. This is the base of the sampling theorem. Figure A.3 illustrates the filtering operation over the spectrum of the signal $x(t)$.
Let us note that if the signal $x(t)$ does not have a band-limited spectrum, it has to be filtered with a function which Fourier transform is band-limited. Filtering operation must be realized before sampling otherwise the translated spectra overlap.
The **Nyquist-Shannon sampling theorem** asserts that the sampling rate ν_s of a signal must be at least twice as great as the highest frequency ν_M in this signal, in order to convert this signal from an analogical to a digital form without loss of information. This theorem is the base of the digital conversion of signals:

$$\nu_s \geq 2 \times \nu_M. \tag{A.6}$$

If the conditions of the sampling theorem are satisfied (for instance, $\nu_s = 2\nu_M = 1/\tau$), the reconstitution of the signal is obtained with a Fourier transform of Eq. (A.5):

$$x(t) = \mathrm{sinc}\left(\frac{t}{\tau}\right) \otimes x_s(t)\,, \tag{A.7}$$

where $\mathrm{sinc}(t) = \sin(\pi t)/\pi t$. Using Eq. (A.4), the last expression can be rewritten as:

$$x(t) = \sum_{n=-\infty}^{+\infty} x(n\tau)\,\mathrm{sinc}\left(\frac{t - n\tau}{\tau}\right). \tag{A.8}$$

This study is carried out in the context of one-dimension signal, but it can be extended to multi-variable signals and images. In our case, we are used to working with gray-scale images, which are represented as two-dimensional arrays of real number describing the relative intensity of pixels[1] located at the intersections of row and column sample locations. Hereafter, we present our choices to achieve a correct description of the coronagraphic behavior with our simulator.

[1] pixels or picture elements, we will name them points in the numerical simulations to avoid confusion with detector pixels.

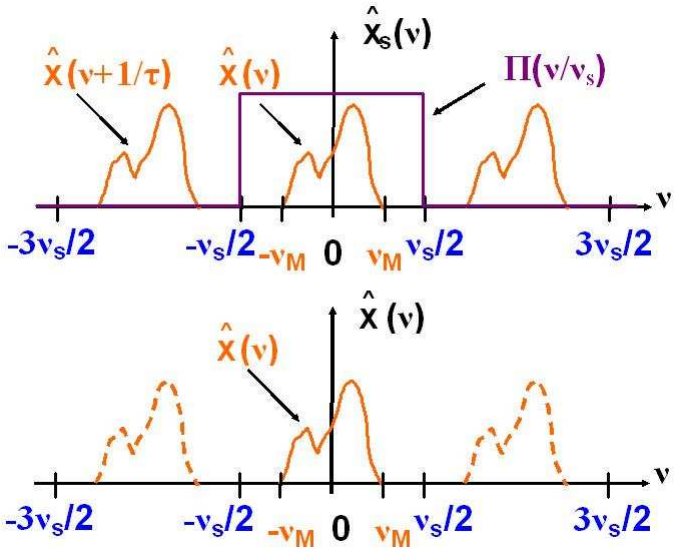

Figure A.3: At the bottom, schematic representation of $\hat{x}_s(\nu)$, a properly sampled band-limited signal. In purple, we can see the application of a low-pass filter (here $\Pi(\nu/\nu_s)$) to remove the images and at the bottom, the original spectrum $\hat{x}(\nu)$ which will allow to recover the original signal from the samples.

Appendix B

Semi-analytical coronagraphic propagations using Matrix Fourier Transform

In the following, we recall the main steps given by Soummer et al. (2007) to compute semi-analytical coronagraphic propagations using Matrix Fourier Transform.

B.1 Principle of the algorithm method

Let us remind the analytical expression of the field in the Lyot plane, already given in Eq. (III.1):

$$\Psi_C(\boldsymbol{r}) = (\Psi_A(\boldsymbol{r}) - \epsilon\,\mathcal{F}\left[\mathcal{F}\left[\Psi_A(\boldsymbol{r})\right] M(\boldsymbol{r})\right]) L(\boldsymbol{r})\,. \tag{B.1}$$

This expression points out the fact that the calculus of the two Fourier transforms is only required within the mask and Lyot stop areas of respective index functions M and L. In the following, we rewrite the steps given by Soummer et al. (2007) and which allow to perform the semi-analytical propagation from the entrance pupil to the Lyot plane:
— Define the pupil field amplitude without zero padding as a $N_A \times N_A$ array, where N_A is the diameter of the pupil in points.
— Calculate the FT to an arbitrary fine sampling inside the area limited to the occulting mask as as a $N_B \times N_B$ array, with e.g. $N_B = 40$ for a $5\,\lambda/D$ mask with $m = 8$. m is a coefficient related to the resolution of the FT in the image plane.
— Calculate the FT of this previous field amplitude inside an area limited to the pupil ($N_A \times N_A$ array).
— Reverse the spatial axes because two successive FTs restore the function while changing the sign of the variable, and subtract the result from the pupil field amplitude (An inverse FFT can also be used between plane B and plane C to avoid reversing the axis).
Soummer et al. (2007) make us also note that for convenience all masks (pupil and occulter) are defined with their centers located on the pixel $N_A/2 + 1$ (or $N_B/2 + 1$), and that the focal plane mask can be defined using the gray pixel approximation, as for the calculated FFT method. Several

methods exist in the literature to calculate partial FTs. In the following, we describe the matrix-based method proposed by Soummer et al. (2007).

B.2 Matrix Fourier transform

The simple matrix Fourier transform (MFT) can be used for the semi-analytical method. In order to restrict the computation of the FT of the pupil to the image plane size m expressed in resolution element units (λ/D), we choose the sampling step in plane B such that: $du = m/N_B$. We compute the Riemann sum directly using a matrix formulation of the sampled Continuous Fourier transform:

$$\begin{pmatrix} \hat{F}(u_0) \\ \cdots \\ \hat{F}(u_k) \\ \cdots \\ \hat{F}(u_{N_B}-1) \end{pmatrix} = \begin{pmatrix} e^{-2i\pi x_0 u_0} & \cdots & e^{-2i\pi x_k u_0} & \cdots & e^{-2i\pi x_{N_A-1} u_0} \\ \cdots & \cdots & \cdots & \cdots & \cdots \\ e^{-2i\pi x_0 u_k} & \cdots & e^{-2i\pi x_k u_k} & \cdots & e^{-2i\pi x_{N_A-1} u_k} \\ \cdots & \cdots & \cdots & \cdots & \cdots \\ e^{-2i\pi x_0 u_{N_B-1}} & \cdots & e^{-2i\pi x_k u_{N_B-1}} & \cdots & e^{-2i\pi x_{N_A-1} u_{N_B-1}} \end{pmatrix} \begin{pmatrix} f(x_0) \\ \cdots \\ f(x_k) \\ \cdots \\ f(x_{N_A}-1) \end{pmatrix} \tag{B.2}$$

which can be written as:

$$\hat{F}(\mathbf{U}) = e^{-2i\pi \mathbf{U}\mathbf{X}^T} \cdot f(\mathbf{X}), \tag{B.3}$$

where $\mathbf{U} = (u_0 \cdots u_{N_B-1})^T$, $\mathbf{X} = (x_0 \cdots x_{N_A-1})^T$, and $\exp(\cdot)$ is the element-wise exponential of a matrix. two dimensional FTs can be implemented straightforwardly as follows:
— Define the four vectors $\mathbf{U} = (u_0 \cdots u_{N_B-1})^T$, $\mathbf{X} = (x_0 \cdots x_{N_A-1})^T$, $\mathbf{V} = (v_0 \cdots v_{N_B-1})^T$, $\mathbf{Y} = (y_0 \cdots y_{N_A-1})^T$.
— The vector elements are $x_k = y_k = (k - N_A/2) \times 1/N_A$ and $u_l = v_l = (l - N_B/2) \times m/N_B$, for $k = [0, \cdots, N_A - 1]$ and $l = [0, \cdots, N_B - 1]$.
— The two-dimension FT is obtained by computing the two matrix products:

$$\hat{F}(\mathbf{U}, \mathbf{V}) = \frac{m}{N_A N_B} e^{-2i\pi \mathbf{U}\mathbf{X}^T} \cdot f(\mathbf{X}, \mathbf{Y}) \cdot e^{-2i\pi \mathbf{Y}\mathbf{V}^T}, \tag{B.4}$$

where the normalization coefficient $m/N_A N_B$ imposes the conservation of energy according to the Parseval theorem: the energy in the limited area FT is a fraction of the total energy of the FT, corresponding to the limited area, which was calculated.
— With this definition, the Fourier transform is centered in a similar fashion to the FFT, with the zero frequency at the pixel $N_B/2 + 1$.
I would like to thank Rémi Soummer for suggesting me the use of the semi-analytical method and MFT and indicating me the typos present in the manuscript of Soummer et al. (2007).

B.3 References

R. Soummer, L. Pueyo, A. Sivaramakrishnan, and R. J. Vanderbei. Fast computation of Lyot-style coronagraph propagation. *Optics Express*, 15, 15935–15951, 2007.

Appendix C

Publications

C.1 Paper sent to a referred journal

C.1.1 Experimental results with a second-generation phase mask coronagraph

Astronomy & Astrophysics manuscript no. articulo01˙3b
March 3, 2009

Experimental results with a second-generation Roddier & Roddier phase mask coronagraph

M. N'Diaye[1,2], K. Dohlen[1], S. Cuevas[2], P. Lanzoni[1], F. Chemla[3], C. Chaumont[3], R. Soummer[4], and E. T. Griffiths[5]

[1] Laboratoire d'Astrophysique de Marseille, UMR6110, OAMP, CNRS/Université de Provence
38 rue Frdric Joliot-Curie, 13388 Marseille cedex 13, France
e-mail: mndiaye@astroscu.unam.mx, Kjetil.Dohlen@oamp.fr
[2] Instituto de Astronomía, Universidad Nacional Autónoma de México
Apartado Postal 70-264 Ciudad Universitaria, 04510 México D.F., Mexico
e-mail: chavoc@astroscu.unam.mx
[3] GEPI, Observatoire de Paris, 5 Place Jules Janssen, 92195 Meudon Cedex, France
e-mail: fanny.chemla@obspm.fr
[4] Space Telescope Science Institute, 3700 San Martin Drive, Baltimore, MD 21218, USA
e-mail: soummer@stsci.edu
[5] American Museum of Natural History, 79th Street at Central Park West, New York, NY 10024, USA

Received ********; accepted ********

ABSTRACT

Context. Coronagraphic techniques are required to observe substellar mass companions close to nearby bright stars by direct imagery. Phase mask coronagraphs are particularly interesting because they give access to the innermost regions. The first such concept was proposed by Roddier & Roddier in 1997. While its principle was validated experimentally a decade ago, the achieved brightness attenuation was too low to be conclusive, probably due to the imperfect thickness profile of the mask.
Aims. We have manufactured and tested a second-generation Roddier & Roddier coronagraph in preparation for the development of more elaborate phase mask designs, planned to be used in the future European Extremely Large Telescope.
Methods. A monolithic phase mask was made by ion beam machining. Experimentally obtained coronagraphic images were compared with simulated images.
Results. Good agreement with theory was obtained. Peak attenuation of 216 was achieved, and a contrast of $\sim 10^{-5}$ was measured at $5.7\,\lambda/D$. Particularly interesting are the results exploring contrasts obtained at different distances from the star for different mask dimensions, confirming predictions made in the literature.

Key words. Instrumentation: high angular resolution – Techniques: high angular resolution – Telescopes – Methods: laboratory

1. Introduction

Direct detection and imagery of faint stellar companions, like extrasolar planets or brown dwarfs, is one of the most exciting challenges of contemporary observational astrophysics. Such imagery will in particular give access to spectral analysis of the emitted or reflected light from these objects, providing data about atmospheric composition. The detection and quantification of bio-signals (like water [H_2O], oxygen [O_2], ozone [O_3]...) will bring elements of response about the possible presence of life (Woolf & Angel 1998). With images of faint companions, it will also be possible to better understand mechanisms of planetary formation (Burrows & Sharp 1999) and calibrate the current atmospheric evolution models (Marley et al. 1999). However, planetary stellar companions are predicted to be very faint compared to their host star; reduction of the diffracted star light by the aid of coronagraphic devices is therefore required.
At the end of the 20^{th} century, Claude and François Roddier proposed a new coronagraphic concept (Roddier & Roddier 1997) based on replacing the usual opaque occulting disk with a small transparent phase mask, referred to as the Roddier and Roddier phase mask (RRPM). They showed that if the central core of the stellar diffraction pattern was delayed by a π phase change, then destructive interference occurred within the pupil, displacing virtually all of the starlight into a halo surrounding the geometric pupil image. Removing this energy by the aid of a Lyot stop in the following pupil plane was shown to lead to an important reduction of diffracted starlight in the final image projected onto the detector or into a spectrographic instrument.
In 1998, Claude and François Roddier with co-investigators from the Institute for Astronomy of the University of Hawaii joined forces with colleagues at the University of Mexico (UNAM), including one of us (SC), in order to realize the first RRPM and to test experimentally the theoretical predictions. This first-generation phase mask was made by photo-lithographic deposition of an appropriately sized spot of SiO_2 of thickness 700 nm and diameter 200 μm.
While the results of this experiment, described in detail in Guyon et al. (1999), clearly validated the principles of this new coronagraphic concept, it achieved only a modest peak intensity attenuation of $\mathcal{A}_{exp} = 16$. Theoretically, adjusting carefully the size of the mask to the size of the diffraction pattern (or vice-versa, by the aid of a variable iris entrance pupil), a peak intensity attenuation of infinity could have been achieved.
The modest attenuation achieved was explained by the rounded

edges of this first-generation mask. It was therefore clear that technological improvements would be required to push this concept further. This conclusion, together with the double chromatism suffered by the RRPM, both in terms of phase delay and lateral dimension, made the concept sufficiently unattractive to remain virtually unexplored in the literature since then. It did open the road for other phase mask concepts, however, in particular the Four-quadrant phase mask (FQPM, Rouan et al. 2000) which has been extensively studied (Riaud et al. 2001) and tested (Riaud et al. 2003; Mawet et al. 2006) and which currently equip high-contrast imaging projects on ground (Boccaletti et al. 2004; Gratadour et al. 2005) and, soon, in space (Baudoz et al. 2006). It also spurred the development of a phase-mask coronagraph more directly related to the RRPM, the Dual-zone phase mask (DZPM, Soummer et al. 2003b). This concept is based on a small structure covering the central core of the stellar diffraction pattern, but instead of a single phase retardation, this mask includes a second, annular phase retarder surrounding the Roddier-style cylindrical phase disk. None of the retardations being π, achromatic destructive interference is reached by a three-vector nulling, rather than a two-vector nulling as in the original RRPM concept.
Thanks to its large potential for wide-band coronagraphy, the DZPM concept has been preselected as a candidate for the EPICS planet finder instrument (Kasper et al. 2008) for the European Extremely Large Telescope (E-ELT). In this context, a proof of concept experiment has been initiated in the framework of the European Union FP7 program. In preparation for this work, and in order to test the improvements during the last decade of the capacity of micro-optics technology to produce straight-edged phase structures, we decided to repeat the test of the RRPM using a new, second-generation, phase mask. The results of this experiment are reported in this paper. In section 2, we describe the design of this new mask and the technology with which it was manufactured. In section 3, we describe the experimental setup and measurement protocol and in section 4, we present results of the experiments.

2. Design and manufacture of the second-generation Roddier & Roddier phase mask

While the deposition of a cylindrical spot of SiO_2 on a fused silica substrate could be considered a good option for the RRPM, it was judged risky because an inevitable index difference between mask and substrate would lead to interference effects whose impact on the coronagraphic performance is difficult to model and predict. Also, edge effects due to the lift-off of the excess mask material may be expected, as was probably the case in the first-generation mask. An alternative, monolithic option has therefore been investigated, where the phase dot is machined into the substrate by the aid of photo-lithographic ion beam etching. This technique had already been experimented in the context of the development of a segment phasing concept based on a modified Zernike phase contrast sensor (Dohlen et al. 2006), and although the masks were an order of magnitude larger in this case, the results were sufficiently good that its miniaturization seemed reasonable.

The mask fabrication, effectuated at the GEPI laboratory of the Observatory of Paris, included the following steps:
1. Deposition of photoresist onto the substrate
2. Exposition of a small circular region by the aid of a mechanical mask
3. Reactive ion etching of the substrate
4. Cleaning of the substrate

The excellent shape of masks made by this process has been proven by scanning electronic microscopy (SEM), see Figure 1. While a slight rounding of the edges can be seen, the uniformity of the mask depth is seen to be extraordinary.
The optimal diameter of the RRPM was estimated by Roddier & Roddier (1997) to be about $1.05\,\lambda/D$, corresponding to an integral of the electric field over the Lyot stop equal to zero, i.e. an infinite central peak attenuation. Recent research (Ferrari et al. 2007) shows that increasing the mask size to around $1.5\,\lambda/D$ leads to improved contrast in the surrounding halo although the peak attenuation is reduced. To demonstrate this effect experimentally using a source of $\lambda = 677$ nm, we designed our mask to a diameter of 65 μm, allowing for a variable focal ratio of the coronagraphic bench ranging from $F \sim 50$ to $F \sim 100$.
Mask thickness e is given by the equation:

$$(n-1)e = \lambda/2, \quad (1)$$

where n is substrate refractive index. For fused silica, $n = 1.46$, and so the optimal mask depth was 740 nm.

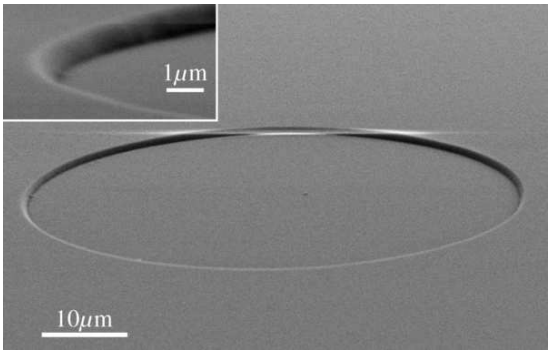

Fig. 1. Scanning electron microscope image of the Roddier & Roddier phase mask, showing real proportions of the full mask (main image) and a zoom on the edge (inset). The edge is remarkably well defined and the depth uniformity is virtually perfect. The images were obtained using an environmental scanning electron microscope, Extended Pressure-SEM (Zeiss Evo 60). To avoid the deposition of a metallic coating onto the component, which would have excluded its future use, we used the low-air pressure, or 'environmental', settings. The horizontal streak seen at the top of the mask is an artefact due to the accumulation of charges along the sharp edges of the mask, caused by the absence of a conductive coating.

3. Experimental setup

3.1. Description of the assembly

The optical design of the coronagraphic assembly is shown in Figure 2(a). The diode laser source is spatially filtered through a 5 μm pinhole and collimated by the lens L1. A variable iris P1 defines the entrance pupil plane (A) of the system. To avoid excessive bench dimensions, a pupil size of 1-2 mm is used. We adjust the entrance pupil diameter, hence the dimension of

the diffraction pattern projected onto the fixed mask, in order to change the relative mask diameter.
The lens L2 provides an image plane (B), in which the RRPM is placed, and also a pupil plane (C), in which the Lyot stop is located. While this setup appears ideal in the sense of minimizing optics, hence aberrations, it does not provide a telecentric beam to the coronagraph, but this does not appear to be of importance for this concept.
The following lens L3 projects the coronagraphic image (D) onto the camera. It also projects the pupil onto a plane (E) some 100 mm behind the image plane, allowing rapid switching between image and pupil plane observations by sliding the camera between these positions.
Focal mask and Lyot stop are mounted on *xyz* micro-positioning stages, allowing both lateral and focus adjustment of these components. Once optimal positioning has been determined, the only adjustments necessary to perform the measurement protocol described below are a lateral (x) movement of the mask to remove or replace it onto the stellar image (a displacement of a few 100 μm is sufficient), and diameter of the entrance pupil and the Lyot stop. A picture of the optical bench can be seen in Figure 2(b).
Images were recorded using an 8-bit camera. To obtain acceptable dynamic range, 3 images were taken at different exposure times from 0.04 ms to 1 s, and composite images were created by extracting annular zones from each image. For each exposure time, a corresponding dark image was taken and subtracted from the scientific images. The resulting image quality proved sufficient for this experiment.

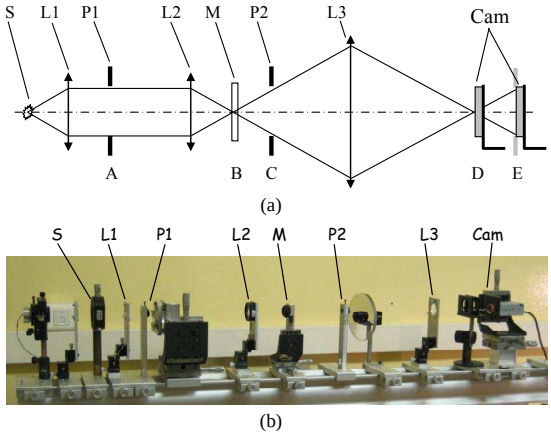

Fig. 2. Coronagraph experiment setup. S: source; L1: collimating lens; P1: variable diaphragm in the entrance pupil (plane A); L2: coronagraph lens; M: coronagraph mask (plane B); P2: variable diaphragm Lyot stop (plane C); L3: imaging lens; Cam: movable camera (planes D and E). (a): Schematic representation of the experimental setup. Vertical scale is exaggerated for clarity. (b): Photograph of the experimental setup.

3.2. Experimental protocol

3.2.1. Adjustment of pupil size

The focal mask is removed from the beam and the camera is located in pupil plane E. A wide Lyot stop aperture is chosen in order to observe the entrance pupil. The iris P1 is adjusted to the desired size as measured off the TV monitor, see Fig. 3(a). As the focal mask is replaced into the beam, the pupil image is transformed, rejecting light into a halo surrounding the geometrical pupil, see Figs. 3(b), 3(c) and 3(d), corresponding to the mask radii of 0.455 λ/D, 0.516 λ/D and 0.741 λ/D, respectively. The efficiency of this rejection and the distribution of the residual intensity within the pupil depends upon the size of the entrance iris. The Lyot stop iris P2 is now closed down so as to eliminate the bright halo, leaving only the residual light within the geometrical pupil. To account for mis-alignments and scatter, the Lyot pupil must always be slightly smaller than the entrance pupil.

3.2.2. Image acquisition

The camera is now slid forwards to the image plane D and the coronagraph mask is removed in order to observe the uncoronagraphic image. Camera exposure time is adjusted to the minimum (0.04 ms), and a variable neutral density (ND) filter is adjusted so as to just avoid saturation of the PSF peak. Images are then acquired at 0.04 ms, 4 ms and 400 ms, in order to constitute a fiducial reference image, see Fig. 4(a). Exact pupil size is deduced from comparing this image with a theoretical Airy pattern.
The coronagraphic mask is then placed into the beam, carefully adjusted to optimize symmetry in the coronagraphic image. Again a series of images is taken, the first one with an exposure time adjusted to just avoid saturation without changing the ND filter, then one or two more images with exposure times ranging up to the maximum allowable of 1 s. Figs. 4(b), 4(c) and 4(d) show composite images for the same three mask radii as considered above.

4. Experimental results

4.1. Results in the pupil plane

The key to understanding the Roddier and Roddier coronagraphic principle lies in the pupil plane. Simple Fourier optics allows us to appreciate the nulling effect due to the beam diffracted by the coronagraphic mask, shifted π radians out of phase, as it interferes with the original top-hat pupil. Since the phase mask is smaller than the stellar Airy pattern, the diffracted beam is broader than the original pupil and it extends beyond the geometrical pupil and since the mask is hard-edged, we expect to see diffraction rings.
Figs. 5(a), 5(b) and 5(c) compare the theoretical coronagraphic intensity profiles in the coronagraph exit pupil plane C with the experimental intensity profiles in the same plane. Again, the images correspond to the mask radii considered above, of respectively 0.455 λ/D, 0.516 λ/D and 0.741 λ/D.
The measured profiles compare well with the theoretical predictions, and the dark diffraction ring is clearly seen. Inside the pupil, the intensity falls sharply, indicating the destructive interference due to the good matching of the field strength of the diffracted beam phase shifted by π radians and the undiffracted beam. For the larger mask, the residual is stronger, but well apodized as expected.

4.2. Results in the image plane

Azimuthally averaged profiles of the coronagraphic and non coronagraphic images have been calculated, see Figs. 6(a), 6(b) and 6(c). The non coronagraphic profile is compared with the

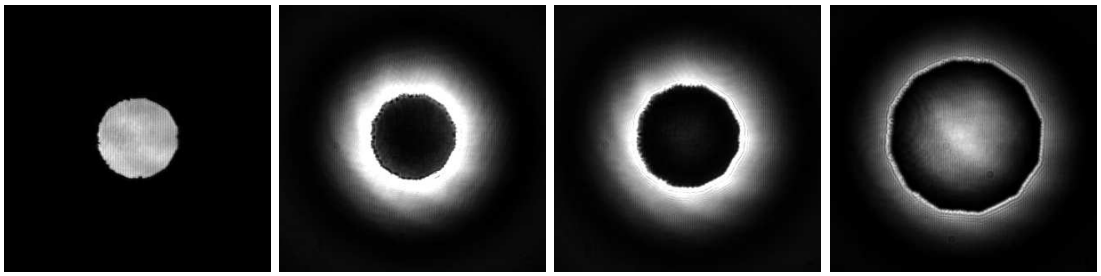

(a) (b) (c) (d)

Fig. 3. Set of pictures obtained in the pupil plane E. (a): Non coronagraphic exit pupil image. (b), (c) and (d): Coronagraphic exit pupil images without Lyot stop corresponding to the mask radii of 0.455 λ/D, 0.516 λ/D and 0.741 λ/D, respectively.

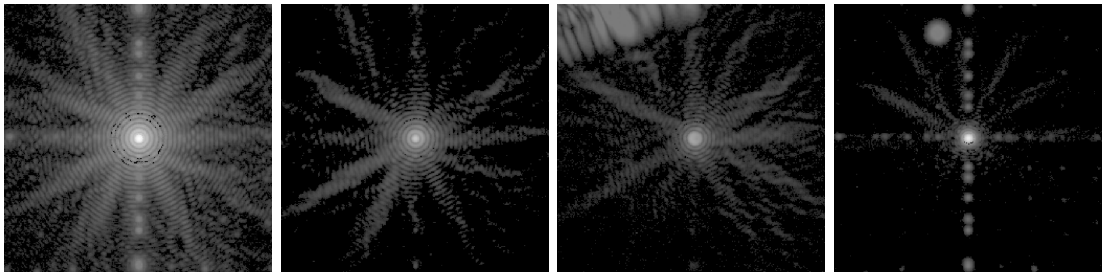

(a) (b) (c) (d)

Fig. 4. Reconstructed images thanks to pictures taken in the image plane D at different exposure times. All the images are normalized to the peak of the un-coronagraphic image. The gray scale is logarithmic, ranging from 1 (white) to 10^{-7} (black). (a): Non coronagraphic image. (b), (c) and (d): Coronagraphic images with Lyot stop corresponding to the mask radii of 0.455 λ/D, 0.516 λ/D and 0.741 λ/D, respectively.

Table 1. Angular separations of the intensity peak and first five bright rings of the Airy diffraction pattern.

	Intensity peak	1^{st} bright ring	2^{nd} bright ring	3^{rd} bright ring	4^{th} bright ring	5^{th} bright ring
Angular separation in λ/D	0.00	1.64	2.68	3.70	4.71	5.71

theoretical Airy pattern, indicating a very good correspondence. This comparison turned out to be useful in optimizing the image analysis approach, allowing to understand some unexpected features of the camera such as exposure-time saturation for the shortest exposure times, leading us to implement a non-linear exposure-time correction.

Theoretical coronagraph images were calculated using the semi-analytic method based on matrix Fourier transforms described by Soummer et al. (2007). The measured coronagraphic profile corresponds well with the theoretical prediction down to a contrast of around 10^{-6}, both for the 0.455 λ/D mask (Fig. 6(a)) and the 0.516 λ/D case (Fig. 6(b)). For the 0.741 λ/D case (Fig. 6(c)), however, the correspondence with theory is less good. Still, the contrast performance in the field is clearly better than in the other cases.

In order to investigate the effect of varying mask size, we have calculated the intensity at different distances from the star, plotted as a function of mask radius, both for theoretical and measured profiles. Figure 7 displays these results. We considered six distances from the main optical axis, corresponding to the central peak and the first five bright rings of the Airy diffraction pattern (see Table 1). At each of these positions, we averaged the intensity of the coronagraphic image over an annulus of width λ/D. Theoretical results are plotted as lines, and experimental data are plotted as points. All results are normalized with respect to the central intensity of the un-coronagraphed image, averaged in the same way.

The theoretical curves clearly show that the mask giving the optimal peak attenuation, seen here to reach beyond 10^4, does not correspond to the optimal performance in terms of contrast in the field. At the 5^{th} Airy ring, an improvement by a factor of about 10 can be expected by increasing the mask radius to around 0.65 λ/D. The experimental measurements confirm this result in spite of some loss of performance in the case of larger mask sizes. Indeed, as was already seen in Fig. 6(a), the measurements fit very well with theory for mask radii smaller than 0.55 λ/D, with an average difference between experimental and theoretical intensity less than 0.21 magnitudes, see Table 2. For larger masks, differences up to 1.7 magnitudes are observed.

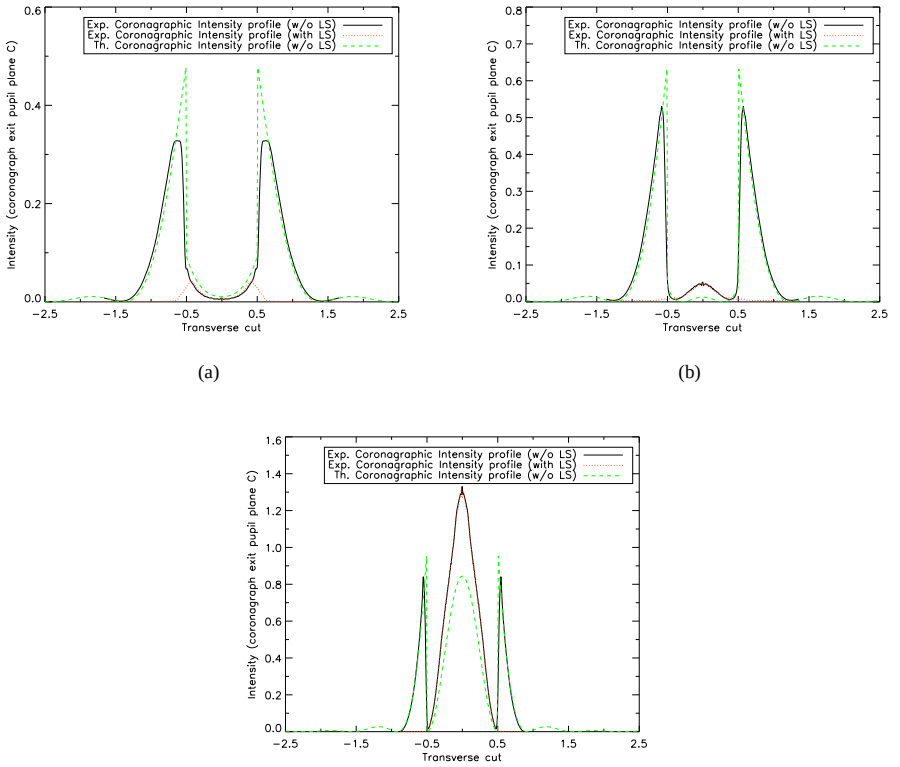

Fig. 5. Experimental and theoretical intensity profiles achieved in the re-imaged pupil plane C in the presence of the RRPM. Mask radii are estimated to be $0.455\,\lambda/D$ (a), $0.516\,\lambda/D$ (b) and $0.741\,\lambda/D$ (c), respectively. LS stands for Lyot stop. See text for a detailed description of the plot.

Table 2. Averaged difference between the experimental and theoretical intensity values for different mask radii. We exclude the central peak values from the averages.

Mask radius in λ/D	0.294	0.304	0.338	0.359	0.455	0.516	0.645	0.656	0.741	0.851	0.930
$\overline{\Delta I}$ in stellar magnitudes	0.12	0.21	0.06	0.07	0.07	0.09	1.67	1.72	1.54	1.54	1.66

5. Discussion and conclusion

The main goal of our experiment, demonstrating that improved technology was capable of providing a significant improvement of coronagraphic performance compared with the original RRPM demonstrator of 1999, has clearly been reached. In particular, while the original experiment was limited to a peak attenuation of 16, we have measured attenuation as high as 216. It is believed that the main improvement is in the mask profile, where our device has been seen to have a very sharp edge.

We have also provided a quantitative evaluation and experimental demonstration of the apodizing effect expected for larger phase masks, as described by Ferrari et al. (2007), in spite of a deterioration of the experimental results for mask radii larger than $0.55\,\lambda/D$. We believe the main reasons for this deterioration are linked to features of our experimental setup, combined with the high peak intensity and increased aperture size corresponding to the larger mask diameters. In particular, a family of ghosts are observed along the vertical axis, probably due to internal reflections between the detector surface and the double detector window. These ghosts are invisible in the case of the small masks (Figs. 5b and c), but clearly seen both in the non-coronagraphic image (Fig. 5a) and in the large-mask coronagraphic image (Fig. 5d). Deficiencies in terms of optical quality of the bench also become more important in the case of the larger mask size, where the entrance pupil was enlarged so as to reduce the focal ratio. This stresses the optical setup both in terms of source uniformity, optical aberrations, and surface quality. Other error sources include mechanical stability and adjustment accuracy. All adjustments are manual, with direct TV images as the only aid to alignment. Slight misadjustments cause spillage of light back into the pupil, hence reduced coronagraphic efficiency.

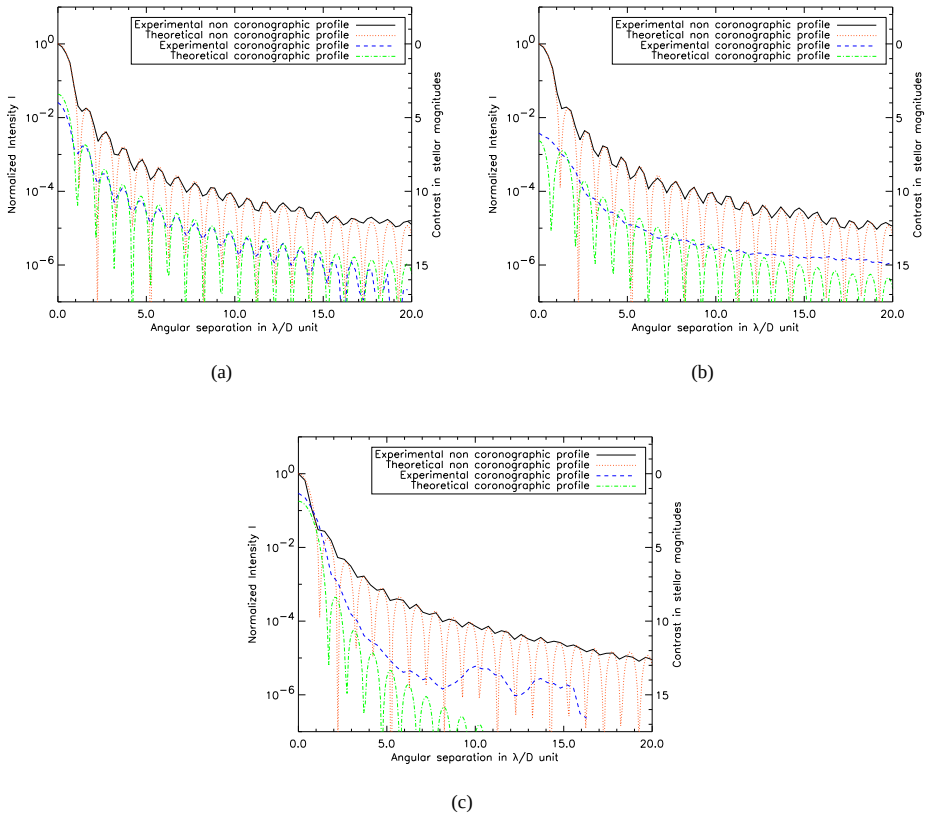

Fig. 6. Radial profiles of the experimental and theoretical images achieved in the presence or not of the RRPM. Mask radii are estimated to be 0.455 λ/D (a), 0.516 λ/D (b) and 0.741 λ/D (c), respectively.

Thanks to this technological demonstration, we believe the RRPM, especially in its apodized version expected to act as a perfect monochromatic coronagraph (Guyon & Roddier 2000; Aime et al. 2002; Soummer et al. 2003a), could find its place in astrophysical instruments when spectral bandwidth can be traded against access to small inner working angles. It can also be used as a tool for experimental studies of coronagraphic imaging: our bench has already served this purpose, demonstrating the effect of dust and cosmetic defects in high contrast imaging systems (Dohlen 2008). Furthermore, our results clearly pave the way for the achromatic Dual Zone coronagraph (Soummer et al. 2003b). A more elaborated version of our bench is currently being prepared where we plan to implement an apodized version of the RRPM coronagraph, as well as the prototype DZPM coronagraph which is being developed for the E-ELT study.

Acknowledgements. We are grateful for a grant from the Grupo Santander (Spain) through Encuentros Astrofísicos Blas Cabrera (UNAM-IAC), and our home institutions for their support. M. N'Diaye is supported by a fellowship from the Foreign Office of the Mexican Government.

References

Aime, C., Soummer, R., & Ferrari, A. 2002, A&A, 389, 334
Baudoz, P., Boccaletti, A., Riaud, P., et al. 2006, PASP, 118, 765
Boccaletti, A., Riaud, P., Baudoz, P., et al. 2004, PASP, 116, 1061
Burrows, A. & Sharp, C. M. 1999, ApJ, 512, 843
Dohlen, K. 2008, in Society of Photo-Optical Instrumentation Engineers (SPIE) Conference Series, Vol. 7017, Society of Photo-Optical Instrumentation Engineers (SPIE) Conference Series
Dohlen, K., Langlois, M., Lanzoni, P., et al. 2006, in Society of Photo-Optical Instrumentation Engineers (SPIE) Conference Series, Vol. 6267, Society of Photo-Optical Instrumentation Engineers (SPIE) Conference Series
Ferrari, A., Soummer, R., & Aime, C. 2007, Comptes Rendus Physique, 8, 277
Gratadour, D., Rouan, D., Boccaletti, A., Riaud, P., & Clénet, Y. 2005, A&A, 429, 433
Guyon, O., Roddier, C., Graves, J. E., et al. 1999, PASP, 111, 1321
Guyon, O. & Roddier, F. J. 2000, in Presented at the Society of Photo-Optical Instrumentation Engineers (SPIE) Conference, Vol. 4006, Proc. SPIE Vol. 4006, p. 377-387, Interferometry in Optical Astronomy, Pierre J. Lena; Andreas Quirrenbach; Eds., ed. P. J. Lena & A. Quirrenbach, 377–387

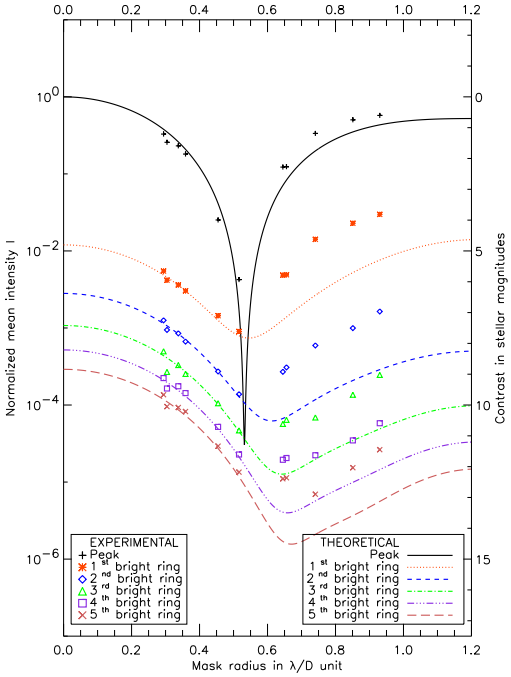

Fig. 7. Normalized image plane intensity at different field positions as a function of RRPM mask radius. The field positions considered correspond to bright rings in the uncoronagraphic image, whose radial distances from the central star are given in Table 1. Theoretical intensities are shown as lines, experimental values are shown as points. See text for a detailed description of this plot.

Kasper, M. E., Beuzit, J.-L., Verinaud, C., et al. 2008, in Presented at the Society of Photo-Optical Instrumentation Engineers (SPIE) Conference, Vol. 7015, Society of Photo-Optical Instrumentation Engineers (SPIE) Conference Series
Marley, M. S., Gelino, C., Stephens, D., Lunine, J. I., & Freedman, R. 1999, ApJ, 513, 879
Mawet, D., Riaud, P., Baudrand, J., et al. 2006, A&A, 448, 801
Riaud, P., Boccaletti, A., Baudrand, J., & Rouan, D. 2003, PASP, 115, 712
Riaud, P., Boccaletti, A., Rouan, D., Lemarquis, F., & Labeyrie, A. 2001, PASP, 113, 1145
Roddier, F. & Roddier, C. 1997, PASP, 109, 815
Rouan, D., Riaud, P., Boccaletti, A., Clénet, Y., & Labeyrie, A. 2000, PASP, 112, 1479
Soummer, R., Aime, C., & Falloon, P. E. 2003a, A&A, 397, 1161
Soummer, R., Dohlen, K., & Aime, C. 2003b, A&A, 403, 369
Soummer, R., Pueyo, L., Sivaramakrishnan, A., & Vanderbei, R. J. 2007, Optics Express, 15, 15935
Woolf, N. & Angel, J. R. 1998, ARA&A, 36, 507

C.2 Conference Proceedings

C.2.1 Coronagraph feasibility studies on FRIDA
First light science with the GTC, Miami, USA, 2006

To appear in "First Light Science with the GTC (2006)" *RevMexAA(SC)*

CORONAGRAPH FEASIBILITY STUDIES ON FRIDA

M. N'Diaye[1,2], S. Cuevas[1], K. Dohlen[2]

We propose a way to introduce stellar coronagraphy within FRIDA (inFRared Imager and Dissector for Adaptive Optics [AO] system of the Gran Telescopio Canarias, GTC). We represent the FRIDA coronagraph performance that could be achieved. We also give a few words about the usefulness and limits of coronagraphy.

FRIDA is being designed to provide high quality imaging in broad and narrow band, and spatially resolved spectroscopy with the use of an Integral Field Unit. The presence of a stellar coronagraph inside its optical assembly would allow to reach the direct imaging of faint objects close to brilliant stars, like exoplanets or circumstellar disks, and a spectral analysis of them.

The study is focused here on the main two focal plane mask coronagraph: the Classical Lyot Coronagraph (CLC, an opaque mask) and the Roddier & Roddier Coronagraph (CRC, a π phase shifting mask). GTC aperture is hexagonal so, to improve the starlight extinction results, a inscribed circular diaphragm is placed in the entrance pupil. Adding an adequate Gaussian apodization mask to the aperture allows the increase of the coronagraph performance. It can be designed by means with a doublet of lenses with the same refraction index and where the divergent one is in an absorbing neutral density glass characterized by the Optical Density (OD). The presence of the telescope secondary mirror shadow within the entrance aperture, associated with the coronagraph focal plane mask, makes appear a central illumination at the coronagraph exit pupil center. To block these undesired diffraction effects, an obscuration disk is put in the corresponding plane.

The coronagraph configuration for FRIDA is illustrated in Figure 1 and the corresponding results in Figure 2. Choosing $OD = 0.10$ for the Gaussian apodization mask provides a star intensity decrease by a factor 10^6 (or 15 magnitudes).

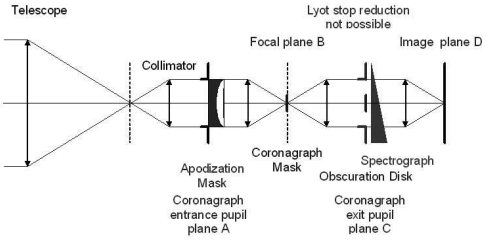

Fig. 1. Configuration for FRIDA optical assembly.

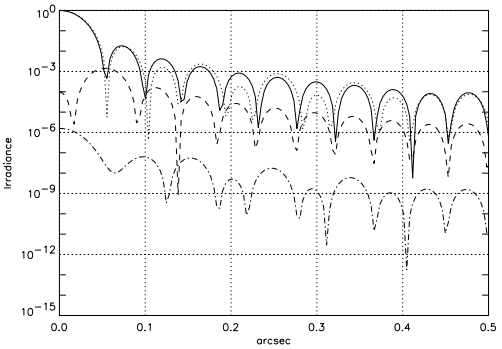

Fig. 2. Plot in log scale of the axial image intensity profile for a CRC with a Gaussian apodized centrally obstructed circular aperture (dash dot) compared with the Airy pattern (solid), the only apodized (dotted) and the CRC (dashed) profiles. All profiles are normalized to the central intensity of the Airy pattern and represented at 2.2 μm.

In the case of ground-based observations, coronagraphs reduce the coherent part of the AO corrected Point Spread Function (PSF) and Differential imaging technique defeats the speckles noise in the PSF halo. So, both combined in FRIDA are expected to allow the study of faint companions.

REFERENCES

Aime, C., & Soummer, R. 2004, ApJ, 612, L85
López, J. A., et al. 2006, RevMexAA Ser. Conf., 26, 151
Marois, C., et al. 2004, ApJ, 615, L61
Roddier, F., & Roddier, C. 1997, PASP, 109, 815
Soummer, R., et al. 2003, A&A, 397, 1161

[1]Instituto de Astronomía, UNAM, Apartado Postal 70-264 Ciudad Universitaria, 04510 México, D.F., México (mndiaye, chavoc@astroscu.unam.mx).

[2]Laboratoire d'Astrophysique de Marseille, 2 place Leverrier, 13248 Marseille, Cedex 4, France (Kjetil.Dohlen@oamp.fr)

C.2.2 Apodized Pupil Lyot Stop, working without Lyot stop
***Advanced Infrared Technology and Applications 9*, León, Mexico, 2007**

Apodized Pupil Lyot Stop, working without Lyot stop

Mamadou N'Diaye[1,2], Kjetil Dohlen[2] and Salvador Cuevas[1]

[1] Instituto de Astronomía, UNAM

Apartado Postal 70-264 Ciudad Universitaria, 04510 México, D.F., México

mndiaye@astroscu.unam.mx, chavoc@astroscu.unam.mx

[2] Laboratoire d'Astrophysique de Marseille, OAMP

2 place Leverrier, 13248 Marseille, Cedex 4, France

Kjetil.Dohlen@oamp.fr

Abstract: In the context of high contrast imaging, the Apodized Pupil Lyot Coronagraph (Soummer, 2005) is a combination of an apodization placed in the input pupil, an opaque mask in the following focal plane and a Lyot stop in the coronagraph exit pupil plane. This diaphragm blocks the rejected starlight that is left outside the exit pupil. In this work, we propose to remove this Lyot stop. Good attenuation of the star image intensity can be reached. Furthermore, we add a Differential Imaging method to this coronagraph in order to defeat residual speckles. This is the main noise source appearing in a star image, obtained with a ground-based instrument equipped with Adaptive Optics system. This configuration gives very promising results and could be applied on instruments in progress, like FRIDA (inFraRed Imager and Dissector for the Adaptive optics system of the Gran Telescopio Canarias).
Keywords: Infrared Astronomy, High angular resolution, Adaptive Optics

1. Introduction

1.1 Astronomical context

Extrasolar planets (or exoplanets) are planets orbiting a star other than the Sun. Interest for them has not stopped increasing, since the first official exoplanet detection was realized by Mayor and Queloz in 1995 [1], with radial velocity measurements. To date, the count of known exoplanet candidates stands at more than 265 [2]. Almost of all these detections were done with indirect methods, and mainly the radial velocity one. The next step consists of direct imaging these faint substellar companions.

Imaging these faint objects will allow reaching astronomical data about them, complementary to those obtained with indirect detection. Their spectrum analysis will lead to identification of atomic and molecular lines and provide to astronomers, information about their atmospheric chemical composition. It will allow accessing to planetary companion mass, better understanding the planetary formation mechanism [3] and calibrating atmospheric evolution models [4]. The eventual detection of bio-signals (like water [H2O], oxygen [O2], ozone [O3]…) could bring elements of response about the presence of life apart from the Earth [5].

However and until now, only one extrasolar planet has been imaged [6]. Imaging substellar companions and extrasolar planets in particular, is a very difficult task. To make terrestrial observations, ground-based telescopes equipped with very efficient Adaptive Optics (AO) system are expected. Our terrestrial atmosphere distorts the wave fronts coming from stellar objects. AO allows correcting the aberrations induced by the atmospheric turbulence. It aims at exploiting the diffraction-limited potential of ground-based telescopes. Other techniques are required beyond AO system, to go on increasing the contrast at small angular separations and allow imaging faint companions close to bright stars. Stellar coronagraphy raises hope to reach this goal.

1.2 Stellar coronagraphy

Stellar coronagraphy represents a first step to achieve high contrast imaging. Poetically, it consists of eclipsing artificially an observed bright star allowing to see dim companions, thanks to an optical setup. Concretely, the stellar coronagraph aims at decreasing the diffracted starlight intensity.
Several coronagraphic devices were proposed during the last decade. Let mention the Achromatic Interfero Coronagraph [7, 8], based on the Michelson interferometer to create destructive interferences and achieve bright star extinction. But, mayor part of the coronagraphic designs uses a focal plane mask [9-13]. The mask is centered in the focal plane of the telescope aperture, where the on-axis bright star is imaged. Moreover, it is designed to not alter an off-axis substellar companion. Coronagraphic masks can be divided in two categories: the opaque mask that directly blocks the starlight contribution [9] whereas the phase mask cancels the star with destructive interferences [10]. Another way consists in apodizing the entrance pupil (an image of the telescope aperture) [14,15], to attenuate starlight intensity. Wings of the on-axis bright star Point Spread Function (PSF) are then smoothed and can let appear an off-axis faint companion. Apodized entrance pupils and focal plane mask can also be combined [16-19], to go on increasing the image contrast.
Theoretically, all these coronagraphs achieve very good results and should work very well with space-based instruments. However, coronagraph performance is limited in the case of ground-based instruments equipped with AO. It is mainly due to the residual aberrations present within the star diffracted light. They form a noisy background which prevents from detecting faint objects close to bright star and represent a limitation for coronagraphy. Therefore, additional techniques are needed in order to make direct detection of faint objects.

1.3 Differential Imaging method

Residual speckles result from the non perfect AO correction of wavefront aberrations, caused by the atmospheric turbulence. They represent the main noise source and must be tackled in order to detect faint objects [20]. To defeat them, several techniques were proposed recently.
The Angular Differential Imaging [21,22] consists of combining several images acquired at the same time, but at different field angles to subtract quasi-static speckles. Theoretically, this technique gives perfect results but in practice is limited by the quasi-static speckle time evolution. On the other hand, the Simultaneous Spectral Differential Imaging (SSDI) [23] method uses two o three images, taken simultaneously at different but close wavelengths. These images are spectrally rescaled before being subtracted from one another, taking advantage of the wavelength dependence of the speckles. Let mention the spectral deconvolution method [24], which can be seen as a general case of the SSDI technique. Indeed, several frames of a stellar object are taken simultaneously and at different wavelength. They form a data cube, in which images can be extracted to be recombined after wavelength rescaling.
In this paper, focus will be made here on the SSDI method. This process technique allows reducing speckle noise and enhancing faint companions. Images are taken at two or three different wavelengths that span a well-known resolved absorption line, in the spectrum of the substellar companion. For instance, one can cite the methane (CH4) absorption break in H-band for brown dwarfs and Jupiter-like planet [25]. Thus, after rescaling and subtraction between images, speckle noise is attenuated and the substellar companion enhanced. No operation is applied to the faint object, since it is just present in one of the two or three processed frames. SSDI method has already been experimented in laboratory and planned to be apply on work in progress instruments, like Gemini Planet Imager [26] or SPHERE on the Very Large Telescope [27]. The present study will focus on the SSDI application in FRIDA, the work in progress instrument for the Gran Telescopio Canarias [28].

1.4 FRIDA, a work in progress instrument for the GTC

FRIDA (in**F**ra**R**ed **I**mager and **D**issector for the **A**daptive optics system of the 10.4 m Gran Telescopio Canarias [GTC]) is being designed as a diffraction limited instrument with broad and narrow band

imaging and integral field spectroscopy (IFS) capabilities to operate in the wavelength range 0.9-2.5 μm. FRIDA will be installed at the Nasmyth A platform behind GTCAO (the Adaptive Optics system of the GTC). It will use diffraction-limited optics to avoid degrading the Strehl ratio (It represents the ratio between the intensity peaks of the studied image and the perfect image that would provide the system, in absence of any aberration) delivered by the GTCAO system in the near-infrared.
The 10.4m Gran Telescopio Canarias is currently being installed in the Observatorio del Roque de los Muchachos on the island of La Palma. The "standard seeing scenario" of this astronomical site assumes a Fried parameter r0=0.15 m. (it defines the radius of coherence within an incoming wave front) and a turbulent windspeed v=10 $m \cdot s^{-1}$ [29]. GTCAO is supposed to have a performance similar to an Adaptive Optics system with the following deformable mirror and sub-aperture geometry: 21 actuators and 20 sub-apertures placed across the long axis of the telescope pupil [30]. If wavefront sensor measurements are considered perfect (ideal detector), the achieved Strehl ratio in H-band should be 0.607.
This should be the expected Strehl ratio delivered by the AO system to FRIDA. These characteristics represent the initial constraints to image substellar companion with FRIDA. Upgrade paths are already planned for FRIDA to do high contrast imaging, since the introduction of a stellar coronagraph was considered in the optical design.

1.5 Feasibility study to do high contrast imaging with FRIDA

Three coronagraphic configurations are proposed for FRIDA. The first one is the Classical Lyot Coronagraph (CLC) based on the focal plane opaque mask [8]. The second option is the Classical Roddier Coronagraph (CRC), which uses a π-phase mask [9]. Whereas the third solution thought for FRIDA is an improvement of the Classical Lyot Coronagraph, with in addition an apodization placed in the entrance pupil. Like CLC or CRC, Apodized Pupil Lyot Coronagraph (APLC) [19] uses a Lyot stop, a diaphragm present in the re-imaged pupil plane to block the star diffracted light. Indeed, light present outside the coronagraph exit pupil comes from the rejection done by the coronagraphic mask. Unfortunately, APLC cannot be used in its traditional version for FRIDA, since mechanical constraints prevent from putting a Lyot stop in its spectrograph pupil plane.
Therefore, we decide to study the APLC working without Lyot stop (APLC w/o LS). In Section 2, we report its theoretical performance. We determine the coronagraphic gain reached with the APLC w/o LS for two instrumental cases: the theoretical space-based telescope "GTC + FRIDA" and the ground-based instrument "GTC + GTCAO + FRIDA". We evaluate the achieved performance and we consider the intensity attenuation loss, induced by the absence of Lyot stop.
We follow this study, by simulating the combination "APLC w/o LS + Simultaneous Spectral Differential Imaging method". The purpose is to quantify the star intensity attenuation that can be reached with this association. The direct application is done for FRIDA in this paper. In section 3, we detail the main results achieved for the ground based instrument "GTC + AO + FRIDA". The different results, presented here, would allow evaluating which contrast can be achieved with this instrument.

2. Apodized Pupil Lyot Coronagraph, working without Lyot stop

2.1 Apodized Pupil Lyot coronagraph (APLC)

The Apodized Pupil Lyot Coronagraph (APLC) is an improvement, of the Classical Lyot Coronagraph, proposed by R. Soummer (see [19]). APLC is a combination of an apodization placed in the input pupil, an opaque mask in the following focal plane and a Lyot stop in the coronagraph exit pupil. This diaphragm is used to block the rejected starlight that is left outside the coronagraph exit pupil. Fig. 1 gives an illustration of the APLC optical setup. Optimization methods were proposed for APLC to allow performance being rather insensitive to telescope designs [31]. APLC is being manufactured by the Lyot project team [32] and planned to be included in several work in progress instruments, like the Gemini Planet Imager (see [26]) or SPHERE, the planet finder instrument for the Very Large Telescope (see [27]). An APLC is also scheduled for EPICS, the planet hunter for the future European Extremely Large Telescope [33]. Here, we consider the introduction of an APLC within the FRIDA optical assembly.

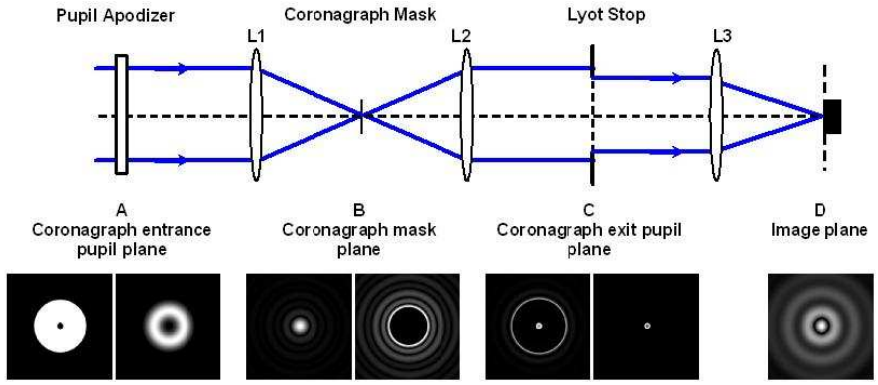

Fig. 1: Schematic illustration of the Apodized Pupil Lyot Coronagraph, with the respective images in each plane. From left: images in the coronagraph entrance pupil plane A, before and after apodization of the pupil, images in the focal plane before and after application of an opaque mask, images in the coronagraph re-imaged pupil plane, before and after application of a Lyot stop (diameter equal to 90% the entrance pupil diameter) and the coronagraphic image in the image plane D.

2.2 Apodized Pupil Lyot coronagraph, working without Lyot stop (APLC w/o LS)

In the case of FRIDA, the insertion of a classical APLC was made impossible, because of mechanical constraints. Fig. 2 shows the FRIDA optical assembly in its Integral Field Spectroscopy (IFS) mode. If the pupil apodizer can be inserted in the FRIDA first pupil plane and the opaque mask in the FRIDA second image plane, the introduction of a Lyot stop is made impossible in its second pupil plane, in which the FRIDA diffraction gratings takes place there. However, the entrance pupil apodizer concentrates the on-axis star light on the opaque mask. A proper choice of the apodization allows focusing a maximum of star diffracted light on the coronagraphic mask. Hence, the amount of the star residual energy present in the re-imaged pupil plane is not very significant inside, but also outside the exit pupil. One can wonder how crucial the presence of the Lyot stop is and if its absence affects the APLC performance. To reconsider the insertion of the APLC within FRIDA design, we decide to study the performance of this coronagraph working without Lyot stop.

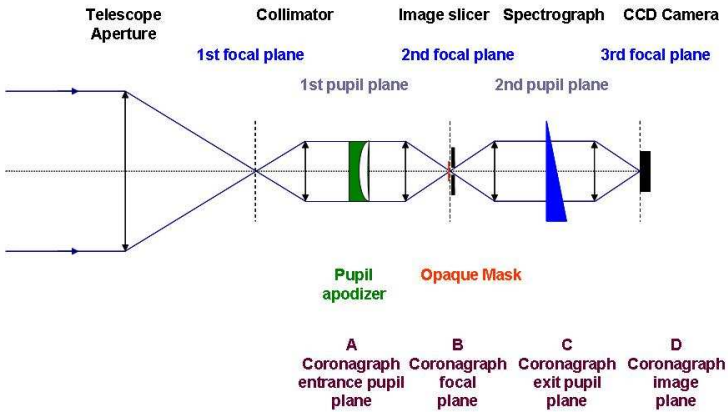

Fig. 2: Simplified representation of the FRIDA optical assembly in IFS mode. In this scheme, the elements of the Apodized Pupil Lyot Coronagraph are inserted: the pupil apodizer is put in the 1st pupil plane, the opaque mask in the second focal plane. However, the Lyot stop cannot be introduced in the second pupil plane for some mechanical constraints (presence of the spectrograph diffractive elements in this plane).

2.3 Obtained results with this configuration, for FRIDA

Apodized Pupil Lyot Coronagraph working without Lyot stop (APLC w/o LS) is one of the adopted coronagraphic configurations for FRIDA. We want to quantify the attenuation intensity reached in this case. In Integral Field Spectroscopy (IFS) mode, FRIDA presents four systems of lenses (see Fig. 2 for a schematic representation). In our study to come, we will consider our optical system free of aberrations. In IFS mode, FRIDA should be able to work in low, intermediate and high power spectral resolution R. We decide to focus this study on low spectral resolution (R=1500) in H-band (central wavelength of observation: λ=1.65µm) and images are considered monochromatic.
GTC associated to a field rotator will provide a circular entrance pupil to FRIDA. Moreover, GTC central obstruction size is equal to 12% of the primary mirror diameter. As we mention previously, we do not use Lyot stop at all. Three different radii were chosen for the opaque mask: 2.30λ/D, 2.80λ/D and 3.15λ/D. Apodizations are computed for these different mask sizes and entrance pupil geometry. The respective apodizer throughputs are represented in Fig. 3. In the following sections, we quantify the coronagraphic performance, first for the space-based instrument "GTC + FRIDA equipped with APLC w/o LS" and furthermore for the ground-based instrument "GTC + GTCAO, the adaptive optics system of the GTC + FRIDA equipped with APLC w/o LS".

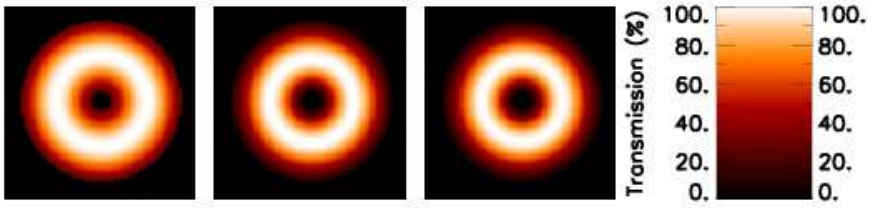

Fig. 3: From left: Apodizer throughput computed for a 12% centrally obscured entrance pupil with the following radii 2.30λ/D, 2.80λ/D and 3.15λ/D for the opaque mask.

2.3.1 Attenuation intensity reached with APLC w/o LS: space-based instrument case.

Fig. 4 gives the coronagraphic PSF profiles, for different opaque mask size, compared to the non coronagraphic one. These simulation results are calculated in the case of the space-based instrument "GTC + FRIDA equipped with APLC w/o LS".
A theoretical gain can be reached, in stellar magnitudes: 1.53, 4.06 and 5.01, for the respective opaque masks of radius 2.30λ/D, 2.80λ/D and 3.15λ/D. These values are achieved at an angular distance of 4.0λ/D from the main optical axis. These results show the efficiency of the APLC, in absence of Lyot stop. APLC w/o LS succeeds in reaching star attenuation intensity. Moreover, its coronagraphic gains are interesting for a space-based instrument, which could not insert a Lyot stop in its optical assembly.

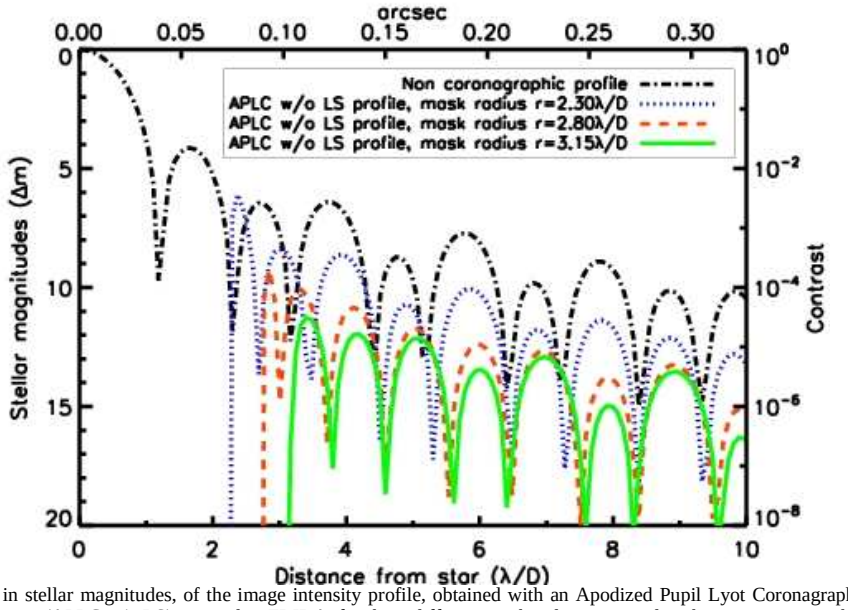

Fig. 4: Plot, in stellar magnitudes, of the image intensity profile, obtained with an Apodized Pupil Lyot Coronagraph working without Lyot stop (APLC w/o LS) inserted in FRIDA, for three different mask radii, compared to the non coronagraphic profile. The wavelength of study chosen here is λ= 1.65μm. These results are achieved for the space-based instrument "GTC + FRIDA".

2.3.2 Attenuation intensity reached with APLC w/o LS: ground-based instrument case.

Let also remind that we assume that GTC is equipped with its Adaptive Optics system (GTCAO). The software CAOS (Case for Adaptive Optics System [34]) is used to simulate the starlight coming from GTCAO and entering through FRIDA. So, APLC w/o LS installed within FRIDA receives AO corrected wave fronts and they naturally contain residual errors, since the AO correction is not perfect. To carry out this study, we work with 160 statistically independent phase screens and we choose the mean "standard seeing scenario" of the ORM astronomical site for our analysis: r_0= 15 cm at λ= 0.5 μm and a turbulent velocity of 10 $m \cdot s^{-1}$. We use an on axis-bright guide star at null zenith angle. The simulation considers the following deformable mirror and sub aperture geometry: 21 actuators and 20 sub apertures placed across the long axis of the telescope pupil. The wavefront sensor measurements are considered perfect (ideal detector). The achieved Strehl ratio in H band is 0.607.

2.3.3 Discussion

In Fig. 5, we can observe the obtained results with APLC w/o LS for the ground-based instrument "GTC + AO + FRIDA". A theoretical gain can be reached, in stellar magnitudes: 1.44, 2.16 and 2.41, for the respective opaque masks of radius 2.30λ/D, 2.80λ/D and 3.15λ/D. These values are achieved at an angular distance of 4.0λ/D from the main optical axis. Using APLC w/o LS for FRIDA remains interesting since star brightness attenuation is realized. Moreover, we avoid detector saturation, in which the coronagraphic image will be formed. The core and the first one or two bright rings of the star image are occulted by the coronagraphic opaque mask. Hence, we increase the FRIDA image dynamic range.

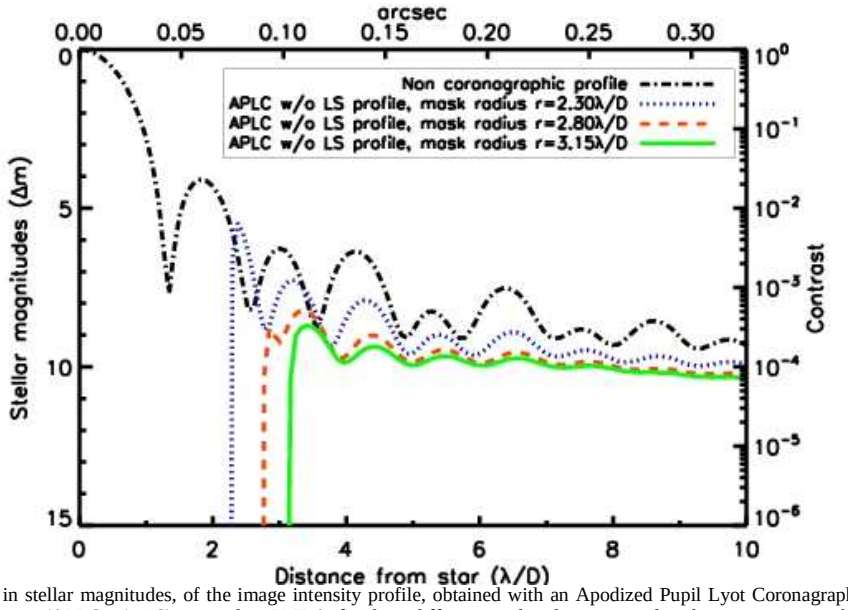

Fig. 5: Plot, in stellar magnitudes, of the image intensity profile, obtained with an Apodized Pupil Lyot Coronagraph working without Lyot stop (APLC w/o LS) inserted in FRIDA, for three different mask radii, compared to the non coronagraphic profile. The wavelength of study chosen here is λ= 1.65µm. These results are achieved for the ground-based instrument "GTC + GTCAO + FRIDA".

2.3.4 To increase the contrast: need to add a differential imaging method

However, the performance of APLC w/o LS is limited by the speckle noise. If we want to detect some faint companions in the star vicinity, a combination of the stellar coronagraph with Differential Imaging techniques is required. Residual speckles are the main source noise and the major obstacle for the direct detection of substellar companions [20]. Simultaneous Spectral Differential Imaging (SSDI) method allows tackling these speckles present in the coronagraphic image [23]. In the next section, we propose to give some first results about simulations of the association "GTC + GTCAO + FRIDA equipped with APLC w/o LS + Simultaneous Spectral Differential Imaging method".

3. Addition of a Differential Imaging method

3.1 Interest and description of the Simultaneous Spectral Differential Imaging method

Simultaneous Spectral differential Imaging (SSDI) method aims to remove the speckle noise, the main obstacle for the detection of substellar companions. We use the wavelength dependence of the residual speckles to suppress them.
In its basic version (Simple Differential Imaging [SDI] method), SSDI consists of taking simultaneously two star PSF images at close wavelengths. These images are precisely similar, except for known scale and intensity factors. Image processing allows compensating these terms. Residual speckles are rescaled in both images and reduced with a subtraction between the two frames. The predicted attenuation corresponds to $A_2 \sim 2\sigma_\varphi^2 \, \Delta\lambda/\lambda$, where σ_φ^2 is the wavefront phase variance and $\Delta\lambda$, the bandpass separation.
Double Differential Imaging (DDI) method is an improvement of the SDI one. It generalizes the technique to three simultaneous images taken at close wavelengths. Three frames are combined in a double difference, to strongly damp the residual speckle. It results a theoretical attenuation $A_3 \sim A_2^2$.

3.2 Simultaneous Spectral Differential Imaging, a feasible method with FRIDA

FRIDA should be able to provide a data cube of images, when it works in IFS mode. Indeed, thanks to its Integral Field Unit Spectrograph, FRIDA should give several simultaneous and wide field images of the observed stellar object at different wavelengths. Several image processing could be applied to extract new astronomical data about the images. In particular, extracting three images at different wavelengths from the FRIDA data cube will be possible. Therefore, applying SSDI method with FRIDA becomes something realizable and realistic. Thus, high contrast imaging can be reached with FRIDA. The idea is to use three simultaneous coronagraphic images obtained with APLC w/o LS at different wavelengths. The next step consists in combining them with the SSDI method. In the following section, we present the simulation results obtained in this configuration. FRIDA is assumed to work in low spectral resolution ($R= \lambda/\Delta\lambda = 1500$). Let remind that images have a Strehl ratio S= 0.607.

3.3 Simulation results for FRIDA with the APLC w/o LS configuration

3.3.1 Attenuation intensity reached in this case

Fig. 6 shows the obtained results when FRIDA is equipped with APLC w/o, in IFS mode. In this case, the achieved star intensity attenuation is, in stellar magnitudes: 1.44 when we just use APLC w/o LS, 10.21 when the coronagraph is associated to SDI technique and 15.55 when the coronagraph is combined to DDI method. These results are achieved at an angular distance of 4.0λ/D from the main optical axis.

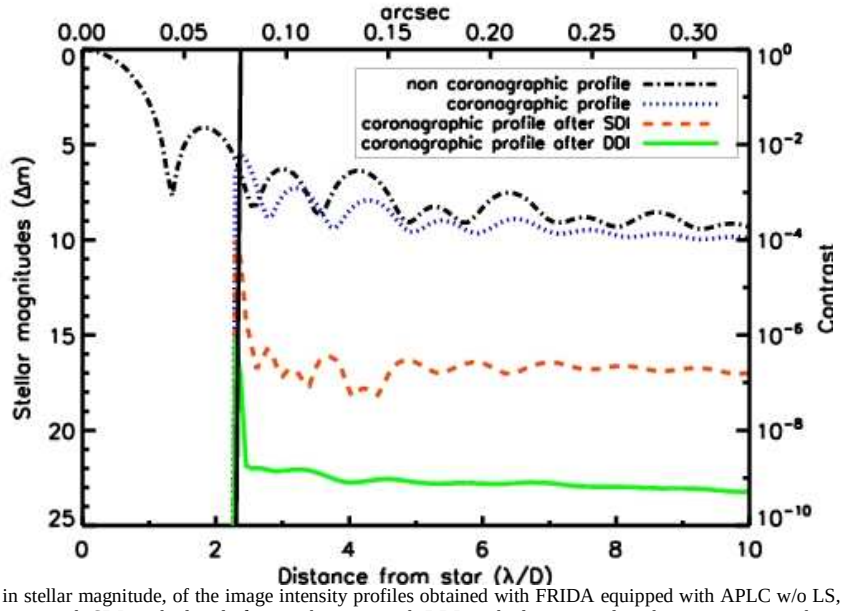

Fig. 6: Plot, in stellar magnitude, of the image intensity profiles obtained with FRIDA equipped with APLC w/o LS, first alone, after combination with SDI method and after combination with DDI method, compared to the non coronagraphic profile. The opaque mask radius is r=2.30λ/D (mask area delimited by the black vertical line). These results are obtained in presence of initial wavefront errors (Strehl ratio:S=0.607). The wavelengths of study, chosen for this simulation, are λ_1= 1.6489 µm, λ_2= 1.6500 µm and λ_3= 1.6511 µm (H-band).

3.3.2 Discussion

These attenuation values are in good agreement with the predictions. Attenuation of the coronagraphic PSF is achieved, in stellar magnitudes: 8.76 for the SDI method and 14.10 for the DDI one (theoretical values: 7.94 for SDI and 15.88 for DDI). These first results are encouraging for FRIDA to do direct

detection of faint substellar companions. Of course, they deserve to be adjusted with other noise sources fainter than the speckle contribution. SSDI methods were thought to defeat the residual speckles, the main source noise and reach the photon noise limit. Its association with APLC w/o LS is promising. It will allow FRIDA and other work in progress instruments doing high contrast imaging and detecting faint substellar companions close to bright stars.

4. Conclusion

Apodized Pupil Lyot Coronagraph working without Lyot stop (APLC w/o LS) is a combination of an apodization placed in the input pupil and an opaque mask in the following focal plane. In this APLC configuration, the Lyot stop is removed. Indeed, little rejected starlight is left outside the coronagraph exit pupil and can be let unblocked, as the Lyot stop used to do. This coronagraphic solution can prove to be interesting for instruments, where no Lyot stop could be inserted. FRIDA, the work in progress instrument for the Gran Telescopio Canarias (GTC), belongs to this category. We presented the results for FRIDA equipped with APLC w/o LS and showed that it provides encouraging star brightness attenuation, despite the absence of the diaphragm.

In addition, we added a Differential Imaging method, an image processing technique to defeat the residual speckles. Indeed, the source noise is the main one appearing in the AO compensated images and prevent from detecting substellar companions close to bright stars. First results are very promising. This technique is feasible with FRIDA, since this instrument will provide an image data cube thanks to its Integral Field Unit Spectrograph. The observer will select two or three simultaneous images from this FRIDA data cube and apply the appropriate SSDI method. Thus, doing high contrast imaging becomes feasible for the combination "GTC + GTCAO + FRIDA equipped with APLC w/o LS + SSDI method" and for similar work in progress instruments.

In the present work, only residual speckles were considered as a source noise. The next study to come will present the analysis of the other noise sources (photon noise, common and non common path aberrations…) for FRIDA. The interest is to make the most complete study for FRIDA and other work in progress instruments.

It will help determining which kind of substellar companions could be detected and imaged, for FRIDA equipped with APLC w/o LS (and stellar coronagraph in general) and SSDI method. It will be possible to extend this study to future instruments, for instance EPICS, the planet hunter of the European Extremely Large Telescope. With these future instruments, detection and characterization of brown dwarfs, Jupiter-like planets and maybe terrestrial planets will become achievable for astronomical community in the next two decades.

5. References and notes

1. M. Mayor and D. Queloz, "A Jupiter-mass companion to a solar-type star" Nature **378**, pp. 355-359 (1995).
2. J. Schneider, "The Extrasolar Planets Encyclopedia", http://exoplanet.eu/
3. A. Burrows and C. M. Sharp, "Chemical Equilibrium Abundances in Brown Dwarf and Extrasolar Giant Planet Atmospheres" ApJ **512**, pp.543-563 (1999).
4. M. Marley et al., "Reflected Spectra and Albedos of Extrasolar Giant Planets. I. Clear and Cloudy Atmospheres" ApJ **513**, pp. 879-893 (1999).
5. N. Woolf and R. J. Angel, "Astronomical Searches for Earth-Like Planets and Signs of Life" ARA&A **36**, pp. 507-538 (1998).
6. G. Chauvin et al., "A giant planet candidate near a young brown dwarf" A&A **425**, pp. L29-L32 (2004).
7. J. Gay and Y. Rabbia, "Principe d'un coronographe interférentielle" Comptes rendus de l'Académie des Sciences Paris **322 Ser. II b**, pp. 265-271 (1996).
8. P. Baudoz, Y. Rabbia and J. Gay, "Achromatic Interfero Coronagraph: I Formalism and theoretical capabilities for ground-based observations" A&A **141**, pp. 319-329 (2000).

9. B. Lyot, "The study of the Solar Corona without an eclipse" Journal of the Royal Astronomical Society of Canada **27**, pp. 265-280 (1933).
10. F. Roddier and C. Roddier, "Stellar coronagraphy with phase mask" PASP **109**, pp. 815-820 (1997).
11. D. Rouan et al., "The Four Quadrant Phase Mask Coronagraph. I. Principle" PASP **112**, pp. 1479-1486 (2000).
12. R. Soummer et al., "Achromatic dual-zone stellar phase mask coronagraph" A&A **403**, pp. 369-381 (2003).
13. D. Mawet et al., "Annular Groove Phase Mask Coronagraph" ApJ **633**, pp. 1191-1200 (2005).
14. P. Nisenson and C. Papaliolios, "Detection of Earth-like planets using apodized telescopes" ApJ **548**, pp. L201-L205 (2001).
15. O. Guyon, "Phase-induced amplitude apodization of telescope pupils for extrasolar terrestrial planet imaging" A&A **404**, pp. 379-387 (2003).
16. C. Aime et al., "Total coronagraphic extinction of rectangular apertures using linear prolate apodization" A&A **389**, pp. 334-344 (2002).
17. R. Soummer et al., "Stellar Coronagraphy with prolate apodized circular apertures" A&A **397**, pp. 1161-1172 (2003).
18. C. Aime, "Principle of an Achromatic Prolate Apodized Lyot Coronagraph" PASP **117**, pp. 1112-1119 (2005).
19. R. Soummer, "Apodized Pupil Lyot Coronagraph for arbitrary telescope apertures", ApJ **618**, pp. L161-L164 (2005).
20. R. Racine et al., "Speckle noise and the detection of faint companion" PASP **111**, pp.587-594 (1999).
21. C. Marois et al., "Angular Differential Imaging: a powerful technique for high contrast imaging" ApJ **641**, pp.556-564 (2006).
22. D. Lafrenière et al., "A New Algorithm for Point-Spread Function Subtraction in High-Contrast Imaging: A Demonstration with Angular Differential Imaging" ApJ **660**, pp. 770-780 (2007).
23. C. Marois et al., "Efficient Speckle Noise Attenuation in Faint Companion Imaging" PASP **112**, pp. 91-96 (2000).
24. W. B. Sparks and H. C. Ford, "Imaging Spectroscopy for Extrasolar Planet Detection" ApJ **578**, pp. 543-564 (2002).
25. E. D. Rosenthal et al., "Efficient Detection of Brown Dwarfs Using Methane-Band Imaging" Nature **384**, pp. 243-244 (1996).
26. B. Macintosh et al., "Gemini Planet Imager" Proc. SPIE **6272**, 62720L (2006).
27. J.-L. Beuzit et al, "SPHERE: a planet finder instrument for the VLT" The Messenger **125**, pp. 29-34 (2006).
28. J. A. López et al., "FRIDA: Near Infrared Imager and Integral Field Spectroscopy for the GTC" RevMexAA Ser. Conf. **28**, pp 69-72 (2007).
29. A. M. Varela and C. Expósito Glez, "Sky Quality Group", http://www.otri.iac.es/sitesting/index.php?flash=1
30. N. Devaney et al., "Preliminary design and plans for the GTC adaptive optics system", Proc. SPIE **5490**, pp. 913-923 (2004).
31. P. Martinez et al., "Optimization of apodized pupil Lyot coronagraph for ELTs" A&A **474**, pp. 671-678 (2007).
32. B. Oppenheimer et al., "The Lyot project: toward exoplanet imaging and spectroscopy" Proc. SPIE **5490**, pp. 433-442 (2004).
33. M. Kasper et al., "EPICS: A Planet Hunter for the European ELT", presented at the conference In the Spirit of Bernard Lyot: The Direct Detection of Planets and Circumstellar Disks in the 21st Century, University of California, Berkeley, CA, USA, June 04 - 08, 2007.
34. M. Carbillet et al., "Modelling astronomical adaptive optics - I. The software package CAOS", MNRAS **356**, pp. 1263-1275 (2005).

C.2.3 Gaussian Apodized Pupil Roddier Coronagraph
***Advanced Infrared Technology and Applications 9*, León, Mexico, 2007**

Gaussian Apodized Pupil Roddier Coronagraph

Mamadou N'Diaye[1,2], Salvador Cuevas[1] and Kjetil Dohlen[2]

[1] Instituto de Astronomía, UNAM

Apartado Postal 70-264 Ciudad Universitaria, 04510 México, D.F., México

mndiaye@astroscu.unam.mx, chavoc@astroscu.unam.mx

[2] Laboratoire d'Astrophysique de Marseille, OAMP

2 place Leverrier, 13248 Marseille, Cedex 4, France

Kjetil.Dohlen@oamp.fr

Abstract: Gaussian Apodized Pupil Roddier Coronagraph (GAPRC) is an extension of the Roddier & Roddier's phase mask technique with prolate apodized circular aperture, proposed by Soummer (2003). The apodization transmission function was obtained with prolate spheroidal functions. Theoretically, the corresponding pupil apodizer allows reaching perfect starlight extinction, in presence of circular apertures. In our coronagraphic configuration, a Gaussian apodization is used instead of the prolate spheroidal one. Very good star brightness attenuation is achieved with GAPRC. Furthermore, we propose an optical device to build the Gaussian apodization. This device is an afocal doublet of lenses, presenting the same refractive index and where the divergent one is on absorbing glass.
Keywords: Infrared Astronomy, High angular resolution, Adaptive Optics

1. Introduction

1.1 Astronomical and historical context

Detection and characterization of faint substellar objects are very difficult, but exciting challenges. Imaging directly dim companions, like brown dwarfs or extrasolar planets, will provide data to raise issues, unsolved by indirect detection. For instance, it will be possible to analyze and characterize the chemical composition of the substellar companion atmosphere. This information will allow determining the presence and amount of bio-signals, like water (H_2O), ozone (O_3) or oxygen (O_2), on a detected extrasolar planet. On the other hand, answers will be obtained about mechanisms of planetary formation [1]. Calibration of the atmospheric evolution models [2] will also be improved.
However, imaging faint substellar companions close to nearby bright stars is very difficult. The main reason results from the difference of brightness between host stars and their orbiting companions. For instance, contrast ratios of about 10^6 (infrared) to 10^{10} (optical) are expected between young stars of about 100 Myr and extrasolar giant planets [3]. It becomes necessary to decrease the starlight intensity to enhance image of the faint companion. Optical devices are required to reach this goal. In that way, coronagraphy is a very promising solution to achieve brightness attenuation of an observed star.
The solar coronagraph was invented in the early 30s by French astronomer Bernard Lyot [4]. Its objective consisted in occulting the solar disk. In 1931, he took the first picture of the solar corona in absence of Sun eclipse and in 1939 he recorded a movie named "*les flammes du soleil*"(flames of the Sun). It dealt with movements of the solar protuberances and could have been realized, thanks to its coronagraph and some filters.
Coronagraph has known resurgence recently. Indeed, astronomical community has realized that it could help reducing the brightness of an observed star. For about ten years, many high contrast coronagraph designs have been proposed.

1.2 Stellar coronagraphy

Most of the coronagraphic concepts are reviewed and described in [5]. First of all, let mention the "Interferometric" coronagraphs [6-9]. They look much like nulling interferometers: they rely on interferometric combination of discrete beams derived from the entrance pupil. On the other hand, several coronagraphs are based on the modification of the pupil complex amplitude, thanks to apodization of the entrance pupil [10,11]. It allows yielding a star Point Spread Function (PSF), suitable for high contrast imaging. Nevertheless, most of the stellar coronagraphs use a focal plane mask. The Classical Lyot Coronagraph derives from the solar coronagraph invented by Lyot [4]: it uses an occulting mask. Indeed, this mask takes place in the focal plane of the telescope aperture, where an on-axis bright star PSF is formed. Furthermore, several focal plane mask coronagraphs have been proposed [12-15]. Most of them consist of changing the Lyot coronagraph opaque mask, by a phase mask. Here, we mainly focus on the π-phase mask, proposed by Roddier & Roddier in 1997 [12]. All the others focal plane phase masks represent design improvements of this basic one.
Ideal monochromatic case is considered in the present study. The concept of the Classical Roddier Coronagraph (CRC) was proposed by François and Claude Roddier in 1997 [12]. Illustration of its optical assembly is given in Fig. 1. It consists of using a π-phase mask in the focal plane B of the telescope aperture and the Lyot stop (a diaphragm) in the following coronagraph pupil plane C. Coronagraphic image is therefore obtained in the re-imaged focal plane D. The π-phase mask is centered on the image of an on-axis brilliant star. It introduces an optical path difference over half of the corresponding complex amplitude. Therefore, destructive interferences are created. The non-masked and the masked star diffracted light combine in the coronagraph exit pupil plane. It leads to starlight rejection outside the coronagraph exit pupil. Thereafter, the rejected starlight present outside this re-imaged pupil plane C is blocked by the Lyot stop. Hence, attenuation of star brightness is reached and visible in the coronagraph image plane.

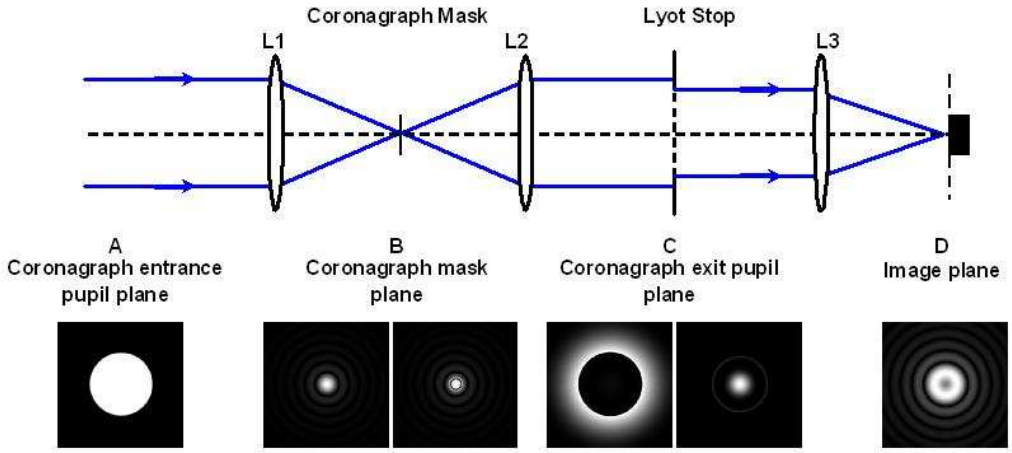

Fig. 1: Schematic illustration of the Classical Roddier Coronagraph, with the respective images in each plane. From left: image in the coronagraph entrance pupil plane A, images in the focal plane before and after application of a π-phase mask, images in the coronagraph re-imaged pupil plane, before and after application of a Lyot stop (diameter equal to 90% the entrance pupil diameter) and the coronagraphic image in the image plane D. Image contrast is increased in this figure in each frame for a better visibility.

To improve the performance of Roddier & Roddier's phase mask technique, the entrance pupil can be apodized. A proper choice of the apodization transmission function leads to a perfect star image extinction. R. Soummer showed that in the case of circular apertures, prolate spheroidal functions are those which lead to the perfect extinction of an on-axis bright star image [16]. Their formalism, developed

independently by Slepian [17] and Heurtly [18], is very sophisticated and does not carry out to direct and simple analytic expressions. Therefore, the computation and fabrication of the corresponding apodization can appear very complicated.

1.3 Gaussian Apodization added to Roddier & Roddier's phase mask technique

The graph representation of a prolate spheroidal function is very close to the Gaussian one. Hence, we propose to substitute the prolate spheroidal pupil apodizer by a Gaussian one in addition of the Roddier & Roddier's phase mask technique. This change of apodization transmission function leads to a coronagraph, named "Gaussian Apodized Pupil Roddier Coronagraph" (GAPRC). This coronagraphic configuration is an association of a Gaussian pupil apodizer placed in the input pupil (image of the telescope aperture), a π-phase mask in the following focal plane and a Lyot stop in the coronagraph exit pupil plane.
In section 2, we quantify the performance achieved by GAPRC inserted in a space-based instrument. We do not achieve a perfect star extinction like in the case proposed by R. Soummer. Nevertheless, the starlight attenuation results, achieved by GAPRC, remain very interesting.
On the other hand, we study the application of GAPRC in the ground-based instrument "Gran Telescopio Canarias (GTC) + GTCAO (The Adaptive Optics [AO] system of the GTC) + FRIDA (the future Infrared imager and an Integral Field Unit Spectrograph for the GTC [19])". FRIDA was presented by S. Cuevas during this AITA congress [20]. In section 3, we estimate the coronagraphic gain that could reach GAPRC in presence of AO compensated images. Residual speckles are the main noise source, present in this system. They represent a limitation for the coronagraph performance. To defeat this noise, we propose to combine Simultaneous Spectral Differential Imaging (SSDI) method to GAPRC. We will show that this association gives promising results for "GTC + GTCAO + FRIDA" to reach high contrast imaging.
To conclude, in section 4, we propose an optical design of the Gaussian pupil apodizer. The device is an afocal doublet of lenses, presenting the same refractive index and the divergent one is made on absorbing glass. Some commercial glasses are proposed to allow realizing this Gaussian pupil apodizer for GAPRC.

2. Performance of Gaussian apodized Pupil Roddier Coronagraph

2.1 Description of GAPRC

2.1.1 Focal plane π-phase mask with prolate apodized circular aperture

The Classical Roddier Coronagraph (CRC) [12] is an improvement of the Lyot coronagraph. It allows achieving contrast ratios better than those initially reached with the opaque mask. Moreover, observations can be done at smaller angular separation. Indeed, the π-phase mask diameter is smaller than the PSF core size; whereas the opaque mask radius is usually greater than the second PSF bright ring one.
However, the π-phase does not lead to the perfect extinction of an on-axis bright star. Improvements of the focal plane mask coronagraph were proposed [21,22]. They usually consist in adding an upstream pupil apodizer to the focal plane mask coronagraph. The optimal transmission function for apodization depends on the shape of the entrance pupil and the used mask. Soummer et al. [16] found the ideal solution for circular apertures. In the case of Roddier & Roddier's phase mask technique, prolate spheroidal functions [17,18] are expected for the apodization transmission. Theoretically, the corresponding pupil apodizer, added to the π-phase mask, allow perfectly canceling an on-axis star image. Nevertheless, the complexity of their formalism leads us to look for similar functions. We have noticed that graphical representation of the prolate spheroidal functions is very close to the Gaussian one.

2.1.2 Changing the prolate spheroidal apodization for a Gaussian one

Hence, we decide to change the prolate spheroidal apodization by a Gaussian one. It simplifies the numerical implementation of the apodization.
The transmission function T of the Gaussian pupil apodizer writes:

$$T(r) = \exp\left(-\frac{\alpha r^2}{4D}\right). \qquad (1)$$

r denotes the radial coordinate in the pupil plane, D the pupil diameter and α the absorption constant of the pupil apodizer. The objective consists in finding the best value for α to reach the best starlight attenuation. We consider for our study that D= 25 mm. Furthermore, we propose an optical design to realize the pupil apodizer, as we will see in section 4.
In the following paragraph, we report the performance of the corresponding coronagraph: Gaussian Apodized Pupil Roddier Coronagraph (GAPRC).

2.2 Results for a space-based instrument

2.2.1 Description of the parameters

The present study of GAPRC is realized first for a space-based instrument. We choose to work with the parameters of "GTC + FRIDA". FRIDA is an Infrared Imager and an Integral Field Spectrograph for the GTC. FRIDA characteristics are described in details in [20]. We consider our present system free from any aberration.
GTC diameter aperture is equal to 10.4 m. GTC central obstruction size is equal to 12 % of the primary mirror diameter. We decide to work in the near infrared, in H-band and in a monochromatic case (central wavelength of observation λ=1.65 μm). GTC is associated to a field rotator. So, a circular entrance pupil will be provided to FRIDA.
Thus, we work with a centrally obstructed circular aperture. Therefore, the secondary mirror shadow appears in the entrance pupil (image of the telescope aperture). Its association with the focal plane phase mask leads to a star diffracted light concentration at the coronagraph exit pupil center. Hence, the coronagraph performance is limited by this central illumination. We propose to block it with an obscuration disk at the coronagraph exit pupil center. Its size is relied on the diameter of the central obscuration, present in the entrance pupil.

2.2.2 Results, coronagraphic gain achieved by GAPRC

Fig. 2 gives the coronagraphic PSF profiles, obtained with GAPRC and CRC, compared to the non coronagraphic one. In both cases, the π-phase mask radius is equal to 0.54λ/D. For the Gaussian pupil apodizer, we choose $\alpha = 0.233\ m^{-1}$.These simulation results are calculated in the case of the space-based instrument "GTC + FRIDA equipped with GAPRC or CRC". A theoretical gain can be reached, in stellar magnitudes: 4.72 and 12.00, for respectively CRC and GAPRC. These values are achieved at an angular distance of 2.0λ/D from the main optical axis. These results show an increase of the coronagraphic performance reached with GAPRC: about 7 stellar magnitudes, in comparison with CRC.

2.2.3 Discussion

The addition of the Gaussian pupil apodizer allows Roddier & Roddier's phase mask technique achieving a substantial coronagraphic gain. These results are very encouraging in the case of application in a space-based instrument. Indeed, they appear very promising for the direct detection of faint substellar companions close to bright stars. In the following section, we will quantify the coronagraphic performance of GAPRC in the case of the ground-based instrument "GTC + GTCAO (the Adaptive Optics [AO] system of the GTC) + FRIDA".

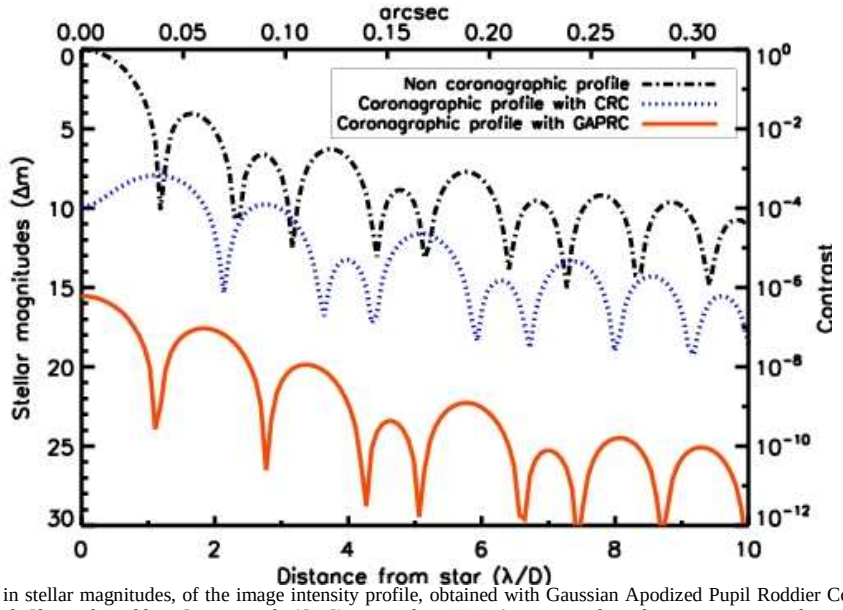

Fig. 2: Plot, in stellar magnitudes, of the image intensity profile, obtained with Gaussian Apodized Pupil Roddier Coronagraph (GAPRC) and Classical Roddier Coronagraph (CRC) inserted in FRIDA, compared to the non coronagraphic profile. The wavelength of study chosen here is λ= 1.65μm. These results are achieved for the space-based instrument "GTC + FRIDA".

2.3 Results for the ground-based instrument:"GTC + GTCAO + FRIDA"

2.3.1 Characteristics and parameters of "GTC + GTCAO + FRIDA"

We repeat the previous study, but this time in the case of the ground-based telescope "GTC + GTCAO + FRIDA". This time, we assume that GTC is equipped with its Adaptive Optics system (GTCAO) [23]. The software CAOS (Case for Adaptive Optics System [24]) is used to simulate the starlight coming from GTCAO and entering through FRIDA. So, our coronagraph (CRC or GAPRC) theoretically inserted in FRIDA receives AO corrected wave fronts. They naturally contain residual errors, since the AO correction is not perfect. To carry out this study, we work with 160 statistically independent phase screens. We also choose the mean "standard seeing scenario" of the Observatorio del Roque de los Muchachos (GTC astronomical site) for our analysis: r_0= 15 cm at λ= 0.5 μm and a turbulent velocity of 10 $m \cdot s^{-1}$. We use an on axis-bright guide star at null zenith angle. The simulation considers the following deformable mirror and sub aperture geometry for GTCAO: 21 actuators and 20 sub apertures placed across the long axis of the telescope pupil. The wavefront sensor measurements are considered perfect (ideal detector). The achieved Strehl ratio in H band is 0.607. Let quantify the coronagraphic gain, reached with this ground-based instrument equipped with GAPRC or CRC.

2.3.2 Results, good coronagraphic performance, and discussion

In Fig. 3, we can observe the obtained results with CRC and GAPRC for the ground-based instrument "GTC + AO + FRIDA". A theoretical gain can be reached, in stellar magnitudes: respectively 2.56 and 3.29, both with a π-phase mask of radius 0.54λ/D. For the Gaussian pupil apodizer, we go on working with an absorption constant α= 0.233 m^{-1}. These values are achieved at an angular distance of 2.0λ/D from the main optical axis. This time, the gain obtained with GAPRC is not much better than with CRC: less than 1 stellar magnitude. Similar star brightness attenuations are realized. However, in both cases, we keep on avoiding detector saturation, in which the coronagraphic image will be formed. Hence, image dynamic range is increased.

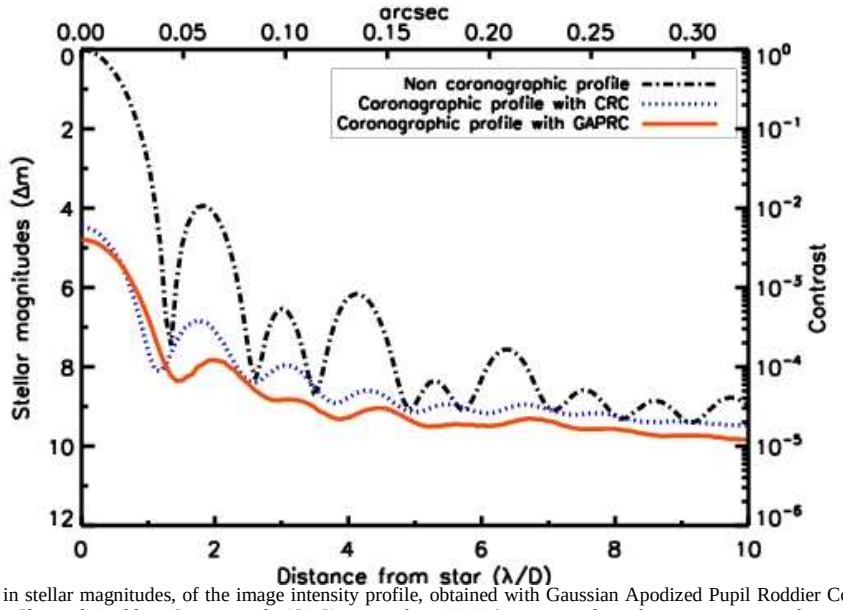

Fig. 3: Plot, in stellar magnitudes, of the image intensity profile, obtained with Gaussian Apodized Pupil Roddier Coronagraph (GAPRC) or Classical Roddier Coronagraph (CRC) inserted in FRIDA, compared to the non coronagraphic profile. The wavelength of study chosen here is λ= 1.65µm. These results are achieved for the ground-based instrument "GTC + GTCAO + FRIDA".

2.3.3 Limitation due to residual speckles in AO compensated images

The achieved brightness attenuation is not good enough to hope observing substellar companions in the star vicinity. Residual speckles limit coronagraph performance. They represent the main noise source appearing in the AO compensated images [25]. Hence, speckle noise has to be defeated, if we want to image dim companions.
A solution consists of using the Simultaneous Spectral Differential Imaging (SSDI) [26] method behind the coronagraph process. In the next section, we propose to give some first results about simulations of the association "GTC + GTCAO + FRIDA equipped with GAPRC + Simultaneous Spectral Differential Imaging method".

3. Addition of Simultaneous Spectral Differential Imaging method

3.1 SSDI: a method to remove residual speckles

3.1.1 Principle and description of the SSDI method

Residual Speckles are the main noise present in AO compensated images [25]. They have to be tackled in order to enhance the image of faint substellar companions.
Simultaneous Spectral Differential Imaging (SSDI) method [26] aims to remove the speckle noise. In its basic version (Simple Differential Imaging [SDI] method), SSDI consists of taking simultaneously two star PSF images at close wavelengths. These images are precisely similar, except for known scale and intensity factors. Image processing allows compensating these terms. Residual speckles are rescaled in both images and reduced with a subtraction between the two frames. The predicted attenuation corresponds to $A_2 \sim 2\sigma_\varphi^2 \Delta\lambda/\lambda$, where σ_φ^2 is the wavefront phase variance and $\Delta\lambda$, the bandpass separation.

Double Differential Imaging (DDI) method is an improvement of the SDI one. It generalizes the technique to three simultaneous images taken at close wavelengths. Three frames are combined in a double difference, to strongly damp the residual speckles. It results a theoretical attenuation $A_3 \sim A_2^2$.

3.1.2 Feasibility with FRIDA: data cube of images obtained with its IFU spectrograph

FRIDA should be able to provide a data cube of images, when it works in Integral Field Spectroscopy (IFS) mode. Indeed, thanks to its Integral Field Unit Spectrograph, FRIDA should give several simultaneous and wide field images of the observed stellar object at different wavelengths. Several image processing could be applied to extract new astronomical data about the images. In particular, extracting three images at different wavelengths from the FRIDA data cube will be possible. Therefore, applying SSDI method with FRIDA becomes something realizable and realistic. Thus, high contrast imaging can be reached with FRIDA. The idea is to use three simultaneous coronagraphic images obtained with GAPRC at different wavelengths. The next step consists in combining them with SSDI method. In the following section, we present the simulation results obtained in this configuration. FRIDA is assumed to work in low spectral resolution mode ($R = \lambda/\Delta\lambda = 1500$). Our coronagraphic Images will have a spectral bandpass separation $\Delta\lambda = 0.0011$ µm. Let remind that images have a Strehl ratio S= 0.607.

3.2 Application post GAPRC

3.2.1 Results achieved for the association "GAPRC + SSDI" applied in FRIDA

Fig. 4 shows the obtained results when FRIDA is equipped with GAPRC, in IFS mode. In this case, the achieved star intensity attenuation is, in stellar magnitudes: 3.29 when we just use GAPRC, 10.04 when the coronagraph is associated to SDI technique and 15.14 when the coronagraph is combined to DDI method. These results are achieved at an angular distance of 2.0λ/D from the main optical axis.

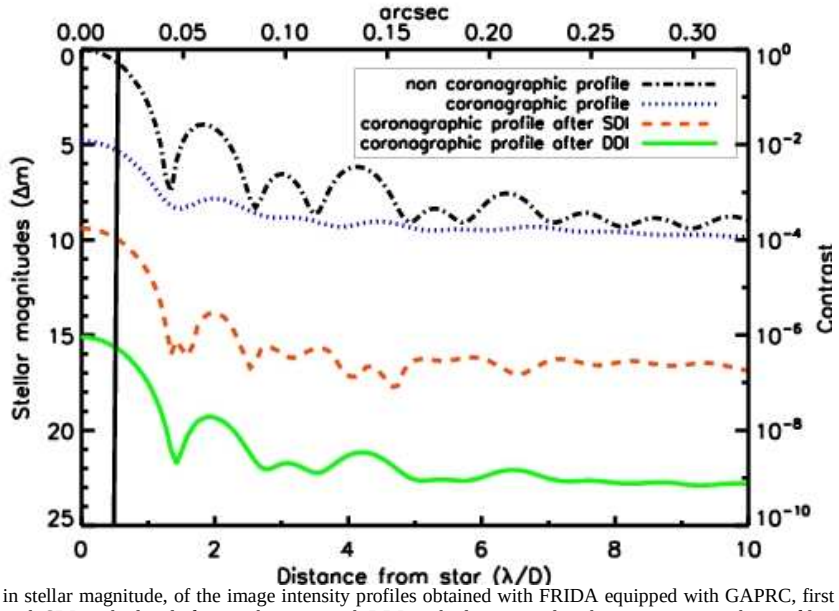

Fig. 4: Plot, in stellar magnitude, of the image intensity profiles obtained with FRIDA equipped with GAPRC, first alone, after combination with SDI method and after combination with DDI method, compared to the non coronagraphic profile. The π-phase mask radius is r=0.54λ/D (mask area delimited by the black vertical line). These results are obtained in presence of initial wavefront errors (Strehl ratio:S=0.607). The wavelengths of study, chosen for this simulation, are λ_1= 1.6489 µm, λ_2= 1.6500 µm and λ_3= 1.6511 µm (H-band).

3.2.2 Discussion

Attenuation of the coronagraphic PSF is achieved, in stellar magnitudes: 6.75 for the SDI method and 11.85 for the DDI one (theoretical values: 7.94 for SDI and 15.88 for DDI). The performance of the association "GAPRC + SSDI method" applied in ground-based instruments, like "GTC + GTCAO + FRIDA", is promising to do direct detection of faint substellar companions. The present results deserve to be adjusted with other noise sources fainter than the speckle contribution. SSDI methods were thought to defeat the residual speckles, the main source noise and reach the photon noise limit. It would allow FRIDA and other work in progress instruments doing high contrast imaging and detecting faint substellar companions close to bright stars.

4. Afocal doublet of lenses as Gaussian pupil Apodizer

4.1 Description of the device

The Gaussian apodizer presents a transmission function, described in Eq. (1). The absorption constant absorption used in our previous simulations is $\alpha = 0.233\ m^{-1}$.
The Gaussian pupil apodizer transmits more starlight close to the pupil center and less at the pupil edge. We propose to design the Gaussian apodizer with an afocal doublet of lenses. A schematic representation is given in Fig. 5. Both lenses have to present the same refractive index to avoid adding optical aberrations. Their thermal expansion coefficient must be equal, if lenses are stuck. Furthermore, the divergent one is made with an absorbing neutral density glass, characterized by its Optical Density (OD). The corresponding transmission function can be expressed as follow:

$$T_{doublet}(r) = \exp\left(-\frac{OD \ln 10 \times r^2}{2R}\right), \qquad (2)$$

where R denotes the curvature ray of the divergent lens.
We can make an analogy with Eq. (1). It leads to R= 2D and OD= α/ ln 10. With our previous value of α, we obtain OD=0.10 for the absorbing neutral density glass.

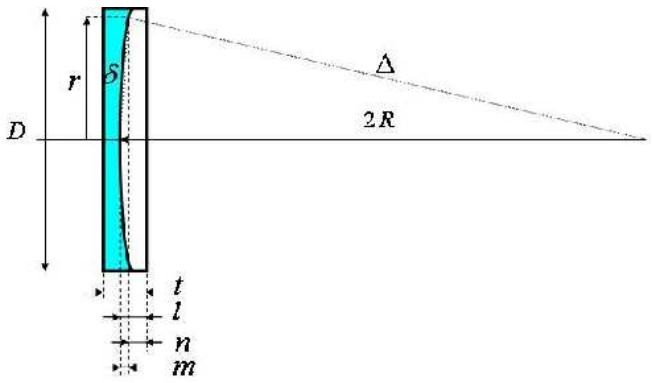

Fig. 5: The doublet with all the parameters intervening in the calculus of the transmission function.

4.2 Feasibility with commercial glasses

This value OD is typical and can be found in the manufacturer glasses, depending on the wavelength of study. Commercial Glasses SCHOTT NG11® [27] or HOYA C500® [28] seems to be some interesting solutions for the divergent lens, if we work in H-band.

This Gaussian apodizer will be feasible if we find a convergent lens glass, with the same refractive index and thermal expansion coefficient than the divergent lens glass. We will present the corresponding study in a further work.

5. Conclusion

Gaussian Apodized Pupil Roddier Coronagraph (GAPRC) proves to be a combination of a Gaussian pupil apodizer in the entrance pupil plane, a π-phase mask in the following focal plane and a Lyot stop in the coronagraph exit pupil plane. We propose to use Gaussian apodization instead of prolate spheroidal one for the input pupil. Indeed, graph representations of the Gaussian and prolate spheroidal functions are very similar. Moreover, Gaussian functions are easier to compute. They are also simpler for the fabrication of the corresponding pupil apodizer. GAPRC gives very satisfying results, since it is applied to a space-based instrument. Indeed, a 12.00-stellar magnitude attenuation of an on-axis star PSF is expected. This result is achieved at an angular distance of $2.0\lambda/D$ from the main optical axis. However, in the case of a ground-based instrument, the performance of GAPRC is limited by the residual speckles appearing in AO compensated images. For the same angular distance, the coronagraphic gain is no more 3.29 stellar magnitudes. We have studied the case of "GTC + GTCAO + FRIDA" and noticed that coronagraphic performances achieved with GAPRC are hardly better than those reached with the Classical Roddier Coronagraph.
The residual speckle is the main source noise, and must be tacked to image faint substellar companions. To defeat this noise, we propose to add the Simultaneous Spectral Differential Imaging method (SSDI). We simulate the combination GAPRC + SSDI method applied on the ground-based "GTC + GTCAO + FRIDA". The results are very encouraging, since an attenuation of the initial PSF, is achieved: until 15.14 in stellar magnitudes. Of course, these results need to be adjusted with the other source noises. However, the first approximation allows being optimistic. The possible detection and characterization of faint substellar companions seems to be reachable with ground-based instruments.
Furthermore, we propose a design for the Gaussian pupil apodizer: an afocal doublet of lenses. Glasses with the same refractive index and thermal expansion coefficient should be used for both lenses. The divergent one has to be made with an absorbing neutral density glass. We have showed that with commercial glasses, it should be possible to make this afocal doublet of lenses. The next step will be the fabrication of the Gaussian pupil apodizer. We will detail it and the results in a future paper. GAPRC could benefit to EPICS, the future planet hunter instrument for the European Extremely Large Telescope [29]. This coronagraph configuration can represent a good option for the detection of substellar companions and in particular, giant extrasolar planets.

6. References and notes

1. A. Burrows and C. M. Sharp, "Chemical Equilibrium Abundances in Brown Dwarf and Extrasolar Giant Planet Atmospheres" ApJ **512**, pp.543-563 (1999).
2. M. Marley et al., "Reflected Spectra and Albedos of Extrasolar Giant Planets. I. Clear and Cloudy Atmospheres" ApJ **513**, pp. 879-893 (1999).
3. A. Burrows et al., "Spectra and Diagnostics for the Direct Detection of Wide-Separation Extrasolar Giant Planets" ApJ **609**, pp. 407-416 (2004).
4. B. Lyot, "The study of the Solar Corona without an eclipse" Journal of the Royal Astronomical Society of Canada **27**, pp. 265-280 (1933).
5. O. Guyon et al., "Theoretical Limits on Extrasolar Terrestrial Planet Detection with Coronagraphs" ApJ Suppl. Ser. **167**, pp. 81-99 (2006).
6. J. Gay and Y. Rabbia, "Principe d'un coronographe interférentielle" Comptes rendus de l'Académie des Sciences Paris **322 Ser. II b**, pp. 265-271 (1996).
7. P. Baudoz, Y. Rabbia and J. Gay, "Achromatic Interfero Coronagraph: I Formalism and theoretical capabilities for ground-based observations" A&A **141**, pp. 319-329 (2000).
8. B. P. Mennesson et al., "Optical Planet Discoverer: how to turn a 1.5-m class space telescope into a powerful exo-planetary systems imager" Proc. SPIE **4860**, pp. 32-44 (2003).

9. O. Guyon and M. Shao, "The Pupil-swapping Coronagraph" PASP **118**, pp. 860-865 (2006).
10. P. Nisenson and C. Papaliolios, "Detection of Earth-like planets using apodized telescopes" ApJ **548**, pp. L201-L205 (2001).
11. O. Guyon, "Phase-induced amplitude apodization of telescope pupils for extrasolar terrestrial planet imaging" A&A **404**, pp. 379-387 (2003).
12. F. Roddier and C. Roddier, "Stellar coronagraphy with phase mask" PASP **109**, pp. 815-820 (1997).
13. D. Rouan et al., "The Four Quadrant Phase Mask Coronagraph. I. Principle" PASP **112**, pp. 1479-1486 (2000).
14. R. Soummer et al., "Achromatic dual-zone stellar phase mask coronagraph" A&A **403**, pp. 369-381 (2003).
15. D. Mawet et al., "Annular Groove Phase Mask Coronagraph" ApJ **633**, pp. 1191-1200 (2005).
16. R. Soummer et al., "Stellar Coronagraphy with prolate apodized circular apertures" A&A **397**, pp. 1161-1172 (2003).
17. D. Slepian, "Prolate Spheroidal Wave Functions, Fourier Analysis and Uncertainty - IV:Extensions to Many Dimensions; Generalized Prolate Spheroidal Functions", Bell Syst. Techn. J. **43**, pp. 3009-3057 (1964).
18. J. Heurtley, "Hyperspheroidal functions-optical resonators with circular mirrors" in *Proceedings of Symposium on Quasi-Optics*. ed. (Polytechnic Press, 1964), pp. 367-375.
19. J. A. López et al., "FRIDA: Near Infrared Imager and Integral Field Spectroscopy for the GTC" RevMexAA Ser. Conf. **28**, pp 69-72 (2007).
20. S. Cuevas et al., "FRIDA: Integral-field spectrograph and imager for the adaptive optics system of the Gran Telescopio Canarias", this conference.
21. C. Aime et al., "Interferometric apodization of rectangular apertures. Application to stellar coronagraphy", A&A **379**, p.697-707 (2001).
22. C. Aime et al., "Total coronagraphic extinction of rectangular apertures using linear prolate apodization" A&A **389**, pp. 334-344 (2002).
23. N. Devaney et al., "Preliminary design and plans for the GTC adaptive optics system", Proc. SPIE **5490**, pp. 913-923 (2004).
24. M. Carbillet et al., "Modelling astronomical adaptive optics - I. The software package CAOS", MNRAS **356**, pp. 1263-1275 (2005).
25. R. Racine et al., "Speckle noise and the detection of faint companion" PASP **111**, pp.587-594 (1999).
26. C. Marois et al., "Efficient Speckle Noise Attenuation in Faint Companion Imaging" PASP **112**, pp. 91-96 (2000).
27. SCHOTT, "Optical glass filters",
http://www.us.schott.com/optics_devices/filter/english/us/index.html
28. HOYAOPTICS, "Color filter glasses",
http://www.hoyaoptics.com/color_filter/color_compensating.htm
29. M. Kasper et al., "EPICS: A Planet Hunter for the European ELT", presented at the conference In the Spirit of Bernard Lyot: The Direct Detection of Planets and Circumstellar Disks in the 21st Century, University of California, Berkeley, CA, USA, June 04 - 08, 2007.

C.2.4 High contrast imaging feasibility studies for FRIDA
SPIE Astronomical Instrumentation, Marseilles, France, 2008

High contrast imaging feasibility study for FRIDA

Mamadou N'Diaye[a,b], Salvador Cuevas[a] and Kjetil Dohlen[b]*

[a]Instituto de Astronomía, Universidad Nacional Autónoma de México
Apartado Postal 70-264 Ciudad Universitaria, 04510 México D.F., Mexico
[b]Laboratoire dAstrophysique de Marseille, UMR6110, CNRS/Université de Provence
2 place Le Verrier, 13248 Marseille Cedex 4, France

ABSTRACT

FRIDA will be an Infrared Imager and an Integral Field Spectrograph (IFS) for the $10.4\,m$ Gran Telescopio Canarias (GTC). This instrument is scheduled to be installed in 2010, at the Nasmyth A platform of the GTC, behind GTCAO (the Adaptive Optics [AO] system of the GTC). FRIDA design incorporates straightforward upgrade paths for focal plane masks. In this work, we analyze the capability of FRIDA to provide high dynamic range images. Different coronagraphic configurations could be inserted within FRIDA optical assembly. We quantify numerically their performance in presence of AO compensated wavefronts. Thereafter, numerical simulations about the Simultaneous Spectral Differential Imaging[1] (SSDI) method are presented. This technique aims to suppress the AO residual speckles and can be applied to selected frames of the data cube, provided by FRIDA in IFS mode. Therefore, we estimate the starlight attenuation that could be reached with the association "Coronagraph + SSDI method" for the ground-based instrument "GTC + GTCAO + FRIDA".

Keywords: high angular resolution, coronagraphy, adaptive optics, image processing

1. INTRODUCTION

1.1 Direct detection & characterization of faint substellar companions

In the field of astronomical instrumentation, imaging substellar companions, like brown dwarfs or extrasolar planets, represents a very exciting but challenging technical problem to overcome. For instance, a Jovian planet is about 10^6 times fainter than its parent star at a wavelength $\lambda = 1.6\,\mu m$. Increasing the image contrast will allow to make appear such close-in objects which are initially drowned in the star scattered light. Thus, new astronomical data about them can be reached to facilitate their characterization. The further analysis of their spectrum will carry out to the identification of atomic and molecular lines and provide information to astronomers about their atmospheric chemical composition. It will also allow to have access to the planetary companion mass, better understand the planetary formation mechanism and calibrate the current atmospheric evolution models.

Our terrestrial atmosphere distorts the wave fronts coming from stellar objects. Ground-based telescopes are equipped with very efficient Adaptive Optics (AO). AO allows to correct the aberrations induced by the atmospheric turbulence in order to exploit the diffraction-limited potential of ground-based telescopes. However, other techniques beyond AO system are required to strongly attenuate the star diffracted light at small angular separations and allow imaging of faint companions close to bright stars. Diffraction suppression systems and image processing techniques constitute some of the promising solutions developed these past few years to reach this goal. Indeed, they aim to increase the dynamic range of the images provided by "ground-based telescope + AO system" to downstream science instruments. In this contribution, we propose to focus us on the case of FRIDA,[2] the future science instrument for the AO system of the GTC.

*E-mail: mndiaye@astroscu.unam.mx, chavoc@astroscu.unam.mx, Kjetil.Dohlen@oamp.fr

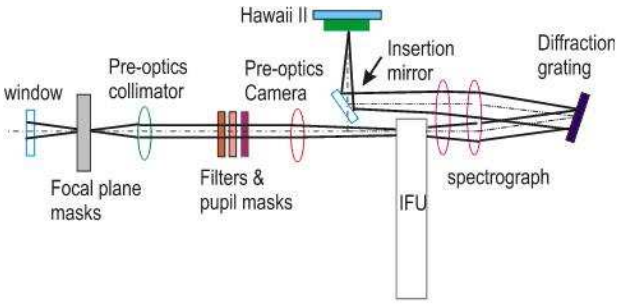

Figure 1. FRIDA conceptual design

1.2 FRIDA: presentation and description

FRIDA[2] (in**F**ra**R**ed **I**mager and **D**issector for the **A**daptive optics system of the $10.4\,m$ Gran Telescopio Canarias [GTC]) is being designed as a diffraction limited instrument with broad and narrow band imaging and integral field spectroscopy (IFS) capabilities to operate in the wavelength range $0.9 - 2.5\,\mu m$. FRIDA will be installed at the Nasmyth A platform behind GTCAO[3] (the Adaptive Optics system of the GTC). It will use diffraction-limited optics to avoid degrading the Strehl ratio delivered by the GTCAO system in the near-infrared. The basic concept of FRIDA is shown in Fig. 1.

In the diffraction limited imaging mode, FRIDA will provide a comprehensive set of broad and narrow band filters. The same detector (Teledyne Hawaii II) will be used for Imaging and Integral Field Spectroscopy (IFS) modes. Mode switching will be easily performed and the larger field of view in imaging mode ($20.48 \times 20.48\,arcsec^2$ and $40.96 \times 40.96\,arcsec^2$) will facilitate field recognition for the IFS mode, where the field of view is small. The integral field spectrograph will provide a wide range of spectral resolutions, from low $R \sim 1500$ and medium $R \sim 4000$ to high $R \sim 30000$, the latter is a unique capability of FRIDA among integral field spectrographs operating in large telescopes with AO systems. Upgrade paths for high contrast imaging using Lyot or phase masks and pupil apodizers have also been considered in the design.

1.3 GTCAO: characteristics and performance

The $10.4\,m$ Gran Telescopio Canarias is currently being installed in the Observatorio del Roque de los Muchachos on the island of La Palma. The standard seeing scenario assumes a Fried parameter $r_0 = 15\,cm$ at $\lambda = 0.5\,\mu m$ and a wind velocity $v = 10\,m \cdot s^{-1}$. GTCAO, the adaptive optics system of the GTC,[3] will offer high-order correction in the near-infrared while the tip-tilt correction will be provided by the secondary mirror of the GTC. The AO system will initially operate with a single deformable mirror conjugated to the GTC pupil. Moreover, GTCAO is planned to have a performance similar to the following deformable mirror and subaperture geometry: 21 actuators and 20 subapertures placed across the long axis of the telescope pupil. In addition, the system will employ a Shack-Hartmann wavefront sensor. "GTCAO + FRIDA" will be mounted on fixed positions at the Nasmyth station. However, they will not be attached to the GTC Nasmyth derotator. GTCAO will perform his own field derotation, therefore the GTC pupil image will rotate in the FRIDA pupil planes. In the following, the pupil masks are circular in order to not introduce a pupil rotator.

1.4 GTCAO simulations

In our following simulations, GTCAO is modeled with the CAOS software,[4] assuming the geometry previously described for the system. Furthermore, the wavefront sensor measurements are supposed to be perfect (ideal detector) and our simulations are made considering 189 phase screens, following the Kolmogorov statistics. We achieve a Strehl ratio $S = 0.552$ at $\lambda = 1.57\,\mu m$ (methane absorption line in H-band). It corresponds to a residual wavefront variance $\sigma_\varphi^2 = 0.594\,rad^2$, basing us on the Marechal approximation $S \simeq \exp(-\sigma_\varphi^2)$ and where φ

denotes the wavefront phase term.

1.5 Upgrade paths & high contrast imaging for FRIDA

Since upgrade paths are scheduled for high contrast imaging, different coronagraphic designs could be inserted within the FRIDA optical layout. Our goal consists in considering several coronagraphic configurations for FRIDA and estimating the starlight attenuation they could respectively reach. Numerical simulations about coronagraphy in presence of AO compensated wavefronts are given in Sec. 2. Thereafter, we investigate the possibility of adding some image processing techniques to coronagraphy in order to remove the AO residual speckles. Indeed, frames with very small bandpass separation $\Delta\lambda$ can be obtained with the data cube provided by FRIDA in IFS mode. Thus, specialized observation schemes and post-processing algorithms can be considered for FRIDA and constitute a promising solution to increase its image dynamic range. In Sec. 3, we present the numerical results obtained with the combination of simultaneous AO coronagraphic images achieved at different but close wavelengths. The contrast gain that FRIDA could perform will be quantified and we will discuss the relevancy of the results.

2. AO CORONAGRAPHIC OPTIONS & PERFORMANCE FOR FRIDA

2.1 Stellar coronagraphy: review

The stellar coronagraph is an optical device which represents a first step to achieve high contrast imaging: it aims to avoid detector saturation while reducing the star diffracted light. Several coronagraphic devices were proposed during the last decade and a good review can be found in the literature.[5] Our coronagraph feasibility study for FRIDA will be focused on the following coronagraph configurations: the classical focal plane mask and the apodized pupil mask coronagraphs.

Major part of the coronagraphic concepts are based on a mask centered at the telescope focal plane in which an observed on-axis bright star is imaged. Moreover, the spot is carefully designed to not alter the image of an eventual off-axis substellar companion. Coronagraphic masks can be split into two categories: on the one hand, opaque masks directly block the starlight contribution whereas on the other hand, phase masks cancel the star image by introducing destructive interferences. Furthermore, a Lyot stop takes place in the re-imaged pupil plane to block the rejected starlight outside the geometric pupil. These configurations (focal plane mask + Lyot stop) can be classified as the classical focal plane mask coronagraphs.

Another coronagraphic approach consists in apodizing the entrance pupil (a re-imaged telescope aperture) to smooth the wings of an observed on-axis bright star Point Spread Function (PSF). This allows to increase the contrast in the substellar companion search area. Entrance pupil apodizer and focal plane mask can also be associated to decrease the intensity of the parent star image. These concepts (pupil apodizer + focal plane mask + eventually Lyot stop) can be classified as the apodized pupil mask coronagraphs.

2.2 The different coronagraph configurations for FRIDA

Fig. 2 gives a schematic representation of the FRIDA optical layout for coronagraph feasibility studies. This simplified version of the FRIDA conceptual design (see Fig. 1) allows to establish where focal plane masks, apodizations or diaphragms can be collocated. The observation of the FRIDA optical scheme enables the identification of three focal and two pupil planes for this GTC instrument. In Imaging mode, the camera takes place in the 2^{nd} focal plane whereas in IFS mode, the detector is located in the 3^{rd} focal plane as shown in our illustration. Furthermore, when FRIDA operates in IFS mode, the image slicer is present in the 2^{nd} focal plane while the Integral Field Unit spectrograph appears in the 2^{nd} pupil plane. Taking into account these mechanical considerations, we can determine some feasible coronagraphic configurations for FRIDA.

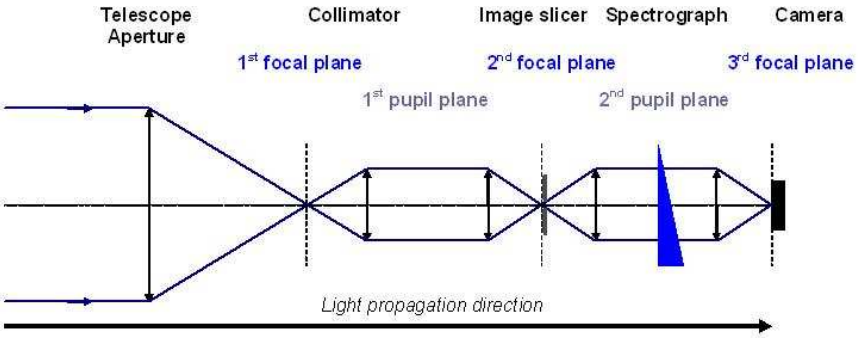

Figure 2. Schematic representation of the FRIDA optical layout for coronagraphy studies.

Our study is focused on coronagraphs using focal plane masks, Lyot stop and eventually pupil apodizers. On the one hand, Lyot or phase masks can be inserted in the 1^{st} focal planes while introducing the Lyot stop in the 1^{st} pupil plane. On the other hand, apodization could be inserted in the 1^{st} pupil plane, the coronagraphic masks and pupil stop included respectively in the 2^{nd} focal and pupil planes, in which the IFU and the spectrograph take place respectively. To avoid making FRIDA optical scheme more complicated at level of system engineering, these last possibilities for coronagraphy were set aside. Therefore, this strongly reduces the number of coronagraphic solutions for FRIDA. Indeed, even if a pupil apodizer could be inserted in the 1^{st} pupil plane, unfortunately no mask and no Lyot stop could be added respectively in the 2^{st} focal and pupil planes. This stress eliminates the possibility of introducing a conventional Apodized Pupil Lyot or Phase Mask Coronagraph.[6]

Hence, we decide to consider four coronagraphic configurations for FRIDA. On the one hand, we present the coronagraphic schemes adopted for FRIDA: the Classical Lyot Coronagraph (CLC, an opaque mask + Lyot stop) and the Classical Roddier Coronagraph[7] (CRC, a Roddier & Roddier phase mask + Lyot stop). On the other hand, we describe two feasible coronagraphic solutions for FRIDA: the Apodized Pupil Lyot Coronagraph[8] (APLC) and the Stop-less Lyot Coronagraph[9] (SLLC) which is an APLC working without Lyot stop. In the following section, we estimate the starlight attenuation that can be achieved by each one of these configurations. The present approach is limited to FRIDA working in IFS mode. In this study, we work with the characteristics of GTC (diameter $D = 10.4\,m$) and the pupil is circular with a circular central obscuration (central obstruction: 12%) to avoid a pupil rotator (see Sec. 1.3).

2.3 Contrast gain reachable for each configuration: numerical results

2.3.1 Classical Lyot and Roddier Coronagraphs

FRIDA can be equipped with CLC or CRC since an opaque mask, or a Roddier & Roddier (R&R) phase mask, and a Lyot stop can be inserted respectively in the 1^{st} focal and pupil planes of the optical assembly. These coronagraph configurations are valid whatever the operating mode used for FRIDA. A schematic illustration of FRIDA supplied with CLC or CRC is given in Fig. 3. The Lyot stop is composed of a diaphragm and an obscuration disk to compensate the diffraction effects due to the telescope secondary mirror. The diameter of the obscuration disk and the aperture size of the diaphragm are respectively equal to 0.12 and 0.90 times the geometric pupil diameter. In our numerical simulations, we propose to estimate numerically the contrast gain reached by CLC and CRC. We choose to work with an opaque mask and a R&R phase mask radius of respectively $r = 2.30\,\lambda/D$ and $0.55\,\lambda/D$.

Since we work in IFS mode, a monochromatic point source in H-band ($\lambda = 1.57\,\mu m$) was considered here. Fig. 4 represents on the left plot the intensity profiles obtained for FRIDA equipped with CLC or CRC and on the right plot the $5\,\sigma$ detectability graphs for each one of the previous intensity profiles. The numerical simulations show that some star brightness attenuation can be reached, for instance, we obtain a contrast gain

Table 1. Contrast gain reached with CLC or CRC configuration for FRIDA

Coronagraph mask, radius	**Contrast gain in stellar mag. Δm at an angular separation (in λ/D):**						
	2.0	4.0	6.0	8.0	10.0	12.0	20.0
Opaque mask, $2.30\,\lambda/D$		0.84	0.59	0.16	0.05	0.11	0.03
R&R phase mask, $0.55\,\lambda/D$	2.25	1.54	0.75	0.15	0.09	0.14	0.06

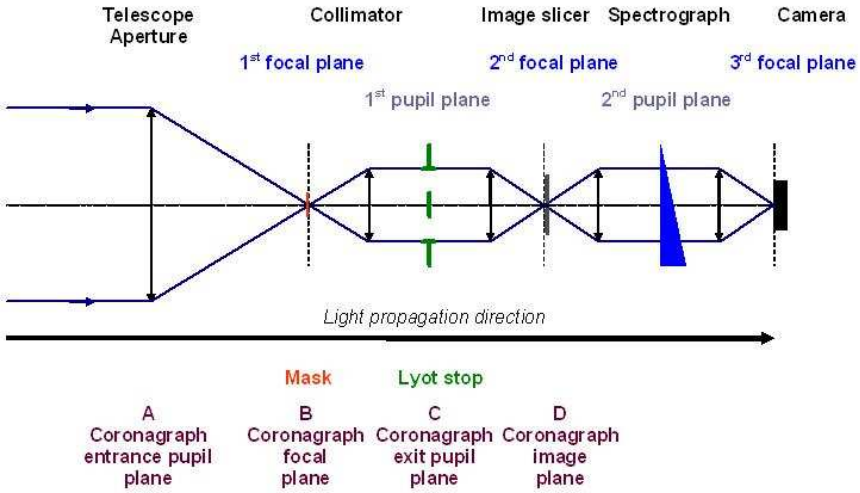

Figure 3. Simplified representation of the FRIDA optical assembly in IFS mode. In this scheme, the elements of the Classical Lyot or Roddier Coronagraph are inserted in the 1^{st} pupil and focal planes of FRIDA.

in stellar magnitudes: $\Delta m = 0.84$ and 1.54 with respectively the opaque and R&R phase masks. These results were calculated estimating the azimuth averaged intensity values, before and after coronagraphy, for the angular separation $4.0\,\lambda/D$ from the main optical axis. Table 1 summarizes the contrast gain results that can be reached with CLC and CRC at a given angular distance from the the main optical axis.

2.3.2 Apodized Pupil and Stop-less Lyot Coronagraphs

Fig. 5 gives illustrations of the optical scheme of FRIDA equipped respectively with SLLC and APLC. For the numerical simulations, we keep the same value of opaque mask radius than that previously used for the CLC configuration: $r = 2.30\,\lambda/D$. The corresponding pupil apodizer is represented in Fig. 6.

The intensity profiles achieved with SLLC and APLC for "GTC + GTCAO + FRIDA" can be observed on Fig. 7 left plot and the $5\,\sigma$ detectability graphs for each one of the previous intensity profiles on the right one. These numerical results are achieved in presence of AO corrected wavefronts. A theoretical attenuation can be reached, in stellar magnitudes: $\Delta m = 1.68$ and 0.86 for respectively APLC and SLLC. These values are obtained estimating the azimuth averaged intensity over a ring of radius $4.0\,\lambda/D$ and width $1.0\,\lambda/D$. Table 2 summarizes the contrast gain results that can be reached with SLLC and APLC at a given angular distance from the main optical axis. It can be noticed that SLLC and APLC provide very encouraging results of attenuation, sometimes better than those obtained with CLC. Unfortunately, within the FRIDA team, decision was taken to not conserve these coronagraphic possibilities for FRIDA.

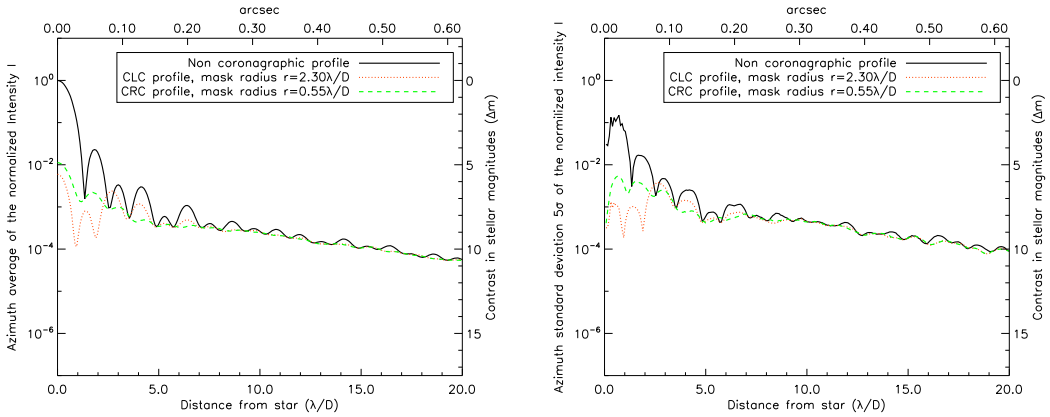

Figure 4. **Left**: Azimuth averaged profiles of the non coronagraphic PSF and coronagraphic images obtained with CLC or CRC alone, for a 12% centrally obstructed telescope (GTC case), considering a monochromatic point source in H-band ($\lambda = 1.57\,\mu m$). These results are obtained in presence of AO corrected wavefronts. **Right**: Profiles of the azimuth standard deviation 5σ of the normalized intensities I. Simulations are carried out with the characteristics of "GTC + GTCAO + FRIDA".

Table 2. Contrast gain reached with SLLC or APLC configuration for FRIDA

Coronagraph	**Contrast gain in stellar mag. Δm at an angular separation (in λ/D):**					
	4.0	6.0	8.0	10.0	12.0	20.0
APLC	1.68	0.75	0.19	0.12	0.14	0.09
SLLC	0.86	0.51	0.10	0.04	0.07	0.05

2.4 Discussion

All these coronagraph configurations will allow to avoid detector saturation and provide a first interesting contrast gain for FRIDA. The previous tables indicate that CRC provides the best starlight attenuations. However, the GTC focal ratio presents an average value $f/17$ and therefore, the R&R phase mask diameter will be $29.4\,\mu m$ at $\lambda = 1.57\,\mu m$. This is a technological and challenging stress to overcome. APLC also constitutes a promising solution for high contrast imaging, but this configuration was not kept. Indeed, during the FRIDA design development, it was considered that the introduction of a pupil stop in the 2^{nd} pupil plane would make the FRIDA scheme too complicated. This stress led us to consider a new coronagraphic scheme: SLLC. But, unfortunately, some recent changes within FRIDA optical design did not allow any longer the insertion of masks in the 2^{nd} focal plane. At the moment, CLC constitutes the most viable coronagraph configuration for FRIDA.

Furthermore, coronagraph performance proves to be limited: the achieved attenuation values are too weak to allow enhancing the images of eventual faint substellar companions. This is mainly due to the residual aberrations present within the AO compensated wavefronts. They form a noisy background which prevents from detecting faint objects close to bright star and represent a limitation for coronagraphy.[10] Therefore, additional techniques are required if we want to make direct detection of dim stellar objects.

3. AO RESIDUAL SPECKLE NOISE SUPPRESSION FOR FRIDA

3.1 Sources of speckle noise

Ground-based telescopes require very efficient Adaptive Optics (AO) systems to correct wavefront errors due to atmospheric turbulence. Even with a downstream diffraction suppression system like coronagraphy, the faint source detection for current 8-10 m class telescopes remains limited by residual speckles.[10] These speckles are due

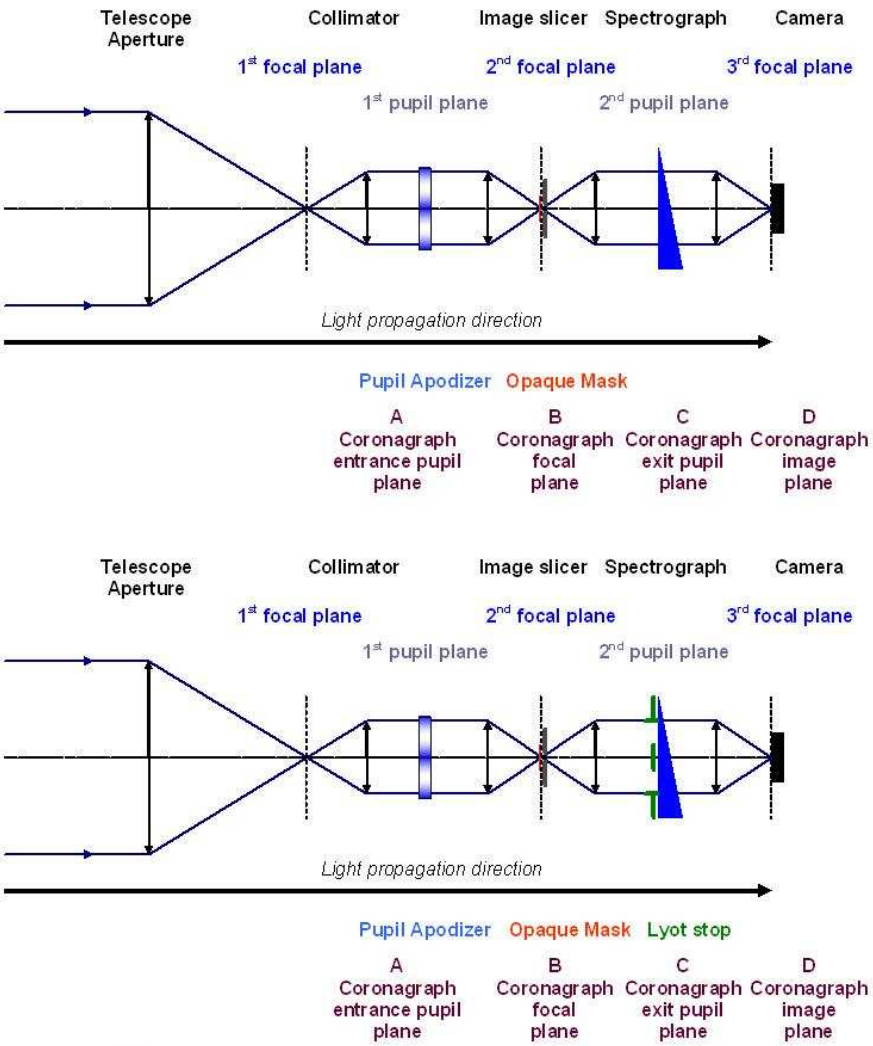

Figure 5. Same as Fig. 3, but here, the Classical Lyot Coronagraph is replaced by the Stop-less Lyot Coronagraph (top) or the Apodized Pupil Lyot Coronagraph (bottom).

to limitations in the AO correction system, corresponding to atmospheric turbulence residuals, and non-common path instrumental aberrations. The atmospheric turbulence residuals are short-lived, with lifetime of a few to a few hundred milliseconds.[11] For total exposures times of tens of minutes, these speckles average down to a smooth halo. Non-common path instrumental aberrations originate from the differential optical path between wavefront sensor and science channels. They result in a mixture of static and slowly varying speckles, with lifetimes comparable to the exposure time. The resulting image therefore consists of a smooth halo onto which is superimposed a residual speckle pattern.

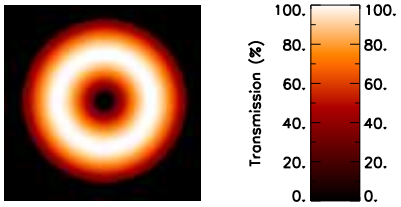

Figure 6. Pupil apodizer throughput determined for a 12 % centrally obstructed circular aperture (GTC case) and for an opaque mask radius: $r = 2.30\,\lambda/D$.

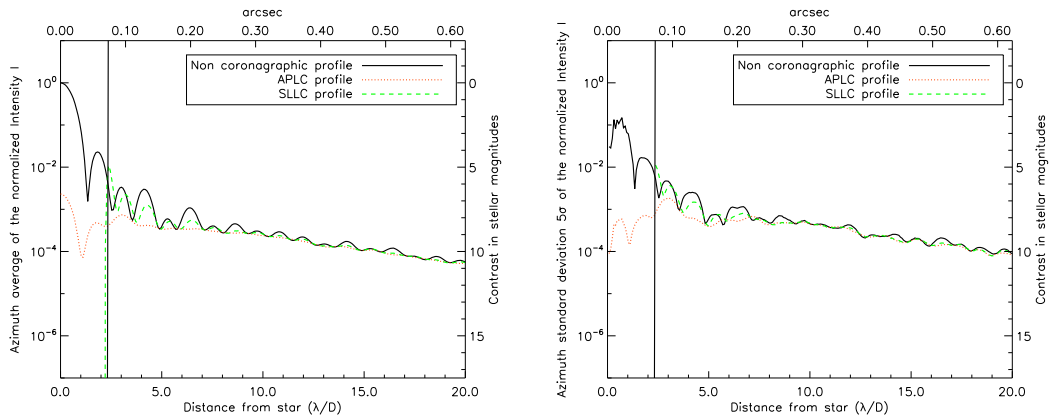

Figure 7. Same as Fig. 4, but here, CLC and CRC are replaced by the Stop-less Lyot Coronagraph and the Apodized Pupil Lyot Coronagraph. The opaque mask of radius $2.30\,\lambda/D$ is delimited by a vertical line.

3.2 Azimuth symmetric component removal and SSDI: methods to reduce speckle noise

Several methods were recently developed to attenuate the speckle noise[12] and therefore, enhance faint substellar companion images drowned in the bright star PSF. Here, we remind the principle of the Simultaneous Spectral Differential Imaging[1] (SSDI) method: this is the technique we choose to compute for FRIDA. This image processing method aims to reduce the AO residual speckles: it takes advantage of the chromaticity of the speckle location while keeping intact image of the faint substellar companions. It consists in the combination of two or three images taken at the same time and close wavelengths in the IFS mode. These simultaneous images are selected in and out of a deep absorption feature of the companion spectrum (e.g. CH_4 in the H-band). After scaling and subtracting the images, it results in a removal of the residual starlight while leaving the companion light intact. A generalization of this technique was proposed.[13] Here, we consider the SSDI technique as a particular case of a proposed algorithm in the literature.[14]

A first image processing can be realized before the application of the SSDI method. It consists in removing the azimuth symmetric component from the coronagraphic images.[13] An azimuth average of a coronagraphic image is estimated to obtain a radial profile. Thereafter, this calculated component is extended azimuthally to obtain an image of the halo, which will be substracted from the coronagraphic image. This operation allows to provide a halo free coronagraphic image and reach a first contrast gain to our coronagraphic images. The halo free coronagraphic profile is obtained by averaging azimuthally the intensity of the halo free coronagraphic image. This operation can be applied to three coronagraphic images taken simultaneously at three close wavelengths before processing them with the SSDI technique.

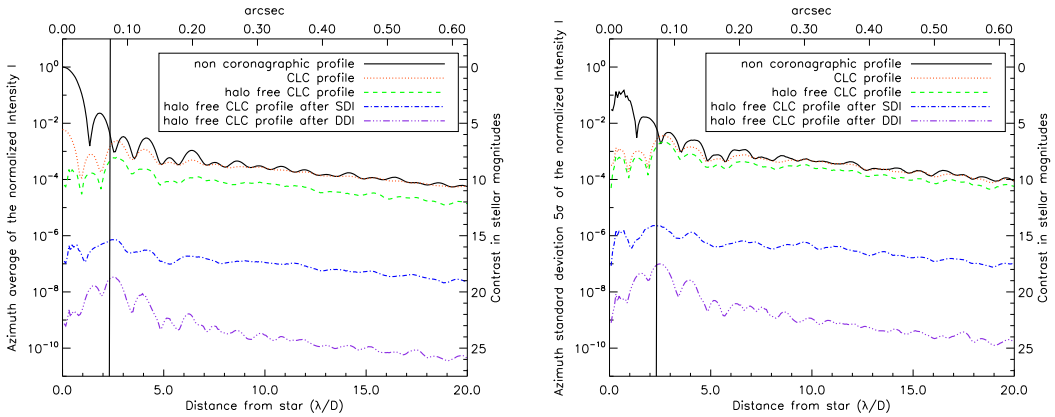

Figure 8. **Left**: Azimuth averaged profiles of the non coronagraphic PSF and images obtained with CLC and different image processing techniques, for a 12% centrally obstructed telescope (GTC case), in H-band. **Right**: Profiles of the azimuth standard deviation 5σ of the normalized intensities I. The opaque mask of radius $2.30\,\lambda/D$ is delimited by a vertical line.

In the following lines, we briefly review the SSDI formalism.[1] Let us name I_1, I_2 and I_3 three halo free coronagraphic images at λ_1, λ_2 and λ_3 in the coronagraphic image plane, rescaled and resized with respect to the wavelength. The simple differential imaging (SDI) can be expressed by:

$$d_{12} = I_1 - I_2, \tag{1}$$

and the double differential imaging (DDI) can be written as:

$$dd = (I_1 - I_2) - k \times (I_1 - I_3), \tag{2}$$

with $k = (S_1 - S_2)/(S_1 - S_3)$ and where S_i denotes the Strehl ratio of the image I_i.

3.3 Numerical results

Once removed the azimuth symmetric component, we compute the SSDI technique with halo free coronagraphic images. The present approach is applied to the ground-based instrument we considered until now: "GTC + GTCAO + FRIDA". We make the following assumption: FRIDA is supplied with CLC and works in IFS mode. FRIDA should provide a data cube of images at several wavelengths and it will be possible to select those of our interest. Furthermore, FRIDA is supposed to work in its low spectral resolution mode ($R \sim 1500$). Three CLC images are extracted from the FRIDA data cube in and out of one companion absorption feature, at the respective wavelengths $\lambda_1 = 1.5700\,\mu m$ (feature of the target's object spectrum), $\lambda_2 = 1.5710\,\mu m$ and $\lambda_3 = 1.5720\,\mu m$. Thereafter, halo is removed from each of CLC frames. In the present simulations, we did not rescale and resize the images because bandpass separations are very small compared with the array dimensions with which we worked (1024×1024). The Strehl ratio values S_1, S_2 and S_3 of the images, calculated with the Marechal approximation, are respectively: 0.552061, 0.552472 and 0.552883 and therefore, $k = 0.5$.

Fig. 8 gives on the left plot, the azimuth averaged intensity profiles achieved after each step to reach high contrast imaging and on the right plot, the $5\,\sigma$ detectability graphs for each one of the previous intensity profiles. On the left plot, the profiles represent successively from the top: the AO corrected image, the CLC images before and after removal of the azimuth symmetric component, and the halo free CLC images after application of SDI or DDI technique. On the right plot, the $5\,\sigma$ value gives us an idea about the detectability of a faint substellar companion in presence of residual speckles. The achieved values remains faint enough to consider the different

Table 3. Contrast gain reached with CLC configuration and additional image processing techniques for FRIDA

Profile	**Contrast gain in stellar mag. Δm at an angular separation (in λ/D):**					
	4.0	6.0	8.0	10.0	12.0	20.0
CLC profile	0.84	0.59	0.16	0.05	0.11	0.03
Halo free CLC profile	2.43	2.13	1.62	1.40	1.44	1.43
Halo free CLC profile after SDI	9.64	9.04	8.73	8.44	8.42	8.35
Halo free CLC profile after DDI	13.93	14.54	14.83	14.99	15.13	15.28

azimuth averaged intensity profiles as good representations of their respective images.

Fig. 8 left plot allows us to confirm that some additional intensity attenuations can be reached between the halo free CLC profile and the same one after application of respectively SDI or DDI. With CLC, the removal of the azimuth symmetric component and the application of the SDI or DDI technique, a contrast gain $\Delta m = 9.64$ (with SDI) or 13.93 (with DDI) can be achieved. These values are obtained estimating the azimuth averaged intensity over a range of width $1.0\,\lambda/D$ centered around the angular separation of $4.0\,\lambda/D$ from the main optical axis. Table 3 summarizes the contrast gain results that can be reached with CLC associated with image processing techniques, at a given angular distance from the the main optical axis.

3.4 Discussion

3.4.1 Non common path instrumental aberrations

These first results are very encouraging for the direct detection of dim substellar companions close to bright stars. However, in our numerical simulations, we consider AO residual speckles but quasi-static residual speckles were not taken into account. Quasi-static residual speckles are due to the non-common path errors present within an instrument. In the case of FRIDA, the phase errors are estimated to be equal to $50\,nm$ what corresponds to a variance of these quasi-static speckles $\sigma^2_{\varphi_2} = 0.040\,rad^2$ at $\lambda = 1.57\,\mu m$. In comparison, the variance of the AO residual speckles is $\sigma^2_{\varphi_1} = 0.594\,rad^2$. Considering the optical aberrations present within FRIDA would naturally carry out to a re-adjustment of the Strehl ratio of their images: $S = 0.537$ instead of 0.552 at $\lambda = 1.57\,\mu m$. The difference is negligible at level of image quality. Moreover, several techniques were developed these past few years to overcome the quasi-static speckles: in particular, we can mention the Angular Differential Imaging.[15]

3.4.2 A concrete case...

Simulations about the achievable contrast gain with "coronagraphy + image processing methods" are very promising. However, they have to be relativized: a comparison with the different noise source thresholds is required to validate them. A more realistic analysis would allow to determine accurately the class of faint sources we can hope to image. In the following approach, we decide to consider a more concrete case. It aims to give an first idea about the potential of these techniques for FRIDA. Fig. 9 refers to Fig. 8 but here, the normalized intensity values were replaced by those of a $4.60\,mag$ star in H-band and are now expressed in amount of photons (or photo-electrons). Furthermore, photon noise and readout noise thresholds were also added. A 1 hour time exposure was considered to plot the different profiles and we assume that this total exposure time is split in 4 to allow dithering and for the sky subtraction.

The characteristics of the FRIDA detector[16] allow to determine an image dynamic range $\Delta m = 10.75\,mag$ for the GTC science instrument. In the context of high contrast imaging, we want to fully benefit from this range of values. In FRIDA IFS mode at $R = 1500$ and working with fine scale ($0.01\,arcsec/pixel$ in the spatial direction), the limiting magnitude (or readout noise) will be equal to 20.7, in presence of a bright natural guide star. Hence, a $9.95\,mag$ star is the brightest one observable by FRIDA without risk of detector saturation, while reaching the limiting magnitude. The interest of the coronagraph results in its ability to increase this value and therefore, observe stars brighter than those of $9.95\,mag$ without detector saturation. The application of CLC

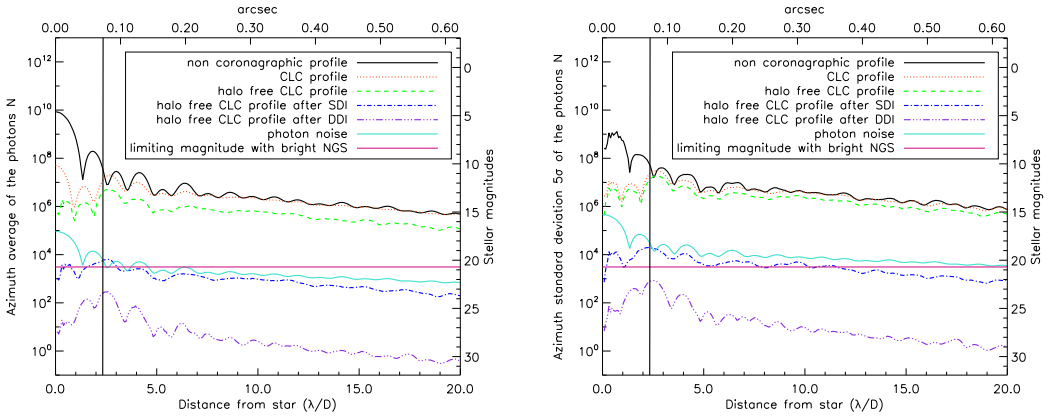

Figure 9. Same as Fig. 8 but here, the normalized intensity values were replaced by those of a 4.60 mag star in H-band and are now expressed in amount of photons. Furthermore, photon noise and readout noise thresholds were also added.

will mainly consist in reducing the PSF diffraction core. Here, since we consider a 4.60 mag star, CLC use will imply a $\sim 11\,mag$ maximum of intensity as shown in Fig. 9.

We work in IFS mode at $R = 1500$ therefore, images present in the FRIDA data cube are separated by a bandwidth $\Delta\lambda \simeq 1\,nm$. In this mode, it is assumed that each slice projects to two pixels which can be identified as a resolution element (resel). At $R = 1500$, the covered bands are $H + K$ or equivalently $1.4 - 2.4\,\mu m$ in bandpass and therefore, the width is equal to $1\,\mu m$. Since the detector format is 2048×2048, we will obtain $1000\,resel$ of bandwidth $1\,nm$. In presence of CLC, the maximum number of photo-electrons is $\sim 10^8$ and the maximum number of photo-electrons per exposure is 10^5, thus, 1000 exposures are required to achieve the presented result. It gives an integration time $t_{int} = 3.6\,s$. Fig. 9 left plot allows to notice that with the association "CLC + azimuth symmetric component removal + SDI", it would be possible to reach the photon or readout noise limit and maybe detect a $19\,mag$ substellar companion close to a $4.6\,mag$ brilliant star. At $4\lambda/D$ from the main optical axis, the limit is imposed by the photon noise and/or the read noise.

A quick comparison could be done with a previous study about *AB Doradus A*[13] using some image processing techniques but no coronagraph. *AB Dor A* and *AB Dor C* are respectively a $4.6\,mag$ star and its $9.6\,mag$ low-mass companion in K-band. Their angular separation is about $0.2\,arcsec$. The SINFONI AO system provided a mean Strehl ratio $S = 0.36$. In our case, the parent star presents the same magnitude than *AB Dor A* but in H-band and in our simulations, $S = 0.55$. Hence, the star halo presents a $\sim 12\,mag$ threshold at $0.2\,arcsec$ instead of $10\,mag$. So, an eventual $9.6\,mag$ low-mass companion in H-band would be already detectable with the simple AO system. The addition of coronagraphy and image processing methods would facilitate the enhancement of *AB Dor C* or also allow to detect fainter companions at the same angular separation with FRIDA. These predictions allow to be optimistic about the ability of FRIDA to provide high contrast imaging.

4. CONCLUSION

First numerical results of the association "coronagraph + image processing techniques" are promising for FRIDA. Indeed, detector saturation can be avoided while reaching a first increase of the image contrast with a coronagraphic device. Furthermore, two or three coronagraphic images taken at the same time can be combined: we can start removing the azimuth symmetric component for each one of them to achieve a first contrast gain. Thereafter, SSDI technique can be applied to provide some additional starlight attenuation. An extension of the

SSDI technique to more than three images was suggested[14] and would carry out to a complete characterization of an eventual dim stellar object. However, these first estimates constitute a first step and prove to be very encouraging for FRIDA to do direct detection of faint substellar companions close to bright stars.

ACKNOWLEDGMENTS

We are grateful for a grant from the Grupo Santander (Spain) through Encuentros Astrofísicos Blas Cabrera (UNAM-IAC), and our home institutions for their support. M. N'Diaye is supported by a fellowship from the Foreign Office of the Mexican Government.

REFERENCES

[1] Marois, C., Doyon, R., Racine, R., and Nadeau, D., "Efficient Speckle Noise Attenuation in Faint Companion Imaging," *Public. of the Astron. Soc. Pac.* **112**, 91–96 (Jan. 2000).

[2] López, J. A., Bringas, V., Cuevas, S., Díaz, J. J., Eikenberry, S. S., Espejo, C., Flores, R., Fuentes, F. J., Gallego, J., Garzón, F., Hammersley, P., Pelló, R., Prieto, A., Sánchez, B., and Watson, A., "FRIDA: The first instrument for the adaptive optics system of GTC," in [*Revista Mexicana de Astronomia y Astrofisica Conference Series*], *Revista Mexicana de Astronomia y Astrofisica* **29**, 18–20 (June 2007).

[3] Devaney, N., Bello, D., Femenia, B., Castro, J., Villegas Lopez, A., Reyes, M., and Fuensalida, J. J., "Preliminary design and plans for the GTC adaptive optics system," in [*Advancements in Adaptive Optics. Edited by Domenico B. Calia, Brent L. Ellerbroek, and Roberto Ragazzoni. Proceedings of the SPIE, Volume 5490, pp. 913-923 (2004).*], Bonaccini Calia, D., Ellerbroek, B. L., and Ragazzoni, R., eds., *Presented at the Society of Photo-Optical Instrumentation Engineers (SPIE) Conference* **5490**, 913–923 (Oct. 2004).

[4] Carbillet, M., Vérinaud, C., Femenía, B., Riccardi, A., and Fini, L., "Modelling astronomical adaptive optics - I. The software package CAOS," *MNRAS* **356**, 1263–1275 (Feb. 2005).

[5] Guyon, O., Pluzhnik, E. A., Kuchner, M. J., Collins, B., and Ridgway, S. T., "Theoretical Limits on Extrasolar Terrestrial Planet Detection with Coronagraphs," *ApJS* **167**, 81–99 (Nov. 2006).

[6] Soummer, R., Aime, C., and Falloon, P. E., "Stellar coronagraphy with prolate apodized circular apertures," *A&A* **397**, 1161–1172 (Jan. 2003).

[7] Roddier, F. and Roddier, C., "Stellar Coronograph with Phase Mask," *Public. of the Astron. Soc. Pac.* **109**, 815–820 (July 1997).

[8] Soummer, R., "Apodized Pupil Lyot Coronagraphs for Arbitrary Telescope Apertures," *ApJL* **618**, L161–L164 (Jan. 2005).

[9] N'Diaye, M., Dohlen, K., and Cuevas, S. *In preparation* (2008).

[10] Racine, R., Walker, G. A. H., Nadeau, D., Doyon, R., and Marois, C., "Speckle Noise and the Detection of Faint Companions," *Public. of the Astron. Soc. Pac.* **111**, 587–594 (May 1999).

[11] Macintosh, B., Poyneer, L., Sivaramakrishnan, A., and Marois, C., "Speckle lifetimes in high-contrast adaptive optics," in [*Astronomical Adaptive Optics Systems and Applications II. Edited by Tyson, Robert K.; Lloyd-Hart, Michael. Proceedings of the SPIE, Volume 5903, pp. 170-177 (2005).*], Tyson, R. K. and Lloyd-Hart, M., eds., *Presented at the Society of Photo-Optical Instrumentation Engineers (SPIE) Conference* **5903**, 170–177 (Aug. 2005).

[12] Marois, C., "Speckle Noise Attenuation in Coronagraphy and High-Contrast Imaging," in [*In the Spirit of Bernard Lyot: The Direct Detection of Planets and Circumstellar Disks in the 21st Century*], Kalas, P., ed. (June 2007).

[13] Thatte, N., Abuter, R., Tecza, M., Nielsen, E. L., Clarke, F. J., and Close, L. M., "Very high contrast integral field spectroscopy of AB Doradus C: 9-mag contrast at 0.2arcsec without a coronagraph using spectral deconvolution," *MNRAS* **378**, 1229–1236 (July 2007).

[14] Sparks, W. B. and Ford, H. C., "Imaging Spectroscopy for Extrasolar Planet Detection," *ApJ* **578**, 543–564 (Oct. 2002).

[15] Marois, C., Lafrenière, D., Doyon, R., Macintosh, B., and Nadeau, D., "Angular Differential Imaging: A Powerful High-Contrast Imaging Technique," *ApJ* **641**, 556–564 (Apr. 2006).

[16] Watson, A. M., "FR/FR-SC/040: Signal and Noise estimates," FRIDA technical note, Centro de Radioastronomía y Astrofísica - Universidad Nacional Autónoma de México (jun 2007).